NATIONAL TECHNICAL UNIVERSITY OF ATHENS

DOCTORAL THESIS

Geometrically Non-Linear Beam Modeling of Wind Turbine Blades under Static and Dynamic Loadings

Author:
Anthoula PANTELI

Supervisor:
Dr. Konstantinos SPILIOPOULOS

A thesis submitted in fulfillment of the requirements
for the degree of Doctor of Philosophy

in the

Institute of Structural Analysis and Antiseismic Research
School or Civil Engineering

March 1, 2023

Declaration of Authorship

I, Anthoula PANTELI, declare that this thesis titled, "Geometrically Non-Linear Beam Modeling of Wind Turbine Blades under Static and Dynamic Loadings" and the work presented in it are my own. I confirm that:

- This work was done wholly or mainly while in candidature for a research degree at this University.
- Where any part of this thesis has previously been submitted for a degree or any other qualification at this University or any other institution, this has been clearly stated.
- Where I have consulted the published work of others, this is always clearly attributed.
- Where I have quoted from the work of others, the source is always given. With the exception of such quotations, this thesis is entirely my own work.
- I have acknowledged all main sources of help.
- Where the thesis is based on work done by myself jointly with others, I have made clear exactly what was done by others and what I have contributed myself.

Signed:

_____

Date:

_____

«Το πρώτο σου χρέος, εχτελώντας τη θητεία σου στη ράτσα, είναι να νιώσεις μέσα σου όλους τους προγόνους. Το δεύτερο, να φωτίσεις την ορμή τους και να συνεχίσεις το έργο τους. Το τρίτο σου χρέος, να παραδώσεις στο γιο τη μεγάλη εντολή να σε ξεπεράσει.»

Νίκος Καζαντζάκης

"*Your first duty, fulfilling your tenure in the breed, is to feel inside all your ancestors. The second one, to illuminate their momentum and continue their work. Your third debt, to hand over to your son the great command to overcome you.*"

Nikos Kazantzakis

NATIONAL TECHNICAL UNIVERSITY OF ATHENS

Abstract

Institute of Structural Analysis and Antiseismic Research
School or Civil Engineering

Doctor of Philosophy

Geometrically Non-Linear Beam Modeling of Wind Turbine Blades under Static and Dynamic Loadings

by Anthoula PANTELI

In this thesis, three main studies are performed. The first study contains the investigation in structural analysis of two geometrically non-linear beam models, the Simo-Reissner (SR) and the Green-Lagrange (GL) beam models. These models are compared with each other both theoretically and numerically. Moreover, the strain-invariant formulation, that accounts for the numerical invariance of the internal elastic energy under a rigid-body rotation of the finite element, is implemented for both approaches. This is a new development for the GL beam model. The second study regards the investigation of two time integration algorithms, which are considered as Newmark-type algorithms, for rigid-body dynamics with large 3D rotations. In the third study, the geometrically exact SR beam model and one of the two Newmark-type time integration scheme are integrated into the multi-body dynamics code hGAST, for the aeroelastic analysis of the coupled wind turbine system. The results obtained for the slender wind turbine blades are compared to those derived by the sub-body (SB) technique, which is a method to capture the geometric non-linearity using the multi-body concept at the body level combined with linear beam elements. Interesting conclusions are extracted from this work. Regarding statics, it is shown that 1) because of the extra strain terms of the GL beam model compared to the SR beam model, which contain the square of the curvatures of the beam reference line, a different approximation of the axial and shear strain measures inside the beam element is obtained, and 2) the invariant formulation, originally proposed for the SR beam model, functions well for the GL beam model, too. Regarding dynamics, the accuracy and stability of each time integration algorithm are depicted in the response of the well-known example of the fast symmetrical top, either for short or long simulation time. Finally, the results obtained for the coupled wind turbine system show a very good behaviour of the geometrically exact beam modeling of the blades, for both uniform and stochastic inflow conditions.

Acknowledgements

I would like to express my gratitude to the following people:

- my supervisor, Professor Konstantinos Spiliopoulos, who trusted me and gave to me the great opportunity to do this research work by staying in my country. His support has been precious in many ways, either on the scientific or on the human part, throughout this beautiful "equilibrium" path of life that sometimes needed many "iterations" to converge.

- Professor Spyridon Voutsinas for our creative conversations.

- Professor Kiriakos Giannakoglou for being there when I needed him, as the 3rd member of the advisory committee.

- Associate Professor Vasilis Riziotis for his support on the part of our work related to the wind turbines, and for being a member of the examining committee.

- Professor Gordan Jelenić for accepting me at the faculty of civil engineering of the university of Rijeka through the ERASMUS+ programme, and for being a member of the examining committee.

- the other two members of the examining committee, Professor Vissarion Papadopoulos and Professor Evangelos Sapountzakis.

- former Assistant Professor Maja Gaćeša for her enthusiasm and support.

- my 'mechanical engineering' colleague, Dr. Dimitris Manolas, for his passion, his great knowledge and his felicitous comments on my work.

- my 'structural engineering' colleagues, Amalia Argyridi, Antonis Siokas, Pagina Syrimi, Kostis Kapasakalis, Maria Tavlaki, George Stavroulakis, Yiannis Kapogiannis, Yiannis Kalogeris, Maria Kardala, Alexander Karatarakis, Theophilos Manitaras, Konstantinos Mpaskourelos, George Papazafeiropoulos, and Kimonas Antoniadis, for our lovely time during our scientific and other conversations, inside and outside the lab.

- Lia Theofanidou, Eleana Boni, Eva Konti, Jenny Mitsoura, Rania Sagka, Mika Stylianou, and all the other administration and secretary stuff for helping us with the necessary document works.

I would like to thank my parents, Nikos and Christina, for giving to me my wings; my brothers, Manolis and Mihalis, for being my company in my whole life; my friends from Kefalos, Vaggelitsa, Stamatia, Ioanna, Maria, for being my extended family; and my friend, Evangelos Katsavrias, who showed me the beauty of exploring our nature and was there in the difficult time with optimism and power.
I am so much thankful to my husband, Ilias, and our sons, Yiannis and Nikos. They give me the strength to go on every single day. Also, I could not have finished this thesis without the incredible support from my mother in law Mairi; her love and care are invaluable. I thank

very much my sister in law Vaso, and my grand mother in law Vasiliki, for being next to us taking care of us. I so much appreciate and love them.

Finally, I would like to gratefully acknowledge the financial support I received as a scholar from the following foundations: the Foundation for Education and European Culture, the Leventis Foundation, the Fanourakis Foundation, and the NTUA Special Account for Research Grants.

All of you above have contributed in a precious way to the improvement of myself, as a human and as a scientist. I have to share this work with you.

Anthoula Panteli
Athens, February 2023

Contents

List of Figures

List of Tables

List of Abbreviations

BECAS	**BE**am **C**ross section **A**nalysis **S**oftware
BEMT	**B**lade **E**lement **M**omentum **T**heory
DEL	**D**amage **E**quivalent **L**oads
DLC	**D**esign **L**oad **C**ase
DOF	**D**egree **O**f **F**reedom
DTU	**T**echnical **U**niversity of **D**enmark
FEM	**F**inite **E**lement **M**ethod
GL	**G**reen-**L**agrange
hGAST	**G**eneral **h**ydro-**A**eroelastic **S**tructural **T**ool
IEC	**I**nternational **E**lectrotechnical **C**ommission
LHS	**L**eft **H**and **S**ide
NTUA	**N**ational **T**echnical **U**niversity of **A**thens
RHS	**R**ight **H**and **S**ide
RWT	**R**eference **W**ind **T**urbine
SR	**S**imo-**R**eissner
SB	**S**ub-**B**ody
WT	**W**ind **T**urbine

To the companion of my life, Ilias
To our sons, Yiannis and Nikos

Chapter 1

Introduction

1.1 Motivation

Wind energy is an important sustainable, renewable source of energy. This is converted into mechanical power through wind turbines, which subsequently, turns electric generators to produce electricity. An overview of wind energy and wind turbine design one could study in Burton et al., 2001; Manwell, Mcgowan, and Rogers, 2009; Chiras, 2010. Currently, wind energy technology development points towards larger rotors with thin, lightweight, and flexible blades that are deployed offshore. Related to this, advanced numerical aero-mechanical tools are required that can accurately predict the aeroelastic behaviour of such rotors. From the structural point of view, their large size (e.g., a rotor can have a diameter that is about 180 m) results to the need of powerful numerical tools that can analyze slender, beam-like, structures which undergo large displacements. Current state-of-the-art in the aeroelastic analysis of wind turbine blades is based on 1D beam modeling. They are preferable over 2D shell and 3D solid models, because they are cost effective and, for most applications, equally accurate in predicting internal forces and moments along the blade structure. In Júnior et al., 2019, it is shown that the beam model is in very good agreement with the shell model except from the case of local buckling of a wind turbine blade, that cannot be predicted using a conventional beam model (a generalized beam model could be used, instead, Argyridi, 2019).

The main subject of this work is the theoretical and numerical investigation of two beam models that appear in the literature for simulating slender structural members that undergo large translations and rotations. Based on this investigation, the main objective of this work is the adoption of the most reliable beam model in the applications. Another objective is the extension of the structural part of the comprehensive hydro-servo-aero-elastic code hGAST developed at the Fluids Section of the Mechanical Engineering School of NTUA (Riziotis and Voutsinas, 1997), for the coupled analysis of a wind turbine system. Two issues are involved in this project: the one is the choice of an appropriate beam model to simulate the wind turbine blades, and the other is the modification of the solution procedure to be consistent with systems that undergo large 3D rotations. Therefore, the geometrically exact SR beam model is integrated into the multi-body dynamics software hGAST, while the Newmark-type time integration algorithm in Simo and Vu-Quoc, 1988 is used.

A typical wind turbine onshore configuration consists of five components, i.e., three blades, a shaft and a tower, from which the blades can undergo large translations and rotations, while

the strains are kept small. Couplings between the deformation states of tension, shear in two directions, bending in two directions, and twist are present during their motion. Although the SB technique, that captures this geometric non-linearity based on a multi-body concept, has already been implemented into hGAST, an approach that is geometrically exact improves the accuracy using a coarser discretization compared to the SB modeling. Moreover, this approach can function on its own, without the need of a preceding work on a multi-body formulation. Therefore, a geometrically exact beam model that satisfies the assumptions of large displacements and small strains is chosen for the analysis of the coupled wind turbine system. The *geometrically exact* term used for this formulation implies that "*the relationships between the configuration and the strain measures are consistent with the virtual work principle and the equilibrium equations at a deformed state regardless of the magnitude of displacements and rotations*", as it is clarified in Crisfield and Jelenić, 1999.

1.2 State of the art

The beam models are used for the deformation and motion analysis of those structural members whose cross-section dimensions are much smaller than the longitudinal one. Because of this slenderness property, the 3D non-linear continuum mechanics problem may be decoupled into one 2D cross-section (usually linear) problem and one 1D geometrically non-linear beam problem (Berdichevsky, 2009). In Hodges, 2006, the whole beam modeling process is presented in detail. The derived one-dimensional element that is available in finite element codes is simple use, and suitable for the engineering design, even for the design of complex structural systems. Examples of such systems are found e.g., in civil, mechanical, aerospace, marine and biological engineering. Applications can be the deployable tents, the large wind turbine blades, the masts, the antennas, the tower cranes, etc., see e.g., Hinkelmann, Lumpe, and Rothert, 1985.

The essential beam theory (rod theory) assumes that the cross-sectional plane remains planar and rigid during deformation. A comprehensive study in the history of the rods' mechanics, including planar and spatial elastica investigated by the theorists and experimentalists of almost 350 years of research, is given in Goss, 2003. Some improved theories include the out-of-plane warping under both torsion and shear, and the in-plane warping (or distorsion), see e.g., Petrov and Géradin, 1998; Simo and Vu-Quoc, 1991. The more recent, advanced (or higher-order) beam theories assume additional cross-section deformation states (Dikaros, 2016). Higher-order kinematics of beams is also used in Silvestre, Camotim, and Silva, 2011; Abambres, Camotim, and Silvestre, 2014, where the GBT (Generalized Beam Theory) is presented. Also, the GBT together with the ICM (Implicit Corotational Method) that takes into account the geometric non-linearity is formulated in Miranda et al., 2017.

Focusing here on the geometrically non-linear beam modeling with planar and rigid cross-sections, different three-dimensional working pairs that fully account for the internal elastic energy are used to derive a geometrically non-linear 1D beam theory with small strains. In Pai, Palazotto, and Greer, 1998, various strain and stress definitions for a geometrically non-linear analysis are investigated, concluding that the Jaumann working pair (Pai and Nayfeh,

1994; Hodges, 2006) is the most appropriate one. The other two most popular working pairs are the first Piola-Kirchhoff stresses combined with displacement gradients (Simo, 1985) and the second Piola-Kirchhoff stresses combined with Green-Lagrange strains (Sapountzakis and Dikaros, 2011; Bauchau, 2011). A theoretical and numerical comparison between the 1D beam models starting from these working pairs, i.e., a) the SR beam model (Reissner, 1981; Simo, 1985) and b) the GL beam model (Bathe and Bolourchi, 1979; Dvorkin, Onate, and Olivier, 1988) can be found in Panteli and Spiliopoulos, 2020. In most of the codes employing a geometrically exact beam model, the deformation gradient tensor with the first Piola-Kirchhoff stress tensor is used. This formulation has originally been presented in Simo, 1985 where the equivalent strain measures for the beam element are derived. Regarding the numerical implementation, in Simo and Vu-Quoc, 1986a, the corresponding computational aspects have been proposed, where the connection to the rotation manifold $SO(3)$ is shown, setting the ground for a mathematical explanation of the incremental non-linear analysis of beams. A displacement-based finite element implementation is followed, as in most relevant works.

As far as the numerical procedures are concerned, they can be separated into two categories (Crisfield and Jelenić, 1999): the so called degenerate-continuum beam formulations (see e.g., Bathe and Bolourchi, 1979; Dvorkin, Onate, and Olivier, 1988; Bathe, 1996; Crisfield, 1997) that start with the continuum equilibrium equations, and the direct 1D continuum models (see e.g., Reissner, 1972; Reissner, 1981; Simo, 1985; Simo and Vu-Quoc, 1986a and the most recent works Sonneville, Cardona, and Brüls, 2014; Gaćeša, 2015; Gaćeša and Jelenić, 2015) that are derived directly from the resultant form of the differential equilibrium equations. In the first category, the approximated virtual work equation is given at an arbitrary material particle of the cross-section, while in the second category, this equation is given at the reference point of the beam.
Regarding the spatial discretization of the problem, much effort has been made in the recent years for the development of an objective (or strain-invariant under superposed rigid-body rotations of the beam element) and a path-independent finite element formulation. In Crisfield and Jelenić, 1999, the way is paved for such investigations, where the topic is raised for the SR beam element. In Jelenić and Crisfield, 1999, the same researchers propose a discrete formulation that preserves the objectivity of the continuum problem and the history independence of its solution. The crucial point in Jelenić and Crisfield, 1999, which should be applied to all formulations where the rotation parameters are involved, is to ensure the consistency with the configuration space which is inhabited by the orthogonal tensors describing the orientation of the cross-section, i.e., the 3D rotation group $SO(3)$. For this reason, the cross-section orientation matrix is decomposed into two matrices (decomposition in a co-rotational manner): the one which describes the orientation of the element and the one which describes the local cross-section rotation relatively to the element. To ensure the strain invariance under a rigid-body rotation of the element, the implementation presented in Jelenić and Crisfield, 1999 is used by some researchers in the wind energy sector (*BeamDyn Theory*). Alternatively, the fixed pole formulation (Bottasso, Borri, and Trainelli, 2002)

can be adopted that automatically guarantees the numerical invariance. Other finite element developers who have done research on the 3D beam formulation regarding the invariance properties of objectivity and path-independence, e.g., Romero and Armero, 2002, present the directors, their variations and velocities, to be chosen as the nodal kinematic variables in discrete dynamic equilibrium equations, instead of the corresponding rotations, their variations and angular velocities; the same idea is presented in discrete static equilibrium equations for the degenerate-continuum formulations in Bathe, 1996; Crisfield, 1997. Also, Betsch and Steinmann, 2002 followed a similar formulation. The constraint equation imposed on the directors, for the conservation of their orthonormality, retains the invariance of these models. Recently, a single map that belongs to the group $SE(3)$ is used for the description of beam kinematics. This means that these formulations do not split the motion of the material particle into two parts, i.e., the displacement of the beam reference point and the rotation of the cross-section. On the contrary, they treat the motion of the material particle as a whole, see e.g., Bottasso and Borri, 1998. Some other works on this subject are given in Sonneville, Cardona, and Brüls, 2014; Gaćeša, 2015; Gaćeša and Jelenić, 2015. The above finite element procedures refer to shear-deformable rods. In case of shear-free Kirchhoff rods, that are used to model very slender beams more efficiently, Meier, Popp, and Wall, 2014; Meier, Popp, and Wall, 2015 have proposed an objective and path-independent formulation.

The state-of-the-art, that is included in the above literature, refers to rod-like beam structures with solid and symmetric cross-sections. But, the wind turbine blades have a general-shaped cross-section, i.e., an airfoil, constructed by an anisotropic and inhomogeneous material. They are primarily made of composite materials that combine fibers with polymer resins to form glass-or carbon-fiber-reinforced polymers (GFRP or CFRP). Therefore, an anisotropic beam element is needed for their simulation that is independent from the way that the geometric non-linearity is taken into account. Recent research is based on the investigation of the appropriate shape functions a beam has to possess for capturing the material couplings accurately, regardless of it is a linear or a non-linear one. For an anisotropic Timoshenko beam element in 3D, the interested reader can see in Ghiringhelli, 1997; Bazoune, Khulief, and Stephen, 2003; Luo, 2008; Kim, Hansen, and Branner, 2013; Stäblein and Hansen, 2016.

For studying the dynamics of beams, many algorithms for analyzing beams subjected to time dependent loading are presented in the literature. They can roughly be separated into two categories: to those that do not account for the conservation of the total energy and the momentum, and to those that they do retain the total energy and sometimes the total momentum, too (conserving algorithms). The second type of algorithms are designed to be unconditionally stable. The Newmark method given in Newmark, 1959 for linear systems, which is extended to problems with large rotations by some researchers, is not conserving. Newmark-type methods for non-linear systems are given e.g., in Simo and Vu-Quoc, 1988; Cardona and Géradin, 1988; Ibrahimbegović and Mikdad, 1998; Mäkinen, 2001. Conserving time integrators for non-linear beam problems are given in Simo, Tarnow, and Doblare, 1995 and

Ibrahimbegović and Mamouri, 2002. Herein, two time integration algorithms from the literature are presented. These are given in: 1) Simo and Vu-Quoc, 1988, and 2) Mäkinen, 2001; Cardona and Géradin, 1988. These algorithms share the following common feature: They establish the equilibrium at the time instant t_{n+1}, where the equation of the rate of angular momentum balance is solved, thus, they are both considered as Newmark-type schemes. However, the motivation of studying both of them is that the first algorithm uses the Newmark scheme for the angular velocities and accelerations, whereas the second algorithm uses the Newmark scheme for the first and second derivatives of the rotation vector, respectively.

Regarding the structural dynamics part inside the framework of a multi-body dynamics software, the comprehensive state-of-the-art tools for the coupled aero-elasto-dynamic analysis of wind turbine systems use 1D structural members to simulate all flexible components of the structure. According to Gambier and Balzani, 2019, there are several aero-elastic design tools for the time domain analysis of wind turbines, some of which are commercial (e.g., Bladed from DNV GL, Hassan, 2011, Cp-Lambda, Bottasso and Croce, 2006-2015, from Politecnico di Milano and HAWC2 from DTU, Larsen and Hansen, 2021), while other are open source (e.g., FAST, Jonkman and Buhl, 2005, from National Renewable Energy Laboratory). An overview of the most popular aeroelastic codes can be found in Wang, Liu, and Kolios, 2016; Ageze, Hu, and Wu, 2017. One can divide these simulation tools into two main categories, regarding the type of the 1D beam structural model used. The first category employs 1D geometrically non-linear beam elements, e.g., latest versions of FAST (Wang et al., 2017; *BeamDyn Theory*) and Cp-Lambda (Bauchau, Damilano, and Theron, 1995), while the second uses 1D linear beam elements combined with a multi-body approach at the body level in order to capture the geometric non-linearity, e.g., HAWC2 and hGAST (Riziotis and Voutsinas, 1997; Manolas, Riziotis, and Voutsinas, 2015; Bagherpour et al., 2018; Manolas et al., 2020; Manolas, 2015). A comparison between the two approaches can be found in Pavese et al., 2015 where benchmark cases of beams undergoing extreme translations and rotations are analyzed in order to showcase that, in such extreme conditions, a multi-body approach implemented at the component level can accurately predict the elastic deflections. Another comparison between state-of-the-art aeroelastic tools adopting the above two non-linear beam approaches is performed in Manolas et al., 2015 within the course of INNWIND.EU project. The beam models employed, are found to well compare against a 3D Finite Element Method (FEM) solver up to the seventh mode shape, consistently predicting strong coupling effects. The models are also tested in static and dynamic/turbulent calculations and overall good agreement is found, including cases where the bending-torsion geometrically non-linear effect is triggered due to the high flap-wise deflections. It is worth mentioning that for the beam modeling of wind turbine blades, which are made by composite materials, a pre-processor to compute the cross-sectional stiffness and inertia properties along the length of the beam-like member is needed, based on either the FEM (Blasques, 2012; Yu et al., 2002a) or the thin lamination theory (Saravanos et al., 2006; Serafeim et al., 2022).

1.3 Contribution of the thesis

The thesis contributes to the clarification of several special issues that concern the development of a geometrically non-linear beam model. This is achieved through the theoretical and numerical investigation of two beam models that appear in the literature, which are used to simulate slender members subjected to large translations and rotations. Another contribution of this work is the extension of the existing multi-body dynamics code hGAST, with regard to its structural dynamics part. The original version (Riziotis, Chaviaropoulos, and Voutsinas, 1996; Riziotis and Voutsinas, 1997; Riziotis, 2003) used linear Euler-Bernoulli beam theory. Since then hGAST went through several revisions and extensions. Inside the course of the present thesis, a geometrically non-linear beam modeling is integrated into the hGAST software that analyzes the coupled wind turbine system, for capturing the behaviour of the blades imposed to wind loading. Considering the presence of large rotations as the degrees of freedom of the system, the beam stiffness and inertia, and the solution procedure (the time integration algorithm) should be consistent to the rotation manifold $SO(3)$. Therefore, the issues that had to be investigated are:

1. The beam models that are available in the literature, and also appropriate to capture well the behaviour of the wind turbine blades; they undergo large translations and rotations, but the strains are kept small.

2. The time integration algorithms that are available in the literature, and also appropriate for geometrically non-linear problems with large rotations.

3. The extension of the multi-body dynamics code hGAST regarding the above two issues: the geometrically-exact beam modeling and the consistency to the manifold $SO(3)$ of the time integration scheme.

Regarding the statics of beams, a comparative study between two models on the geometrically non-linear beam modeling is presented. The kinematics refer to the essential theory, known also as the Special Theory of Cosserat Rods (Antman, 2005). A degenerate-continuum beam model (Dvorkin, Onate, and Olivier, 1988; Bathe, 1996) (that uses the working pair Green-Lagrange strains/ second Piola-Kirchhoff stresses) is reduced to 1D after the integration in the cross-sectional domain has been performed analytically (see also Chen and Agar, 1993 where the same concept is followed), and the derived model is then compared to the 1D beam model that uses the SR strains and resultant stresses (Simo and Vu-Quoc, 1986a; Jelenić and Crisfield, 1999; Reissner, 1981) (which has been derived from the working pair displacement gradients/ first Piola-Kirchhoff stresses). To have a clear comparison between the GL and the SR beam model the idea to formulate the first one (Dvorkin, Onate, and Olivier, 1988; Bathe, 1996) in 1D arose naturally. Also, various computational advantages arise through the use of the 1D formulation as compared to the 3D formulation (Chen and Agar, 1993). The two beam models, the SR and the GL beam models, that have been developed starting from different three-dimensional working pairs, are compared, using an iterative and an invariant formulation. The numerical, strain invariant, treatment of the rotational unknowns that has been originally proposed in Jelenić and Crisfield, 1999 is

described on the manifold $SO(3)$. This geometric illustration given on the rotation manifold $SO(3)$ clarifies the way of creating an invariant 3D beam element with large rotations: one should refer to the same tangent space on $SO(3)$ when interpolation is performed. The beam models are used in a 3D geometrically non-linear analysis of a shear-deformable beam with rigid cross-sectional plane. Note that shearing is included as a first refinement of the classical Euler-Bernoulli theory (Yu et al., 2002b). Planar and spatial examples are solved, in order to examine the performance of the beam models.
The novel aspects of this work are: 1) the 1D formulation of the beam model which uses the GL strain tensor components so that is comparable to the SR beam model, 2) the demonstration of the numerical behaviour of this 1D model after incorporating an invariant update procedure described on the rotation manifold $SO(3)$, and 3) the comparison of the different strain measures of the two beam models through the use of numerical examples.

Regarding the dynamics part of this work, the geometrically exact SR beam model is incorporated into the multi-body aeroelastic code hGAST for the analysis of the wind turbine system. The original model is extended to general-shaped cross sections with inhomogeneous and anisotropic material. The default modeling option for highly flexible wind turbine blades in hGAST is the SB modeling combined with the linear Timoshenko beam element (Manolas, Riziotis, and Voutsinas, 2015), while in the past the second order Euler-Bernoulli beam model, in which terms up to second order are retained (Hodges and Dowell, 1974), and the fully non-linear shear deformable beam derived from 3D continuum with Green-Lagrange strains and second Piola-Kirchhoff stresses (Dvorkin, Onate, and Olivier, 1988) were studied (Manolas, Riziotis, and Voutsinas, 2015; Panteli, Manolas, and Spiliopoulos, 2016). In the SB context, large deflections and rotations gradually build up, whereas non-linear dynamics are introduced by imposing to each sub-body the deflections and rotations of preceding sub-bodies as rigid body, non-linear motions. In this work, hGAST is being further improved with the addition of a higher fidelity beam model, i.e., the geometrically exact SR beam model, Simo, 1985; Simo and Vu-Quoc, 1986a. The improvement concerns the fact that as non-linearities become more pronounced, the number of sub-bodies used in the multi-body analysis needs to increase in order to accurately capture these effects, while the SR beam model provides the same level of accuracy without increasing the spatial discretization. In this regard, cases of excessive deflections of lightweight and highly flexible blades can be dealt with, without needing to consider an overwhelming number of sub- bodies to achieve the desired level of accuracy. The strain-invariant formulation presented in Jelenić and Crisfield, 1999 and also investigated in Panteli and Spiliopoulos, 2020 is considered using the same implementation details as in Jelenić and Crisfield, 1999. The tool is verified in statics and dynamics against well-known benchmark examples that undergo large translations and rotations. In statics, the verification is performed against the 45-degree cantilever subjected to a fixed load at the tip (Bathe and Bolourchi, 1979), while the generality of the cross-section is verified according to Bagherpour et al., 2018. In dynamics, the results presented herein provide a comparison between the geometrically exact and the SB modeling in aeroelastic computations for the DTU-10MW RWT. The comparisons between the two techniques, the

geometrically exact and the multi-body approaches, result to the conclusion that both models can predict the geometric non-linearity sufficiently, except from the torsion moment at the root, and the angle of attack at the tip of the blade. It is shown that many sub-bodies are necessary to predict the same deformation state as with the SR model. The novel aspects of this work are the following:

1. A thorough assessment of the capabilities of the two most popular modeling options amongst Wind Energy community is performed. The two options have been developed within the same tool, as opposed to other similar works as in Pavese et al., 2015. The obvious advantage of the above approach is that any deviations or uncertainties related to the numerical details of the models (e.g., time integration scheme) or to modeling assumptions (e.g., modeling of lumped properties such as the generator inertia or nacelle mass) are eliminated.

2. The SR model is enriched with additional (non-diagonal) stiffness terms that account for the generality of the cross-sectional shape, as well as for the heterogeneity and the anisotropy of the material.

3. The SR model is enriched with extra inertial terms arising from the multi-body dynamics formulation adopted to describe the coupled dynamic behavior of the wind turbine system. Inertial terms due to the rigid-body or elastic motion of the previous bodies are introduced in the geometrically exact beam model.

1.4 Outline

The present work is divided into three main parts. The first part (chapter 3) includes the study of the two geometrically non-linear beam models theory in statics, the SR and the GL beam models theory, and the comparison between them. Also, the invariant formulation originally presented in Jelenić and Crisfield, 1999 is proposed to be incorporated into the GL beam model in order to be consistent with the rotation manifold $SO(3)$ at the implementation level. The second part (chapter 4) includes the study of the two Newmark-type time integration algorithms in rigid-body dynamics; 1) the Simo's & Vu-Quoc's (Simo and Vu-Quoc, 1988), and 2) the Mäkinen's (Mäkinen, 2001), together with Cardona's & Géradin's (Cardona and Géradin, 1988). In addition, the first algorithm is then used in dynamics of beams. The third part (chapter 5) includes the application of the SR beam model and the Simo's & Vu-Quoc's time integration algorithm in dynamics of the wind turbine system. Firstly, their implementation into the multi-body dynamics code hGAST is verified against benchmark examples, and secondly, the DTU-10MW RWT is analyzed.
Analytically, the thesis outline is as follows:
In chapter 2, some mathematical preliminaries on Lie groups are presented. The properties of the rotation manifold $SO(3)$ that are essential to develop a consistent to the configuration step-by-step analysis for the beam element are given.
In chapter 3, the theory for the two geometrically non-linear beam models that are investigated in the present work, the SR and the GL beam models, is presented; a comparison

between them is made regarding the strains that they use. The question that is given an effort to be answered in this chapter, is the reason that the SR beam model prevails in the geometrically non-linear regime with small strains against the GL beam model. Moreover, the iterative and invariant implementations inside the framework of displacement-based finite elements are explained, while the invariant formulation is also tested for the GL beam model (the original work on the invariant formulation of the SR beam model is given in Jelenić and Crisfield, 1999). These implementations refer to the way of treating the rotation parameters inside the finite element framework. The superiority of the invariant formulation is shown for both the SR and GL models through benchmark numerical examples.

In chapter 4, the two time integration algorithms, the Simo's & Vu-Quoc's and the Mäkinen's algorithms, for rigid-bodies with large 3D rotations, are investigated in order to use one of them into the dynamics of beams. The superiority of the Simo's & Vu-Quoc's scheme regarding stability, and the superiority of the Mäkinen's scheme regarding accuracy are depicted in the response of the well-known Lagrange's top example. Moreover, the dynamics of beams is presented for the SR beam model using the Simo's & Vu-Quoc's time integration scheme for large rotations.

In chapter 5, the incorporation of the SR beam model and the modification of the Newmark-type time integration algorithm for large rotations into the hGAST software is developed. The coupled wind turbine system is analyzed under a uniform and stochastic inflow for the onshore version of DTU 10-MW RWT.

In chapter 6, the overview of this work is presented, together with the ideas for further research.

Chapter 2

Mathematical preliminaries on Lie groups

2.1 Introduction

The geometrically exact beam theory involves manipulation and computation in the 3D geometry. As it is clearly noted out in Eade, 2017, without a coherent framework for representing and working with 3D transformations these tasks are cumbersome. Transformations must be composed, inverted, differentiated and interpolated. Lie groups address all these operations in a thorough way. Lie theory was developed by the mathematician Marius Sophus Lie in the 19^{th} century. The theory is based on continuous groups; here the focus lies on matrix Lie groups, i.e., groups whose elements are all matrices. From them the matrix Lie group, $SO(3)$, that corresponds to proper rotations in 3D is of interest.
In the present work, the configuration of the beam subjected to large rotations is $\mathbb{R}^3 \times SO(3)$, where $SO(3)$ means the *Special Orthogonal Group*, the geometric structure of which is a *manifold*. Geometric or structure preserving methods became important in the numerical analysis from 1990's. Along this line, the consistent to the geometry derivation of the beam model, is important for its efficiency. [In several research works like in Sonneville, Cardona, and Brüls, 2014; Gaćeša, 2015, instead of using the previous composition to describe the kinematics, the *Special Euclidean Group* denoted by $SE(3)$ is used, that is inspired by screw theory, and expresses a general deformation map that "includes" the previous two, i.e. the vector space $\mathbb{R}^3$ and the manifold $SO(3)$, in one, i.e. the manifold $SE(3)$.]
In the following, the properties of the $SO(3)$, a) as a *manifold*, which is also *differentiable* and b) as a *matrix group*, are presented. The sets that are in line with the above two definitions are called matrix Lie groups. Their description given in this chapter is necessary to understand the numerical issues of large rotations. Among the literature given that is directed to elementary issues of Lie groups is Hall, 2000, while a book directed to applications in physics is Gilmore, 1974. In Mäkinen, 2008 and the references reported therein, one can also read about the mathematical background of 3D rotations.

2.2 The matrix Lie group $SO(3)$

The terminology $SO(3)$ given to the rotation group means the *Special Orthogonal* group. In a general case one could see it as $SO(n)$; in the present work $n = 2$ or $n = 3$, meaning the group of rotations in 2D or 3D, respectively. Focusing from now on to $SO(3)$, its name is consistent with its properties as follows

$$SO(3) = \{\boldsymbol{\Lambda} : \mathbb{R}^3 \to \mathbb{R}^3 \| \boldsymbol{\Lambda}^T \boldsymbol{\Lambda} = \boldsymbol{I}_3, det(\boldsymbol{\Lambda}) = 1\} \tag{2.1}$$

where $\boldsymbol{I}_3$ is the identity matrix in 3D and $\boldsymbol{\Lambda}$ is a 3×3 real matrix; that is a linear transformation of $\mathbb{R}^3$ which preserves the norm $|(x, y, z)|^2 = x^2 + y^2 + z^2$. The first property refers to the **orthogonality**, that is also proven by the orthonormality of the column vectors that consistitute the matrix $\boldsymbol{\Lambda}$ (Hall, 2000), i.e.,

$$\sum_{l=1}^{3} \boldsymbol{\Lambda}_{lj} \boldsymbol{\Lambda}_{lk} = \delta_{jk}, \quad 1 \leq j, k \leq 3 \tag{2.2}$$

where δ_{jk} is the Kronecker delta that is equal to 1 if $j = k$ and equal to 0 if $j \neq k$. Indeed, in the beam theory models presented in the following chapters, the rotation matrix $\boldsymbol{\Lambda}$ contains in its columns the cross-section directors that are unit and normal to each other. The second property refers to the characterization **special**, which means the proper rotation. If the corresponding determinant is -1, then the matrix expresses a reflection, not a rotation. The group that contains both rotations and reflections in 3D is the orthogonal group $O(3)$, without the 'S' in front of its name. Thus, $SO(3)$ is a sub-group of the group $O(3)$. The set of rotation matrices $SO(3)$ in eq. (2.1) is a matrix Lie group. Every matrix Lie group is a Lie group which means that (Mueller, 2013)

- $SO(3)$ is a *differentiable (smooth) manifold*, and simultaneously,
- $SO(3)$ is a *group*

Without using formal mathematical terms, but a conceptual approach, the above two definitions are given. From *Manifold*; *Differentiable manifold*,

"*Manifold* is a topological space that locally resembles Euclidean space near each point. As it is depicted in fig. 2.1, any manifold M can be described by a collection of charts U, also known as an atlas."
"*Differentiable manifold* is a type of manifold that is locally similar enough to a vector space to allow one to do calculus. One may apply ideas from calculus while working within the individual charts, since each chart lies within a vector space to which the usual rules of calculus apply. If the charts are suitably compatible

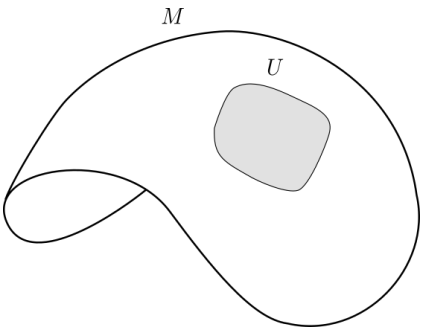

FIGURE 2.1: The manifold M as a union of charts U.

(namely, the transition from one chart to another is differentiable), then computations done in one chart are valid in any other differentiable chart."

As far as the *group* definition is concerned, in Hall, 2000, one can read the definitions and some examples of groups. $SO(3)$ as a group is the set of rotations accompanied by the product operation of the group, which is the matrix multiplication operation (or composition). Given the set and the operation, there are four properties that must be satisfied for having a group. These are:

1. *Closure*: The product of two elements of $SO(3)$ is again an element of $SO(3)$.
2. *Associativity*: For all $\boldsymbol{\Lambda}, \boldsymbol{R}, \boldsymbol{A} \in SO(3)$,
$$\boldsymbol{\Lambda}\,(\boldsymbol{R}\,\boldsymbol{A}) = (\boldsymbol{\Lambda}\,\boldsymbol{R})\,\boldsymbol{A} \tag{2.3}$$
3. *Existence of an identity*: There exists an element $\boldsymbol{I}_3$ in $SO(3)$ such that for all $\boldsymbol{\Lambda} \in SO(3)$,
$$\boldsymbol{\Lambda}\boldsymbol{I}_3 = \boldsymbol{I}_3\boldsymbol{\Lambda} = \boldsymbol{\Lambda} \tag{2.4}$$
4. *Existence of inverses*: For all $\boldsymbol{\Lambda} \in SO(3)$, there exists $\boldsymbol{R} \in SO(3)$,
$$\boldsymbol{\Lambda}\boldsymbol{R} = \boldsymbol{I}_3 \tag{2.5}$$

Since $\boldsymbol{\Lambda}\boldsymbol{A} \neq \boldsymbol{A}\boldsymbol{\Lambda}$ for all $\boldsymbol{\Lambda}, \boldsymbol{A} \in SO(3)$, the group is said to be *non-commutative*, or *non-abelian* (Hall, 2000).

Collecting the properties of the differentiable manifold and the group, the rotation group $SO(3)$ as a real Lie group is defined as follows (*Lie group*; Hall, 2000): $SO(3)$ as a real Lie group is a real smooth manifold in which the group operation (the matrix multiplication operation in this case) and inversion are smooth maps. Note that, while Lie groups are transformation groups acting on manifolds, matrix Lie groups are linear transformations on vector spaces (abelian groups that act on free vectors). For example, $SO(3)$ acts on $\mathbb{R}^3$ as follows (Mueller, 2013)

$$\boldsymbol{y} = \boldsymbol{\Lambda}\,\boldsymbol{x}, \boldsymbol{\Lambda} \in SO(3), \boldsymbol{x} \in \mathbb{R}^3$$

2.3 Parametrization of rotations

As it is depicted in fig. 2.2, rotations can be described by frame transformations (Mueller, 2013). The frame $\boldsymbol{V}$ that is fixed onto the body is called *material* and is moving together with the body, while the frame $\boldsymbol{e}$ is the well-known *inertial* frame. Let $\boldsymbol{X}_{\boldsymbol{V}} = (\xi, \eta, \zeta)$ be the coordinates measured for a point of the body in the frame $\boldsymbol{V}$, and $\boldsymbol{X}_{\boldsymbol{e}} = (x, y, z)$ be the coordinates measured for the same point in the frame $\boldsymbol{e}$. The relation between them is written as

$$\boldsymbol{X_e} = \boldsymbol{\Lambda}\, \boldsymbol{X_V} \tag{2.6}$$

There are a variety of ways to represent rotations, e.g., by orthogonal matrices with determinant 1, by axis and rotation angle, by quaternions, as a sequence of three rotations (Euler angles). In the present work, the axis-angle representation and the sequence of three rotations are of interest.

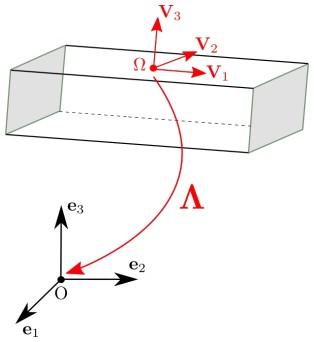

FIGURE 2.2: Transformation $\boldsymbol{\Lambda}$ from the body-fixed $\boldsymbol{V}$ to the spatial frame $\boldsymbol{e}$.

2.3.1 Axis-angle representation

The axis-angle representation of a rotation parameterizes a rotation in a 3D Euclidean space using two quantities: the unit vector $\boldsymbol{e}$ indicating the direction of the axis of rotation, and the angle θ describing the magnitude of the rotation about the axis (*Axis-angle representation*). In fig. 2.3, this type of representation is shown, that is defined by the rotation vector $\theta\boldsymbol{e}$.

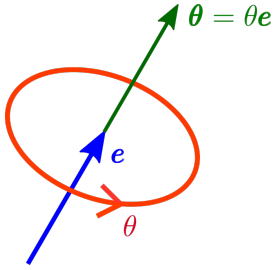

FIGURE 2.3: Axis - angle representation defined by the rotation vector $\theta\boldsymbol{e}$.

2.3.2 The Euler angles

The Euler angles, that have been introduced by Leonhard Euler, are three angles describing the orientation or rotation of a body w.r.t. a fixed coordinate system. The three elemental rotations may be extrinsic (rotations about the axes of the original coordinate system, which is assumed to remain stationary), or intrinsic (rotations about the axes of the rotating coordinate system, attached to the moving body, which changes its orientation after each elementary rotation). In Argyris, 1982, there is an analysis of the procedure that is followed to elegantly result to a transformation or rotation matrix in the case of multiple rotations about fixed or follower axes. In the present work, the Euler angles in an intrinsic sense are used. The elementary rotations (that define 1-parameter subgroup of $SO(3)$) form the following matrices about the 3 spatial axes,

$$\boldsymbol{\Lambda}_1 = \begin{bmatrix} 1 & 0 & 0 \\ 0 & cosa_1 & -sina_1 \\ 0 & sina_1 & cosa_1 \end{bmatrix}; \boldsymbol{\Lambda}_2 = \begin{bmatrix} cosa_2 & 0 & sina_2 \\ 0 & 1 & 0 \\ -sina_2 & 0 & cosa_2 \end{bmatrix}; \boldsymbol{\Lambda}_3 = \begin{bmatrix} cosa_3 & -sina_3 & 0 \\ sina_3 & cosa_3 & 0 \\ 0 & 0 & 1 \end{bmatrix} \tag{2.7}$$

One possibility to get the rotation matrix, that is depicted in fig. 2.2, is the following

$$\boldsymbol{\Lambda} = \boldsymbol{\Lambda}_2 \, \boldsymbol{\Lambda}_3 \, \boldsymbol{\Lambda}_1 \tag{2.8}$$

The above order of applying the rotations, taking into account that the elementary rotations are performed about follower axes, means that e.g. in fig. 2.4, the cross-section of a beam that is located along the ξ axis is firstly subjected to twist about the ξ axis (expressed by $\boldsymbol{\Lambda}_1$), then it is subjected to bending about the ζ axis (expressed by $\boldsymbol{\Lambda}_3$), and finally it is subjected to bending about the η axis (expressed by $\boldsymbol{\Lambda}_2$). In fig. 2.4, this concept is shown, assuming that $\Omega\xi\eta\zeta$ is the material coordinate system and $Oxyz$ is the spatial coordinate system. Of course, this is not the only possibility to form a transformation matrix based on Euler angles; the order is chosen depending on the physics of the problem that is analyzed. The non-uniqueness of the resulting matrix is a disadvantage of the specific representation of rotations.

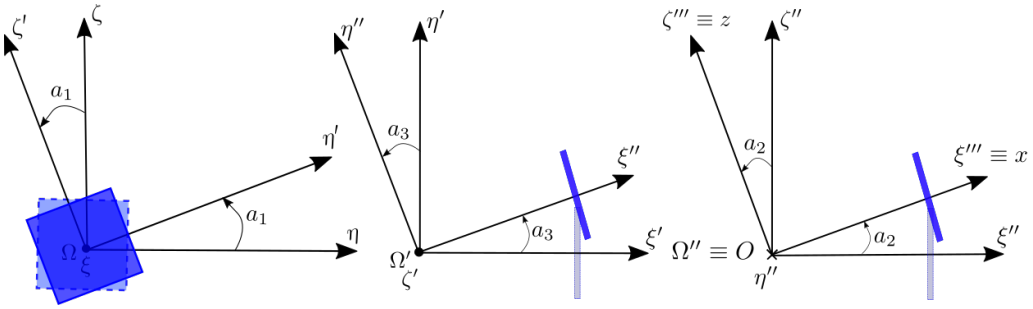

(A) Rotation a_1 about the ξ axis.

(B) Rotation a_3 about the ζ' axis.

(C) Rotation a_2 about the η'' axis.

FIGURE 2.4: Derivation of the transformation matrix.

2.4 Tangent space and Lie algebra of $SO(3)$

"In mathematics, the *tangent space* of a manifold generalizes to higher dimensions the notion of tangent planes to surfaces in three dimensions and tangent lines to curves in two dimensions. In differential geometry, one can attach to every point x of a differentiable manifold a tangent space - a real vector space that intuitively contains the possible directions in which one can tangentially pass through x. The elements of the tangent space at x are called the tangent vectors at x. This is a generalization of the notion of a vector, based at a given initial point, in an Euclidean space. The dimension of the tangent space at every point of a connected manifold is the same as that of the manifold itself. For example, if the given manifold is a 2 - sphere, then one can picture the tangent space at a point

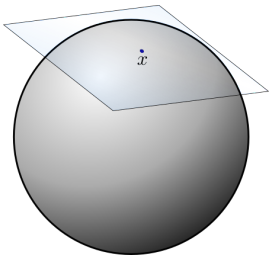

FIGURE 2.5: The tangent space of a single point x on a sphere. A vector in this tangent space represents a possible velocity at x (*Tangent space*).

as the plane that touches the sphere at that point and is perpendicular to the sphere's radius through the point, fig. 2.5." (*Tangent space*)

Lie algebra (Mueller, 2013)

Restricting attention to matrix Lie groups simplifies the definition of the Lie algebra. To define the Lie algebra, there is the need to define the Lie bracket first. Performing a Taylor expansion of the rotation matrix $\boldsymbol{\Lambda}$ (eq. (2.8)) in terms of $\boldsymbol{a} = (a_1, a_2, a_3)$, the following expression is derived

$$\boldsymbol{\Lambda}(\boldsymbol{a}) = \boldsymbol{\Lambda}(\mathbf{0}) + \sum_i a_i \boldsymbol{X}_i + O\left(a^2\right) \tag{2.9}$$

$\boldsymbol{X}_i$ are called the *generators* of the Lie group $SO(3)$. If $\boldsymbol{c}$ and $\boldsymbol{c}'$ are two rotation vectors so that $\boldsymbol{\Lambda}(\boldsymbol{c}) = \boldsymbol{\Lambda}(\boldsymbol{a})\boldsymbol{\Lambda}(\boldsymbol{\beta})$ and $\boldsymbol{\Lambda}(\boldsymbol{c}') = \boldsymbol{\Lambda}(\boldsymbol{\beta})\boldsymbol{\Lambda}(\boldsymbol{a})$ then

$$\boldsymbol{\Lambda}(\boldsymbol{a})\boldsymbol{\Lambda}(\boldsymbol{\beta}) = \boldsymbol{\Lambda}(\boldsymbol{c}) \approx \boldsymbol{\Lambda}(\mathbf{0}) + \sum_i c_i \boldsymbol{X}_i \tag{2.10}$$

$$\boldsymbol{\Lambda}(\boldsymbol{\beta})\boldsymbol{\Lambda}(\boldsymbol{a}) = \boldsymbol{\Lambda}(\boldsymbol{c}') \approx \boldsymbol{\Lambda}(\mathbf{0}) + \sum_i c'_i \boldsymbol{X}_i \tag{2.11}$$

The difference between these two matrices is written as

$$\boldsymbol{\Lambda}(\boldsymbol{a})\boldsymbol{\Lambda}(\boldsymbol{\beta}) - \boldsymbol{\Lambda}(\boldsymbol{\beta})\boldsymbol{\Lambda}(\boldsymbol{a}) = \sum_{i,j} a_i \beta_j \left(\boldsymbol{X}_i \boldsymbol{X}_j - \boldsymbol{X}_j \boldsymbol{X}_i\right) = \sum_i \left(c_i - c'_i\right) \boldsymbol{X}_i \tag{2.12}$$

The *matrix commutator* in eq. (2.12) defines the Lie bracket on $SO(3)$

$$[\boldsymbol{X}_i, \boldsymbol{X}_j] := \boldsymbol{X}_i \boldsymbol{X}_j - \boldsymbol{X}_j \boldsymbol{X}_i = \sum_k c_{ij}^k \boldsymbol{X}_k \;\text{ with }\; c_{ij}^k := \frac{(c_k - c'_k)}{a_i \beta_j} \tag{2.13}$$

c_{ij}^k are the structure constants of the Lie algebra $so(3)$ of the Lie group $SO(3); c_{ij}^k := \epsilon_{ij}^k$, where ϵ_{ij}^k is the Levi-Civita symbol.

Definition

A finite-dimensional Lie algebra $\mathfrak{g}$ is a finite-dimensional vector space equipped with a Lie bracket $[\cdot, \cdot]$ so that (Mueller, 2013)

1. $\boldsymbol{X}, \boldsymbol{Y} \in \mathfrak{g} \leftrightarrow [\boldsymbol{X}, \boldsymbol{Y}] \in \mathfrak{g}$
2. $[\boldsymbol{X}, a\boldsymbol{Y} + b\boldsymbol{Z}] = [\boldsymbol{X}, a\boldsymbol{Y}] + [\boldsymbol{X}, b\boldsymbol{Z}], a, b \in \mathbb{K} = \mathbb{R}, \mathbb{C}$ (bilinearity)
3. $[\boldsymbol{X}, \boldsymbol{Y}] = -[\boldsymbol{Y}, \boldsymbol{X}]$ (skew symmetry)
4. $[\boldsymbol{X}, [\boldsymbol{Y}, \boldsymbol{Z}]] + [\boldsymbol{Y}, [\boldsymbol{Z}, \boldsymbol{X}]] + [\boldsymbol{Z}, [\boldsymbol{X}, \boldsymbol{Y}]] = 0$ (Jacobi identity)

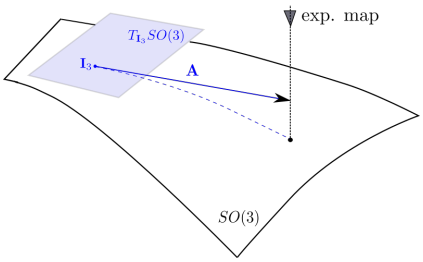

FIGURE 2.6: Geometric depiction of the Lie algebra $so(3)$ and the exponential map of the skew-symmetric matrix $\boldsymbol{A}$.

Regarding the Lie algebra $\mathfrak{g}$ of a Lie group G, this can be thought as the tangent space to the identity element of G. For example, in the case of $SO(3)$, the Lie algebra $so(3)$ can be

depicted as the tangent plane $T_{\boldsymbol{I}_3}SO(3)$ to the identity element $\boldsymbol{I}_3$ of $SO(3)$ (fig. 2.6). The generators of $so(3)$ are the derivatives of the elementary rotation matrices (eq. (2.7)) about each axis, evaluated at the identity,

$$\boldsymbol{G}_1 := \frac{\vartheta}{\vartheta a}\boldsymbol{\Lambda}_1|_{a=0} = \begin{bmatrix} 0 & 0 & 0 \\ 0 & 0 & -1 \\ 0 & 1 & 0 \end{bmatrix} = \hat{\boldsymbol{e}}_1 \tag{2.14}$$

$$\boldsymbol{G}_2 := \frac{\vartheta}{\vartheta a}\boldsymbol{\Lambda}_2|_{a=0} = \begin{bmatrix} 0 & 0 & 1 \\ 0 & 0 & 0 \\ -1 & 0 & 0 \end{bmatrix} = \hat{\boldsymbol{e}}_2 \tag{2.15}$$

$$\boldsymbol{G}_3 := \frac{\vartheta}{\vartheta a}\boldsymbol{\Lambda}_3|_{a=0} = \begin{bmatrix} 0 & -1 & 0 \\ 1 & 0 & 0 \\ 0 & 0 & 0 \end{bmatrix} = \hat{\boldsymbol{e}}_3 \tag{2.16}$$

Since,

$$[\hat{\boldsymbol{e}}_i, \hat{\boldsymbol{e}}_j] = \widehat{\hat{\boldsymbol{e}}_i \boldsymbol{e}_j} = \widehat{\boldsymbol{e}_i \times \boldsymbol{e}_j}$$

$\mathbb{R}^3$ is a Lie algebra with cross product as Lie bracket, isomorphic to $so(3)$. Moreover, eqs. (2.14) to (2.16) express the basis of $so(3)$, thus, an element of $so(3)$ can be represented as a linear combination of the generators:

$$\boldsymbol{\omega} \in \mathbb{R}^3 \mapsto \omega_1 \boldsymbol{G}_1 + \omega_2 \boldsymbol{G}_2 + \omega_3 \boldsymbol{G}_3 \in so(3) \tag{2.17}$$

Therefore, to define the Lie algebra $so(3)$ of the matrix Lie group $SO(3)$, that is the linear space of second order skew symmetric tensors (Romero, 2004)

$$so(3) := \{\boldsymbol{\Omega} : \mathbb{R}^3 \to \mathbb{R}^3 \| \boldsymbol{\Omega} + \boldsymbol{\Omega}^T = \boldsymbol{0}\} \tag{2.18}$$

Also, as it is shown in eq. (2.17), every skew tensor $\boldsymbol{\Omega}$ has a unique associated vector, $\boldsymbol{\omega} \in \mathbb{R}^3$ called its axial vector, such that for all $\boldsymbol{x} \in \mathbb{R}^3$ (Romero, 2004)

$$\boldsymbol{\Omega}\,\boldsymbol{x} = \boldsymbol{\omega} \times \boldsymbol{x} \tag{2.19}$$

where $'\times'$ denotes the vector product in $\mathbb{R}^3$. The general form of $\boldsymbol{\Omega}$ is

$$\boldsymbol{\Omega} = \begin{bmatrix} 0 & -\omega_3 & \omega_2 \\ \omega_3 & 0 & -\omega_1 \\ -\omega_2 & \omega_1 & 0 \end{bmatrix} \tag{2.20}$$

The matrices in the Lie algebra are not themselves rotations; the skew-symmetric matrices are derivatives. An infinitesimal rotation matrix has the form $\boldsymbol{I}_3 + \boldsymbol{\Omega} d\theta$, where $d\theta$ is vanishingly small. In this case, the order in which infinitesimal rotations are applied is irrelevant. In other words, the multiplication of infinitesimal rotation matrices is commutative.

2.5 The exponential mapping - from Algebra to Group

In the theory of Lie groups, the exponential map is a map from the Lie algebra $\mathfrak{g}$ to the Lie group G which allows to recapture the local group structure from the Lie algebra, *Exponential map (Lie theory)*, i.e.

$$exp : \mathfrak{g} \rightarrow G \tag{2.21}$$

In the case of the matrix Lie groups, like the $SO(3)$ rotation group, the definition of the exponential map coincides with the matrix exponential that is given by the following series expansion (see fig. 2.6 for a geometric illustration)

$$exp\boldsymbol{A} = \sum_{k=0}^{\infty} \frac{\boldsymbol{A}^k}{k!} \tag{2.22}$$

To compute the exponential map from $so(3)$ to $SO(3)$ without computing the full matrix exponential, the Rodrigues' rotation formula is used. This is the most important relation in the 3D large rotations regime and is given as follows

Given a vector $\boldsymbol{\alpha}$ and its norm $\alpha = \|\boldsymbol{\alpha}\| = \sqrt{\alpha_1^2 + \alpha_2^2 + \alpha_3^2}$, the Rodrigues' formula reads

$$\boldsymbol{R} = \boldsymbol{I}_3 + \frac{sin\alpha}{\alpha}\boldsymbol{A} + \frac{1 - cos\alpha}{\alpha^2}\boldsymbol{A}^2 \tag{2.23}$$

where $\boldsymbol{A}$ is the 3×3 skew-symmetric matrix $\hat{\boldsymbol{\alpha}}$ of the vector $\boldsymbol{\alpha}$. The properties of the exponential mapping are collected in the following (Mueller, 2013)

- $exp\,\boldsymbol{0} = \boldsymbol{I}_3$
- $exp\,\boldsymbol{A}$ is invertible, and $(exp\,\boldsymbol{A})^{-1} = exp(-\boldsymbol{A})$
- $exp(a+b)\boldsymbol{A} = exp\,a\boldsymbol{A}\,exp\,b\boldsymbol{A}$
- if the Lie group G is commutative (this is not the case for the $SO(3)$), i.e. $\boldsymbol{AB} = \boldsymbol{BA}$, then $exp(\boldsymbol{A}+\boldsymbol{B}) = exp(\boldsymbol{A})\,exp(\boldsymbol{B})$
- if $\boldsymbol{C}$ is invertible, then $\boldsymbol{C}\,(exp\,\boldsymbol{A})\,\boldsymbol{C}^{-1} = exp\left(\boldsymbol{CAC}^{-1}\right)$

Verification of the Rodrigues' formula

To verify that the RHS of eqs. (2.22) and (2.23) are identical, the trigonometric functions in eq. (2.23) are expanded into series in α

$$\begin{aligned}\boldsymbol{R} = \boldsymbol{I}_3 &+ \left(1 - \frac{\alpha^2}{3!} + \frac{\alpha^4}{5!} - ... + (-1)^n \frac{\alpha^{2n}}{(2n+1)!} \pm ...\right)\boldsymbol{A} \\ &+ \left(\frac{1}{2!} - \frac{\alpha^2}{4!} + \frac{\alpha^4}{6!} - ... + (-1)^n \frac{\alpha^{2n}}{(2n+2)!} \pm ...\right)\boldsymbol{A}^2\end{aligned} \tag{2.24}$$

It is observed that

$$\boldsymbol{A}^3 = -\alpha^2 \boldsymbol{A} \qquad \boldsymbol{A}^4 = -\alpha^2 \boldsymbol{A}^2 \tag{2.25}$$

$$\boldsymbol{A}^5 = +\alpha^4 \boldsymbol{A} \qquad \boldsymbol{A}^6 = +\alpha^4 \boldsymbol{A}^2 \tag{2.26}$$

leading to the recurrence formulae

$$\boldsymbol{A}^{2n-1} = (-1)^{n-1} \alpha^{2(n-1)} \boldsymbol{A} \qquad \boldsymbol{A}^{2n} = (-1)^{n-1} \alpha^{2(n-1)} \boldsymbol{A}^2 \tag{2.27}$$

By applying eq. (2.27) in eq. (2.24), the eq. (2.22) is deduced into the series in $\boldsymbol{A}$ (Argyris, 1982).

Remark on the implementation of the Rodrigues' formula

Both functions of α appearing in eq. (2.23) have removable singularities at $\alpha = 0$. This should be taken into account, by e.g. including a test regarding the smallness of α relative to a tolerance and replacing these functions by some truncated Taylor expansions for small α (eq. (2.24)).

In case of using the axis/angle representation (fig. 2.3), and taking into account the generators of $so(3)$ in eqs. (2.14) and (2.16) the rotation matrix is given as follows

$$\boldsymbol{\Lambda}(\theta \boldsymbol{e}) = exp(\theta\, \boldsymbol{G}_1\, e_1 + \theta\, \boldsymbol{G}_2\, e_2 + \theta\, \boldsymbol{G}_3\, e_3) \tag{2.28}$$

In case of using the 3 Euler angles, i.e. the 3 consecutive rotations a_1, a_2, a_3 parametrization (fig. 2.4), the rotation matrix is given by the matrix multiplication of 3 consecutive exponential mappings, which are

$$\boldsymbol{\Lambda}_1 = exp(a_1\, \boldsymbol{G}_1); \quad \boldsymbol{\Lambda}_2 = exp(a_2\, \boldsymbol{G}_2); \quad \boldsymbol{\Lambda}_3 = exp(a_3\, \boldsymbol{G}_3) \tag{2.29}$$

Thus,

$$\boldsymbol{\Lambda}(a_1, a_2, a_3) = exp(a_2\, \boldsymbol{G}_2)\, exp(a_3\, \boldsymbol{G}_3)\, exp(a_1\, \boldsymbol{G}_1) \tag{2.30}$$

2.6 Actions of the Lie group $SO(3)$

The compound rotation composed of successive rotations is also a rotation itself and induces a Lie group structure with an underlying Lie algebra (Mäkinen, 2008). This can be met in an iterative/incremental analysis where the corresponding iterative/incremental rotation is applied on a specific orientation to give a new orientation. This composition of rotations can be performed using two ways, taking advantage of the left and right actions of the Lie group.

Left action or Left translation: $$L_{\boldsymbol{\Lambda}}\left(\Delta \boldsymbol{\Lambda}^{mat.}\right) = \boldsymbol{\Lambda}\, \Delta \boldsymbol{\Lambda}^{mat.} = \boldsymbol{\Lambda} exp\left(\hat{\boldsymbol{\Theta}}\right) \tag{2.31}$$

Right action or Right translation: $$R_{\boldsymbol{\Lambda}}\left(\Delta \boldsymbol{\Lambda}^{spat.}\right) = \Delta \boldsymbol{\Lambda}^{spat.}\, \boldsymbol{\Lambda} = exp\left(\hat{\boldsymbol{\theta}}\right) \boldsymbol{\Lambda} \tag{2.32}$$

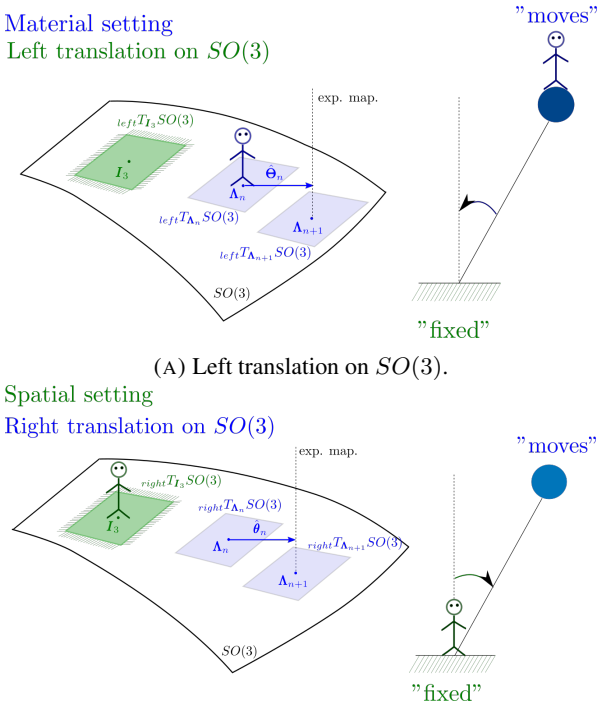

(A) Left translation on $SO(3)$.

(B) Right translation on $SO(3)$.

FIGURE 2.7: Left and Right translations on $SO(3)$.

where the infinitesimal rotation expressed by $\Delta\boldsymbol{\Lambda}$ is applied in a material and a spatial setting, respectively. In the first case, the iterative/incremental material rotation vector, $\boldsymbol{\Theta}$, with respect to the base point $\boldsymbol{\Lambda} \in SO(3)$ is used, while, in the second case the corresponding spatial counterpart, $\boldsymbol{\theta}$, is used. The left action means that the orientation $\boldsymbol{\Lambda}$ is imposed on the exponential map of the rotation vector $\boldsymbol{\Theta}$, while the right action means that the orientation $\boldsymbol{\Lambda}$ is employed first, and the exponential map of the rotation vector $\boldsymbol{\theta}$ follows. This concept is geometrically illustrated in fig. 2.7 during the time step $[n, n+1]$ of a step by step analysis. The manifold $SO(3)$ is depicted together with the tangent spaces $T_{\boldsymbol{I}_3}SO(3)$, $T_{\boldsymbol{\Lambda}_n}SO(3)$, $T_{\boldsymbol{\Lambda}_{n+1}}SO(3)$, either left or right, at the base points $\boldsymbol{I}_3, \boldsymbol{\Lambda}_n, \boldsymbol{\Lambda}_{n+1} \in SO(3)$, respectively. The skew-symmetric matrices of the incremental rotation vectors, the material $\boldsymbol{\Theta}$ and the spatial $\boldsymbol{\theta}$ rotation vectors, belong to the tangent spaces at $\boldsymbol{\Lambda}_n$ that changes in each incremental step. The figures follow the presentation in Mäkinen, 2001; Mäkinen, 2008. The fig. 2.7a refers to the material setting. It shows the observer (in blue color) to be in motion together with the object, while he/she observes the change of the object's orientation (or his/her orientation) relative to the fixed (in green color) orientation. The rotation measured by the observer is illustrated by the arrow that starts from the observer's orientation (or object's orientation) (that is changing) and ends at the fixed orientation. The fig. 2.7b refers to the spatial setting. It shows the observer (in green color) to be fixed at space and observes the object (in blue color) that is rotating. The rotation measured by the observer is illustrated by the arrow that starts from the observer's orientation (that is fixed) and ends at the object's orientation (that is changing).

The other two actions (the so-called inner automorphism and adjoint transformation, Mäkinen, 2008; Mueller, 2013) of the Lie group $SO(3)$ are, in essence, the following very useful relations:

$$\Delta\boldsymbol{\Lambda}_{spat.} = \boldsymbol{\Lambda}\Delta\boldsymbol{\Lambda}_{mat.}\boldsymbol{\Lambda}^T \qquad \text{(inner automorphism)} \tag{2.33}$$

$$\hat{\boldsymbol{\theta}} = \boldsymbol{\Lambda}\hat{\boldsymbol{\Theta}}\boldsymbol{\Lambda}^T \qquad \text{(adjoint transformation)} \tag{2.34}$$

Finally, the last action, the so-called adjoint action of $SO(3)$ on its algebra results to a very useful expression that is

$$Ad_{\boldsymbol{\Lambda}}\left(\hat{\boldsymbol{\theta}}\right) = \boldsymbol{\Lambda}\hat{\boldsymbol{\theta}}\boldsymbol{\Lambda}^T = \widehat{\boldsymbol{\Lambda}\boldsymbol{\theta}} \tag{2.35}$$

Chapter 3

Beam theory with large rotations and its Finite Element formulation

3.1 Introduction

In this chapter, the main core of the thesis is presented. The two beam models that have been investigated are presented in detail, and the differences between them are given. The first model is called the *Green-Lagrange (GL)* model (Dvorkin, Onate, and Olivier, 1988; Bathe, 1996), while, the second model is called the *Simo-Reissner (SR)* model (Simo, 1985). Their name refers to the type of strains they use. In the first case, a generalized axial/shear strain and twist/bending vector is derived from the 3D GL strain tensor and its conjugate working pair. In the second case, the SR generalized axial/shear strain and twist/bending vector is used, which is derived from the 3D deformation gradient tensor and its conjugate working pair. After the presentation of the theoretical analysis of the beam models, their numerical implementation issues are given. These issues mainly concern the rotational degrees of freedom which 'inhabit' onto a differentiable manifold in space, that has the resemblance to an Euclidean space just in a small neighborhood of it. The mathematical background on Lie groups described in chapter 2 is used for developing the displacement-based finite element formulation of the beam models. A further manipulation is performed in linearization and discretization procedures in order to have a strain-invariant implementation. To obtain the so-called configuration-dependent shape functions resulting to the strain-invariance under a rigid-body rotation of the element (Jelenić and Crisfield, 1999), the Lie algebra is performed in the same tangent plane at each iteration of the incremental step. This technique is used for the first time in the GL beam model and it is shown that it functions the same well as in the SR beam model. Finally, the numerical results also include the iterative implementation, i.e. the original implementation technique provided in Simo, 1985, to emphasize the superiority of the invariant technique. The benchmark examples that are solved verify the integrity of the code for both the non-linear beam models in the statics regime.

3.2 Kinematics

The kinematics of a prismatic beam member, either curved or not, is given. The member is decomposed into segments which are straight and have a double-symmetric compact cross-section; any general shape may be used within the following assumptions, though, given that the cross-sectional properties are defined at the outset. To simplify the comparative study between the SR and the GL beam models, the properties associated with the non-symmetry of the cross-section are not presented in this case. The kinematic assumptions are: 1) The cross-section of the beam remains a rigid plane during deformation (Bernoulli hypothesis), hence warping is not included. 2) Shear deformation is taken into account, and is assumed constant in the cross-section as a consequence of the previous non-warping assumption. 3) Small strains are assumed. The reference bases used in kinematics are (fig. 3.1)

- $\boldsymbol{e}_j, j = 1-3$, is the fixed spatial basis of an orthogonal Cartesian coordinate system.
- $\boldsymbol{V}_i(\xi), i = 1-3$, is the orthonormal moving basis, attached to each cross-section, where ξ is the length variable along the line of the beam centroids (beam axis); η, ζ are the cross-section coordinates measured in the system defined by the $\boldsymbol{V}$ frame. In the deformed configurations, for instance, at time $t + \Delta t$, the vector ${}^{t+\Delta t}\boldsymbol{V}_1$ is normal to the cross-section, while the vectors ${}^{t+\Delta t}\boldsymbol{V}_2$, ${}^{t+\Delta t}\boldsymbol{V}_3$ are collinear to its principal axes. Since shear deformation is taken into account, the vector ${}^{t+\Delta t}\boldsymbol{V}_1$ is not necessarily tangent to the beam centroidal line.

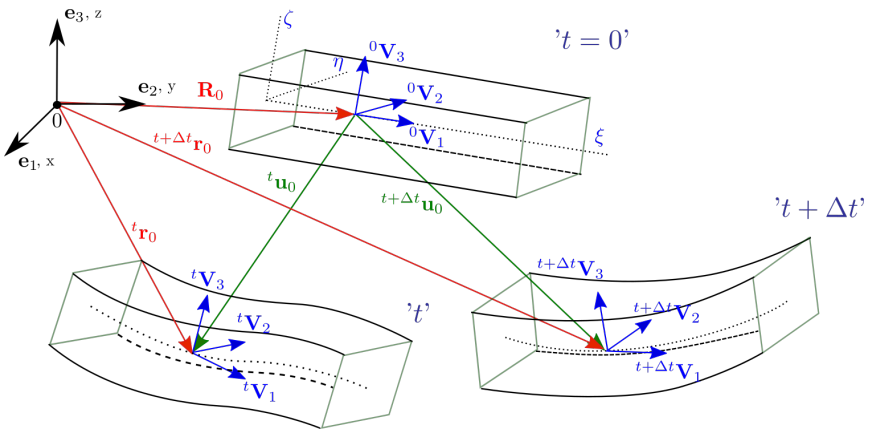

FIGURE 3.1: Initial and deformed configurations of the beam.

3.2.1 Initial and deformed configurations

The cross-section orientation is expressed via the orthogonal transformation $\xi \rightarrow \boldsymbol{\Lambda}(\xi) \in SO(3)$, $SO(3)$ is the special orthogonal group, thus, the components of the moving basis vectors ${}^0\boldsymbol{V}$ and ${}^{t+\Delta t}\boldsymbol{V}$ at the initial and deformed at $t + \Delta t$ states, respectively, are given by

$$\begin{aligned} {}^0\boldsymbol{V}_i(\xi) &= {}^0\Lambda_{ji}(\xi)\,\boldsymbol{e}_j \\ {}^{t+\Delta t}\boldsymbol{V}_i(\xi) &= {}^{t+\Delta t}\Lambda_{ji}(\xi)\,\boldsymbol{e}_j,\ i,j = 1-3 \end{aligned} \tag{3.1}$$

The configuration at t in fig. 3.1 appears just for completeness, since it is a converged state in the numerical procedure followed in the present work.
The position vectors $\boldsymbol{R}$ and ${}^{t+\Delta t}\boldsymbol{r}$ of an arbitrary material particle (ξ, η, ζ) of the beam are given by

$$\begin{aligned} \boldsymbol{R}(\xi,\eta,\zeta) &= \quad \boldsymbol{R}_0(\xi) + \quad {}^0\boldsymbol{\Lambda}(\xi) \left\{0 \quad \eta \quad \zeta\right\}^T \\ {}^{t+\Delta t}\boldsymbol{r}(\xi,\eta,\zeta) &= {}^{t+\Delta t}\boldsymbol{r}_0(\xi) + {}^{t+\Delta t}\boldsymbol{\Lambda}(\xi) \left\{0 \quad \eta \quad \zeta\right\}^T \end{aligned} \tag{3.2}$$

where T is the transposition symbol, $\boldsymbol{R}_0(\xi)$ and ${}^{t+\Delta t}\boldsymbol{r}_0(\xi)$ are the position vectors of the beam reference point at the initial and deformed states, respectively, while the corresponding orientation matrices, ${}^0\boldsymbol{\Lambda}$ and ${}^{t+\Delta t}\boldsymbol{\Lambda}$, are given by (see also eq. (2.23) where a similar form of the same formula can be used)

$$\boldsymbol{\Lambda}(\xi) = exp(\hat{\boldsymbol{\alpha}}(\xi)) = cos\alpha \boldsymbol{I}_3 + \frac{sin\alpha}{\alpha}\hat{\boldsymbol{\alpha}} + \frac{1-cos\alpha}{\alpha^2}\boldsymbol{\alpha}\otimes\boldsymbol{\alpha} \tag{3.3}$$

which takes as input either the orientation vector ${}^0\boldsymbol{\alpha}$, that expresses the initial cross-sectional angles, or the orientation vector ${}^{t+\Delta t}\boldsymbol{\alpha}$, that expresses the deformed cross-sectional angles at $t+\Delta t$; $\boldsymbol{I}_3$ is the 3×3 identity matrix, α is the Euclidean norm of vector $\boldsymbol{\alpha}$, $\hat{\boldsymbol{\alpha}}(\xi)$ is the skew-symmetric matrix formed by the relation $\hat{\boldsymbol{\alpha}}(\xi) = -e^{ij}_k \alpha^k \boldsymbol{e}_i \boldsymbol{e}^T_j$; e^{ij}_k is the permutation symbol and $i,j,k = 1-3$ (see chapter 2). The above formula is the well-known Euler-Rodrigues formula (details of its derivation are given e.g. in Crisfield, 1997; Argyris, 1982).

The displacement vector ${}^{t+\Delta t}\boldsymbol{u}$ of an arbitrary material particle (ξ, η, ζ) at $t+\Delta t$ is equal to the difference between the expressions in eq. (3.2), i.e.

$${}^{t+\Delta t}\boldsymbol{u}(\xi,\eta,\zeta) = {}^{t+\Delta t}\boldsymbol{u}_0(\xi) + \eta \left(exp({}^{t+\Delta t}\hat{\boldsymbol{\theta}}) - \boldsymbol{I}_3\right) {}^0\boldsymbol{V}_2(\xi) + \zeta \left(exp({}^{t+\Delta t}\hat{\boldsymbol{\theta}}) - \boldsymbol{I}_3\right) {}^0\boldsymbol{V}_3(\xi) \tag{3.4}$$

with components u_i; $i = 1-3$ w.r.t. the global basis $\boldsymbol{e}$ and u_ξ, u_η, u_ζ w.r.t. the initial cross-sectional basis ${}^0\boldsymbol{V}$. In addition, ${}^{t+\Delta t}\boldsymbol{u}_0(\xi) = {}^{t+\Delta t}\boldsymbol{r}_0(\xi) - \boldsymbol{R}_0(\xi) = u_{0i}\,\boldsymbol{e}_i = u_{0\xi}{}^0\boldsymbol{V}_1 + u_{0\eta}{}^0\boldsymbol{V}_2 + u_{0\zeta}{}^0\boldsymbol{V}_3$, expresses the translation of the beam centroid, while $(exp({}^{t+\Delta t}\boldsymbol{\theta}) - \boldsymbol{I}_3)\,{}^0\boldsymbol{V}_2 = {}^{t+\Delta t}\boldsymbol{V}_2(\xi) - {}^0\boldsymbol{V}_2$ and $(exp({}^{t+\Delta t}\boldsymbol{\theta}) - \boldsymbol{I}_3)\,{}^0\boldsymbol{V}_3 = {}^{t+\Delta t}\boldsymbol{V}_3(\xi) - {}^0\boldsymbol{V}_3$ express the rotation between the initial and deformed states of the cross-section assigned to the beam centroid; $exp({}^{t+\Delta t}\hat{\boldsymbol{\theta}})$ with ${}^{t+\Delta t}\boldsymbol{\theta} = \theta_i\,\boldsymbol{e}_i = \theta_\xi{}^0\boldsymbol{V}_1 + \theta_\eta{}^0\boldsymbol{V}_2 + \theta_\zeta{}^0\boldsymbol{V}_3$ is given by eq. (3.3) (superscript ${}^{t+\Delta t}$ has been omitted from the above components for convenience).

Along the above lines, the three-dimensional problem has been reduced to the problem of determining 6 one-dimensional kinematic parameters (3 position components of the reference line and 3 orientation components of the cross-section). The abstract configuration space $\boldsymbol{\Phi}$ of the rod can be formulated as (${}^0L$ is the initial length of the beam):

$$\boldsymbol{\Phi} = \{(\mathbf{r}_0, \boldsymbol{\Lambda}), \mathbf{r}_0 : (0, {}^0L) \rightarrow R^3, \boldsymbol{\Lambda} : (0, {}^0L) \rightarrow SO(3)\} \tag{3.5}$$

3.2.2 Perturbation of the deformed configuration at $t + \Delta t$

During the incremental/ iterative Newton-Raphson procedure, a perturbation of the unknown configuration at $t + \Delta t$ has to be performed, given that the configuration at t is known. Thus,

- The perturbed position of the centroidal line relative to ${}^{t+\Delta t}\boldsymbol{r}_0(\xi)$ is

$$ {}^{t+\Delta t,\epsilon}\boldsymbol{r}_0(\xi) = {}^{t+\Delta t}\boldsymbol{r}_0(\xi) + \epsilon\, \delta\boldsymbol{u}_0(\xi) \tag{3.6}$$

  where $\delta\boldsymbol{u}_0(\xi) = \delta u_{0i}\boldsymbol{e}_i = \delta u_{0\xi}{}^0\boldsymbol{V}_1 + \delta u_{0\eta}{}^0\boldsymbol{V}_2 + \delta u_{0\zeta}{}^0\boldsymbol{V}_3$; $i = 1-3$ is a vector field, interpreted, for $\epsilon > 0$, as superposed infinitesimal displacement onto the centroidal line (Simo and Vu-Quoc, 1986a).

- The perturbed orthogonal transformation relative to ${}^{t+\Delta t}\boldsymbol{\Lambda}(\xi)$ is

$$ {}^{t+\Delta t,\epsilon}\boldsymbol{\Lambda}(\xi) = exp\left({}^{t+\Delta t}\hat{\boldsymbol{\theta}}(\xi) + \epsilon\delta\hat{\boldsymbol{\theta}}(\xi)\right)\, {}^0\boldsymbol{\Lambda}(\xi) \tag{3.7}$$

$$ {}^{t+\Delta t,\epsilon}\boldsymbol{\Lambda}(\xi) = exp\left(\epsilon\delta\boldsymbol{\Psi}(\xi)\right) exp\left({}^{t+\Delta t}\hat{\boldsymbol{\theta}}(\xi)\right)\, {}^0\boldsymbol{\Lambda}(\xi) \tag{3.8}$$

  where $\delta\hat{\boldsymbol{\theta}}(\xi)$ and $\delta\boldsymbol{\Psi}(\xi)$ are skew-symmetric tensor fields, interpreted, for $\epsilon > 0$, as superposed infinitesimal rotation vector and spin, respectively, onto the moving frame (Simo and Vu-Quoc, 1986a). Using eq. (3.8), and taking into account eq. (3.1), the cross-section directors ${}^{t+\Delta t,\epsilon}\boldsymbol{V}_i$ are written as

$$ {}^{t+\Delta t,\epsilon}\boldsymbol{V}_i = exp(\epsilon\delta\boldsymbol{\Psi}(\xi))exp({}^{t+\Delta t}\hat{\boldsymbol{\theta}}(\xi))\, {}^0\boldsymbol{V}_i(\xi); \quad i = 1-3 \tag{3.9}$$

3.3 Simo-Reissner beam model

The widely known Simo-Reissner (SR) beam model is derived from the spatial-material working pair quantities: the displacement gradients and the 1st Piola-Kirchhoff stresses. In the following, the independent variable ξ is omitted from the RHS, for convenience. Also, (,) denotes the spatial derivative relative to the ξ coordinate.

3.3.1 1D strain measures and stress resultants

The consistent 1D strain vectors naturally arise using the extended polar decomposition of the deformation gradient tensor that is presented in Auricchio, Carotenuto, and Reali, 2008, together with the principle of virtual work in terms of the 1st Piola-Kirchhoff stress tensor and the variation of the deformation gradient tensor. The material axial/shear strain vector, $\boldsymbol{\Gamma}(\xi)$, is given by Simo, 1985; Simo and Vu-Quoc, 1986a

$$ \boldsymbol{\Gamma}(\xi) = \boldsymbol{\Lambda}^T\, \boldsymbol{r}_{0,\xi} - \begin{Bmatrix} 1 \\ 0 \\ 0 \end{Bmatrix} \tag{3.10}$$

where $\boldsymbol{\Lambda}$ is the orientation matrix at the deformed state. The material twist/bending strain vector, $\boldsymbol{K}(\xi)$, is given by the axial vector of the skew-symmetric tensor $\hat{\boldsymbol{K}}(\xi)$ (Simo, 1985; Simo and Vu-Quoc, 1986a)

$$\hat{\boldsymbol{K}}(\xi) = \boldsymbol{\Lambda}^T \boldsymbol{\Lambda}_{,\xi} \tag{3.11}$$

The material is assumed homogeneous, isotropic and linear elastic. Thus, the material axial/shear force and twist/bending moment vectors, $\boldsymbol{F}(\xi)$ and $\boldsymbol{M}(\xi)$, are defined as follows

$$\boldsymbol{F}(\xi) = \boldsymbol{C}^{F\Gamma}\, \boldsymbol{\Gamma} \tag{3.12}$$

$$\boldsymbol{M}(\xi) = \boldsymbol{C}^{MK}\, \boldsymbol{K} \tag{3.13}$$

where

$$\boldsymbol{C}^{F\Gamma} = \begin{bmatrix} EA & & \\ & GA_\eta & \\ & & GA_\zeta \end{bmatrix}; \quad \boldsymbol{C}^{MK} = \begin{bmatrix} GJ_t & & \\ & EI_\eta & \\ & & EI_\zeta \end{bmatrix} \tag{3.14}$$

is the material setting of the constitutive tensors, E and G are the Young's and shear modulus, A, A_η and A_ζ are the cross-section area and the two reduced cross-section areas in the directions of principal axes of inertia, J_t is the torsional moment of inertia, while I_η and I_ζ are the two principal moments of inertia.

3.3.2 Principle of virtual work

The weak form of the equilibrium equation of the body at the perturbed state $(t + \Delta t, \epsilon)$ is given by

$$\int_{^0L} \left({}^{t+\Delta t,\epsilon}F_j\, \delta\, {}^{t+\Delta t,\epsilon}\Gamma_j + {}^{t+\Delta t,\epsilon}M_j\, \delta\, {}^{t+\Delta t,\epsilon}K_j \right) d\xi = \delta\, {}^{t+\Delta t,\epsilon}W_{ext}; \quad j = \xi, \eta, \zeta \tag{3.15}$$

where ${}^0L$ is the initial line length. The beam stress and virtual strain measures refer to the material axes ξ, η, ζ at $(t + \Delta t, \epsilon)$, while $\delta\, {}^{t+\Delta t,\epsilon}W_{ext}$ expresses the external virtual work at $(t + \Delta t, \epsilon)$; ${}^{t+\Delta t,\epsilon}F_j$ and ${}^{t+\Delta t,\epsilon}M_j$ are the components of the material internal force and moment vectors $\boldsymbol{F}(\xi)$ and $\boldsymbol{M}(\xi)$ given by eqs. (3.12) and (3.13), respectively, while $\delta\, {}^{t+\Delta t,\epsilon}\Gamma_j$ and $\delta\, {}^{t+\Delta t,\epsilon}K_j$ are the components of the virtual material strain vectors $\delta\boldsymbol{\Gamma}$ and $\delta\boldsymbol{K}$ given by Simo, 1985; Simo and Vu-Quoc, 1986a

$$\delta\boldsymbol{\Gamma} = \boldsymbol{\Lambda}^T \overset{\triangledown}{\delta\boldsymbol{\gamma}}(\xi) = \boldsymbol{\Lambda}^T \left(\delta\boldsymbol{r}_{0,\xi} + {}^{t+\Delta t}\boldsymbol{r}_{0,\xi} \times \delta\boldsymbol{\psi} \right) \tag{3.16}$$

$$\delta\boldsymbol{K} = \boldsymbol{\Lambda}^T \overset{\triangledown}{\delta\boldsymbol{\kappa}}(\xi) = \boldsymbol{\Lambda}^T\, \delta\boldsymbol{\psi}_{,\xi} \tag{3.17}$$

where the symbol $\triangledown$ means the co-rotational derivative *Continuum Mechanics*, $\delta\boldsymbol{r}_0$ is given by the directional derivative of eq. (3.6) w.r.t. ϵ, for $\epsilon = 0$, and $\delta\boldsymbol{\psi}$ is the axial vector of the matrix $\delta\boldsymbol{\Psi}$ (eq. (3.8)).

For the linearization of the internal virtual work given by eq. (3.15) about the configuration at $t + \Delta t$, the reader is referred to the appendix A.1.

3.4 Green-Lagrange beam model

In this section, the 1D formulation of a degenerate-continuum model (Dvorkin, Onate, and Olivier, 1988; Bathe, 1996), where the working pair consists of material objects, the GL strains and 2nd Piola-Kirchhoff stresses, is developed. In the following, the independent variables ξ, η, ζ (in the 3D expressions) and ξ (in the 1D expressions) are omitted from the RHS for convenience. Also, (,) denotes the spatial derivative relative to the ξ, η, ζ coordinates.

3.4.1 Strains and stresses

The GL strain components are

$$\epsilon_{ij}(\xi,\eta,\zeta) = 0.5\left(\underbrace{u_{i,j}+u_{j,i}}_{\text{linear}}+\underbrace{u_{k,i}u_{k,j}}_{\text{non-linear}}\right); \quad i,j,k=\xi,\eta,\zeta \tag{3.18}$$

Because of the assumption that the cross-section shape does not change during deformation, the non-vanishing components are $\epsilon_{\xi\xi}$, $\epsilon_{\xi\eta}$, and $\epsilon_{\xi\zeta}$, given w.r.t. the initial cross-sectional frame ${}^0\boldsymbol{V}$ (Dvorkin, Onate, and Olivier, 1988).

The 2nd Piola-Kirchhoff stress components w.r.t. the initial cross-sectional basis ${}^0\boldsymbol{V}$, because of the assumption of homogeneous, isotropic and linear elastic material, are defined as

$$S_{ij}(\xi,\eta,\zeta) = C_{ijrs}\,\epsilon_{rs}; \quad i,j,r,s=\xi,\eta,\zeta \tag{3.19}$$

where C_{ijrs} is a fourth-rank tensor of material constants and ϵ_{rs} is given by eq. (3.18). Taking into account the assumption of the rigidity of the cross-section, and consequently, the relations $\epsilon_{\eta\eta} = \epsilon_{\zeta\zeta} = \epsilon_{\eta\zeta} = 0$ for the vanishing components of the strains at the lateral directions, the stress-strain law in Voigt notation is reduced to the following relation

$$\begin{Bmatrix} S_{\xi\xi} \\ S_{\xi\eta} \\ S_{\xi\zeta} \end{Bmatrix} = \begin{bmatrix} \frac{E(1-\nu)}{(1+\nu)(1-2\nu)} & 0 & 0 \\ 0 & kG & 0 \\ 0 & 0 & kG \end{bmatrix} \begin{Bmatrix} \epsilon_{\xi\xi} \\ 2\epsilon_{\xi\eta} \\ 2\epsilon_{\xi\zeta} \end{Bmatrix} \tag{3.20}$$

where E is the Young's modulus, ν is the Poisson's ratio, $G = \frac{E}{2(1+\nu)}$ is the shear modulus multiplied by the shear correction factor k (e.g. Dvorkin, Onate, and Olivier, 1988). In this work, the Young's modulus E alone is used for the axial stress-strain relation.

3.4.2 Principle of virtual work

In a weak form, that is suitable for the FEM, the equilibrium equation of the body at $(t+\Delta t, \epsilon)$ is given by Bathe, 1996

$$\delta W_{int}(\xi,\eta,\zeta) = \int_{{}^0V} {}^{t+\Delta t,\epsilon}S_{ij}\,\delta\,{}^{t+\Delta t,\epsilon}\epsilon_{ij}\,d\,{}^0V = \delta\,{}^{t+\Delta t,\epsilon}W_{ext}; \quad i,j=\xi,\eta,\zeta \tag{3.21}$$

where ${}^0V$ is the initial volume, ${}^{t+\Delta t,\epsilon}S_{ij}$ are the 2nd Piola-Kirchhoff stress components given by eq. (3.19), $\delta {}^{t+\Delta t,\epsilon}W_{ext}$ is the external virtual work, and $\delta {}^{t+\Delta t,\epsilon}\epsilon_{ij}$ are the virtual strain components derived from eq. (3.18) as follows

$$\delta\epsilon_{ij}(\xi,\eta,\zeta) = 0.5\left(\delta u_{i,j} + \delta u_{j,i} + {}^{t+\Delta t}u_{k,i}\,\delta u_{k,j} + \delta u_{k,i}\,{}^{t+\Delta t}u_{k,j}\right); \quad i,j,k = \xi,\eta,\zeta \tag{3.22}$$

where δu_i are the virtual displacement components of an arbitrary material particle (ξ,η,ζ) w.r.t. the initial cross-sectional basis ${}^0\boldsymbol{V}$. The corresponding vector form is given in relation with the unknown set of variables $(\delta\boldsymbol{u}_0, \delta\boldsymbol{\psi})$ as

$$\delta\boldsymbol{u}(\xi,\eta,\zeta) = \delta\boldsymbol{u}_0 + \eta\underbrace{\left(\delta\boldsymbol{\psi}\times{}^{t+\Delta t}\boldsymbol{V}_2\right)}_{\delta\boldsymbol{V}_2} + \zeta\underbrace{\left(\delta\boldsymbol{\psi}\times{}^{t+\Delta t}\boldsymbol{V}_3\right)}_{\delta\boldsymbol{V}_3} \tag{3.23}$$

where $\delta\boldsymbol{u}_0$, $\delta\boldsymbol{V}_2$ and $\delta\boldsymbol{V}_3$ are given after taking the directional derivative w.r.t. ϵ, for $\epsilon = 0$, of eqs. (3.6) and (3.9), respectively.

3.4.3 1D strain measures and stress resultants

The basic kinematic assumption of undeformable beam cross-sections (whose kinematics are uniquely defined by the cross-section centroid position and orientation, see eqs. (3.2) and (3.4), and the corresponding variation in eq. (3.23)) is inserted into the virtual work terms of eq. (3.21). Based on this constrained virtual work expression, pairs of force/moment stress resultants as well as translational/rotational strain measures associated with the resulting 1D beam theory are identified (the left superscript ${}^{t+\Delta t,\epsilon}$ is omitted in the following for convenience).

The terms of the internal virtual work equation (eq. (3.21)) in relation to normal ('n') and shear ('s') stresses are

$$\delta W_{\text{int,n}}(\xi,\eta,\zeta) = \int_{{}^0V}\left(S_{\xi\xi}\,\delta\epsilon_{\xi\xi}\right)d^0V \overset{eq.\ (3.19)}{=} \int_{{}^0V}\left[\left(E\epsilon_{\xi\xi}\right)\delta\epsilon_{\xi\xi}\right]d^0V \tag{3.24}$$

$$\begin{aligned}\delta W_{\text{int,s}}(\xi,\eta,\zeta) &= \int_{{}^0V}\left(S_{\xi\eta}\,2\delta\epsilon_{\xi\eta} + S_{\xi\zeta}\,2\delta\epsilon_{\xi\zeta}\right)d^0V \\ &\overset{eq.\ (3.19)}{=} \int_{{}^0V}\left[\left(kG\,2\epsilon_{\xi\eta}\right)2\delta\epsilon_{\xi\eta} + \left(kG\,2\epsilon_{\xi\zeta}\right)2\delta\epsilon_{\xi\zeta}\right]d^0V\end{aligned} \tag{3.25}$$

Incorporating into eqs. (3.24) and (3.25) the expressions for strains and their variations, eqs. (3.18) and (3.22), where the displacement gradients and their variations are given by the differentiation along ξ,η,ζ of eq. (3.4) and eq. (3.23), respectively, the following terms

arise

$$
\begin{aligned}
&\delta W_{\text{int,n}}(\xi,\eta,\zeta) = \\
&\int_{{}^0L} \Bigg\{ \underbrace{\left(\delta u_{0\xi,\xi} + \boldsymbol{u}_{0,\xi}^T\,\delta\boldsymbol{u}_{0,\xi}\right)}_{\delta\Gamma_\xi(\xi)} \\
&\underbrace{\int_{{}^0A} E\left[\left(u_{0\xi,\xi} + 0.5\boldsymbol{u}_{0,\xi}^T\,\boldsymbol{u}_{0,\xi}\right) + \eta^2\left(0.5\boldsymbol{V}_{2,\xi}^T\,\boldsymbol{V}_{2,\xi}\right) + \zeta^2\left(0.5\boldsymbol{V}_{3,\xi}^T\,\boldsymbol{V}_{3,\xi}\right)\right] d^0A}_{F_\xi(\xi)} \\
&+ \underbrace{\left(\delta V_{3\xi,\xi} + \boldsymbol{u}_{0,\xi}^T\,\delta\boldsymbol{V}_{3,\xi} + \boldsymbol{V}_{3,\xi}^T\,\delta\boldsymbol{u}_{0,\xi}\right)}_{\delta K_\eta(\xi)} \underbrace{\int_{{}^0A} E\zeta^2\left(V_{3\xi,\xi} + \boldsymbol{u}_{0,\xi}^T\,\boldsymbol{V}_{3,\xi}\right) d^0A}_{M_\eta(\xi)} \\
&+ \underbrace{\left(\delta V_{2\xi,\xi} + \boldsymbol{u}_{0,\xi}^T\,\delta\boldsymbol{V}_{2,\xi} + \boldsymbol{V}_{2,\xi}^T\,\delta\boldsymbol{u}_{0,\xi}\right)}_{-\delta K_\zeta(\xi)} \underbrace{\int_{{}^0A} E\eta^2\left(V_{2\xi,\xi} + \boldsymbol{u}_{0,\xi}^T\,\boldsymbol{V}_{2,\xi}\right) d^0A}_{-M_\zeta(\xi)} \\
&+ \underbrace{\left(\boldsymbol{V}_{3,\xi}^T\,\delta\boldsymbol{V}_{3,\xi}\right)}_{\delta K_{\eta,nl,2}(\xi)} \underbrace{\int_{{}^0A} E\left[\zeta^2\left(u_{0\xi,\xi} + 0.5\boldsymbol{u}_{0,\xi}^T\,\boldsymbol{u}_{0,\xi}\right) + \eta^2\zeta^2\left(0.5\boldsymbol{V}_{2,\xi}^T\,\boldsymbol{V}_{2,\xi}\right) + \zeta^4\left(0.5\boldsymbol{V}_{3,\xi}^T\,\boldsymbol{V}_{3,\xi}\right)\right] d^0A}_{M_{R1}(\xi)} \\
&+ \underbrace{\left(\boldsymbol{V}_{2,\xi}^T\,\delta\boldsymbol{V}_{2,\xi}\right)}_{\delta K_{\zeta,nl,2}(\xi)} \underbrace{\int_{{}^0A} E\left[\eta^2\left(u_{0\xi,\xi} + 0.5\boldsymbol{u}_{0,\xi}^T\,\boldsymbol{u}_{0,\xi}\right) + \eta^4\left(0.5\boldsymbol{V}_{2,\xi}^T\,\boldsymbol{V}_{2,\xi}\right) + \eta^2\zeta^2\left(0.5\boldsymbol{V}_{3,\xi}^T\,\boldsymbol{V}_{3,\xi}\right)\right] d^0A}_{M_{R2}(\xi)} \\
&+ \underbrace{\left(\boldsymbol{V}_{3,\xi}^T\,\delta\boldsymbol{V}_{2,\xi} + \boldsymbol{V}_{2,\xi}^T\,\delta\boldsymbol{V}_{3,\xi}\right)}_{\delta K_{\zeta\eta,nl,2}(\xi)} \underbrace{\int_{{}^0A} E\eta^2\zeta^2\left(\boldsymbol{V}_{2,\xi}^T\,\boldsymbol{V}_{3,\xi}\right) d^0A}_{M_{R3}(\xi)} \Bigg\} d^0L
\end{aligned}
\tag{3.26}
$$

$$
\begin{aligned}
&\delta W_{\text{int,s}}(\xi,\eta,\zeta) = \\
&\int_{{}^0L} \Bigg\{ \underbrace{\left(\delta V_{2\xi} + \delta\boldsymbol{u}_{0,\xi}^T\,\boldsymbol{V}_2 + \delta\boldsymbol{V}_2^T\,\boldsymbol{u}_{0,\xi}\right)}_{\delta\Gamma_\eta(\xi)} \underbrace{\int_{{}^0A} kG\left(V_{2\xi} + \boldsymbol{u}_{0,\xi}^T\,\boldsymbol{V}_2\right) d^0A}_{F_\eta(\xi)} \\
&+ \underbrace{\left(\delta V_{3\xi} + \delta\boldsymbol{u}_{0,\xi}^T\,\boldsymbol{V}_3 + \delta\boldsymbol{V}_3^T\,\boldsymbol{u}_{0,\xi}\right)}_{\delta\Gamma_\zeta(\xi)} \underbrace{\int_{{}^0A} kG\left(V_{3\xi} + \boldsymbol{u}_{0,\xi}^T\,\boldsymbol{V}_3\right) d^0A}_{F_\zeta(\xi)} \\
&+ \underbrace{\left(\delta\boldsymbol{V}_3^T\,\boldsymbol{V}_{2,\xi} + \delta\boldsymbol{V}_{2,\xi}^T\,\boldsymbol{V}_3\right)}_{\delta K_\xi(\xi)} \underbrace{\int_{{}^0A} kG\left(\eta^2 + \zeta^2\right)\left(\boldsymbol{V}_3^T\,\boldsymbol{V}_{2,\xi}\right) d^0A}_{M_\xi(\xi)} \Bigg\} d^0L
\end{aligned}
\tag{3.27}
$$

In eqs. (3.26) and (3.27), it is taken into account that:

1. $\int_{{}^0A}\eta\ d^0A = \int_{{}^0A}\zeta\ d^0A = \int_{{}^0A}\eta\zeta\ d^0A = \int_{{}^0A}\zeta\eta^2\ d^0A = \int_{{}^0A}\zeta^3\ d^0A = \int_{{}^0A}\zeta^2\eta\ d^0A = \int_{{}^0A}\eta^3\ d^0A = \int_{{}^0A}\eta^3\zeta\ d^0A = \int_{{}^0A}\zeta^3\eta\ d^0A = 0$, because the chosen reference system $\xi\eta\zeta$ passes through the centroid of the cross-section, while η, ζ are the principal axes of inertia; ${}^0A$ is the cross-sectional area measured in the material frame ${}^0\boldsymbol{V}$,

2. ${}^0\boldsymbol{V}_{2,\xi} = {}^0\boldsymbol{V}_{3,\xi} = 0$, because there is no initial curvature,

3. ${}^0\boldsymbol{V}_2^T\,{}^0\boldsymbol{V}_1 = {}^0\boldsymbol{V}_3^T\,{}^0\boldsymbol{V}_1 = 0$, because of the orthogonality property of the cross-section directors (see section 2.2 for justifying this property),

4. the derivatives along ξ of the translational components, $u_{0\eta,\xi}, u_{0\zeta,\xi}$, and of the cross-section directors components, $V_{2\eta,\xi}, V_{3\eta,\xi}$ and $V_{3\zeta,\xi}, V_{3\zeta,\xi}$, cancel out with their opposites.

5. the matrix $\left(exp(\hat{\boldsymbol{\theta}})\right)^T \left(exp(\hat{\boldsymbol{\theta}})_{,\xi}\right)$ is antisymmetric (Appendix A.2.2 in Gaćeša, 2015 for the proof), thus

$$\boldsymbol{V}_3^T\,\boldsymbol{V}_{2,\xi} = {}^0\boldsymbol{V}_3^T \left(exp(\hat{\boldsymbol{\theta}})\right)^T \left(exp(\hat{\boldsymbol{\theta}})_{,\xi}\right) {}^0\boldsymbol{V}_2 = -{}^0\boldsymbol{V}_2^T \left(exp(\hat{\boldsymbol{\theta}})\right)^T \left(exp(\hat{\boldsymbol{\theta}})_{,\xi}\right) {}^0\boldsymbol{V}_3 = -\boldsymbol{V}_2^T\,\boldsymbol{V}_{3,\xi}$$

The internal forces i.e. the axial force F_ξ along the ξ material axis and the shear forces F_η and F_ζ along the η and ζ material axes, are identified in eqs. (3.26) and (3.27), and defined as follows

$$F_\xi(\xi) = \int_{{}^0A} S_{\xi\xi}\; d^0A = EA\,(\Gamma_{\xi,l} + \Gamma_{\xi,nl}) + EI_\zeta\,K_{\zeta,nl,2} + EI_\eta\,K_{\eta,nl,2} \tag{3.28}$$

$$F_\eta(\xi) = \int_{{}^0A} S_{\xi\eta}\; d^0A = k_\eta GA\,(\Gamma_{\eta,l} + \Gamma_{\eta,nl}) \tag{3.29}$$

$$F_\zeta(\xi) = \int_{{}^0A} S_{\xi\zeta}\; d^0A = k_\zeta GA\,(\Gamma_{\zeta,l} + \Gamma_{\zeta,nl}) \tag{3.30}$$

where $S_{\xi\xi}$; $S_{\xi\eta}$; $S_{\xi\zeta}$ are the stress components given by eq. (3.19), $EA = \int_{{}^0A} E\,d^0A$, $EI_\zeta = \int_{{}^0A} E\eta^2\,d^0A$, $EI_\eta = \int_{{}^0A} E\zeta^2\,d^0A$, $GA = \int_{{}^0A} G\,d^0A$, k_η, k_ζ are the shear correction factors, while the 1D strain measures $\Gamma_{\xi,l}$; $\Gamma_{\eta,l}$; $\Gamma_{\zeta,l}$ are the linear components along the system $\xi\eta\zeta$ of the material axial/shear strain vector $\boldsymbol{\Gamma}_l$ which is given by

$$\boldsymbol{\Gamma}_l(\xi) = \begin{bmatrix} \boldsymbol{u}_{0,\xi}^T \\ \left(exp(\hat{\boldsymbol{\theta}})\,{}^0\boldsymbol{V}_2\right)^T \\ \left(exp(\hat{\boldsymbol{\theta}})\,{}^0\boldsymbol{V}_3\right)^T \end{bmatrix} {}^0\boldsymbol{V}_1 \tag{3.31}$$

and $\Gamma_{\xi,nl}$; $\Gamma_{\eta,nl}$; $\Gamma_{\zeta,nl}$ are the corresponding non-linear components of the material axial/shear strain vector $\boldsymbol{\Gamma}_{nl}$ which is given by

$$\boldsymbol{\Gamma}_{nl}(\xi) = \begin{bmatrix} 0.5\,\boldsymbol{u}_{0,\xi}^T \\ \left(exp(\hat{\boldsymbol{\theta}})\,{}^0\boldsymbol{V}_2\right)^T \\ \left(exp(\hat{\boldsymbol{\theta}})\,{}^0\boldsymbol{V}_3\right)^T \end{bmatrix} \boldsymbol{u}_{0,\xi} \tag{3.32}$$

in which the subscripts l and nl means linear and non-linear, respectively; $\boldsymbol{u}_{0,\xi}$ is the derivative along the material axis ξ of the translation vector of the centroid. Adding the eqs. (3.31) and (3.32), the following material axial/ shear strain vector is derived (the variation of its

components is identified in eqs. (3.26) and (3.27))

$$\boldsymbol{\Gamma}(\xi) = \begin{Bmatrix} 0.5\,\left(\boldsymbol{r}_{0,\xi}^T\,\boldsymbol{r}_{0,\xi} - 1\right) \\ \left(exp(\hat{\boldsymbol{\theta}})\,{}^0\boldsymbol{V}_2\right)^T\boldsymbol{r}_{0,\xi} \\ \left(exp(\hat{\boldsymbol{\theta}})\,{}^0\boldsymbol{V}_3\right)^T\boldsymbol{r}_{0,\xi} \end{Bmatrix} \tag{3.33}$$

where the relation $\boldsymbol{r}_{0,\xi} = {}^0\boldsymbol{V}_1 + \boldsymbol{u}_{0,\xi}$ has been used; the axial strain term is different from the corresponding SR term, i.e. $\Gamma_\xi = \boldsymbol{V}_1^T\boldsymbol{r}_{0,\xi} - 1$, while the shear strain terms are the same (see eq. (3.10) for the definition of the material setting of the SR axial/shear strain vector). Moreover, the contribution of curvatures square in the definition of axial force is not present in the material form of eq. (3.12); these non-linear curvature strain measures $K_{\zeta,nl,2};\ K_{\eta,nl,2}$ are (their variation are identified in eq. (3.26))

$$K_{\zeta,nl,2}(\xi) = 0.5\,\left|\left(exp(\hat{\boldsymbol{\theta}})_{,\xi}\right)\,{}^0\boldsymbol{V}_2\right|^2 \tag{3.34}$$

$$K_{\eta,nl,2}(\xi) = 0.5\,\left|\left(exp(\hat{\boldsymbol{\theta}})_{,\xi}\right)\,{}^0\boldsymbol{V}_3\right|^2 \tag{3.35}$$

where the derivative of the Rodrigues formula $exp(\hat{\boldsymbol{\theta}})_{,\xi}$ is given in Ritto-Corrêa and Camotim, 2002.

The internal moments , i.e. the twisting moment M_ξ about the ξ material axis and the bending moments M_η and M_ζ about the η and ζ material axes, are also identified in eqs. (3.26) and (3.27), and defined as follows

$$M_\xi(\xi) = \int_{{}^0A} \left(S_{\xi\zeta}\,\eta - S_{\xi\eta}\,\zeta\right)\,d^0A = k_\xi GI_p\,K_{\xi,nl,1} \tag{3.36}$$

$$M_\eta(\xi) = \int_{{}^0A} S_{\xi\xi}\,\zeta\,d^0A = EI_\eta\,\left(K_{\eta,l} + K_{\eta,nl,1}\right) \tag{3.37}$$

$$M_\zeta(\xi) = -\int_{{}^0A} S_{\xi\xi}\,\eta\,d^0A = EI_\zeta\,\left(K_{\zeta,l} + K_{\zeta,nl,1}\right) \tag{3.38}$$

where $GI_p = \int_{{}^0A} G(\eta^2+\zeta^2)\,d^0A$, k_ξ is the twist correction factor, while the 1D strain measures $K_{\eta,l};\ K_{\zeta,l}$ are the linear components along the system $\xi\eta\zeta$ of the material twist/bending strain vector $\boldsymbol{K}_l$ which is given by

$$\boldsymbol{K}_l(\xi) = \begin{bmatrix} \boldsymbol{0}^T \\ \left(exp(\hat{\boldsymbol{\theta}})_{,\xi}\,{}^0\boldsymbol{V}_3\right)^T \\ -\left(exp(\hat{\boldsymbol{\theta}})_{,\xi}\,{}^0\boldsymbol{V}_2\right)^T \end{bmatrix}\,{}^0\boldsymbol{V}_1 \tag{3.39}$$

and $K_{\xi,nl,1}$; $K_{\eta,nl,1}$; $K_{\zeta,nl,1}$ are the corresponding non-linear components of the material twist/bending strain vector $\boldsymbol{K}_{nl,1}$ which is given by

$$\boldsymbol{K}_{nl,1}(\xi) = \left\{ \begin{array}{c} \left(exp(\hat{\boldsymbol{\theta}})\,{}^0\boldsymbol{V}_3\right)^T \left(exp(\hat{\boldsymbol{\theta}})_{,\xi}\,{}^0\boldsymbol{V}_2\right) \\ 0 \\ 0 \end{array} \right\} + \left[\begin{array}{c} \boldsymbol{0}^T \\ \left(exp(\hat{\boldsymbol{\theta}})_{,\xi}\,{}^0\boldsymbol{V}_3\right)^T \\ -\left(exp(\hat{\boldsymbol{\theta}})_{,\xi}\,{}^0\boldsymbol{V}_2\right)^T \end{array} \right] \boldsymbol{u}_{0,\xi} \tag{3.40}$$

Adding the eqs. (3.39) and (3.40), the following material twist/ bending strain vector is derived (the variation of its components is identified in eqs. (3.26) and (3.27))

$$\boldsymbol{K}(\xi) = \left\{ \begin{array}{c} \left(exp(\hat{\boldsymbol{\theta}})\,{}^0\boldsymbol{V}_3\right)^T \left(exp(\hat{\boldsymbol{\theta}})_{,\xi}\,{}^0\boldsymbol{V}_2\right) \\ \boldsymbol{r}_{0,\xi}^T \left(exp(\hat{\boldsymbol{\theta}})_{,\xi}\,{}^0\boldsymbol{V}_3\right) \\ -\boldsymbol{r}_{0,\xi}^T \left(exp(\hat{\boldsymbol{\theta}})_{,\xi}\,{}^0\boldsymbol{V}_2\right) \end{array} \right\} \tag{3.41}$$

in which the twist term is the same as the corresponding SR term, while the bending terms are different, because for instance $\boldsymbol{r}_{0,\xi}^T \left(exp(\hat{\boldsymbol{\theta}})_{,\xi}\,{}^0\boldsymbol{V}_3\right) \neq {}^{t+\Delta t}\boldsymbol{V}_1^T \left(exp(\hat{\boldsymbol{\theta}})_{,\xi}\,{}^0\boldsymbol{V}_3\right)$ when shear deformation is taken into account (see the axial vector of eq. (3.11) for the definition of the material setting of SR twist/bending curvatures).
Moreover, a further contribution due to the geometric non-linear effects appears through the following higher order term M_R (e.g. Sapountzakis and Dikaros, 2011; Manolas, Riziotis, and Voutsinas, 2015; Houbolt and Brooks, 1956)

$$M_R(\xi) = \int_{{}^0A} S_{\xi\xi}\,(\eta^2+\zeta^2)\,d^0A = EI_p\;(\Gamma_{\xi,l} + \Gamma_{\xi,nl}) + EI_{p\zeta}\,K_{\zeta,nl,2} + EI_{p\eta}\,K_{\eta,nl,2} + EI_{\zeta\eta}\,K_{\zeta\eta,nl,2} \tag{3.42}$$

where $EI_p = \int_{{}^0A} E(\eta^2+\zeta^2)\,d^0A$, $EI_{p\zeta} = \int_{{}^0A} E(\eta^2+\zeta^2)\eta^2\,d^0A$, $EI_{p\eta} = \int_{{}^0A} E(\eta^2+\zeta^2)\zeta^2\,d^0A$, $EI_{\zeta\eta} = \int_{{}^0A} E\eta^2\zeta^2\,d^0A$, while the non-linear curvature strain measure $K_{\zeta\eta,nl,2}$ that appears in this definition is (the variation of this component is identified in eq. (3.26))

$$K_{\zeta\eta,nl,2}(\xi) = \left(exp(\hat{\boldsymbol{\theta}})_{,\xi}\,{}^0\boldsymbol{V}_2\right)^T \left(exp(\hat{\boldsymbol{\theta}})_{,\xi}\,{}^0\boldsymbol{V}_3\right) \tag{3.43}$$

Note that the higher order term M_R can be written as a sum of the following three components (in this way they appear in the virtual work equation (3.26))

$$M_{R1}(\xi) = EI_\eta\,\Gamma_\xi + EI_{\zeta\eta}\,K_{\zeta,nl,2} + EI_{\eta 2}\,K_{\eta,nl,2} \tag{3.44}$$

$$M_{R2}(\xi) = EI_\zeta\,\Gamma_\xi + EI_{\zeta 2}\,K_{\zeta,nl,2} + EI_{\zeta\eta}\,K_{\eta,nl,2} \tag{3.45}$$

$$M_{R3}(\xi) = EI_{\zeta\eta}\,K_{\zeta\eta,nl,2} \tag{3.46}$$

where $EI_{\eta 2} = \int_{{}^0A} E\zeta^4\,d^0A$ and $EI_{\zeta 2} = \int_{{}^0A} E\eta^4\,d^0A$.

1D virtual strain measures

The virtual strain measures $\delta\Gamma_\xi$; $\delta\Gamma_\eta$; $\delta\Gamma_\zeta$ that appear in eqs. (3.26) and (3.27) are the components along the system $\xi\eta\zeta$ of the variation of the axial/shear strain vector $\boldsymbol{\Gamma}$ (eq. (3.33))

$$\delta\boldsymbol{\Gamma} = \begin{Bmatrix} \boldsymbol{r}_{0,\xi}^T\,\delta\boldsymbol{r}_{0,\xi} \\ \boldsymbol{V}_2^T\left(\delta\boldsymbol{r}_{0,\xi} + \boldsymbol{r}_{0,\xi}\times\delta\boldsymbol{\psi}\right) \\ \boldsymbol{V}_3^T\left(\delta\boldsymbol{r}_{0,\xi} + \boldsymbol{r}_{0,\xi}\times\delta\boldsymbol{\psi}\right) \end{Bmatrix} \tag{3.47}$$

Comparing eq. (3.47) to the corresponding SR virtual strain vector (eq. (3.16)), there is a difference in the axial term, i.e. $\boldsymbol{r}_{0,\xi}^T\,\delta\boldsymbol{r}_{0,\xi} \neq \boldsymbol{V}_1^T\left(\delta\boldsymbol{r}_{0,\xi} + \boldsymbol{r}_{0,\xi}\times\delta\boldsymbol{\psi}\right)$, while the shear terms are the same.

The virtual curvature measures $\delta K_\xi;\ \delta K_\eta;\ \delta K_\zeta$ that appear in eqs. (3.26) and (3.27) are the components along the system $\xi\eta\zeta$ of the variation of the twist/bending curvature vector $\boldsymbol{K}$ (eq. (3.41))

$$\delta\boldsymbol{K} = \begin{Bmatrix} \boldsymbol{V}_1^T\delta\boldsymbol{\psi}_{,\xi} \\ (\boldsymbol{V}_3\times\boldsymbol{r}_{0,\xi})^T\delta\boldsymbol{\psi}_{,\xi} + \boldsymbol{V}_{3,\xi}^T\left(\delta\boldsymbol{r}_{0,\xi} + \boldsymbol{r}_{0,\xi}\times\delta\boldsymbol{\psi}\right) \\ -\left[(\boldsymbol{V}_2\times\boldsymbol{r}_{0,\xi})^T\delta\boldsymbol{\psi}_{,\xi} + \boldsymbol{V}_{2,\xi}^T\left(\delta\boldsymbol{r}_{0,\xi} + \boldsymbol{r}_{0,\xi}\times\delta\boldsymbol{\psi}\right)\right] \end{Bmatrix} \tag{3.48}$$

where the relation $(\boldsymbol{V}_2\times\boldsymbol{V}_3)^T = \boldsymbol{V}_1^T$ has been used. Comparing eq. (3.48) to the corresponding SR virtual curvature vector (eq. (3.17)), the bending terms are different, while the twist term is the same. The additional virtual curvature measures $\delta K_{\eta,nl,2};\ \delta K_{\zeta,nl,2};\ \delta K_{\zeta\eta,nl,2}$ which are not present in the SR virtual strains definition are given as

$$\delta K_{\eta,nl,2} = \left(\boldsymbol{V}_3\times\boldsymbol{V}_{3,\xi}\right)^T\delta\boldsymbol{\psi}_{,\xi} \tag{3.49}$$

$$\delta K_{\zeta,nl,2} = \left(\boldsymbol{V}_2\times\boldsymbol{V}_{2,\xi}\right)^T\delta\boldsymbol{\psi}_{,\xi} \tag{3.50}$$

$$\delta K_{\zeta\eta,nl,2} = \left[\left(\boldsymbol{V}_3\times\boldsymbol{V}_{2,\xi}\right)^T + \left(\boldsymbol{V}_2\times\boldsymbol{V}_{3,\xi}\right)^T\right]\delta\boldsymbol{\psi}_{,\xi} \tag{3.51}$$

Remark: The main difference between the SR and GL beam theories is that the strain components in the GL beam theory include the quadratic terms in strains $\boldsymbol{\Gamma}$ and curvatures $\boldsymbol{K}$, which are not present in the SR beam theory. This is also stated in Géradin and Cardona, 2001; Linn, Lang, and Tuganov, 2013; Meier, Wall, and Popp, 2019, where the derivation of the SR beam theory is shown, starting from the GL strains and following the small local strain assumption. A theoretical connection between these two definitions of strain is also given in Auricchio, Carotenuto, and Reali, 2008 (within the framework of the geometrically non-linear beam modeling), and in *Continuum Mechanics* (within the framework of the continuum mechanics).

For the linearization of the internal virtual work given by eq. (3.21) about the configuration at $t + \Delta t$, the reader is referred to the appendix A.2.

3.5 External virtual work

The weak form of the external load part is written as follows (Jelenić and Crisfield, 1999)

$$\delta^{t+\Delta t,\epsilon} W_{ext}(\xi) = \int_{0_L} \left(\delta \boldsymbol{u}_0^T \, \tilde{\boldsymbol{f}} + \delta \boldsymbol{\psi}^T \, \tilde{\boldsymbol{m}} \right) d\xi + \left(\delta \boldsymbol{u}_{0,I}^T \boldsymbol{p}_I + \delta \boldsymbol{\psi}_I^T \boldsymbol{t}_I + \delta \boldsymbol{u}_J^T \boldsymbol{p}_J + \delta \boldsymbol{\psi}_J^T \boldsymbol{t}_J \right) \tag{3.52}$$

where $\tilde{\boldsymbol{f}}(\xi)$ and $\tilde{\boldsymbol{m}}(\xi)$ are force and moment loads and $\boldsymbol{p}_I, \boldsymbol{t}_I, \boldsymbol{p}_J, \boldsymbol{t}_J$ are concentrated forces and torques at $\xi = 0$ and $\xi = {}^0L$; I, J are the start and end nodes of a 2-noded beam element. In case that the external load follows the deformation, the stiffening due to the change of the load vector orientation should be taken into account. For e.g. a concentrated follower load $\boldsymbol{P} = P_j \boldsymbol{V}_j$ that is constant w.r.t. the moving frame, its material components P_j do not change during the motion. But, to include it into the equilibrium equation, the load is written in its spatial setting $\boldsymbol{p}$ as

$$\boldsymbol{p} = \boldsymbol{\Lambda} \boldsymbol{P} \tag{3.53}$$

where $\boldsymbol{\Lambda}$ expresses the load vector orientation.
By taking the directional derivative w.r.t. ϵ, with $\epsilon = 0$, of each unknown of eq. (3.52), results to the following relation, that is the linearized form of the external virtual work

$$\begin{aligned}
d\delta^{t+\Delta t} W_{ext} &= \int_{0_L} \left(\delta \boldsymbol{u}_0^T \, d\tilde{\boldsymbol{f}} + \delta \boldsymbol{\psi}^T \, d\tilde{\boldsymbol{m}} \right) d\xi \; + \; \left(\delta \boldsymbol{u}_I^T d\boldsymbol{p}_I + \delta \boldsymbol{\psi}_I^T d\boldsymbol{t}_I + \delta \boldsymbol{u}_J^T d\boldsymbol{p}_J + \delta \boldsymbol{\psi}_J^T d\boldsymbol{t}_J \right) \\
&= \int_{0_L} \left\{ \delta \boldsymbol{u}_0^T \left(d\boldsymbol{\psi} \times \tilde{\boldsymbol{f}} \right) + \delta \boldsymbol{\psi}^T \left[d\boldsymbol{\psi} \times \boldsymbol{\Lambda} (\boldsymbol{S} \times \tilde{\boldsymbol{F}}) \right] \right\} d\xi \\
&+ \delta \boldsymbol{u}_I^T \left(d\boldsymbol{\psi}_I \times \boldsymbol{p}_I \right) + \delta \boldsymbol{\psi}_I^T \left[d\boldsymbol{\psi}_I \times \boldsymbol{\Lambda}_I (\boldsymbol{S}_I \times \boldsymbol{P}_I) \right] \\
&+ \delta \boldsymbol{u}_J^T \left(d\boldsymbol{\psi}_J \times \boldsymbol{p}_J \right) + \delta \boldsymbol{\psi}_J^T \left[d\boldsymbol{\psi}_J \times \boldsymbol{\Lambda}_J (\boldsymbol{S}_J \times \boldsymbol{P}_J) \right] \\
&= \int_{0_L} \left\{ \delta \boldsymbol{u}_0^T \left(-\tilde{\boldsymbol{f}} \times d\boldsymbol{\psi} \right) + \delta \boldsymbol{\psi}^T \left[-\boldsymbol{\Lambda} (\boldsymbol{S} \times \tilde{\boldsymbol{F}}) \times d\boldsymbol{\psi} \right] \right\} d\xi \\
&+ \delta \boldsymbol{u}_I^T \left(-\boldsymbol{p}_I \times d\boldsymbol{\psi}_I \right) + \delta \boldsymbol{\psi}_I^T \left[-\boldsymbol{\Lambda}_I (\boldsymbol{S}_I \times \boldsymbol{P}_I) \times d\boldsymbol{\psi}_I \right] \\
&+ \delta \boldsymbol{u}_J^T \left(-\boldsymbol{p}_J \times d\boldsymbol{\psi}_J \right) + \delta \boldsymbol{\psi}_J^T \left[-\boldsymbol{\Lambda}_J (\boldsymbol{S}_J \times \boldsymbol{P}_J) \times d\boldsymbol{\psi}_J \right]
\end{aligned} \tag{3.54}$$

where

$$\tilde{\boldsymbol{m}} \overset{\text{eq. (3.2)}}{=} \int_{0_A} \left[(\boldsymbol{r} - \boldsymbol{r}_0) \times \tilde{\boldsymbol{f}} \right] d^0 A = \int_{0_A} \left[(\boldsymbol{\Lambda} \boldsymbol{X}) \times (\boldsymbol{\Lambda} \tilde{\boldsymbol{F}}) \right] d^0 A \tag{3.55}$$

$$= \int_{0_A} \left[\boldsymbol{\Lambda} (\boldsymbol{X} \times \tilde{\boldsymbol{F}}) \right] d^0 A = \boldsymbol{\Lambda} \underbrace{(\boldsymbol{S} \times \tilde{\boldsymbol{F}})}_{\tilde{\boldsymbol{M}}} \tag{3.56}$$

where $\tilde{\boldsymbol{M}}$ is the external, distributed moment in its material setting, and

$$\boldsymbol{S} = \int_{0_A} \boldsymbol{X} \, d^0 A, \boldsymbol{X}^T = \{0 \; \eta \; \zeta\}^T \tag{3.57}$$

From eq. (3.54), one can see that in case of concentrated loads, there is no need to integrate numerically along the length of the beam. In other words, the contribution to the stiffness matrix comes from the DOF's of the node where the load is applied.

3.6 Numerical issues regarding rotations

In this section, the iterative, as originally proposed in Simo and Vu-Quoc, 1986a, and the invariant, as originally proposed in Jelenić and Crisfield, 1999, formulations for the numerical treatment of the rotational unknowns, which are used for the SR and the GL theories, are discussed. A geometric description on the rotation manifold $SO(3)$ is given to show how to update and how to perturb the updated orientation for both techniques when a 2-noded (with the start-node denoted by I, and the end-node denoted by J) beam element is used. In the invariant technique, instead of the update to be performed w.r.t. the current *cross-sectional* orientation, as it is done for the iterative case, this is performed w.r.t. the current 'intermediate' *elemental* orientation.

3.6.1 Updated (trial) and perturbed orientation at $t + \Delta t$

Iterative formulation

In fig. 3.2, the rotation manifold $SO(3)$ is depicted together with the orientation of the cross-sections assigned at the nodes I and J, expressed by ${}^{t+\Delta t}\boldsymbol{\Lambda}_I$ and ${}^{t+\Delta t}\boldsymbol{\Lambda}_J$, respectively. The corresponding tangent planes are also illustrated in addition with the tangent plane at Identity $\boldsymbol{I}_3$. The two orientation matrices correspond to the total rotation vectors $\boldsymbol{\psi}_I$ and $\boldsymbol{\psi}_J$ of the cross-sections, given as the axial vectors of the skew-symmetric matrices $\boldsymbol{\Psi}_I$ and $\boldsymbol{\Psi}_J$ shown in the figure. To construct the perturbed orientation, the spin vectors $\delta\boldsymbol{\psi}_I$ and $\delta\boldsymbol{\psi}_J$ are used, given as the axial vectors of the skew-symmetric matrices $\delta\boldsymbol{\Psi}_I$ and $\delta\boldsymbol{\Psi}_J$, respectively. Therefore, the perturbed orientation ${}^{t+\Delta t,\epsilon}\boldsymbol{\Lambda}_I$ and ${}^{t+\Delta t,\epsilon}\boldsymbol{\Lambda}_J$, using eq. (3.8), are

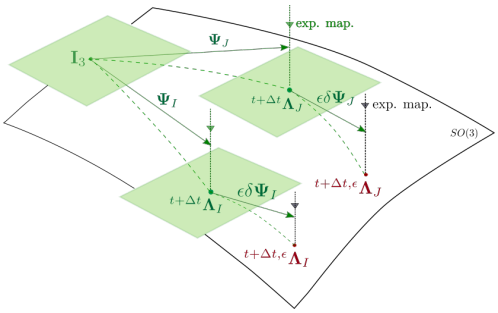

FIGURE 3.2: Iterative formulation (Simo and Vu-Quoc, 1986a): perturbation of the cross-sectional orientation of the $I-$ and $J-$ nodes.

$$
\begin{aligned}
{}^{t+\Delta t,\epsilon}\boldsymbol{\Lambda}_I &= exp(\epsilon\delta\boldsymbol{\Psi}_I)\,{}^{t+\Delta t}\boldsymbol{\Lambda}_I \\
{}^{t+\Delta t,\epsilon}\boldsymbol{\Lambda}_J &= exp(\epsilon\delta\boldsymbol{\Psi}_I)\,{}^{t+\Delta t}\boldsymbol{\Lambda}_J
\end{aligned}
\tag{3.58}
$$

To find the variation of the orientation, $\delta\boldsymbol{\Lambda}_I$ and $\delta\boldsymbol{\Lambda}_J$, the directional derivative w.r.t. ϵ, for $\epsilon = 0$ is performed in eq. (3.58)

$$
\begin{aligned}
\delta\boldsymbol{\Lambda}_I &= \delta\boldsymbol{\Psi}_I\,{}^{t+\Delta t}\boldsymbol{\Lambda}_I = \delta\boldsymbol{\psi}_I \times {}^{t+\Delta t}\boldsymbol{\Lambda}_I \\
\delta\boldsymbol{\Lambda}_J &= \delta\boldsymbol{\Psi}_J\,{}^{t+\Delta t}\boldsymbol{\Lambda}_J = \delta\boldsymbol{\psi}_J \times {}^{t+\Delta t}\boldsymbol{\Lambda}_J
\end{aligned}
\tag{3.59}
$$

Inside the numerical procedure, the spin vectors $\delta\boldsymbol{\psi}_I$ and $\delta\boldsymbol{\psi}_J$ need to be interpolated to express the corresponding quantity at the Gauss point; this is no consistent to the geometric structure of the rotation manifold, because the interpolated quantities do not belong at the same tangent space. This inconsistency inputs a numerical error that is connected to the

distorsion of the elastic strain energy when a rigid-body rotation of the beam element shows up together with its elastic deformation.

Invariant formulation

In figs. 3.3a and 3.3b, the geometric structure, as a smooth manifold, of the rotation group $SO(3)$ is displayed, as previously. In fig. 3.3a, the update of the cross-sectional orientation

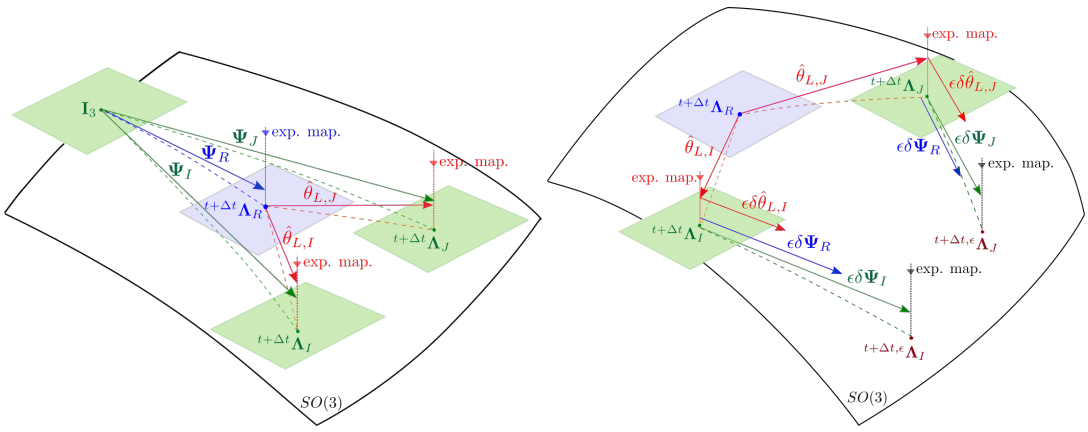

(A) (B)

FIGURE 3.3: Invariant formulation (Jelenić and Crisfield, 1999): (a) update of the cross-sectional orientation of the $I-$ and $J-$ nodes, and (b) perturbation of the cross-sectional orientation of the $I-$ and $J-$ nodes.

of the $I-$ and $J-$ nodes is shown. The *green* tangent planes correspond to two orientations, the fixed and the deformed at $t+\Delta t$, expressed by the orientation matrices $\boldsymbol{I}_3$ (3×3 identity matrix), and ${}^{t+\Delta t}\boldsymbol{\Lambda}_i$; $i=I,J$, respectively, while the *blue* tangent plane corresponds to the 'intermediate' orientation of the element, ${}^{t+\Delta t}\boldsymbol{\Lambda}_R$ at $t+\Delta t$ (the right-subscript $_R$ means *Rigid*, from the rigid-body rotation). The matrix that describes the cross-sections rotation, $\boldsymbol{\psi}_i$, is decomposed into a matrix that expresses the element rotation, $\boldsymbol{\psi}_R$, and a matrix that expresses the local (related to the element) cross-sections rotation, $\boldsymbol{\theta}_{L,i}$. To compute the rotation at the Gauss point, the interpolation is employed just for the latter local rotations of the nodes; this is allowable because this interpolation is performed in one Euclidean space (the space denoted by the *blue* tangent plane at ${}^{t+\Delta t}\boldsymbol{\Lambda}_R$). The above geometric interpretation is depicted in the following relation (Jelenić and Crisfield, 1999)

$$ {}^{t+\Delta t}\boldsymbol{\Lambda}(\xi) = {}^{t+\Delta t}\boldsymbol{\Lambda}_R \, exp\left(\hat{\boldsymbol{\theta}}_L(\xi)\right) \tag{3.60} $$

The order of the rotation matrices multiplication indicates that the local rotation components are given w.r.t. the rotated 'follower' axes $\boldsymbol{V}_R$ instead of the fixed axes (Argyris, 1982), i.e. $exp\left(\hat{\boldsymbol{\theta}}_L\right) = \boldsymbol{\Lambda}^T\left(\boldsymbol{V}\otimes\boldsymbol{V}_R\right)\boldsymbol{\Lambda} = \left(\boldsymbol{e}\otimes\boldsymbol{V}\right)\left(\boldsymbol{V}\otimes\boldsymbol{V}_R\right)\left(\boldsymbol{V}\otimes\boldsymbol{e}\right) = \left(\boldsymbol{e}\otimes\boldsymbol{V}_R\right)\left(\boldsymbol{V}\otimes\boldsymbol{e}\right) = \boldsymbol{\Lambda}_R^T\boldsymbol{\Lambda}$ (the left-superscript ${}^{t+\Delta t}$ has been omitted for convenience).

To perform the eq. (3.60),

- The 'intermediate' orientation of the element, ${}^{t+\Delta t}\boldsymbol{\Lambda}_R$, has to be computed first. For this reason, the relative orientation ${}^{t+\Delta t}\boldsymbol{\Lambda}_{IJ}$ between the start- and end-node is computed as follows (see also fig. 3.4, where ${}^{t+\Delta t}$ as left-superscript has been discarded for convenience):

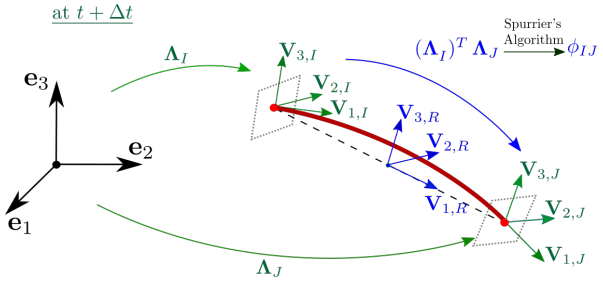

FIGURE 3.4: Reference frame corresponding to the rigid-body rotation of the element.

$$ {}^{t+\Delta t}\boldsymbol{\Lambda}_{IJ} = {}^{t+\Delta t}\boldsymbol{\Lambda}_I^T\, {}^{t+\Delta t}\boldsymbol{\Lambda}_J \tag{3.61} $$

Again, the reversed order of the rotation matrices multiplication indicates that the relative rotation components are given w.r.t. the rotated 'follower' basis $\boldsymbol{V}_I$. Using Spurrier's algorithm (see Appendix B in Simo and Vu-Quoc, 1988, see also the original papers in Klumpp, 1976; Spurrier, 1978), the relative rotation vector $\boldsymbol{\phi}_{IJ}$ is extracted from the corresponding rotation matrix ${}^{t+\Delta t}\boldsymbol{\Lambda}_{IJ}$. The rotation vector that corresponds to the rigid-body rotation of the element w.r.t. the 'follower' basis $\boldsymbol{V}_I$ is assumed to be equal to half of the relative rotation between the start and end nodes, i.e. $\boldsymbol{\phi}_{\text{rigid}} = \frac{1}{2}\boldsymbol{\phi}_{IJ}$. Thus, to compute the components of the orientation matrix ${}^{t+\Delta t}\boldsymbol{\Lambda}_R = \begin{bmatrix}\boldsymbol{V}_{1,R} & \boldsymbol{V}_{2,R} & \boldsymbol{V}_{3,R}\end{bmatrix}$ (fig. 3.4) w.r.t. the fixed basis $\boldsymbol{e}$ the following relation is used,

$$ {}^{t+\Delta t}\boldsymbol{\Lambda}_R = {}^{t+\Delta t}\boldsymbol{\Lambda}_I\, exp\left(\frac{1}{2}\hat{\boldsymbol{\phi}}_{IJ}\right) \tag{3.62} $$

- The local rotation of the cross-sections assigned to each node remains to be computed. The skew-symmetric matrices correspond to the local rotations for the start- and end-node are $\hat{\boldsymbol{\theta}}_{L,I}(\xi) = -\frac{1}{2}\,\hat{\boldsymbol{\phi}}_{IJ}$, $\hat{\boldsymbol{\theta}}_{L,J}(\xi) = \frac{1}{2}\,\hat{\boldsymbol{\phi}}_{IJ}$, respectively.

In fig. 3.3b, the perturbation of the cross-sectional orientation of the $I-$ and $J-$ nodes is shown. In this *invariant* approach, instead of using the infinitesimal spins $\delta\boldsymbol{\psi}_i; i = I, J$ to perturb these orientations at $t + \Delta t$ (see section 3.6.1 that describes the *iterative* case), these can be 'decomposed' into the infinitesimal local rotations $\delta\boldsymbol{\theta}_{L,i}$, to perturb the element orientation, and the infinitesimal spin $\delta\boldsymbol{\psi}_R$ of the element, to perturb the cross-sectional orientations, as it is indicated mathematically by the "chain rule" applied in eq. (3.60), i.e. (Jelenić and Crisfield, 1999):

$$ {}^{t+\Delta t,\epsilon}\boldsymbol{\Lambda}(\xi) = exp\left(\epsilon\delta\boldsymbol{\Psi}_R\right)\, {}^{t+\Delta t}\boldsymbol{\Lambda}(\xi) + {}^{t+\Delta t}\boldsymbol{\Lambda}_R\, exp\left(\hat{\boldsymbol{\theta}}_L(\xi) + \epsilon\delta\hat{\boldsymbol{\theta}}_L(\xi)\right) \tag{3.63} $$

where $\delta\boldsymbol{\Psi}_R(\xi)$, $\delta\hat{\boldsymbol{\theta}}_L(\xi)$ are skew-symmetric tensor fields, interpreted for $\epsilon > 0$, as superposed infinitesimal spin of the element onto the cross-section moving frame at $t + \Delta t$, and superposed infinitesimal local rotation onto the element moving frame at $t + \Delta t$, respectively. Again, the interpolation of the infinitesimal local rotations $\delta\boldsymbol{\theta}_{L,i}$ is employed in one Euclidean space where these quantities belong to. Substituting eq. (3.8) into the LHS of eq. (3.63), employing the directional derivative w.r.t. the scalar parameter ϵ onto eq. (3.63), for $\epsilon = 0$, and after some algebra, the desired relation between the three infinitesimal parameters, the total spins $\delta\boldsymbol{\psi}(\xi)$, the element spins $\delta\boldsymbol{\psi}_R$ and the local rotations $\delta\boldsymbol{\theta}_L(\xi)$, is derived, i.e. (Jelenić and Crisfield, 1999):

$$\delta\boldsymbol{\psi}(\xi) = \delta\boldsymbol{\psi}_R + {}^{t+\Delta t}\boldsymbol{\Lambda}_R\, \boldsymbol{T}(\boldsymbol{\theta}_L(\xi))\, \delta\boldsymbol{\theta}_L(\xi) \tag{3.64}$$

where $\delta\boldsymbol{\psi}(\xi), \delta\boldsymbol{\psi}_R \in \mathbb{R}^3 \cong T_{t+\Delta t}\boldsymbol{\Lambda} SO(3)$, while $\delta\boldsymbol{\theta}_L(\xi) \in \mathbb{R}^3 \cong T_{t+\Delta t}\boldsymbol{\Lambda}_R SO(3)$ and $\boldsymbol{T}(\boldsymbol{\theta}_L(\xi))\, \delta\boldsymbol{\theta}_L(\xi) \in \mathbb{R}^3 \cong T_{t+\Delta t}\boldsymbol{\Lambda} SO(3)$ (where $\cong$ represents an isomorphism); by premultiplying this expression with ${}^{t+\Delta t}\boldsymbol{\Lambda}_R$, the infinitesimal local rotation vector is given in global components. Thus, eq. (3.64) makes sense as all its constituents refer to the same Euclidean space (isomorphic to the spaces illustrated as *green* planes in fig. 3.3b) and have global components. For the derivation of $\boldsymbol{T}(\boldsymbol{\theta}_L)$ (named as the tangential transformation because it is a linear map between tangent spaces; e.g. *blue* and *green* tangent planes in fig. 3.3) see Crisfield, 1997; Simo and Vu-Quoc, 1988; Cardona and Géradin, 1988

$$\boldsymbol{T}(\boldsymbol{\theta}_L) = \frac{sin\theta_L}{\theta_L}\boldsymbol{I} + \frac{1 - cos\theta_L}{\theta_L^2}\hat{\boldsymbol{\theta}}_L + \frac{\theta_L - sin\theta_L}{\theta_L^3}\boldsymbol{\theta}_L \otimes \boldsymbol{\theta}_L \tag{3.65}$$

Remark: For an *objective (or strain-invariant) finite element formulation*: 1) the nodal rotation variables, that are going to be interpolated, have to refer to one Euclidean space that is geometrically illustrated by one tangent plane on the rotation manifold $SO(3)$, 2) the projection of the interpolated variables onto the manifold has to be done close enough to this tangent plane. Otherwise, the computed internal elastic energy is distorted. For a *path-independent finite element formulation*: the Euclidean space into which the linear algebra is employed, expressed here by ${}^{t+\Delta t}\boldsymbol{\Lambda}_R$, is defined so as to be unaffected by the interpolation of previous orientations, see eq. (3.62); moreover it refers to a 'virtual' state which is constructed for being just a convenient orientation (being close to the deformed cross-sectional orientations).

Remark: The spatial discretization of the rotational trial functions, i.e. the iterative spins $d\boldsymbol{\psi}$, that appear in the linearized form of the internal virtual work can be performed using either the classical Lagrangian shape functions (iterative formulation) or the configuration-dependent shape functions (invariant formulation) the extraction of which is described in Jelenić and Crisfield, 1999, based on the update concept presented in the same paper, and also described on the rotation manifold here. For the second case, the element spin vector $d\boldsymbol{\psi}_R$ and the local cross-section rotation vector at the Gauss point $d\boldsymbol{\theta}_L^h$ are written w.r.t. the nodal spin vectors $d\boldsymbol{\psi}_i$; $i = 1, 2$ for a 2-noded element (see also eq. (3.64)), where the interpolation using the classical ${}^0C$ Lagrange polynomials is perfomed for the nodal local

rotation vectors $d\boldsymbol{\theta}_{L,i}$.

A note on two more formulations given in the literature

A note is given for two more techniques that are present in the literature, for completion; they are the so-called incremental and total formulations. These techniques treat the infinitesimal rotations $\delta\boldsymbol{\theta}$ as additive vectors (quantities which can be added to the previous rotation vectors during the numerical update procedure). Because this parameterization does not reflect the real nature of rotations - they are spins that have been transformed by the inverse of the tangential transformation-, it is called a rotation *pseudo*-vector parameterization. From the most formulations based on the rotation *pseudo*-vector parameterization, the considerations about objectivity (or strain-invariance) and/or path-independence in the discrete level are missing. To illustrate this geometrically, in fig. 3.5, the orientation update from t to $t + \Delta t$ and the infinitesimal rotation corrections (additive $\delta\hat{\boldsymbol{\theta}}$ and spin $\boldsymbol{\delta\Psi}$) at $t + \Delta t$ are depicted on the manifold $SO(3)$ for an assumed IJ-noded element. The *blue* tangent planes correspond to the deformed orientation at t (refers to the frame ${}^{t}\boldsymbol{V}$), while, the *green* tangent planes correspond to the deformed orientation at $t + \Delta t$ (refers to the frame ${}^{t+\Delta t}\boldsymbol{V}$), expressed by the orientation matrices ${}^{t}\boldsymbol{\Lambda}_I$, ${}^{t}\boldsymbol{\Lambda}_J$ and ${}^{t+\Delta t}\boldsymbol{\Lambda}_I$, ${}^{t+\Delta t}\boldsymbol{\Lambda}_J$ respectively for each cross-section assigned to the nodes I and J. The interpolation of the rotation parameters, $\boldsymbol{\theta}_I$, $\boldsymbol{\theta}_J$ and $\delta\boldsymbol{\theta}_I$, $\delta\boldsymbol{\theta}_J$, which belong to the tangent spaces $T_{{}^{t}\boldsymbol{\Lambda}_I}SO(3)$ and $T_{{}^{t}\boldsymbol{\Lambda}_J}SO(3)$, will be employed without taking into consideration that these rotation parameters should refer to the same Euclidean space, geometrically illustrated by one tangent plane onto the manifold $SO(3)$. This leads to a *non-objective formulation* (see e.g. Crisfield and Jelenić, 1999 for a mathematical proof). Still, referring to the planes $T_{{}^{t}\boldsymbol{\Lambda}_I}SO(3)$ and $T_{{}^{t}\boldsymbol{\Lambda}_J}SO(3)$ for updating the orientation, leads to a *path-dependent formulation*, because, the spaces orientation that these planes represent depends on the interpolation history. The same are valid for an iterative formulation where one refers to the very previous (not necessarily converged) configuration to perform the update, as it is described in section 3.6.1.

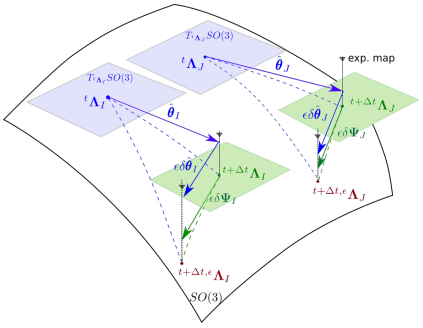

FIGURE 3.5: Incremental formulation.

The total formulation (see fig. 3.6) results to be path-independent. However, the non objectivity cannot be overcome because the projection onto the manifold should be done close enough to the tangent plane. Still, in case that the initial orientation is not the same for all the cross-sections (curved beam) there is the need to construct an initial *virtual* orientation, same for all the cross-sections, that expresses the space on which the interpolation is employed (this is the same idea presented in the invariant

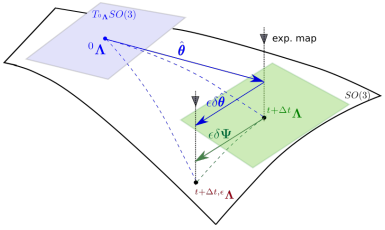

FIGURE 3.6: Total formulation.

formulation by Jelenić and Crisfield, 1999 where this *virtual* orientation is updated within each iteration).
Instead of the rotations, the cross-section directors could be chosen as the unknown parameters at the nodes (referring to the eq. (3.23), the interpolation is now employed for $\delta \boldsymbol{V}_2(\xi)$ and $\delta \boldsymbol{V}_3(\xi)$ instead of $\delta \boldsymbol{\psi}(\xi)$ or $\delta \boldsymbol{\theta}(\xi)$). Again, one should care for objectivity and path-independence. The constraint equation imposed on the directors regarding the conservation of their orthonormality, which is added in Romero and Armero, 2002 and Betsch and Steinmann, 2002, is a solution.

3.7 Spatial discretization method

According to FEM, a finite number of piecewise polynomial shape functions $\boldsymbol{H}(\xi)$ are introduced for the approximation of the solution fields. C^0 continuous shape functions are used for the displacement fields, i.e. u_{01}, u_{02}, u_{03} along the $\boldsymbol{e}_1, \boldsymbol{e}_2, \boldsymbol{e}_3$ axes, and $\theta_1, \theta_2, \theta_3$ about the $\boldsymbol{e}_1, \boldsymbol{e}_2, \boldsymbol{e}_3$ axes (see fig. 3.1). The piecewise classification of the shape functions results from the fact that they are not equal to zero into a *limited* length of the beam, and consequently, they express one local distribution of the fields. After controlling locally each displacement field, using the parameters (dof) and the piecewise shape functions, the discretization of the problem is accomplished together with the transformation of the differential equations into a system of algebraic equations. Because of the piecewise type of the shape functions, it is possible for the equations to be written in a discrete form at the level of each element. Therefore, inside one finite element 'e', the approximated displacement field is written as follows:

$$\boldsymbol{u}^e(\xi) = \boldsymbol{H}^e(\xi)\boldsymbol{d}^e \tag{3.66}$$

where $\boldsymbol{u}^e(\xi) = [u_{01}, u_{02}, u_{03}, \theta_1, \theta_2, \theta_3]^T$ is the vector of the independent displacements (unknown solution fields) along the element,

$$\boldsymbol{d}^e = \left(\underbrace{u_{01}^1, u_{02}^1, u_{03}^1, \theta_1^1, \theta_2^1, \theta_3^1}_{\text{node 1}}, \underbrace{u_{01}^2, u_{02}^2, u_{03}^2, \theta_1^2, \theta_2^2, \theta_3^2}_{\text{node 2}} \right)^T$$

is the vector of the degrees of freedom (dof) of the element, $\boldsymbol{H}^e(\xi)$ is the shape function matrix that, herein, contains the classical Lagrange polynomials. Depending on the type of the shape functions, some techniques of countering for the locking problem may be used (see three ways that counter the shear locking in Chapter 4 from Krenk, 2009). According to Luo, 2008, consistent shape functions can be used that couple the diplacements and rotations, which are constructed from the analytical solution of the homogeneous (no external load) equilibrium equations for a 3D Timoshenko beam. This coupling may be profitable when the numerical locking (shear and membrane locking) phenomena occur, which are expected to be more evident in initially curved beams. Also, by describing the motion using a unique map [without splitting it into two parts - a map for the position and a map for the orientation], the locking phenomena are minimized (Sonneville, Cardona, and Brüls, 2014).

3.7.1 Approximation of the virtual quantities

By turning the beam into a N-noded finite element, the approximation of the distribution of the virtual quantities $\delta\boldsymbol{u}(\xi)$ and $\delta\boldsymbol{\psi}(\xi)$ along the element is defined as

$$\begin{Bmatrix} \delta\boldsymbol{u}(\xi) \\ \delta\boldsymbol{\psi}(\xi) \end{Bmatrix} \doteq \begin{Bmatrix} \delta\boldsymbol{u}^h(\xi) \\ \delta\boldsymbol{\psi}^h(\xi) \end{Bmatrix} = \underbrace{H^i(\xi) \begin{bmatrix} \boldsymbol{I} & \boldsymbol{0} \\ \boldsymbol{0} & \boldsymbol{I} \end{bmatrix}}_{\boldsymbol{H}^i(\xi)} \begin{Bmatrix} \delta\boldsymbol{u}_i \\ \delta\boldsymbol{\psi}_i \end{Bmatrix} \tag{3.67}$$

where the approximated virtual quantities $\delta\boldsymbol{u}^h(\xi)$ and $\delta\boldsymbol{\psi}^h(\xi)$ are used. The shape functions $H^i(\xi)$ are polynomials of degree $N-1$, which satisfy the conditions: $H^i(\xi_j) = \delta^i_j$, $\sum_{i=1}^{N} H^i(\xi) = 1 \; \forall \, \xi \in [0, L]$; $i, j = 1, ..., N$ where $\delta^i_j = 1$ for $i = j$ and $\delta^i_j = 0$ otherwise. The virtual quantities functions interpolated in this way are *configuration independent*.

3.7.2 Trial functions

In the iterative implementation described in section 3.6.1, the Bubnov-Galerkin method is used. In this case, the trial functions are interpolated in the same way as the test functions. In the invariant implementation described in the same section, the Petrov-Galerkin method is used, where the trial functions are interpolated in a different way compared to the test functions. In this case, the approximation of the displacement trial function $[d\boldsymbol{u}(\xi), d\boldsymbol{\psi}(\xi)] \in \mathcal{R}^3$ and its derivative, using the approximated displacement field $[d\boldsymbol{u}^h(\xi), d\boldsymbol{\psi}^h(\xi)]$ and its derivative, is defined as

$$\begin{aligned} d\boldsymbol{u}(\xi) &\doteq d\boldsymbol{u}^h(\xi) = \boldsymbol{H}^i(\xi)\, d\boldsymbol{u}_i \\ d\boldsymbol{u}'(\xi) &\doteq d\boldsymbol{u}^{h'}(\xi) = \boldsymbol{H}^{i'}(\xi)\, d\boldsymbol{u}_i \end{aligned} \tag{3.68}$$

$$\begin{aligned} d\boldsymbol{\psi}(\xi) &\doteq d\boldsymbol{\psi}^h(\xi) = \tilde{\boldsymbol{H}}^i(\xi)\, d\boldsymbol{\psi}_i \\ d\boldsymbol{\psi}'(\xi) &\doteq d\boldsymbol{\psi}^{h'}(\xi) = \tilde{\boldsymbol{H}}^{i'}(\xi)\, d\boldsymbol{\psi}_i \end{aligned} \tag{3.69}$$

where $\tilde{\boldsymbol{H}}^i(\xi)$; $i = 1, ..., N$ is a 3×3 matrix that contains the *generalized shape functions* for the *configuration dependent* interpolation of the spin vector, as they are presented in Jelenić and Crisfield, 1999 and more recently in Dukić, Jelenić, and Gaćeša, 2014.
Following Jelenić and Crisfield, 1999, where the way of constructing the configuration dependent interpolation functions is analyzed, just the local rotations are interpolated, thus (see eq. (3.64))

$$d\boldsymbol{\psi}(\xi) \doteq d\boldsymbol{\psi}^h(\xi) = d\boldsymbol{\psi}_R + {}^{t+\Delta t}\boldsymbol{\Lambda}_R\, \boldsymbol{T}(\boldsymbol{\theta}^h_L(\xi))\, d\boldsymbol{\theta}_{L,i} \tag{3.70}$$

where the variations $d\boldsymbol{\psi}_R$ and $d\boldsymbol{\theta}_{L,i}$ are given as follows

$$d\boldsymbol{\psi}_R = \left[\Delta^{ij}_k \left(\delta^k_I + \delta^k_J \right) \boldsymbol{\Lambda}_R\, \boldsymbol{v}_j\, \boldsymbol{\Lambda}^T_R \right] d\boldsymbol{\psi}_i \tag{3.71}$$

where $\Delta^{ij}_k = \delta^i_1\, \delta^j_1\, \delta^1_k + ... + \delta^i_N\, \delta^j_N\, \delta^N_k$ can be considered as a generalized Kronecker symbol with $\Delta^{ij}_k = 1$ for $i = j = k$, otherwise $\Delta^{ij}_k = 0$; $\delta^k_{I,J} = 1$ for $k = I, J$, otherwise $\delta^k_{I,J} = 0$;

$i, j, k, I, J = 1...N$, where N is the number of the nodes of the element.

$$\boldsymbol{v}_I = \frac{1}{2}\left(\boldsymbol{I}_3 + \frac{1}{\Phi_{IJ}} tan\frac{\Phi_{IJ}}{4}\hat{\boldsymbol{\Phi}}_{IJ}\right) \tag{3.72}$$

$$\boldsymbol{v}_J = \frac{1}{2}\left(\boldsymbol{I}_3 - \frac{1}{\Phi_{IJ}} tan\frac{\Phi_{IJ}}{4}\hat{\boldsymbol{\Phi}}_{IJ}\right) \tag{3.73}$$

$\boldsymbol{I}_3$ is the identity matrix. eq. (3.70) can be inverted for any $\theta_{L,i} \neq \pm 2n\pi; n \in \mathbb{N}$. Considering that $H^i(\xi_j) = \delta^i_j; i = 1...N$,

$$d\boldsymbol{\theta}_{L,i} = \boldsymbol{T}^{-1}(\boldsymbol{\theta}_{L,i})\, \boldsymbol{\Lambda}_R^T \left(d\boldsymbol{\psi}_i - d\boldsymbol{\psi}_R\right) \tag{3.74}$$

Inserting eq. (3.71) into eq. (3.74),

$$d\boldsymbol{\theta}_{L,i} = \boldsymbol{T}^{-1}(\boldsymbol{\theta}_{L,i})\, \boldsymbol{\Lambda}_R^T \left\{ d\boldsymbol{\psi}_i - \left[\Delta^{mj}_k \left(\delta^k_I + \delta^k_J\right) \boldsymbol{\Lambda}_R\, \boldsymbol{v}_j\, \boldsymbol{\Lambda}_R^T \right] d\boldsymbol{\psi}_m \right\} \tag{3.75}$$

Finally, the insertion of eqs. (3.71) and (3.75) into eq. (3.70) gives the following configuration dependent shape functions $\tilde{\boldsymbol{H}}^i(\xi); i = 1...N$; N is the number of the nodes.

$$\begin{aligned}\tilde{\boldsymbol{H}}^i(\xi) = \Delta^{ij}_k\, \boldsymbol{\Lambda}_R \\ &\left\{ \left(\delta^k_I + \delta^k_J\right) \left[\boldsymbol{I}_3 - \boldsymbol{T}(\boldsymbol{\theta}^h_L(\xi))\, H^i(\xi)\, \boldsymbol{T}^{-1}(\boldsymbol{\theta}_{L,i})\right] \boldsymbol{v}_j \right. \\ &\left. + \boldsymbol{T}(\boldsymbol{\theta}^h_L(\xi))\, \boldsymbol{H}^k(\xi)\, \boldsymbol{T}^{-1}(\boldsymbol{\theta}_{L,j}) \right\} \boldsymbol{\Lambda}_R^T\end{aligned} \tag{3.76}$$

where the tangential transformation $\boldsymbol{T}(\boldsymbol{\theta}^h_L(\xi))$ is given by eq. (3.65) for the approximated local rotation vector $\boldsymbol{\theta}^h_L = H^i(\xi)\, \boldsymbol{\theta}_{L,i}$ at $t + \Delta t$, while the inverse of the tangential transformation $\boldsymbol{T}^{-1}(\boldsymbol{\theta}_{L,i})$ that takes as input the local rotation vector $\boldsymbol{\theta}_{L,i}$ of the nodes is given by Ibrahimbegović, Frey, and Kožar, 1995

$$\boldsymbol{T}^{-1}(\boldsymbol{\theta}_{L,i}) = \frac{\theta_{L,i}/2}{tan(\theta_{L,i}/2)}\left(\boldsymbol{I}_3 - \frac{1}{\theta^2_{L,i}}\boldsymbol{\theta}_{L,i} \otimes \boldsymbol{\theta}_{L,i}\right) - \frac{1}{2}\hat{\boldsymbol{\theta}}_{L,i} + \frac{1}{\theta^2_{L,i}}\boldsymbol{\theta}_{L,i} \otimes \boldsymbol{\theta}_{L,i} \tag{3.77}$$

The derivative of the generalized shape functions is given as

$$\begin{aligned}\tilde{\boldsymbol{H}}^{i'}(\xi) = \Delta^{ij}_k\, \boldsymbol{\Lambda}_R \\ &\left\{ -\left(\delta^k_I + \delta^k_J\right) \left[\frac{d}{d\xi}\boldsymbol{T}(\boldsymbol{\theta}^h_L(\xi))\, H^i(\xi)\, \boldsymbol{T}^{-1}(\boldsymbol{\theta}_{L,i}) + \boldsymbol{T}(\boldsymbol{\theta}^h_L(\xi))\, H^{i'}(\xi)\, \boldsymbol{T}^{-1}(\boldsymbol{\theta}_{L,i})\right] \boldsymbol{v}_j \right. \\ &\left. + \left[\frac{d}{d\xi}\boldsymbol{T}(\boldsymbol{\theta}^h_L(\xi))\, \boldsymbol{H}^k(\xi) + \boldsymbol{T}(\boldsymbol{\theta}^h_L(\xi))\, \boldsymbol{H}^{k'}(\xi)\right] \boldsymbol{T}^{-1}(\boldsymbol{\theta}_{L,j}) \right\} \boldsymbol{\Lambda}_R^T\end{aligned} \tag{3.78}$$

where $\frac{d}{d\xi}\boldsymbol{T}(\boldsymbol{\theta}_L)$ equals (Ritto-Corrêa and Camotim, 2002)

$$\frac{d}{d\xi}\boldsymbol{T}(\boldsymbol{\theta}_L) = \boldsymbol{\theta}_L^T\,\boldsymbol{\theta}'_L\frac{\theta_L\,sin\theta_L - 2\,(1-cos\theta_L)}{\theta_L^4}\hat{\boldsymbol{\theta}}_L + \frac{1-cos\theta_L}{\theta_L^2}\hat{\boldsymbol{\theta}}'_L + \frac{1}{\theta_L^2}\left(1-\frac{sin\theta_L}{\theta_L}\right)\left(\hat{\boldsymbol{\theta}}_L\hat{\boldsymbol{\theta}}'_L + \hat{\boldsymbol{\theta}}'_L\hat{\boldsymbol{\theta}}_L\right) + \boldsymbol{\theta}_{\boldsymbol{L}}^T\boldsymbol{\theta}'_L\frac{3\,sin\theta_L - \theta_L(2+cos\theta_L)}{\theta_L^5}\hat{\boldsymbol{\theta}}_L^2 \tag{3.79}$$

3.7.3 Residual vector and stiffness matrix

SR beam model

The residual vector and the stiffness matrix for the SR beam model are presented in Jelenić and Crisfield, 1999, and are repeated here to facilitate the comparison between the SR and GL beam models. Taking into account the virtual work equation in eq. (3.15) and writing it into a matrix form, the residual vector $\boldsymbol{g}$ is given as the difference between the internal $\boldsymbol{q}_k$ and the external $\boldsymbol{q}_e$ force vectors at time $t+\Delta t$ as follows

$$^{t+\Delta t}\boldsymbol{g}^i = \boldsymbol{q}_k^i - \boldsymbol{q}_e^i \tag{3.80}$$

where i is the index that corresponds to the end-nodes I, J of the element. Taking into account that the virtual quantities are interpolated using eq. (3.67)

$$^{t+\Delta t}\boldsymbol{q}_k^i = \int_0^L \begin{bmatrix} H^{i'}\boldsymbol{I} & \boldsymbol{0} \\ -H^i\hat{\boldsymbol{r}}'_0 & H^{i'}\boldsymbol{I}\end{bmatrix}\begin{Bmatrix}\boldsymbol{\Lambda F}\\ \boldsymbol{\Lambda M}\end{Bmatrix} d\xi \tag{3.81}$$

$$^{t+\Delta t}\boldsymbol{q}_e^i = \int_0^L \begin{Bmatrix} H^i\tilde{\boldsymbol{f}}\\ H^i\tilde{\boldsymbol{m}}\end{Bmatrix} d\xi + \delta_I^i\begin{Bmatrix}\boldsymbol{p}_I\\ \boldsymbol{t}_I\end{Bmatrix} + \delta_J^i\begin{Bmatrix}\boldsymbol{p}_J\\ \boldsymbol{t}_J\end{Bmatrix} \tag{3.82}$$

where $\boldsymbol{r}'_0$ is the derivative along the beam length of the position vector of the reference point at the deformed state, while $\boldsymbol{F}$ and $\boldsymbol{M}$ is the material setting of the internal forces and moments given in eqs. (3.12) and (3.13). $\tilde{\boldsymbol{f}}$ and $\tilde{\boldsymbol{m}}$ are the external, distributed loads and moments, while $\boldsymbol{p}_I$, $\boldsymbol{p}_J$, $\boldsymbol{t}_I$, $\boldsymbol{t}_J$ are the external, concentrated loads and moments at the end-nodes I, J of the element.

In the following, the linearized form of the internal virtual work given in appendix A.1 is used to construct the stiffness matrix. Taking into account that the test and trial functions are approximated according to eq. (3.67) and eqs. (3.68) and (3.69), respectively, the stiffness matrix is

$$\boldsymbol{K}_k^{ij} = \int_0^L \begin{bmatrix} \boldsymbol{H}^{i'}\,\boldsymbol{c}^{f\gamma}\,\boldsymbol{H}^{j'} & \boldsymbol{H}^{i'}\left(\boldsymbol{c}^{f\gamma}\hat{\boldsymbol{r}}'_0 - \widehat{\boldsymbol{\Lambda F}}\right)\tilde{\boldsymbol{H}}^j \\ \boldsymbol{H}^i\left(\widehat{\boldsymbol{\Lambda F}} - \hat{\boldsymbol{r}}'_0\boldsymbol{c}^{f\gamma}\right)\boldsymbol{H}^{j'} & \boldsymbol{H}^i\left(-\hat{\boldsymbol{r}}'_0\boldsymbol{c}^{f\gamma}\hat{\boldsymbol{r}}'_0 + \hat{\boldsymbol{r}}'_0\widehat{\boldsymbol{\Lambda F}}\right)\tilde{\boldsymbol{H}}^j \\ & +\boldsymbol{H}^{i'}\left\{\left(-\widehat{\boldsymbol{\Lambda M}}\right)\tilde{\boldsymbol{H}}^j + \boldsymbol{c}^{m\kappa}\tilde{\boldsymbol{H}}^{j'}\right\}\end{bmatrix} d\xi \tag{3.83}$$

where $\boldsymbol{c}^{f\gamma}$ and $\boldsymbol{c}^{m\kappa}$ is the spatial setting of the constitutive matrices in eq. (3.14) given as $\boldsymbol{c}^{f\gamma} = \boldsymbol{\Lambda}\boldsymbol{C}^{F\Gamma}\boldsymbol{\Lambda}^T$ and $\boldsymbol{c}^{m\kappa} = \boldsymbol{\Lambda}\boldsymbol{C}^{MK}\boldsymbol{\Lambda}^T$.

This stiffness matrix corresponds to the invariant implementation, while, for computing the stiffness matrix according to the iterative technique, one should use the classical Lagrangian interpolation polynomials for both the test and trial functions.

GL beam model

The eqs. (3.26) and (3.27) are used to construct the internal force vector for the GL beam model, while the linearization of the weak form of equilibrium equation given in appendix A.2 is used to construct the corresponding stiffness matrix. Same to the SR beam model, the GL beam model is implemented with both an iterative and an invariant technique; the invariant technique is presented in the following.

The residual force vector is

$$^{t+\Delta t}\boldsymbol{g}^i = \boldsymbol{q}_k^i - \boldsymbol{q}_e^i \tag{3.84}$$

where the internal force vector is written in two parts, $\boldsymbol{q}_k^i$ and $\boldsymbol{q}_{k,m^2}^i$, resulting from the internal force and moment vectors $\boldsymbol{F}$ and $\boldsymbol{M}$ with components given in eqs. (3.28) to (3.30) and eqs. (3.36) to (3.38), and the higher-order moment vector $\boldsymbol{M}_R$ with components given in eqs. (3.44) to (3.46), respectively. The external force vector $\boldsymbol{q}_e^i$ is given in eq. (3.82).

$$^{t+\Delta t}\boldsymbol{q}_k^i = \int_0^L \begin{bmatrix} H^{i'}\boldsymbol{I}\boldsymbol{\Lambda}_m & H^{i'}\boldsymbol{I}\boldsymbol{\Lambda}'_{m2} \\ -H^i\hat{\boldsymbol{r}}'_0\boldsymbol{\Lambda}_{m1} & H^{i'}\boldsymbol{I}\boldsymbol{\Lambda}_{m3} - H^i\hat{\boldsymbol{r}}'_0\boldsymbol{\Lambda}'_{m2} \end{bmatrix} \begin{Bmatrix} \boldsymbol{F} \\ \boldsymbol{M} \end{Bmatrix} d\xi \tag{3.85}$$

$$^{t+\Delta t}\boldsymbol{q}_{k,m^2}^i = \int_0^L \begin{bmatrix} \boldsymbol{0} & \boldsymbol{0} \\ \boldsymbol{0} & H^{i'}\boldsymbol{I}\boldsymbol{\Lambda}_{m4} \end{bmatrix} \begin{Bmatrix} \boldsymbol{0} \\ \boldsymbol{M}_R \end{Bmatrix} d\xi \tag{3.86}$$

where the 3×3 matrices $\boldsymbol{\Lambda}_m = [\boldsymbol{r}'_0;\, \boldsymbol{V}_2;\, \boldsymbol{V}_3]$, $\boldsymbol{\Lambda}_{m1} = [\boldsymbol{0};\, \boldsymbol{V}_2;\, \boldsymbol{V}_3]$, $\boldsymbol{\Lambda}_{m2} = [\boldsymbol{0};\, \boldsymbol{V}_3;\, -\boldsymbol{V}_2]$, $\boldsymbol{\Lambda}_{m3} = [\boldsymbol{V}_1;\, \boldsymbol{V}_3\times\boldsymbol{r}'_0;\, -\boldsymbol{V}_2\times\boldsymbol{r}'_0]$, and $\boldsymbol{\Lambda}_{m4} = [\boldsymbol{V}_3\times\boldsymbol{V}'_3;\, \boldsymbol{V}_2\times\boldsymbol{V}'_2;\, \boldsymbol{V}_3\times\boldsymbol{V}'_2 + \boldsymbol{V}_2\times\boldsymbol{V}'_3]$ are used.

The material part of the stiffness matrix is

$$\boldsymbol{K}_{k,m}^{ij} = \int_0^L \begin{bmatrix} \boldsymbol{K}_{k,m}(1,1) & \boldsymbol{K}_{k,m}(1,2) \\ \boldsymbol{K}_{k,m}(2,1) & \boldsymbol{K}_{k,m}(2,2) \end{bmatrix} d\xi \tag{3.87}$$

where the 3×3 sub-matrices $\boldsymbol{K}_{k,m}(1,1)$, $\boldsymbol{K}_{k,m}(1,2)$, $\boldsymbol{K}_{k,m}(2,1)$, $\boldsymbol{K}_{k,m}(2,2)$ are given by

$$\boldsymbol{K}_{k,m}(1,1) = \left[\boldsymbol{H}^{i'}\left(\boldsymbol{\Lambda}_m\boldsymbol{C}^{F\Gamma}\boldsymbol{\Lambda}_m^T + \boldsymbol{\Lambda}'_{m2}\boldsymbol{C}^{MK}\boldsymbol{\Lambda}_{m2}^{T'}\right)\boldsymbol{H}^{j'}\right] \tag{3.88}$$

$$\boldsymbol{K}_{k,m}(1,2) = \begin{bmatrix} \boldsymbol{H}^{i'}\left\{\left(\boldsymbol{\Lambda}_m\boldsymbol{C}^{F\Gamma}\boldsymbol{\Lambda}_{m1}^T + \boldsymbol{\Lambda}'_{m2}\boldsymbol{C}^{MK}\boldsymbol{\Lambda}_{m2}^{T'}\right)\hat{\boldsymbol{r}}'_0\right\}\tilde{\boldsymbol{H}}^j + \\ \boldsymbol{H}^{i'}\left(\boldsymbol{\Lambda}'_{m2}\boldsymbol{C}^{MK}\boldsymbol{\Lambda}_{m3}^T\right)\tilde{\boldsymbol{H}}^{j'} \end{bmatrix} \tag{3.89}$$

$$\boldsymbol{K}_{k,m}(2,1) = \begin{bmatrix} \boldsymbol{H}^{i}\left\{-\hat{\boldsymbol{r}}'_0\left(\boldsymbol{\Lambda}_{m1}\boldsymbol{C}^{F\Gamma}\boldsymbol{\Lambda}_m^T + \boldsymbol{\Lambda}'_{m2}\boldsymbol{C}^{MK}\boldsymbol{\Lambda}_{m2}^{T'}\right)\right\}\boldsymbol{H}^{j'} + \\ \boldsymbol{H}^{i'}\left(\boldsymbol{\Lambda}_{m3}\boldsymbol{C}^{MK}\boldsymbol{\Lambda}_{m2}^{T'}\right)\boldsymbol{H}^{j'} \end{bmatrix} \tag{3.90}$$

$$\boldsymbol{K}_{k,m}(2,2) = \begin{bmatrix} \boldsymbol{H}^{i}\left\{-\hat{\boldsymbol{r}}'_0\left(\boldsymbol{\Lambda}_{m1}\boldsymbol{C}^{F\Gamma}\boldsymbol{\Lambda}_{m1}^T + \boldsymbol{\Lambda}'_{m2}\boldsymbol{C}^{MK}\boldsymbol{\Lambda}_{m2}^{T'}\right)\hat{\boldsymbol{r}}'_0\right\}\tilde{\boldsymbol{H}}^j + \\ \boldsymbol{H}^{i'}\left\{\left(\boldsymbol{\Lambda}_{m3}\boldsymbol{C}^{MK}\boldsymbol{\Lambda}_{m2}^{T'}\right)\hat{\boldsymbol{r}}'_0\tilde{\boldsymbol{H}}^j + \left(\boldsymbol{\Lambda}_{m3}\boldsymbol{C}^{MK}\boldsymbol{\Lambda}_{m3}^T\right)\tilde{\boldsymbol{H}}^{j'}\right\} - \\ \boldsymbol{H}^i\hat{\boldsymbol{r}}'_0\left(\boldsymbol{\Lambda}'_{m2}\boldsymbol{C}^{MK}\boldsymbol{\Lambda}_{m3}^T\right)\tilde{\boldsymbol{H}}^{j'} \end{bmatrix} \tag{3.91}$$

A contribution, $\boldsymbol{K}_{k,m^2}$, from the higher-order moment and curvature vectors is added to the previous material stiffness.

$$\boldsymbol{K}_{k,m^2} = \int_0^L \left\{ \left[\boldsymbol{H}^{i'} \left(\boldsymbol{r}_0' \boldsymbol{I} \begin{bmatrix} EI_\eta & 0 & 0 \\ 0 & EI_\zeta & 0 \\ 0 & 0 & 0 \end{bmatrix} \boldsymbol{\Lambda}_{m4}^T \right) \tilde{\boldsymbol{H}}^{j'} \right] + \left[\boldsymbol{H}^{i'} \left(\boldsymbol{\Lambda}_{m4} \begin{bmatrix} EI_{\eta 2} & EI_{\zeta\eta} & 0 \\ EI_{\zeta\eta} & EI_{\zeta 2} & 0 \\ 0 & 0 & EI_{\zeta\eta} \end{bmatrix} \boldsymbol{\Lambda}_{m4}^T \right) \tilde{\boldsymbol{H}}^{j'} \right] \right\} d\xi \tag{3.92}$$

The geometrically non-linear part of stiffness $\boldsymbol{K}_{k,nl}$ is

$$\boldsymbol{K}_{k,nl} = \int_0^L \begin{bmatrix} \boldsymbol{K}_{k,nl}(1,1) & \boldsymbol{K}_{k,nl}(1,2) \\ \boldsymbol{K}_{k,nl}(2,1) & \boldsymbol{K}_{k,nl}(2,2) \end{bmatrix} d\xi \tag{3.93}$$

where the 3×3 sub-matrices $\boldsymbol{K}_{k,nl}(1,1), \boldsymbol{K}_{k,nl}(1,2), \boldsymbol{K}_{k,nl}(2,1), \boldsymbol{K}_{k,nl}(2,2)$ are given by

$$\boldsymbol{K}_{k,nl}(1,1) = \boldsymbol{H}^{i'} \left(F_\xi \boldsymbol{I} \right) \boldsymbol{H}^{j'} \tag{3.94}$$

$$\boldsymbol{K}_{k,nl}(1,2) = \boldsymbol{H}^{i'} \left(-\widehat{\boldsymbol{\Lambda}_{m1} \boldsymbol{F}} - \widehat{\boldsymbol{\Lambda}_{m2}' \boldsymbol{M}} \right) \tilde{\boldsymbol{H}}^{j} + \boldsymbol{H}^{i'} \left(-\widehat{\boldsymbol{\Lambda}_{m2} \boldsymbol{M}} \right) \tilde{\boldsymbol{H}}^{j'} \tag{3.95}$$

$$\boldsymbol{K}_{k,nl}(2,1) = \boldsymbol{H}^{i} \left(\widehat{\boldsymbol{\Lambda}_{m1} \boldsymbol{F}} + \widehat{\boldsymbol{\Lambda}_{m2}' \boldsymbol{M}} \right) \boldsymbol{H}^{j'} + \boldsymbol{H}^{i'} \left(\widehat{\boldsymbol{\Lambda}_{m2} \boldsymbol{M}} \right) \boldsymbol{H}^{j'} \tag{3.96}$$

$$\begin{aligned} \boldsymbol{K}_{k,nl}(2,2) = {} & \boldsymbol{H}^{i} \left(\hat{\boldsymbol{r}}_0' \widehat{\boldsymbol{\Lambda}_{m1} \boldsymbol{F}} + \hat{\boldsymbol{r}}_0' \widehat{\boldsymbol{\Lambda}_{m2}' \boldsymbol{M}} \right) \tilde{\boldsymbol{H}}^{j} + \boldsymbol{H}^{i'} \left(\left[-\boldsymbol{V}_1;\, \boldsymbol{0};\, \boldsymbol{0} \right] \boldsymbol{M} \right) \times \tilde{\boldsymbol{H}}^{j} \\ & + \boldsymbol{H}^{i} \left(\hat{\boldsymbol{r}}_0' \widehat{\boldsymbol{\Lambda}_{m2} \boldsymbol{M}} \right) \tilde{\boldsymbol{H}}^{j'} + \boldsymbol{H}^{i'} \left(\hat{\boldsymbol{r}}_0' \widehat{\boldsymbol{\Lambda}_{m2}' \boldsymbol{M}} \right) \tilde{\boldsymbol{H}}^{j} \end{aligned} \tag{3.97}$$

A contribution, $\boldsymbol{K}_{k,nl^2}$, form the higher-order moment and curvature vectors is added to the previous geometric stiffness.

$$\boldsymbol{K}_{k,nl^2} = \int_0^L \begin{bmatrix} \boldsymbol{0} & & \boldsymbol{0} \\ \boldsymbol{0} & \boldsymbol{H}^{i'} \left\{ -\hat{\boldsymbol{V}}_3 \left(\widehat{\boldsymbol{\Lambda}_{m5} \boldsymbol{M}_R} \right) - \hat{\boldsymbol{V}}_2 \left(\widehat{\boldsymbol{\Lambda}_{m1} \boldsymbol{M}_R} \right) \right\} \tilde{\boldsymbol{H}}^{j'} \end{bmatrix} d\xi \tag{3.98}$$

where $\boldsymbol{\Lambda}_{m5} = [\boldsymbol{V}_3;\, \boldsymbol{0};\, \boldsymbol{V}_2]$.

Stiffness matrix from the contribution of the follower loading

From eq. (3.54) the stiffness matrix from the contribution of the external follower loading, $\boldsymbol{K}_{k,e}$, is derived.

$$\boldsymbol{K}_{k,e} = \int_0^L \begin{bmatrix} \boldsymbol{0} & \boldsymbol{H}^{i} \left(\widehat{\boldsymbol{\Lambda} \tilde{\boldsymbol{F}}} \right) \tilde{\boldsymbol{H}}^{j} \\ \boldsymbol{0} & \boldsymbol{H}^{i} \left(\widehat{\boldsymbol{\Lambda} \boldsymbol{M}} \right) \tilde{\boldsymbol{H}}^{j} \end{bmatrix} d\xi + \begin{bmatrix} \boldsymbol{0} & \widehat{\boldsymbol{\Lambda} \boldsymbol{P}_j} \\ \boldsymbol{0} & \widehat{\boldsymbol{\Lambda} \boldsymbol{T}_j} \end{bmatrix} \tag{3.99}$$

where $\boldsymbol{P}_j$ and $\boldsymbol{T}_j$ are the external, concentrated follower loads and moments (in their material setting) at the nodes $j = I,\ J$.

3.8 Solution procedure

To solve the geometrically non-linear problems in statics two methods are used, the load control method (load increments are imposed to the system) and the arc-length control method (displacement increments, or, both load and displacement increments are imposed to the system). Inside each increment of load or/and displacement, the full Newton-Raphson iteration scheme is used to achieve convergence.

3.8.1 Load control method

In the load control method, an externally applied load is set as a target to be reached by the structure. In fig. 3.7, the physical (blue line) and the numerical (black line) load-displacement

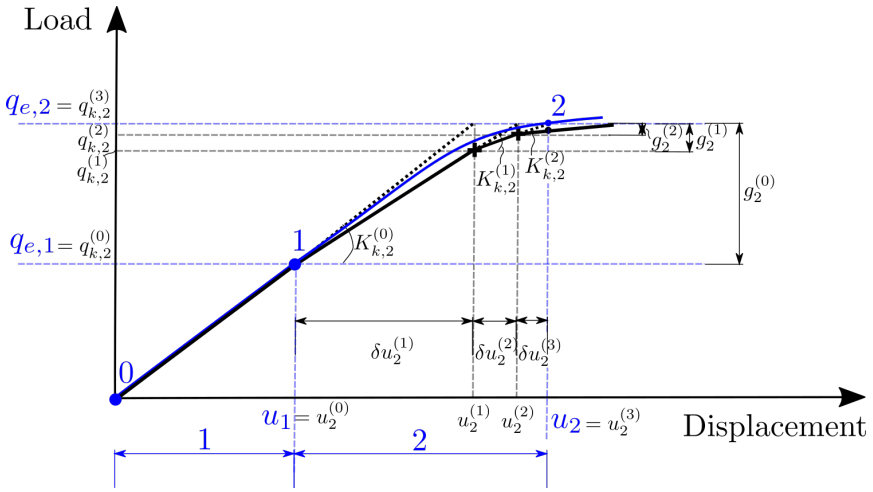

FIGURE 3.7: The load control method: full Newton-Raphson iteration scheme for a single degree of freedom system.

paths are shown, together with the Newton-Raphson iteration scheme used to obtain the numerical path. This path can be obtained using the load control method (the horizontal blue lines show the target of the load) for a system with one degree of freedom. Let us take the increment no. 2, which begins at the equilibrium point 1, and follow the iterations needed to converge to the equilibrium point 2. Considering now that the system consists of more than one degrees of freedom (the quantities shown in fig. 3.7 are tensors of order 1 or 2 instead of order 0), the linearized equilibrium equation solved in the first iteration is given by

$$\boldsymbol{K}_{k,2}^{(0)}\,\delta\boldsymbol{u}_2^{(1)} = -\boldsymbol{g}_2^{(0)} \Leftrightarrow \delta\boldsymbol{u}_2^{(1)} = -\left(\boldsymbol{K}_{k,2}^{(0)}\right)^{-1}\boldsymbol{g}_2^{(0)} \tag{3.100}$$

where $\boldsymbol{K}_{k,2}^{(0)}$ is the tangent stiffness matrix in the first iteration (known), $\delta\boldsymbol{u}_2^{(1)}$ is the first correction of the iterative unknown value, and $\boldsymbol{g}_2^{(0)}$ is the residual in the first iteration given by $\boldsymbol{g}_2^{(0)} = \boldsymbol{q}_{k,2}^{(0)} - \boldsymbol{q}_{e,2}$, where the internal force vector $\boldsymbol{q}_{k,2}^{(0)}$ equals to the externally applied load vector $\boldsymbol{q}_{e,1}$ within a tolerance, and $\boldsymbol{q}_{e,2}$ is the external load vector set as a target for the increment no. 2. The same is valid for the following iterations, 2 and 3, until the achievement of convergence depending on the chosen criterion.

The above linearized equilibrium equation, eq. (3.100), is obtained after the linearization of the response of the finite element system about the conditions at the equilibrium point 2, iteration 0. Specifically, after evaluating the conditions at the equilibrium point 1 which are identical to them at the equilibrium point 2, iteration 0, a Taylor series expansion for the out-of-balance load vector $\boldsymbol{g}(\boldsymbol{u})$ that is required to be equal to zero gives

$$\underbrace{\boldsymbol{g}\left(\boldsymbol{u}_2^{(1)}\right)}_{\boldsymbol{g}_2^{(1)}} = 0 \Leftrightarrow \underbrace{\boldsymbol{g}\left(\boldsymbol{u}_2^{(0)}\right)}_{\boldsymbol{g}_2^{(0)}} + \underbrace{\left[\frac{\partial \boldsymbol{g}}{\partial \boldsymbol{u}}\right]\Big|_{\boldsymbol{u}_2^{(0)}}}_{\boldsymbol{K}_{k,2}^{(0)}} \underbrace{\left(\boldsymbol{u}_2^{(1)} - \boldsymbol{u}_2^{(0)}\right)}_{\delta \boldsymbol{u}_2^{(1)}} + \text{higher-order terms} = 0 \Leftrightarrow$$

$$\boldsymbol{K}_{k,2}^{(0)}\, \delta \boldsymbol{u}_2^{(1)} = -\boldsymbol{g}_2^{(0)} \tag{3.101}$$

where $\boldsymbol{u}$ is the unknown vector, and the higher-order terms are ommited. To find the displacement vector at the end of the step 2, $\boldsymbol{u}_2$, all iterative corrections are added to the previous converged displacement vector at the end of step 1, $\boldsymbol{u}_1$, as follows

$$\boldsymbol{u}_2 = \boldsymbol{u}_1 + \delta \boldsymbol{u}_2^{(1)} + \delta \boldsymbol{u}_2^{(2)} + \delta \boldsymbol{u}_2^{(3)} \tag{3.102}$$

It is worth noting that the above two relations have to be modified when dealing with rotational unknowns, since their characterization as "spins" give to them a "non-additive" feature.

3.8.2 Arc-length control method

In fig. 3.8, the load-displacement curve contains snap-through and snap-back points which are depicted as A and B, respectively (Bonet and Wood, 1997; Papadrakakis, 1998); at these points a dynamic snap happens to the points A' and B' under load control and displacement control, respectively. In this case, the load control method (where, imposing a fixed load increment, the displacement changes) is not suitable to trace the path; even a displacement control method would fail. Notice that if the curve contained just the point A, the displacement control method (where, imposing a fixed displacement increment, the load changes) would be efficient. To trace the path in these cases, where both the load and the displacement change, the so-called arc-length control method is used; this method can be reduced to the displacement control one. The implementation procedure that has been followed is given by Ritto-Corrêa and Camotim, 2008, and is based in previous research works such as Crisfield, 1981; Fafard and Massicotte, 1993; Souza Neto and Feng, 1999 with the work of Riks, 1979 to be the first one for overcoming limit points. Further practical information about the arc-length method one could also get from the FEM text books Bonet and Wood, 1997; Papadrakakis, 1998; Borst et al., 2012b. The code is written in MATLAB (*Arc Length Matlab*). In fig. 3.9, the basic concept of the method is given geometrically combined with a full Newton-Raphson procedure inside each increment of load and displacement. For

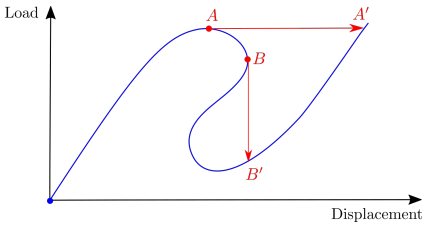

FIGURE 3.8: A load-displacement curve with snap-through A and snap-back B points.

illustrating the method, 3 iterations are depicted in the 2^{nd} increment. A constraint equation

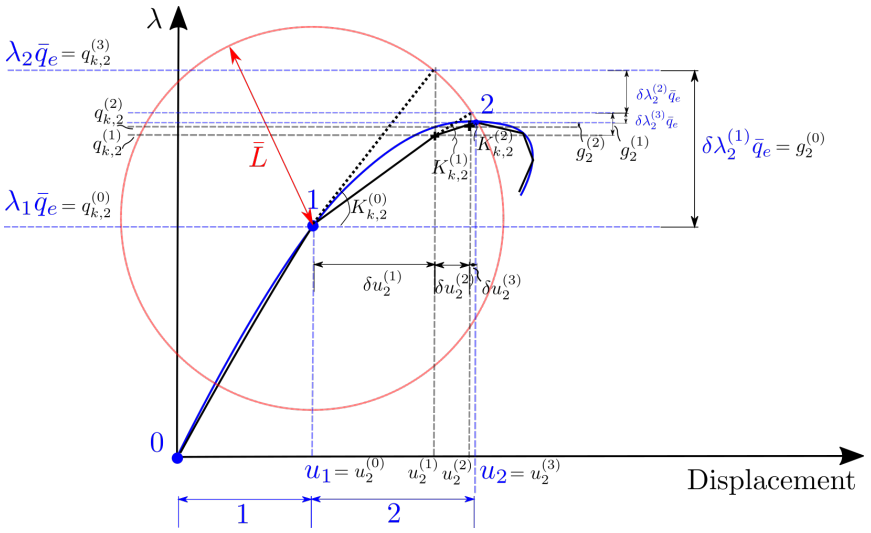

FIGURE 3.9: The arc-length control method: full Newton-Raphson iteration scheme for a single degree of freedom system.

is added to the equilibrium equation to solve for $n+1$ parameters, which are the n DOF's of the problem and the load parameter λ. This (spherical) constraint is geometrically presented using the *red* circle with radius s in the graph, for one degree of freedom system. Notice that, while in the load control method, the tangent line of the equilibrium path at a converged state stops when the fixed load is reached (*blue* dashed line in fig. 3.7), in the arc-length control method, the corresponding tangent line stops after intersecting the constraint surface (*red* circle in fig. 3.9). Considering now a system with more than one degrees of freedom, given that the external load vector is usually written as a linear function of the load parameter λ, e.g. $\boldsymbol{q}_e = \lambda\,\bar{\boldsymbol{q}}_e$, $\bar{\boldsymbol{q}}_e$ is an input parameter that is called a basis loading, the residual force vector in its continuous form is

$$\boldsymbol{g}(\boldsymbol{u},\lambda) = \boldsymbol{q}_k(\boldsymbol{u}) - \lambda\,\bar{\boldsymbol{q}}_e \tag{3.103}$$

where the second term could also depend on $\boldsymbol{u}$ in case of follower loading. The additional equation is given by

$$L^2 = \Delta\boldsymbol{u}^T\Delta\boldsymbol{u} + \psi^2\Delta\lambda = \bar{L}^2 \tag{3.104}$$

where it is enforced that the second power of arc-length measure L^2 is equal to the prescribed value $\bar{L}^2$; Δ means the incremental change and ψ^2 is a scaling factor that renders the product dimensionally consistent (Ritto-Corrêa and Camotim, 2008). The linearized equilibrium equation is obtained, as previously, after the linearization of the response of the finite element system about the conditions at, e.g., step 2, iteration 0. A Taylor series expansion for

the out-of-balance load vector $\boldsymbol{g}(\boldsymbol{u},\lambda)$ that is required to be equal to zero gives

$$\underbrace{\boldsymbol{g}\left(\boldsymbol{u}_2^{(1)},\lambda_2^{(1)}\right)}_{\boldsymbol{g}_2^{(1)}}=0\Leftrightarrow\underbrace{\boldsymbol{g}\left(\boldsymbol{u}_2^{(0)},\lambda_2^{(0)}\right)}_{\boldsymbol{g}_2^{(0)}}+\underbrace{\left[\frac{\partial\boldsymbol{q}_k}{\partial\boldsymbol{u}}\right]\Big|_{\boldsymbol{u}_2^{(0)}}}_{\boldsymbol{K}_{k,2}^{(0)}}\underbrace{\left(\boldsymbol{u}_2^{(1)}-\boldsymbol{u}_2^{(0)}\right)}_{\delta\boldsymbol{u}_2^{(1)}}$$
$$-\underbrace{\left[\frac{\partial\left(\lambda\,\bar{\boldsymbol{q}}_e\right)}{\partial\lambda}\right]}_{\bar{\boldsymbol{q}}_e}\underbrace{\left(\lambda_2^{(1)}-\lambda_2^{(0)}\right)}_{\delta\lambda_2^{(1)}}+\text{higher-order terms}=0\Leftrightarrow$$
$$\boldsymbol{K}_{k,2}^{(0)}\,\delta\boldsymbol{u}_2^{(1)}-\bar{\boldsymbol{q}}_e\,\delta\lambda_2^{(1)}=-\boldsymbol{g}_2^{(0)} \tag{3.105}$$

where $\boldsymbol{u}$ is the unknown displacement vector, and the higher-order terms are ommited. The solution of eq. (3.105) is written in the form

$$\delta\boldsymbol{u}_2^{(1)}=\delta\boldsymbol{u}_{2,\boldsymbol{q}_k}^{(1)}+\delta\lambda_2^{(1)}\,\delta\boldsymbol{u}_{2,\boldsymbol{q}_e}^{(1)} \tag{3.106}$$

where the first and second terms are provided by the following system of equations

$$\boldsymbol{K}_2^{(0)}\delta\boldsymbol{u}_{2,\boldsymbol{q}_k}^{(1)}=-\boldsymbol{g}_2^{(0)} \tag{3.107}$$
$$\boldsymbol{K}_2^{(0)}\delta\boldsymbol{u}_{2,\boldsymbol{q}_e}^{(1)}=\bar{\boldsymbol{q}}_e \tag{3.108}$$

which stems from a decomposition of eq. (3.105). $\delta\lambda$ is provided by the linearization of the constraint relation in eq. (3.104). To update the global variables, the expressions that are used are

$$\boldsymbol{u}_2=\boldsymbol{u}_1+\Delta\boldsymbol{u}_2;\ \Delta\boldsymbol{u}_2=\sum_{i=1-3}\left(\delta\boldsymbol{u}_{2,\boldsymbol{q}_k}^{(i)}+\delta\lambda_2^{(i)}\,\delta\boldsymbol{u}_{2,\boldsymbol{q}_e}^{(i)}\right) \tag{3.109}$$
$$\lambda_2=\lambda_1+\Delta\lambda_2;\ \Delta\lambda_2=\sum_{i=1-3}\left(\delta\lambda_2^{(i)}\right) \tag{3.110}$$

3.8.3 Algorithm

In the framework of hGAST, the load control method is implemented to test several static cases, whereas the arc-length control method is implemented in a separate code to verify the geometrically non-linear modeling in cases with non-trivial equilibrium paths. In hGAST, the new subroutines for statics are given with light green color in the flow chart (fig. 3.10), while the subroutines given in a gray and a light magenta color existed before this work (the variable nb_el refers to sub-bodies that is an entity used to divide the bodies in rigid-bodies, and described further in chapter 5). These are:

- *INITIA_el*: It opens the input files and performs the initial computations. In case of SR model, the following subroutines are called
  - *initializeTopologyData*: It allocates and initializes the position vector and the orientation matrix for the nodes of the elements of each sub-body (in case of SR beam model, the number of sub-bodies is identical to the number of the bodies).

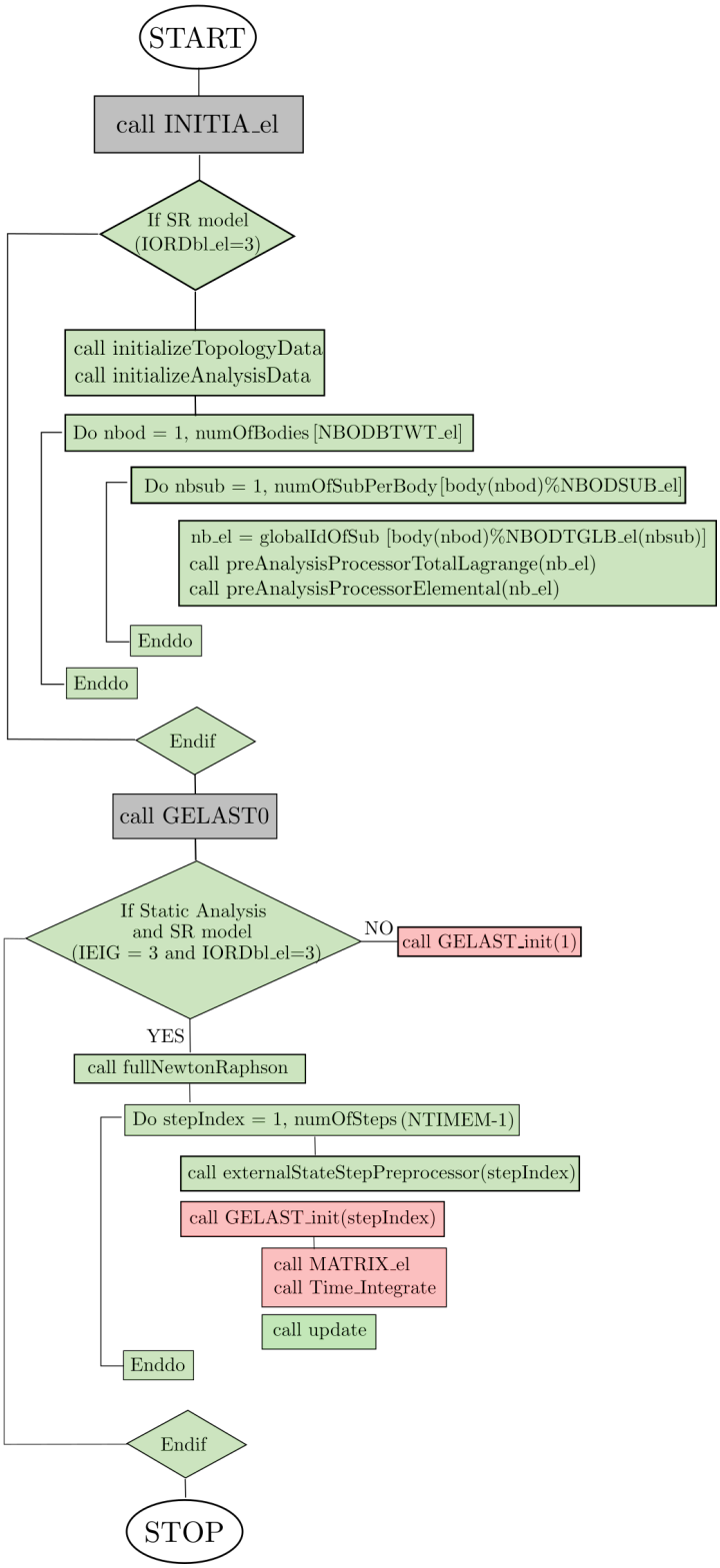

FIGURE 3.10: Algorithm for statics in the framework of hGAST.

– *initializeAnalysisData*: It allocates and initializes the variables for the finite element analysis.

- *preAnalysisProcessorTotalLagrange(nb_el)*: a) It computes the shape functions and their first order derivatives. b) It computes the section angles and the initial cross-section directors, for the nodes of the elements of each sub-body. c) It initializes the output data.
- *preAnalysisProcessorElemental(nb_el)*: a) It computes the Jacobian and its inverse for the integration points of the elements of each sub-body. b) It computes the initial orientation matrix at the Gauss points.

- *GELAST0*: It computes the deflections resulting from a static analysis. In case of SR model, the following subroutines are called
  - *fullNewtonRaphson*: It performs the full Newton-Raphson iterations for each load increment using the subroutines:
    - *externalStateStepPreprocessor(stepIndex)*: It computes the external loading before each step.
    - *GELAST_init(stepIndex)*: It computes all the necessary matrices and vectors which formulate the linearized equilibrium equation; this is solved using the load control method combined with a full Newton-Raphson iteration scheme.
      - *MATRIX_el*: The new subroutines that are written inside *MATRIX_el* are: *SimoElementStiffnessMatrixAndInternalForceVector* and *inertiaAndDampingMatrices* which contain the implementation of the Simo-Reissner beam model.
      - *Time_Integrate*: The linearized equilibrium equation is solved.
      - *update*: This new subroutine is implemented to account for the multiplicative update of rotations, given that the development that is followed uses spin (not the rotation vector that is additive to the previous rotation).

3.9 Numerical results

In this section, several numerical examples are presented in order to compare the two geometrically non-linear beam formulations. In the first two examples, the planar problem is considered, while, in the following examples, the spatial problem is considered as well. The comparison between the two approaches concerns either the displacement and reaction components or the approximation of the strain measures of the two beam models, i.e. the first derived from the displacement gradients (SR model) and the second derived from the Green-Lagrange strains (GL model). In addition, the behaviour of the proposed invariant GL model is examined through the comparison to the invariant SR model. The iterative case for both models is also presented for the 3D problems for completeness. In 2D case has no sense to implement an invariant formulation since the one component of rotation that arises in 2D has an additive character through the numerical procedure. The load control, the displacement control and the arc-length control (Ritto-Corrêa and Camotim, 2008; *Arc Length Matlab*;

Souza Neto and Feng, 1999; Borst et al., 2012a) methods are employed. A reduced numerical quadrature scheme with $n_G = 1$ Gauss point has been applied. A full Newton-Raphson iterative procedure is utilized. Convergence of the finite element solution is established when either or both the relative residual and displacement norms are reduced to the tolerance δ_f and δ_u respectively (Bathe, 1996; Jelenić and Crisfield, 1999), i.e.

$$100\,||^{t+\Delta t}\boldsymbol{\mathcal{R}} - {}^{t+\Delta t}\boldsymbol{F}_{int}^{(\kappa-1)}||_2 < \delta_f\,||^{t+\Delta t}\boldsymbol{\mathcal{R}} - {}^{t}\boldsymbol{F}_{int}||_2 \tag{3.111}$$

where the LHS corresponds to the Euclidean norm of the out-of-balance load vector in iteration κ, while the RHS corresponds to the Euclidean norm of the first residual of the load step.

$$100\,||d\boldsymbol{u}_{0i}||_2 < \delta_u\,||\boldsymbol{u}_{0i}||_2 \tag{3.112}$$

where the components $d\boldsymbol{u}_{0i}$ and $\boldsymbol{u}_{0i}$ constitute the iterative and total nodal translation vector, respectively; $i = 1...3N$, where N is the number of nodes.

3.9.1 2D pure bending rod

A cantilever beam is subjected to an end moment as it is presented in Simo and Vu-Quoc, 1986a; Ibrahimbegović, Frey, and Kožar, 1995. The properties used herein are presented in fig. 3.11, where a circular cross-section is assumed. The moment at the free end equals $M = EI\,\frac{2\pi}{l}$, so as the beam is rolled up into a full closed circle. The number of the elements used are 8. 213 load steps are employed inside a load control method. Convergence of the finite element solution is established when $\delta_f = \delta_u = 10^{-6}$. The moment-translation plots are shown in fig. 3.12, together with the

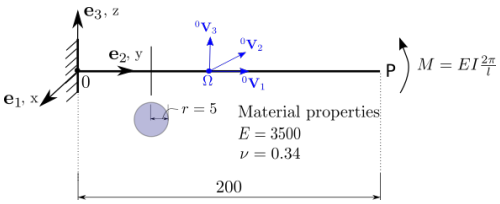

FIGURE 3.11: Pure bending rod: Problem data.

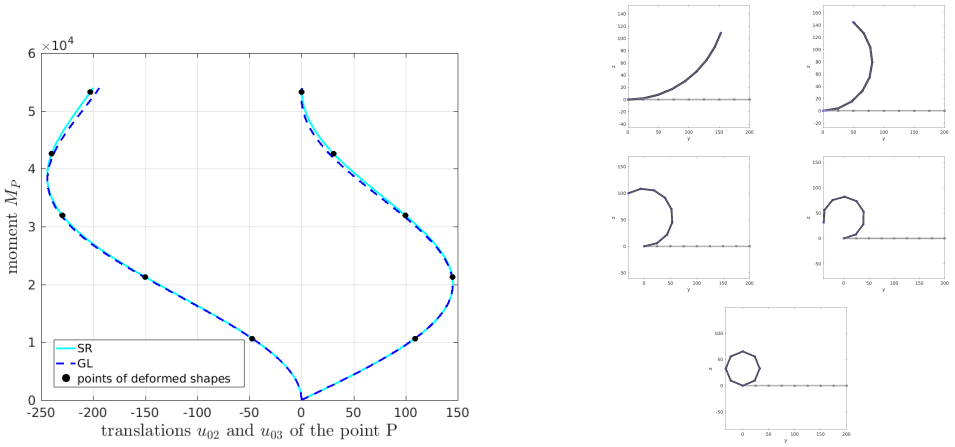

(A) (B)

FIGURE 3.12: Pure bending rod: (a) end moment M_1 vs. translations of the tip using the SR and GL models, and (b) deformed shapes.

selected deformed shapes until the rod becomes a full circle. The results seem to be very similar for the SR and GL models. However, if one looks carefully into the values of the displacements' components, makes the following conclusion: a) the SR model gives exactly $u_{02} = -200$ for the tip axial translation at the end of the analysis, whereas the GL model does not (the corresponding value is $u_{02} = -194.04$); moreover, the GL model gives an additional component of translation, $u_{03} = 0.57$ along the $\boldsymbol{e}_3$ axis, b) the SR model gives exactly $\theta_1 = 360^o$ for the tip rotation at the end of the analysis, whereas the GL model does not (the corresponding value is $\theta_1 = 349.11^o$). The GL model gives different values of the tip deformation because in this case, the neutral axis does not coincide with the centroidal axis, thus, the centroidal axis has strains.

Remark (private communication with Gordan Jelenić): To explain further the difference between the SR and GL beam models in the pure bending problem, the definition of the strain terms in 3D theory (Biot strain and Green-Lagrange strain, respectively) is given for a fiber with initial length α

- Biot strain:

$$\epsilon_B = \frac{\alpha + d\alpha - \alpha}{\alpha} = \frac{(\rho + z)d\phi - \rho d\phi}{\rho d\phi} = \frac{\rho + z - \rho}{\rho} = 1 + \frac{z}{\rho} - 1 = \frac{z}{\rho} \tag{3.113}$$

  where z is the distance between the neutral axis (that coincides to the centroidal axis) and the fiber, ρ is the radius of curvature of the beam, $d\alpha$ is the difference in the length of the fiber, and $d\phi$ is the corresponding angular difference (see fig. 3.13).

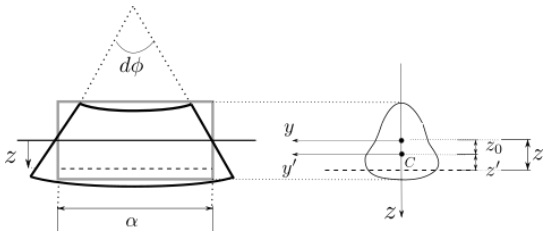

FIGURE 3.13: Pure bending rod: deformation of a fiber with initial length α.

- Green-Lagrange strain:

$$\epsilon_{GL} = \frac{1}{2}\left[\left(\frac{\alpha + d\alpha}{\alpha}\right)^2 - 1\right] = \frac{1}{2}\left[\left(\frac{\rho + z}{\rho}\right)^2 - 1\right] = \frac{z}{\rho} + \frac{1}{2}\left(\frac{z}{\rho}\right)^2 = \epsilon_B + \frac{1}{2}(\epsilon_B)^2 \tag{3.114}$$

  Given that the internal force is zero, and writing the distance z between the fiber and the neutral axis as $z = z_0 + z'$, where z_0 is the distance between the neutral axis and the centroidal axis, and z' is the distance between the centroidal axis and the fiber (see

fig. 3.13), the following relation for the neutral axis is derived

$$N = E\int_A \epsilon_{GL}\, dA = 0 \Leftrightarrow N = E\int_A \left(\frac{z}{\rho} + \frac{z^2}{2\rho^2}\right) dA = 0 \Leftrightarrow$$
$$\frac{E}{\rho}\left(\int_A z\, dA + \frac{1}{2\rho}\int_A z^2\, dA\right) = 0 \Leftrightarrow \underbrace{\int_A z'\, dA}_{=0} + \underbrace{\int_A z_0\, dA}_{z_0 A} + \frac{1}{2\rho}(I_y + A z_0^2) = 0 \Leftrightarrow$$
$$\frac{A}{2\rho}z_0^2 + A z_0 + \frac{I_y}{2\rho} = 0 \Leftrightarrow z_0^2 + 2\rho z_0 + \underbrace{\frac{I_y}{A}}_{i_y^2} = 0 \Leftrightarrow z_0 = -\rho + \sqrt{\rho^2 - i_y^2} \tag{3.115}$$

It is observed from eq. (3.115) that the neutral axis changes during deformation as a function of the radius of curvature and the cross-section properties. Thus, the results obtained on the centroidal axis are different between the two formulations since in the SR formulation the neutral and centroidal axes coincide.

In line with the above explanation the SR model gives one curvature component $K_\eta^h = -3.14159^{-02}$, whereas the GL model predicts a different value of the curvature $K_\eta^h = -3.20503^{-02}$. At the same time an axial strain component $\Gamma_\xi^h = -9.82319^{-03}$ is computed for the GL model.

3.9.2 2D buckling of a double-hinged right-angle frame

The planar example that concerns the buckling of an elastic double-hinged right-angle frame is studied. The frame is subjected to a transverse (fixed) point load applied at one-fifth of the horizontal bar length. This is a demanding 2-D problem that is chosen by several researchers to assess, either the performance of their proposed beam modeling (see e.g. Simo and Vu-Quoc, 1986a; Betsch and Steinmann, 2002; Sonneville, Cardona, and Brüls, 2014; Gaćeša and Jelenić, 2015; Dukić, Jelenić, and Gaćeša, 2014), or, their suggested improvements on the arc-length method (see e.g. Souza Neto and Feng, 1999; Ritto-Corrêa and Camotim, 2008). The geometric and material data is shown in fig. 3.14.

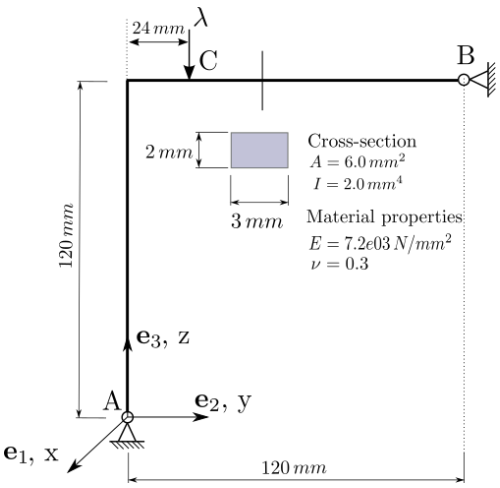

FIGURE 3.14: Doubled-hinged right-angle frame: Problem data (as it is presented in Souza Neto and Feng, 1999).

The frame is discretized by 20 equally-sized two-noded beam elements (10 elements per each bar). The input arc-length method parameters used are: a) arc radius = 3, b) desired iterations = 20, c) cut step = 0.8, is the remaining percentage of the arc radius when the desired number of iterations is reached, d) in the predictor and corrector steps, the selection root criteria described in Ritto-Corrêa and Camotim, 2008 are chosen, e) in both the predictor and

corrector steps, the cylindrical option is chosen. Convergence of the finite element solution is established when $\delta_f = \delta_u = 10^{-7}$.

Remark: It is important to use, inside each iteration, an adaptive to the tracing of the equilibrium path incremental step, i.e. the size of the arc-radius is modified depending either on a desired number of iterations that is given in input, or, on the number of iterations needed to converge in the previous step. In the first case, the step is cut when the desired number of iterations is reached, while, in the second case, the step is cut or amplified based upon the iterations number of the previous step (see relation 4.60 from Borst et al., 2012b). The first option is chosen here to employ a more conservative treatment, by discarding the possible amplification of the step. Also, to avoid cutting the step size when the discriminant of the constraint equation is negative, partial correctors are used in the corrector step (Ritto-Corrêa and Camotim, 2008). In fig. 3.15, the *light grey* configuration

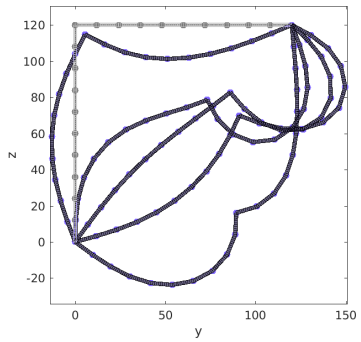

FIGURE 3.15: Doubled-hinged right-angle frame: Initial and deformed configurations.

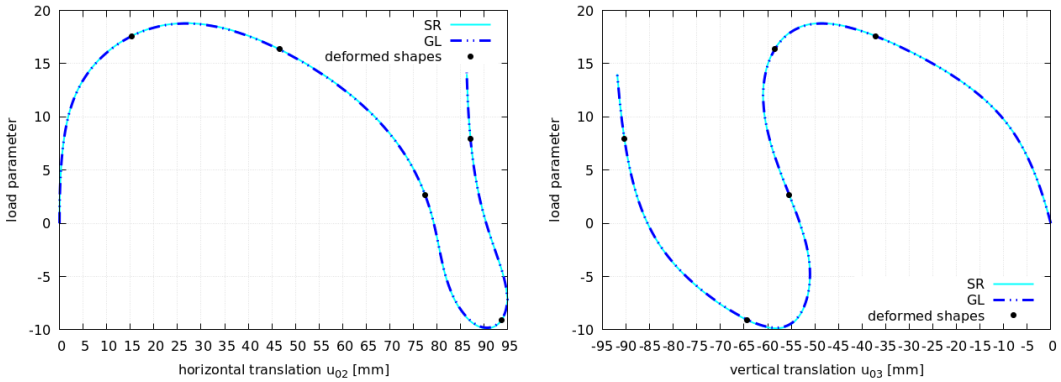

(A) Load-horizontal translation plot of the point C.

(B) Load-vertical translation plot of the point C.

FIGURE 3.16: Doubled-hinged right-angle frame: Equilibrium paths of the point C.

corresponds to the undeformed state, while, the *dark blue* configurations correspond to several deformed states for different levels of the load factor, that are plotted as *black* points in the equilibrium paths shown in figs. 3.16a and 3.16b. In these figures, the equilibrium paths after 213 steps are depicted for the point C, where the load is applied, using the iterative implementation of SR and GL models. The results are identical regarding either the horizontal or the vertical translation of the point C.

3.9.3 A verification 3D example: the 45-degree curved cantilever

This example has been proposed by Bathe and Bolourchi, 1979, while several researchers have used it to assess the performance of their proposed beam models, see e.g. Dvorkin, Onate, and Olivier, 1988; Simo and Vu-Quoc, 1986a; Sonneville, Cardona, and Brüls, 2014; Gaćeša and Jelenić, 2015; Romero and Armero, 2002; Betsch and Steinmann, 2002. Thus, the 45-degree curved cantilever subjected to a fixed load at the tip is studied in order to confirm the performance of the SR and GL models in 3D. The geometric and material data is shown in fig. 3.17a. The member is discretized by 8 equally-sized, two-noded straight beam elements. Convergence of the finite element solution is established when $\delta_f = \delta_u = 10^{-7}$.

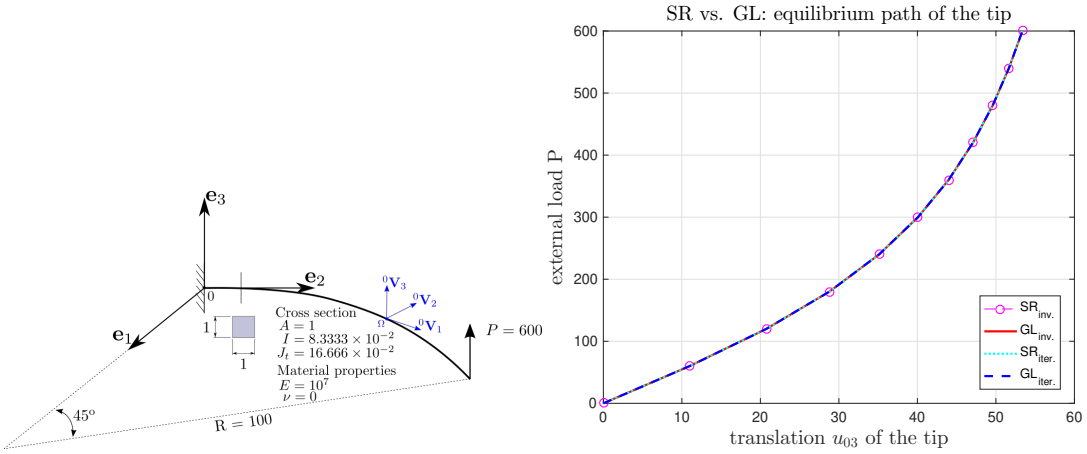

(A) (B)

FIGURE 3.17: 45-degree curved cantilever: (a) problem data and (b) load-vertical translation of the tip.

The graphs presented in figs. 3.17b, 3.18a and 3.18b have been derived using 10 load-steps, although the problem has also been solved using 3 load-steps (see table 3.1). The equilibrium path of the tip for the vertical translation u_{03} is depicted in fig. 3.17b for the SR and GL models, both for their invariant and iterative formulations. One may see that there is hardly any difference between them. The same observations can be made from the figs. 3.18a and 3.18b, where the translations and rotations along the length are shown. In table 3.1, the translational components of the tip, u_{01}; u_{02}; u_{03}, are given when the load has reached its final value, i.e. 600, for the invariant and iterative SR and GL formulations. The final translational components are identical, either in the case of 10 steps, or in the case of 3 steps, for the $SR_{inv.}$ and $GL_{inv.}$ models, while they are not exactly the same for their iterative formulations. This observation verifies that the incorporation into the GL model of the configuration dependent treatment of rotations, offers to this approach the invariance property of path-independence. Moreover, the GL model converges to the correct solution in a similar number of iterations compared to the SR one, and also, their iterative formulations converge to the solution in a slightly smaller number of iterations compared to their invariant ones. Finally, in figs. 3.19a and 3.19b one may see the approximation of the axial/ shear and twist/ bending strain measures along the length. The results for the $SR_{inv.}$ and $SR_{iter.}$ models coincide; the same holds for the $GL_{inv.}$ and $GL_{iter.}$ models. The two components, the axial, Γ^h_ξ, and one of the

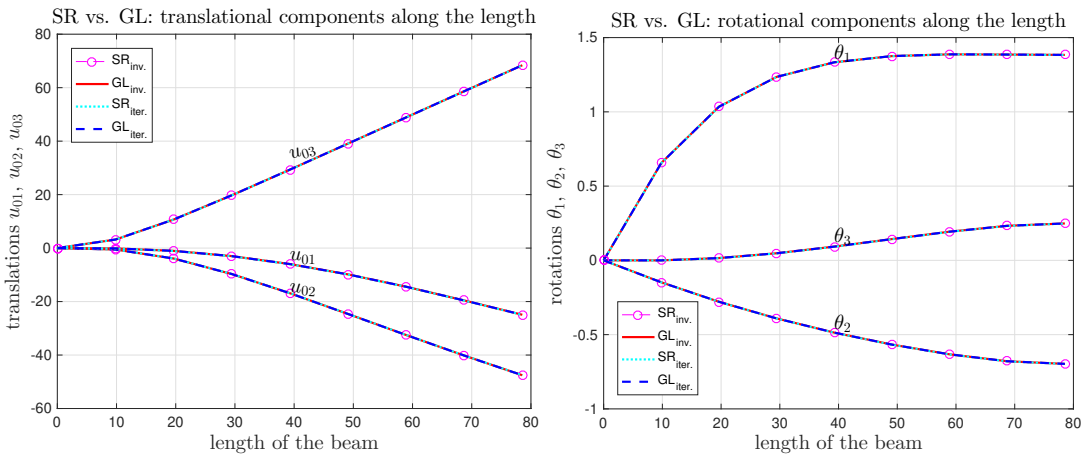

(A) (B)

FIGURE 3.18: 45-degree curved cantilever: (a) translations and (b) rotations along the length.

TABLE 3.1: 45-degree curved cantilever: final tip translation components.

formulation	steps/iterations	u_{01}	u_{02}	u_{03}
$SR_{inv.}$	10/73	-13.48243 /	-23.47852 /	53.37099 /
	3/43	-13.48243	-23.47852	53.37099
$GL_{inv.}$	10/79	-13.48397 /	-23.48420 /	53.37284 /
	3/35	-13.48397	-23.48420	53.37284
$SR_{iter.}$	10/66	-13.48745 /	-23.47779 /	53.36930 /
	3/41	-13.49192	-23.47703	53.36559
$GL_{iter.}$	10/72	-13.48899 /	-23.48348 /	53.37114 /
	3/33	-13.48995	-23.48339	53.37090

two shear components, Γ^h_η, are different in the SR and GL models, either the invariant or the iterative ones; the difference gradually becomes larger towards the support of the cantilever. The GL model presents a divergence from the zero value for both the axial and shear components that is explained according to the remark of section 3.9.1. However, after the numerical integration along the length, the global equilibrium is satisfied for all the models as it may be seen in fig. 3.20. These distributions are very similar to the ones published in Sonneville, Cardona, and Brüls, 2014. The terms that are responsible for this different behaviour of the SR and GL models at the Gauss point are contained in F_ξ, δK_η and δK_ζ. In particular, they are the second and third terms of eq. (3.28) and the second terms in the second and third components of eq. (3.48). In figs. 3.21a and 3.21b, the iterative variant of the SR and GL models with and without the above terms are shown; if one turns them off, the approximation of the strain measures and the internal forces at the Gauss point shows hardly any difference to that of the SR model. However, by omitting these terms one loses the consistency with the 3D formulation, and this has an effect on an increased number of iterations for convergence, e.g. the steps/iterations are 10/118 instead of 10/72 (table 3.1), for the $GL_{iter.}$ model. Regarding the curvature components, they are very similar for all the models. Note that 16 and 32 elements have also been used, and the distribution of the strain measures along the length does not change.

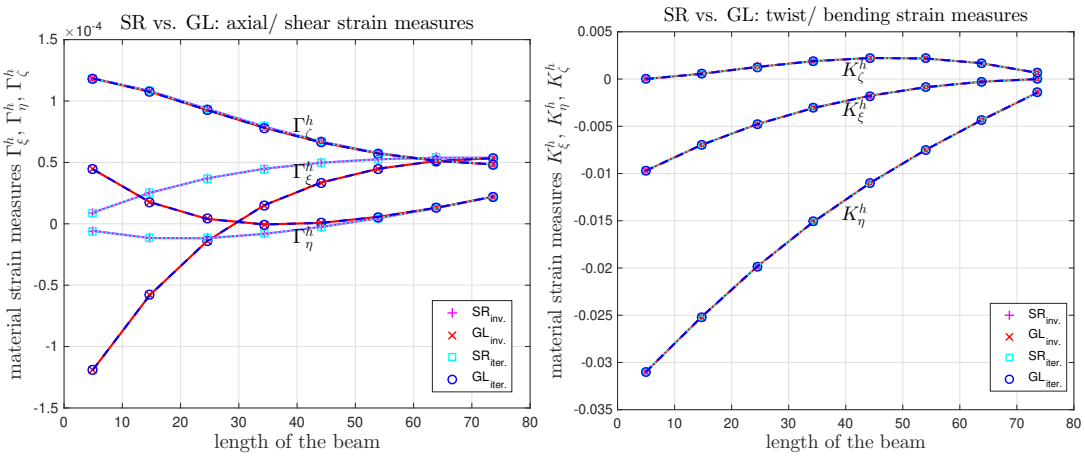

(A) (B)

FIGURE 3.19: 45-degree curved cantilever: approximation of the (a) axial/ shear and (b) twist/ bending strain measures along the length.

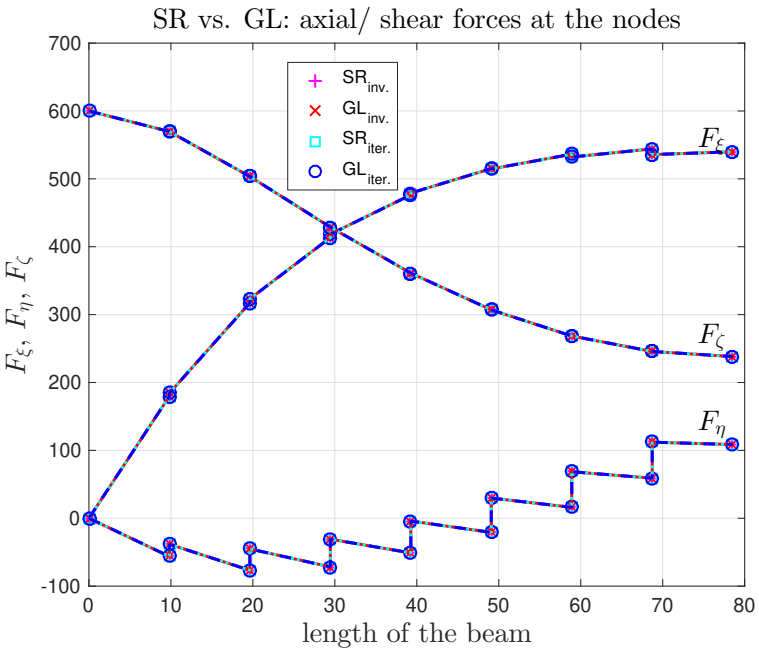

FIGURE 3.20: 45-degree curved cantilever: nodal values of the axial/ shear forces along the length.

3.9.4 A 3D single-element example

In order to further investigate the difference in the strain measures that was depicted in the previous example, the single-element test in Jelenić and Crisfield, 1999 is chosen to be studied next. The element properties are shown in fig. 3.22a. The prescribed, end-point $\boldsymbol{\psi}^1$ and $\boldsymbol{\psi}^2$ rotations, which are applied in one step, are shown in table 3.2. The second column includes the rotational components ψ^1_i and ψ^2_i, $i = 1-3$ of each node 1, 2 without rigid-body rotation, while the fourth column includes the corresponding rotational components ψ'^1_i and ψ'^2_i with the superposed rigid-body rotation $\boldsymbol{\psi}^T_R = [0.2 \;\; 1.2 \;\; -0.5]^T$. Convergence of the finite element solution is established when the displacement norm is reduced to the tolerance

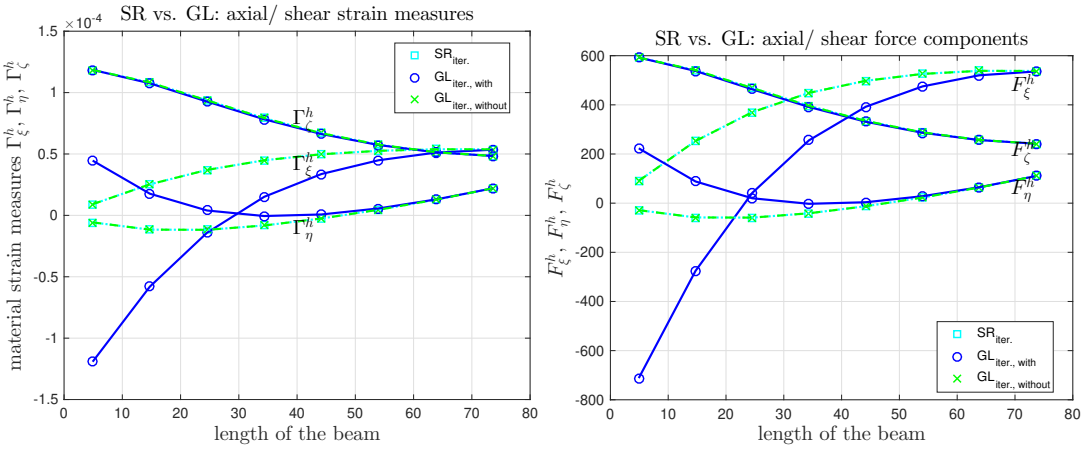

(A) (B)

FIGURE 3.21: 45-degree curved cantilever: approximation of the (a) axial/ shear strain measures and (b) internal forces along the length.

$\delta_u = 10^{-8}$.

TABLE 3.2: Single-element test: prescribed end-point rotations.

$\boldsymbol{\psi}^{1,2}$ [rad]	rotational components without rigid-body rotation	$\boldsymbol{\psi}'^{1,2}$ [rad]	rotational components with rigid-body rotation
ψ^1_1	1.00	ψ'^1_1	1.001456623324399
ψ^1_2	−0.50	ψ'^1_2	0.346797425422351
ψ^1_3	0.25	ψ'^1_3	−0.837171821005534
ψ^2_1	−0.40	ψ'^2_1	0.088491486002004
ψ^2_2	0.70	ψ'^2_2	1.933204771348018
ψ^2_3	0.10	ψ'^2_3	−0.081866017889401

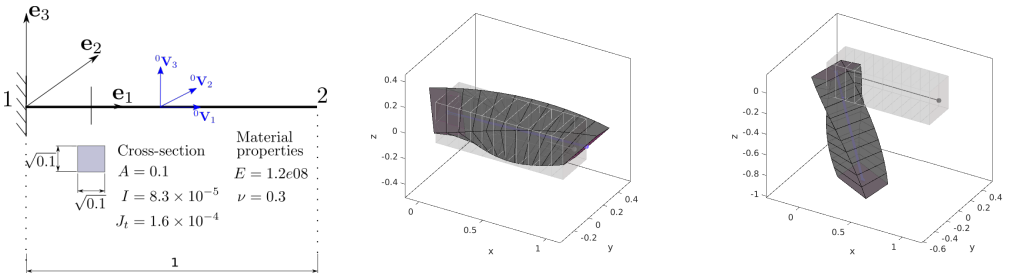

(A) (B) (C)

FIGURE 3.22: Single-element test: (a) problem data, and deformed configurations (b) without and (c) with superposed rigid-body rotation.

In figs. 3.22b and 3.22c, the deformed configurations without and with the superposed rigid-body rotation are shown. The material strain measures at the middle of the element, K^h_ξ; K^h_η; K^h_ζ and Γ^h_ξ; Γ^h_η; Γ^h_ζ, are computed for these configurations, see tables 3.3 and 3.4. In table 3.3, the values of the material twist/ bending strain components are presented for the invariant models ($SR_{inv.}$ and $GL_{inv.}$) and the iterative ones ($SR_{iter.}$ and $GL_{iter.}$). From the penultimate column it is concluded that the twist strain measure is exactly the same for the SR

and GL models, either in their invariant or their iterative formulations. On the other hand, there is a difference of about 7% for their two bending strain components (see eq. (3.41) and the comments below). Note that the strain measures computed by the $SR_{inv.}$ and $SR_{iter.}$ models, either before or after the superposed rigid-body rotation, are the same with the ones reported in Jelenić and Crisfield, 1999, in contrast to the GL models. However, while in the invariant formulations the values remain constant after the superposed rigid-body rotation, in the iterative formulations they do not. This is to be expected, because for instance, for the SR model the approximation of the material rotational strain vector is extracted by the following tensor

$$\hat{\boldsymbol{K}}^h = [\boldsymbol{\Lambda}^h]^T \, \boldsymbol{\Lambda}^h_{,\xi} \overset{eq.\ (3.60)}{=} \left[\boldsymbol{\Lambda}_R \, exp(\boldsymbol{\theta}^h_L)\right]^T \left[\boldsymbol{\Lambda}_R \, exp(\boldsymbol{\theta}^h_L)\right]_{,\xi} = \left[exp(\boldsymbol{\theta}^h_L)\right]^T \left[exp(\boldsymbol{\theta}^h_L)\right]_{,\xi} \tag{3.116}$$

which is unaffected by the rigid-element rotation. The same holds for the GL model. It is shown here that the invariant formulation gives the capability to the $GL_{inv.}$ model not to distort the internal state due to a superposed rigid-body rotation in contrast to the $GL_{iter.}$ one (see the last column of the table).

TABLE 3.3: Single-element test: material twist/bending strain measures without and with superposed rigid-body rotation.

	without rigid-body rot. $(SR_{inv.})$ / $(GL_{inv.})$	with rigid-body rot. $(SR_{inv.})$ / $(GL_{inv.})$	$\frac{(GL_{inv.})-(SR_{inv.})}{(SR_{inv.})}\,100\%$ without / with	
K^h_ξ	$-1.26383/-1.26383$	$-1.26383/-1.26383$	$0.00\%/\ 0.00\%$	
K^h_η	$1.27102/\ 1.18210$	$1.27102/\ 1.18210$	$-7.00\%/-7.00\%$	
K^h_ζ	$-0.42294/-0.39335$	$-0.42294/-0.39335$	$-7.00\%/-7.00\%$	
	without rigid-body rot. $(SR_{iter.})$ / $(GL_{iter.})$	with rigid-body rot. $(SR_{iter.})$ / $(GL_{iter.})$	$\frac{(GL_{iter.})-(SR_{iter.})}{(SR_{iter.})}\,100\%$ without / with	$\frac{\text{with-without}}{\text{without}}\,100\%$ $(SR_{iter.})/(GL_{iter.})$
K^h_ξ	$-1.27465/-1.27465$	$-1.26399/-1.26399$	$0.00\%/\ 0.00\%$	$-0.84\%/-0.84\%$
K^h_η	$1.26756/\ 1.17831$	$1.31371/\ 1.22100$	$-7.04\%/-7.06\%$	$3.64\%/\ 3.62\%$
K^h_ζ	$-0.40350/-0.37509$	$-0.33751/-0.31369$	$-7.04\%/-7.06\%$	$-16.35\%/-16.37\%$

TABLE 3.4: Single-element test: material axial/ shear strain measures without and with superposed rigid-body rotation.

	without rigid-body rotation $(SR_{inv.})$ / $(GL_{inv.})$	with rigid-body rotation $(SR_{inv.})$ / $(GL_{inv.})$
Γ^h_ξ	$0.00000/-0.03522$	$0.00000/-0.03522$
Γ^h_η	$0.00000/-0.03363$	$0.00000/-0.03363$
Γ^h_ζ	$0.00000/\ 0.01119$	$0.00000/\ 0.01119$
	without rigid-body rotation $(SR_{iter.})$ / $(GL_{iter.})$	with rigid-body rotation $(SR_{iter.})$ / $(GL_{iter.})$
Γ^h_ξ	$0.00000/-0.03514$	$0.00000/-0.03578$
Γ^h_η	$0.00000/-0.03379$	$0.00000/-0.03478$
Γ^h_ζ	$0.00000/\ 0.01076$	$0.00000/\ 0.00893$

Finally, as far as the axial/ shear strain vector is concerned, in table 3.4 it is shown that in the

SR models, this is equal to zero as expected. On the other hand, the GL models give a small but no zero strain measure for all the components. These differences are also depicted at the translations of the tip which are different from those computed using the Simo-Reissner strains (see table 3.5). Again, the values for the $SR_{inv.}$ and $SR_{iter.}$ are the same to those reported in Jelenić and Crisfield, 1999.

TABLE 3.5: Single-element test: translations at the second node without the superposed rigid-body rotation.

	$(SR_{inv.})$ / $(GL_{inv.})$	$(SR_{iter.})$ / $(GL_{iter.})$
u_{01}	$-0.02408/-0.05257$	$-0.02009/-0.04919$
u_{02}	$0.20094/\ \ 0.15888$	$0.18605/\ \ 0.14443$
u_{03}	$-0.08490/-0.08185$	$-0.07187/-0.06924$

3.9.5 A challenging 3D example: the deployable circular ring

Finally, the deployable circular ring which was first presented in Goto et al., 1992 to investigate the elastic buckling phenomenon of a non-straight member is studied. This demanding example is utilized to improve the ability of space structures to fold into small packages; it is chosen here because it presents very large rotations in space. The structural model is shown in fig. 3.23. The spatial frame $\mathbf{e}$ is placed at the centre of the ring. The ring has a radius $R = 20$, and is fully supported at one point of its circumference, while at the antipodal point P it is free to move and rotate just along and about the direction defined by the spatial basis vector $\mathbf{e}_1$; at this point a moment M_1 is applied or a prescribed rotation θ_1 is imposed.

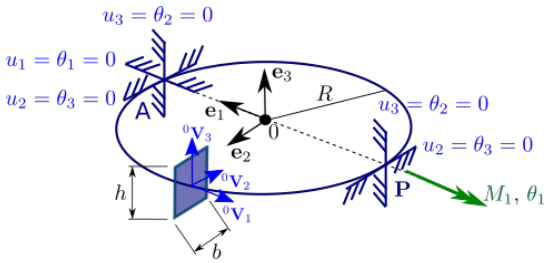

FIGURE 3.23: Circular ring: structural model.

A rectangular cross-section with width b and height h is tested; it belongs to the *slender* region where $\frac{h}{b} = 3 > 1.51$, and the ring does transform into a new ring with a three times smaller diameter Goto et al., 1992. The half model is analyzed. Two methods have been used with identical results: a) applying the half moment combined with the arc-length control method, and b) imposing a rotation of magnitude 2π combined with the displacement control method. 16 elements are used. Both the relative residual and displacement norms are considered as the convergence criteria, while the corresponding tolerance equals to 10^{-6}.
In fig. 3.24a, the reaction moment-rotation curve at the antipodal point P is shown for the SR and GL models, while in fig. 3.24b the deformed shapes at specific time instants that correspond to the points of the graph 3.24a, marked as black, are shown. The results are very similar for each of the two pairs, the $SR_{inv.}$ and $GL_{inv.}$, and the $SR_{iter.}$ and $GL_{iter.}$ beam

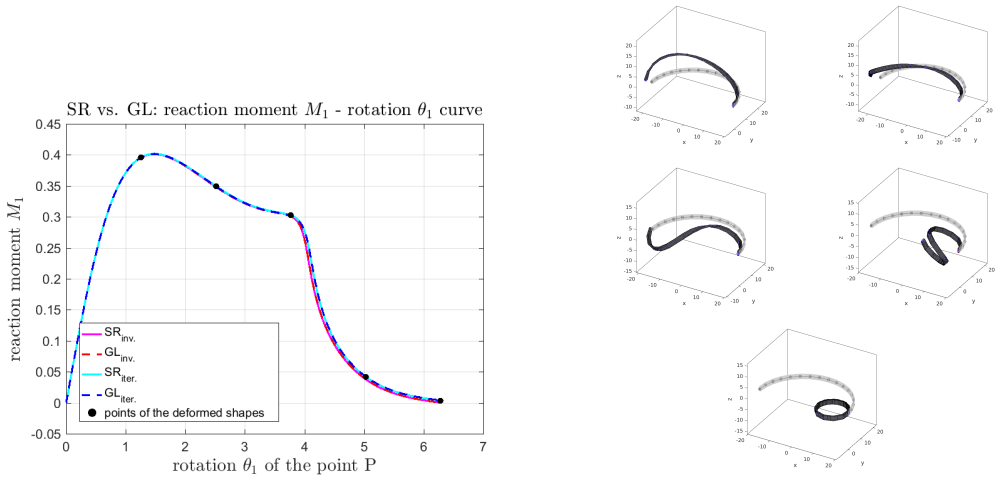

(A) (B)

FIGURE 3.24: Circular ring with $\frac{h}{b} = 3$: (a) reaction moment M_1 vs. rotation θ_1 of the point P using the SR and GL models, and (b) deformed shapes at the selected points.

models. Moreover, these results are also similar to the ones of the reference solution Goto et al., 1992. Regarding the last deformed shape, the structure equilibrates under a zero external load. Indeed, in fig. 3.24a, it is shown that the last point of the graph corresponds to a zero reaction moment. In the invariant implementation though, the values are -6.31×10^{-11} and -1.50×10^{-11}, for the SR and GL models, respectively, while in their iterative formulations the reaction moment has the small value of 3.52×10^{-03}. This observation verifies the invariance and non-invariance properties of the above two implementations. In the same conclusion one would arrive by looking at the fig. 3.25a, where the final translations u_{03} along the half circumference of the ring are plotted when a displacement control method has been used. In this graph, one may see that there is no error in the invariant formulations (straight

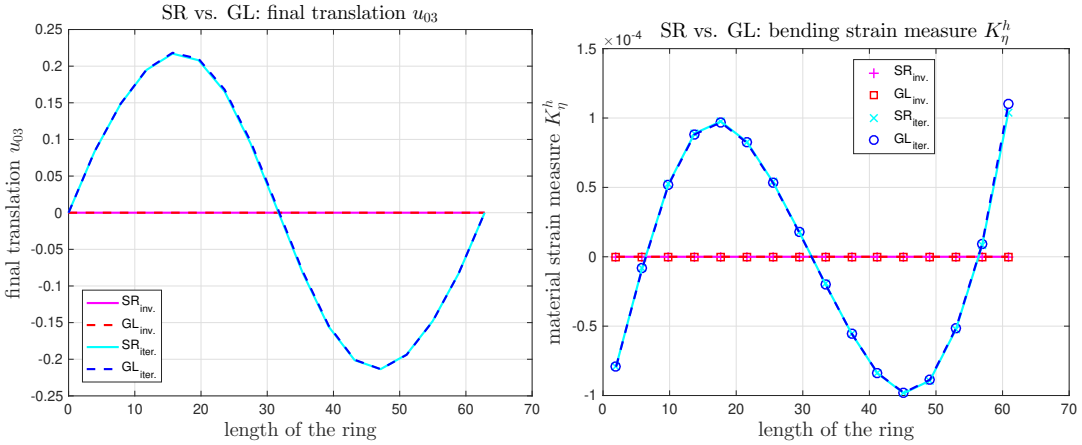

(A) (B)

FIGURE 3.25: Circular ring with $\frac{h}{b} = 3$: (a) final translations u_{03}, and (b) final material bending curvature measure K_η^h along the half circumference.

line at zero), whereas for the iterative formulations there is a discrepancy, antisymmetric for

the SR and GL models, with an almost coincident amplitude. As far as the strain measures are concerned, two conclusions can be drawn observing the results in fig. 3.25b and fig. 3.26:

- in fig. 3.25b, the same pattern with this of fig. 3.25a is depicted, where the approximation at the Gauss point of the final material bending curvature K_η^h is given for the two variants of the SR and GL beam models. This shows again the superiority of the invariant formulation which does not distort the internal elastic state of the element due to a superposed rigid-body rotation in contrast with the iterative one.
- in fig. 3.26, the approximation at the Gauss point of the final material axial strain Γ_ξ^h is shown along the length; there is a small deviation from zero for the GL models (invariant and iterative). On the other hand, using the SR models (invariant and iterative) the material axial strain measure Γ_ξ^h is exactly zero.

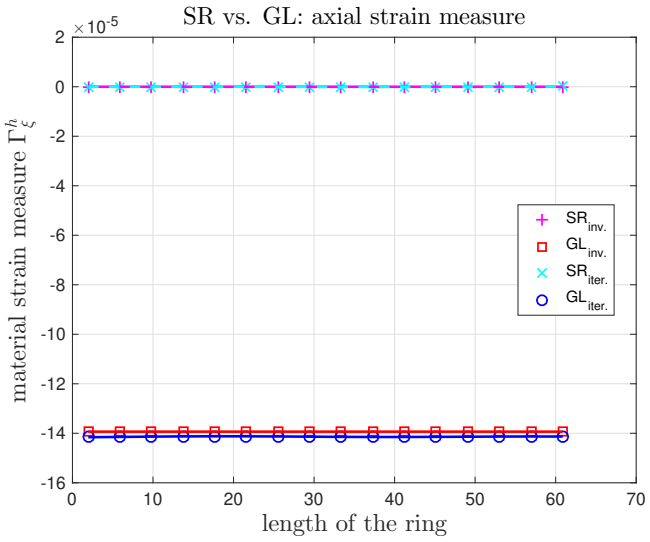

FIGURE 3.26: Circular ring with $\frac{h}{b} = 3$: final material axial strain measure Γ_ξ^h along the half circumference.

Finally, it is well-worth to notice that the iterations needed to converge to the correct solution for the SR model when a displacement control method is used, with 200 steps to complete the whole rotation 2π, are 1000 for the iterative formulation and 1058 for the invariant formulation. The corresponding values for the GL beam model are 1270 and 1311 respectively. The above has an effect on the computational cost, i.e. the iterative SR model needs $cputime = 619.3$ *units of time* with the processor Intel Core i3 CPU M370 @2.40GHz $\times$ 4, while the corresponding GL model needs a slightly increased time by $\approx 4\%$. The invariant SR model needs $cputime = 656.42$ *units of time*, while the corresponding GL model needs an increased time by $\approx 10\%$.

3.9.6 The 45-degree cantilever subjected to a follower load at the tip using the SR model

The example in section 3.9.3 is examined again under a follower load at the tip, in order to verify the code integrity when a configuration dependent excitation is considered. The model

used is the SR with its invariant implementation. This step is necessary for proceeding into the dynamics of beams and wind turbine blades subjected to the aerodynamic loading, in chapters 4 and 5. To test the output, the results presented in Simo and Vu-Quoc, 1986a are given as reference.

In fig. 3.27a, the equilibrium path is shown for the three components of the translation vector at the tip. The reference results are also given after digitizing the corresponding graph in Simo and Vu-Quoc, 1986a. In fig. 3.27b, the deformed configurations of the beam, which correspond to the *black points* on the equilibrium path 3.27a, are depicted. It is observed that the beam is twisted while the load is increasing in the bending direction. Due to the intense twisting the translation u_{03} decreases after reaching its pick value when the load is 600. The two curves, the SR and the reference one, have a slight difference after the pick at 600 for the u_{01} and u_{03} translations which are the most affected components by the geometrically non-linear couplings. On the other hand, the u_{02} component follows the same path for both modelings. Because of the load that follows the configuration of the beam, the twist-bending coupling is more dominated compared to the case of a fixed load at the tip (see section 3.9.3).

In fig. 3.28, the distribution of the translations and rotations along the length of the beam

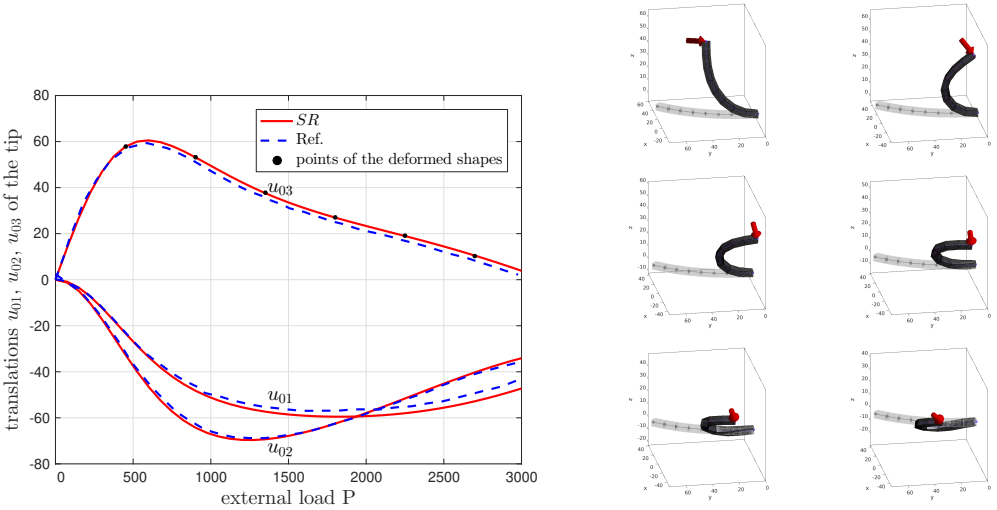

(A) (B)

FIGURE 3.27: 45-degree cantilever subjected to a follower load at the tip: (a) translations u_{01}, u_{02}, u_{03} of the tip vs. external load, and (b) deformed shapes at the selected points.

is depicted for the cases of the follower and the fixed loading when the load has reached the value 600. It is observed that the curve of the translation u_{03} when the load is follower remains below the corresponding curve when the load is fixed, because of the bending-twist coupling that is more pronounced in the case of the follower loading. The same phenomenon is depicted in the curve for the translation u_{01} that has larger values along the length in the follower case compared to the fixed case. This is because the beam is more triggered to bending in $\boldsymbol{e}_1$ direction, that is a result from the twist of the configuration dependent loading. It is worth mentioning that although there is also a difference in the distribution of the axial translation u_{02}, its value at the tip of the beam is almost the same for both modelings.

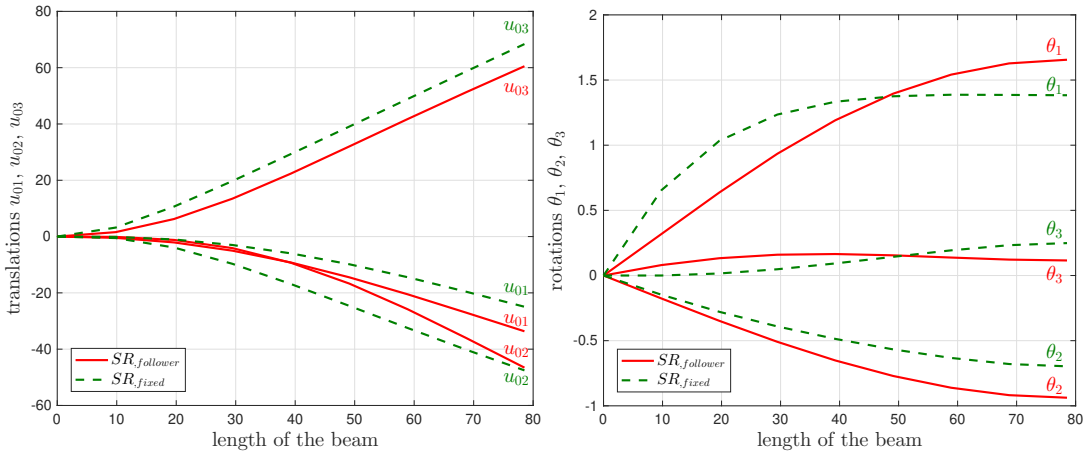

(A) (B)

FIGURE 3.28: 45-degree cantilever subjected to a follower load at the tip: (a) translations u_{01}, u_{02}, u_{03}, and (b) rotations θ_1, θ_2, θ_3 along the length.

The twist angle θ_2 is expected to be more pronounced in the case with the follower loading compared to the fixed loading one, as it is depicted in fig. 3.28b. Moreover, for the other two rotation components, the θ_1 and θ_3, of the follower loading case, their relation is changed compared to the fixed loading case at almost the same point along the length of the beam. Specifically, the θ_1 rotation is getting larger than the corresponding rotation when the load is fixed, whereas, the θ_3 rotation is getting smaller compared to the same rotation in the fixed loading case.

3.10 Conclusions

Two models for geometrically non-linear shear-deformable 3D beams with small strains that are derived from different working pairs are compared. The first one is the Simo-Reissner model (SR model), whereas the second one is the 1D formulation of a degenerate-continuum beam model which uses the Green-Lagrange strains (GL model). The derivation was made in a way so that one may have a clear comparison with the SR model. Two different (regarding rotations) formulations, the iterative and the invariant, are tested within the framework of these two models. The geometric illustration given on the rotation manifold $SO(3)$ clarifies the way of creating an invariant 3D beam element with large rotations: one should refer to the same tangent space on $SO(3)$ when interpolation is performed.

Four variants of a geometrically non-linear finite element formulation are derived (SR invariant, GL invariant, SR iterative, GL iterative) and used in 2D and 3D examples. The numerical results compare the proposed invariant GL model to the other three finite element formulations and the strain measures between the four of them. The main conclusions are:

- The GL model gives a different approximation compared to the SR model, due to the extra strain terms. It is verified numerically that the SR model is better suited for a finite-deformation small-strain beam theory.

- The incorporation to the GL model of the update procedure that splits the rotation into a rigid-body part and a local cross-sectional part, offers the invariance properties to this beam formulation. This implementation may be combined with all the beam models that use spin parameters as the rotational unknowns.

- The invariant formulation, either in the SR or in the GL model, is more suitable for problems with 3D large rotations.

- The SR and GL beam models require similar computational cost to converge to the correct solution.

Chapter 4

Time integration scheme for dynamics with large 3D rotations

4.1 Introduction

In this chapter, the objective is to formulate, implement and verify the dynamics of beams for using the resulting code in the analysis of the wind turbine system. Prior to this, a primary investigation of two time integration schemes in the framework of large 3D rotations is presented. Using the original Newmark integration scheme for structural dynamics, the accuracy cannot be guaranteed in the context of large 3D rotations. The method as it was proposed in Newmark, 1959 works well when accounting for the translational part of the motion, but it has to be modified for correctly computing the contribution of the rotational part; an extension to the rotation group $SO(3)$ has to be developed (Simo and Vu-Quoc, 1988). For this reason, the rigid-body dynamics with large 3D rotations using two schemes is investigated. A reference problem is selected which is the well-known example of fast symmetrical top (Goldstein, Poole, and Safko, 2000). In the next step, one of these two schemes is chosen for the temporal discretization, and tested in benchmark examples of beams where the FEM is used for the spatial discretization. The time integration algorithms of interest are the following:

- the Simo's & Vu-Quoc's algorithm (Simo and Vu-Quoc, 1988)
- the Mäkinen's (that is a non consistent) algorithm (Mäkinen, 2001), and a modification of it, the Cardona's & Géradin's (that is a semi consistent) algorithm (Cardona and Géradin, 1988). Moreover, a fully consistent option of the Mäkinen's algorithm is added.

The property of consistency refers to the way of constructing the tangent operator and the update formula inside the iterative procedure, writing down the formulas that give the kinematics at t_{n+1} for two consecutive iterations and subtracting them. The above techniques share the following common feature: They establish the equilibrium at the time instant t_{n+1}, where the equation of the rate of angular momentum balance is solved. Thus, they are considered as Newmark-type (Newmark, 1959) algorithms. However, the motivation of studying both of them is that the first algorithm (Simo and Vu-Quoc, 1988) uses the Newmark scheme for the angular velocities and accelerations, whereas the second algorithm (Mäkinen, 2001;

Cardona and Géradin, 1988) uses the Newmark scheme for the first and second derivatives of the rotation vector, respectively.

4.2 Rotational dynamics of a Rigid-Body - Equation of motion

The classical Euler's equation for the rigid-body in convective (body or material) co-ordinates (Arnold, 1989; Goldstein, Poole, and Safko, 2000) is:

$$\boldsymbol{J}\boldsymbol{A} + \boldsymbol{\Omega} \times \boldsymbol{J}\boldsymbol{\Omega} = \boldsymbol{\Lambda}^T \boldsymbol{m} \tag{4.1}$$

where $\boldsymbol{J}$ is the inertia tensor, $\boldsymbol{A}$ is the angular acceleration vector, $\boldsymbol{\Omega}$ is the angular velocity vector, all given in a material setting, $\boldsymbol{\Lambda}$ is the orientation tensor, and $\boldsymbol{m}$ is the applied torque at the centre of mass in a spatial setting.
Together with the following initial conditions:

$$\boldsymbol{\Lambda}|_{t=0} = \boldsymbol{\Lambda}_0 \text{ and } \boldsymbol{\Omega}|_{t=0} = \boldsymbol{\Omega}_0 \tag{4.2}$$

the eq. (4.1) defines an *initial value problem* for $(\boldsymbol{\Lambda}(t),\ \boldsymbol{\Omega}(t))$ in $SO(3) \times \mathbb{R}^3$ (Simo and Wong, 1991).

4.2.1 Discrete equation of motion - Residual

The material setting of the residual (that is the equation of motion written in an implicit form) at the time instant t_{n+1} is written as a function of the incremental rotation vector $\boldsymbol{\Theta}_{n+1}$

$$\boldsymbol{g}_{n+1}(\boldsymbol{\Theta}_{n+1}) = \boldsymbol{J}\boldsymbol{A}_{n+1}(\boldsymbol{\Theta}_{n+1}) + \boldsymbol{\Omega}_{n+1}(\boldsymbol{\Theta}_{n+1}) \times \boldsymbol{J}\boldsymbol{\Omega}_{n+1}(\boldsymbol{\Theta}_{n+1}) - \boldsymbol{\Lambda}^T_{n+1}(\boldsymbol{\Theta}_{n+1})\boldsymbol{m} \tag{4.3}$$

where $\boldsymbol{A}_{n+1}(\boldsymbol{\Theta}_{n+1})$ is the angular acceleration vector at t_{n+1}, $\boldsymbol{\Omega}_{n+1}(\boldsymbol{\Theta}_{n+1})$ is the angular velocity vector at t_{n+1}, and $\boldsymbol{\Lambda}_{n+1}(\boldsymbol{\Theta}_{n+1})$ is the orientation tensor at t_{n+1}. In case of the gravitational field, the components of the applied torque $\boldsymbol{m}$ w.r.t. the spatial axes change with the orientation and they are given as

$$\boldsymbol{m}_{n+1}(\boldsymbol{\Theta}_{n+1}) = \boldsymbol{r}_{n+1}(\boldsymbol{\Theta}_{n+1}) \times \boldsymbol{f} = \underbrace{\boldsymbol{\Lambda}_{n+1}(\boldsymbol{\Theta}_{n+1})\, l\boldsymbol{E}_3}_{l\,\boldsymbol{V}_{3,n+1}(\boldsymbol{\Theta}_{n+1})} \times (-mg\,\boldsymbol{e}_3) \tag{4.4}$$

where $\boldsymbol{r}_{n+1}(\boldsymbol{\Theta}_{n+1}) = \boldsymbol{\Lambda}_{n+1}(\boldsymbol{\Theta}_{n+1})\, l\boldsymbol{E}_3$ is the position vector of the centre of mass given in a spatial setting, and $\boldsymbol{f} = -mg\,\boldsymbol{e}_3$ is the gravitational load vector. In fig. 4.1, the kinematics of the rigid-body is shown, and the reference axes that have been used above are depicted. The RHS of eq. (4.1) can also be written as

$$\boldsymbol{M}_{n+1}(\boldsymbol{\Theta}_{n+1}) = \boldsymbol{R} \times \boldsymbol{F}_{n+1}(\boldsymbol{\Theta}_{n+1}) = l\boldsymbol{E}_3 \times \boldsymbol{\Lambda}^T_{n+1}(\boldsymbol{\Theta}_{n+1})(-mg\,\boldsymbol{e}_3) \tag{4.5}$$

which is the applied torque in a material setting; $\boldsymbol{R} = l\boldsymbol{E}_3$ is the position vector of the centre of mass given in a material setting, and $\boldsymbol{F}_{n+1}(\boldsymbol{\Theta}_{n+1}) = \boldsymbol{\Lambda}^T_{n+1}(\boldsymbol{\Theta}_{n+1})(-mg\,\boldsymbol{e}_3)$ is

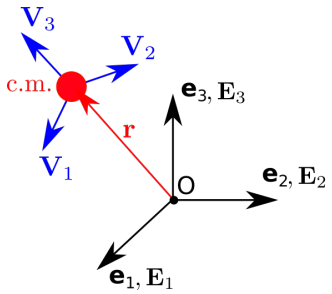

FIGURE 4.1: Kinematics of the rigid-body.

the material counterpart of the gravitational load (it expresses the components of the load $\boldsymbol{f} = -mg\,\boldsymbol{e}_3$ onto the material axes).

4.2.2 Angular velocity and acceleration vectors for the Simo's & Vu-Quoc's scheme

Angular velocity vector at t_{n+1}

The angular velocity vector $\boldsymbol{\Omega}_{n+1}$ at t_{n+1} is given in relation with the material, incremental rotation vector $\boldsymbol{\Theta}_{n+1}$ at t_{n+1} and the converged angular velocity $\boldsymbol{\Omega}_n$ and acceleration $\boldsymbol{A}_n$ vectors at t_n, as

$$\boldsymbol{\Omega}_{n+1} = \frac{\gamma}{h\beta}\boldsymbol{\Theta}_{n+1} \underbrace{+ \left(1 - \frac{\gamma}{\beta}\right)\boldsymbol{\Omega}_n + h\left(1 - \frac{\gamma}{2\beta}\right)\boldsymbol{A}_n}_{\boldsymbol{\Omega}'_n} \tag{4.6}$$

where β, γ are the Newmark constants (Newmark, 1959) and $h = t_{n+1} - t_n$ is the time step. The last two terms that are written as a function of the kinematics at t_n are defined as $\boldsymbol{\Omega}'_n$. The consistent update formula inside the iterative Newton-Raphson procedure is

$$\boldsymbol{\Omega}^{(i+1)}_{n+1} - \boldsymbol{\Omega}^{(i)}_{n+1} = \frac{\gamma}{h\beta}\left(\boldsymbol{\Theta}^{(i+1)}_{n+1} - \boldsymbol{\Theta}^{(i)}_{n+1}\right) \tag{4.7}$$

Angular acceleration vector at t_{n+1}

The angular acceleration vector $\boldsymbol{A}_{n+1}$ at t_{n+1} is given (as previously) in relation with the material, incremental rotation vector $\boldsymbol{\Theta}_{n+1}$ at t_{n+1} and the converged angular velocity $\boldsymbol{\Omega}_n$ and acceleration $\boldsymbol{A}_n$ vectors at t_n, as

$$\boldsymbol{A}_{n+1} = \frac{1}{h^2\beta}\boldsymbol{\Theta}_{n+1} \underbrace{- \frac{1}{h\beta}\boldsymbol{\Omega}_n - \frac{1}{\beta}\left(\frac{1}{2} - \beta\right)\boldsymbol{A}_n}_{\boldsymbol{A}'_n} \tag{4.8}$$

The last two terms that are written as a function of the kinematics at t_n are defined as $\boldsymbol{A}'_n$. The consistent update formula inside the iterative Newton-Raphson procedure is

$$\boldsymbol{A}^{(i+1)}_{n+1} - \boldsymbol{A}^{(i)}_{n+1} = \frac{1}{h^2\beta}\left(\boldsymbol{\Theta}^{(i+1)}_{n+1} - \boldsymbol{\Theta}^{(i)}_{n+1}\right) \tag{4.9}$$

4.2.3 Angular velocity and acceleration vectors for the Mäkinen's / Cardona's & Géradin's scheme

The modified Newmark scheme presented in Mäkinen, 2001 is based on the fact that the standard Newmark scheme is applied on the first and second derivatives of the material, incremental rotation vector instead of the material, angular velocity and acceleration vectors. However, in his work there is no a consistent formula for the angular velocity and acceleration vectors that appears inside the incremental form of the equation of motion. In the following, a semi consistent modification of the Mäkinen's work is also presented, as it had been proposed earlier by Cardona and Géradin, 1988. Moreover, a fully consistent version of the Mäkinen's scheme is added.

To have a relation between the first and second derivatives of the material, incremental rotation vector, and the material, angular velocity and acceleration vectors respectively, the two ways of evaluating the time derivative of the orientation matrix, $\dot{\boldsymbol{\Lambda}}_{n+1}$, at t_{n+1} are taken into account.

1. The first way to form the time derivative of the orientation matrix uses the material, angular velocity vector $\boldsymbol{\Omega}_{n+1}$ at t_{n+1}, as

$$\dot{\boldsymbol{\Lambda}}_{n+1} = \boldsymbol{\Lambda}_{n+1}\hat{\boldsymbol{\Omega}}_{n+1} \tag{4.10}$$

   where $\boldsymbol{\Lambda}_{n+1}$ is given by,

$$\boldsymbol{\Lambda}_{n+1} = \boldsymbol{\Lambda}_n exp(\hat{\boldsymbol{\Theta}}_{n+1}),\ \ \boldsymbol{\Lambda}_n \text{ is the orientation tensor at } t_n. \tag{4.11}$$

2. The second way to form the time derivative of the orientation matrix uses the corresponding derivative of the exponential map of the skew-symmetric matrix $\hat{\boldsymbol{\Theta}}_{n+1}$ of the material, incremental rotation vector $\boldsymbol{\Theta}_{n+1}$ at t_{n+1}, as

$$\dot{\boldsymbol{\Lambda}}_{n+1} = \boldsymbol{\Lambda}_n \frac{d[exp(\hat{\boldsymbol{\Theta}}_{n+1})]}{dt} \tag{4.12}$$

By equating eq. (4.10) and eq. (4.12), the relation between the material, angular velocity vector, $\boldsymbol{\Omega}_{n+1}$, and the first derivative of the material, incremental rotation vector, $\dot{\boldsymbol{\Theta}}_{n+1}$, is derived, as

$$\boldsymbol{\Omega}_{n+1} = \boldsymbol{T}^T_{n+1}(\boldsymbol{\Theta}_{n+1})\dot{\boldsymbol{\Theta}}_{n+1} \tag{4.13}$$

where $\boldsymbol{T}^T_{n+1}(\boldsymbol{\Theta}_{n+1})$ is the transpose of the tangential transformation given by

$$\boldsymbol{T}^T_{n+1}(\boldsymbol{\Theta}_{n+1}) = a_1(\Theta_{n+1})\boldsymbol{I} - a_2(\Theta_{n+1})\hat{\boldsymbol{\Theta}}_{n+1} + a_3(\Theta_{n+1})\boldsymbol{\Theta}_{n+1}\boldsymbol{\Theta}^T_{n+1} \tag{4.14}$$

where $a_1(\Theta_{n+1})$, $a_2(\Theta_{n+1})$ and $a_3(\Theta_{n+1})$ are the trigonometric functions given in appendix B (see also Ritto-Corrêa and Camotim, 2002).

By differentiating eq. (4.13) w.r.t. time, the relation between the material, angular acceleration vector and the first $\dot{\boldsymbol{\Theta}}_{n+1}$ and second derivatives $\ddot{\boldsymbol{\Theta}}_{n+1}$ of the material, incremental

rotation vector is derived as

$$\boldsymbol{A}_{n+1} = \frac{d[\boldsymbol{T}_{n+1}^T(\boldsymbol{\Theta}_{n+1})]}{dt}\,\dot{\boldsymbol{\Theta}}_{n+1} + \boldsymbol{T}_{n+1}^T(\boldsymbol{\Theta}_{n+1})\ddot{\boldsymbol{\Theta}}_{n+1} \tag{4.15}$$

where $\frac{d[\boldsymbol{T}_{n+1}^T(\boldsymbol{\Theta}_{n+1})]}{dt}$ is given by

$$\begin{aligned}\frac{d[\boldsymbol{T}_{n+1}^T(\boldsymbol{\Theta}_{n+1})]}{dt} =& -\alpha_2(\Theta_{n+1})\dot{\hat{\boldsymbol{\Theta}}}_{n+1} + \alpha_3(\Theta_{n+1})(\dot{\boldsymbol{\Theta}}_{n+1}\boldsymbol{\Theta}_{n+1}^T + \boldsymbol{\Theta}_{n+1}\dot{\boldsymbol{\Theta}}_{n+1}^T)\\ &+ b_1(\Theta_{n+1})(\boldsymbol{\Theta}_{n+1}^T\dot{\boldsymbol{\Theta}}_{n+1})\boldsymbol{I} - b_2(\Theta_{n+1})(\boldsymbol{\Theta}_{n+1}^T\dot{\boldsymbol{\Theta}}_{n+1})\hat{\boldsymbol{\Theta}}_{n+1}\\ &+ b_3(\Theta_{n+1})(\boldsymbol{\Theta}_{n+1}^T\dot{\boldsymbol{\Theta}}_{n+1})\boldsymbol{\Theta}_{n+1}\boldsymbol{\Theta}_{n+1}^T\end{aligned} \tag{4.16}$$

where $b_1(\Theta_{n+1})$, $b_2(\Theta_{n+1})$ and $b_3(\Theta_{n+1})$ are the trigonometric functions given in appendix B (see also Ritto-Corrêa and Camotim, 2002).

Angular velocity vector at t_{n+1}

Taking into account eqs. (4.6) and (4.13), the angular velocity vector at t_{n+1} is written as follows

$$\boldsymbol{\Omega}_{n+1} = \boldsymbol{T}_{n+1}^T \left[\underbrace{\frac{\gamma}{h\beta}\boldsymbol{\Theta}_{n+1} + \left(1-\frac{\gamma}{\beta}\right)\dot{\boldsymbol{\Theta}}_n + h\left(1-\frac{\gamma}{2\beta}\right)\ddot{\boldsymbol{\Theta}}_n}_{\dot{\boldsymbol{\Theta}}_{n+1}}\right] \tag{4.17}$$

where $\dot{\boldsymbol{\Theta}}_n$, $\ddot{\boldsymbol{\Theta}}_n$ are the first and second derivatives of the rotation vector at the converged time instant t_n. Notice that they equal to the initial angular velocity and acceleration vectors, respectively, i.e. $\dot{\boldsymbol{\Theta}}_n = \boldsymbol{\Omega}_n$ and $\ddot{\boldsymbol{\Theta}}_n = \boldsymbol{A}_n$.

- The Makinen's update formula (that is non consistent) inside the iterative Newton-Raphson procedure is

$$\boldsymbol{\Omega}_{n+1}^{(i+1)} - \boldsymbol{\Omega}_{n+1}^{(i)} = \frac{\gamma}{h\beta}\left[\boldsymbol{T}_{n+1}^{(i+1)}\right]^T\left(\boldsymbol{\Theta}_{n+1}^{(i+1)} - \boldsymbol{\Theta}_{n+1}^{(i)}\right) \tag{4.18}$$

- The Cardona's & Géradin's update formula (that is consistent) inside the iterative Newton-Raphson procedure is

$$\boldsymbol{\Omega}_{n+1}^{(i+1)} = [\boldsymbol{T}_{n+1}^{(i+1)}]^T \underbrace{\left[\dot{\boldsymbol{\Theta}}_{n+1}^{(i)} + \frac{\gamma}{h\beta}\left(\boldsymbol{\Theta}_{n+1}^{(i+1)} - \boldsymbol{\Theta}_{n+1}^{(i)}\right)\right]}_{\dot{\boldsymbol{\Theta}}_{n+1}^{(i+1)}} \tag{4.19}$$

where

$$\dot{\boldsymbol{\Theta}}_{n+1}^{(i+1)} = \dot{\boldsymbol{\Theta}}_{n+1}^{(i)} + \frac{\gamma}{h\beta}\left(\boldsymbol{\Theta}_{n+1}^{(i+1)} - \boldsymbol{\Theta}_{n+1}^{(i)}\right) \tag{4.20}$$

Angular acceleration vector at t_{n+1}

Taking into account eqs. (4.8) and (4.15), the angular acceleration vector at t_{n+1} is written as follows

$$\boldsymbol{A}_{n+1} = \left[\dot{\boldsymbol{T}}_{n+1}\right]^T \underbrace{\left[\frac{\gamma}{h\beta}\boldsymbol{\Theta}_{n+1} + \left(1-\frac{\gamma}{\beta}\right)\dot{\boldsymbol{\Theta}}_n + h\left(1-\frac{\gamma}{2\beta}\right)\ddot{\boldsymbol{\Theta}}_n\right]}_{\dot{\boldsymbol{\Theta}}_{n+1}} + [\boldsymbol{T}_{n+1}]^T \underbrace{\left[\frac{1}{h^2\beta}\boldsymbol{\Theta}_{n+1} - \frac{1}{h\beta}\dot{\boldsymbol{\Theta}}_n - \frac{1}{\beta}\left(\frac{1}{2}-\beta\right)\ddot{\boldsymbol{\Theta}}_n\right]}_{\ddot{\boldsymbol{\Theta}}_{n+1}} \tag{4.21}$$

- The Makinen's update formula (that is non consistent) inside the iterative Newton-Raphson procedure is

$$\boldsymbol{A}_{n+1}^{(i+1)} - \boldsymbol{A}_{n+1}^{(i)} = \frac{1}{h^2\beta}\left[\boldsymbol{T}_{n+1}^{(i+1)}\right]^T\left(\boldsymbol{\Theta}_{n+1}^{(i+1)} - \boldsymbol{\Theta}_{n+1}^{(i)}\right) + \frac{\gamma}{h\beta}\left[\dot{\boldsymbol{T}}_{n+1}^{(i+1)}\right]^T\left(\boldsymbol{\Theta}_{n+1}^{(i+1)} - \boldsymbol{\Theta}_{n+1}^{(i)}\right) \tag{4.22}$$

- The Cardona's & Géradin's update formula (that is consistent) inside the iterative Newton-Raphson procedure is

$$\boldsymbol{A}_{n+1}^{(i+1)} = \left[\dot{\boldsymbol{T}}_{n+1}^{(i+1)}\right]^T \underbrace{\left[\dot{\boldsymbol{\Theta}}_{n+1}^{(i)} + \frac{\gamma}{h\beta}\left(\boldsymbol{\Theta}_{n+1}^{(i+1)} - \boldsymbol{\Theta}_{n+1}^{(i)}\right)\right]}_{\dot{\boldsymbol{\Theta}}_{n+1}^{(i+1)}} + \left[\boldsymbol{T}_{n+1}^{(i+1)}\right]^T \underbrace{\left[\ddot{\boldsymbol{\Theta}}_{n+1}^{(i)} + \frac{1}{h^2\beta}\left(\boldsymbol{\Theta}_{n+1}^{(i+1)} - \boldsymbol{\Theta}_{n+1}^{(i)}\right)\right]}_{\ddot{\boldsymbol{\Theta}}_{n+1}^{(i+1)}} \tag{4.23}$$

where

$$\ddot{\boldsymbol{\Theta}}_{n+1}^{(i+1)} = \ddot{\boldsymbol{\Theta}}_{n+1}^{(i)} + \frac{1}{h^2\beta}\left(\boldsymbol{\Theta}_{n+1}^{(i+1)} - \boldsymbol{\Theta}_{n+1}^{(i)}\right) \tag{4.24}$$

4.3 Tangent operator

For the derivation of the tangent operator, the linearization of the residual has to be employed. To linearize the residual, this is written at a perturbed state at time $t + \epsilon\Delta t$, and then, the directional derivative w.r.t. ϵ, for $\epsilon = 0$, is performed. This procedure is given in appendix C.

4.3.1 Tangent operator for the Simo's & Vu-Quoc's scheme - consistent linearization

The tangent operator is given by adding its three constituents in eqs. (C.3), (C.12) and (C.24), as

$$\boxed{\boldsymbol{K}_{n+1} = \left\{ \frac{1}{h^2\beta}\, \boldsymbol{J} + \frac{\gamma}{h\beta}\left[(-\boldsymbol{J}\boldsymbol{\Omega}_{n+1}(\boldsymbol{\Theta})) \times + \boldsymbol{\Omega}_{n+1}(\boldsymbol{\Theta}) \times \boldsymbol{J}\right]\right.}$$

$$\boxed{\left. -mgl\left[-\boldsymbol{E}_3 \times \boldsymbol{\Xi}_{D\boldsymbol{\Lambda}^T_{n+1}}(\boldsymbol{e}_3)\right]\right\}} \tag{4.25}$$

4.3.2 Tangent operator for the Mäkinen's / Cardona's & Géradin's scheme - non consistent linearization

The tangent operator is given by adding its three constituents in eqs. (C.4), (C.13) and (C.24), as

$$\boxed{\boldsymbol{K}_{n+1} = \left\{ \frac{1}{h^2\beta}\, \boldsymbol{J}\, \boldsymbol{T}^T_{n+1}(\boldsymbol{\Theta}) + \frac{\gamma}{h\beta}\boldsymbol{J}\, \dot{\boldsymbol{T}}^T_{n+1}(\boldsymbol{\Theta})\right.}$$

$$\boxed{\left. + \frac{\gamma}{h\beta}\left[(-\boldsymbol{J}\boldsymbol{\Omega}_{n+1}(\boldsymbol{\Theta})) \times \boldsymbol{T}^T_{n+1}(\boldsymbol{\Theta}) + \boldsymbol{\Omega}_{n+1}(\boldsymbol{\Theta}) \times \boldsymbol{J}\boldsymbol{T}^T_{n+1}(\boldsymbol{\Theta})\right] - mgl\left[-\boldsymbol{E}_3 \times \boldsymbol{\Xi}_{D\boldsymbol{\Lambda}^T_{n+1}}(\boldsymbol{e}_3)\right]\right\}} \tag{4.26}$$

4.3.3 Tangent operator for the Mäkinen's / Cardona's & Géradin's scheme - consistent linearization

The tangent operator is given by adding its three constituents in eqs. (C.11), (C.20) and (C.24), as

$$\boxed{\boldsymbol{K}_{n+1} = \left\{ \boldsymbol{J}\left(\boldsymbol{\Xi}_{D^2\boldsymbol{T}^T_{n+1}}(\boldsymbol{\Theta}, \dot{\boldsymbol{\Theta}}) + \frac{\gamma}{h\beta}\frac{d[\boldsymbol{T}^T_{n+1}(\boldsymbol{\Theta})]}{dt} + \boldsymbol{\Xi}_{D\boldsymbol{T}^T_{n+1}}(\boldsymbol{\Theta}, \ddot{\boldsymbol{\Theta}}) + \frac{1}{h^2\beta}\boldsymbol{T}^T_{n+1}(\boldsymbol{\Theta})\right)\right.}$$

$$\boxed{+ (-\boldsymbol{J}\boldsymbol{\Omega}_{n+1}(\boldsymbol{\Theta})) \times \left(\boldsymbol{\Xi}_{D\boldsymbol{T}^T_{n+1}}(\boldsymbol{\Theta}, \dot{\boldsymbol{\Theta}}) + \frac{\gamma}{h\beta}\boldsymbol{T}^T_{n+1}(\boldsymbol{\Theta})\right)}$$

$$\boxed{\left. + \boldsymbol{\Omega}_{n+1}(\boldsymbol{\Theta}) \times \boldsymbol{J}\left(\boldsymbol{\Xi}_{D\boldsymbol{T}^T_{n+1}}(\boldsymbol{\Theta}, \dot{\boldsymbol{\Theta}}) + \frac{\gamma}{h\beta}\boldsymbol{T}^T_{n+1}(\boldsymbol{\Theta})\right) - mgl\left[-\boldsymbol{E}_3 \times \boldsymbol{\Xi}_{D\boldsymbol{\Lambda}^T_{n+1}}(\boldsymbol{e}_3)\right]\right\}} \tag{4.27}$$

4.4 Algorithm

The following algorithm has been implemented in MATLAB and includes the time integration schemes discussed above for the rotational rigid-body dynamics, i.e. Simo's & Vu-Quoc's (1988), Makinen's (2001) (with non consistent linearization and update), and Cardona's & Géradin's (1988) (with non consistent linearization yet consistent update); the consistent linearization and update is added. Notice that in all algorithms, the update regarding the rotation is incremental, whereas the update regarding the angular velocities and accelerations is iterative. Moreover, the setting of equilibrium is material, and the material rotation vector is used as the unknown parameter. For the implementation, the following tools have been used: a) the quaternion algebra functions that are available in *Quaternions*, together with b) the functions that are available in *Angle from rotation matrix*. In fig. 4.2, the main functions are given in a gray color, while the secondary functions are given in a light magenta color. These are:

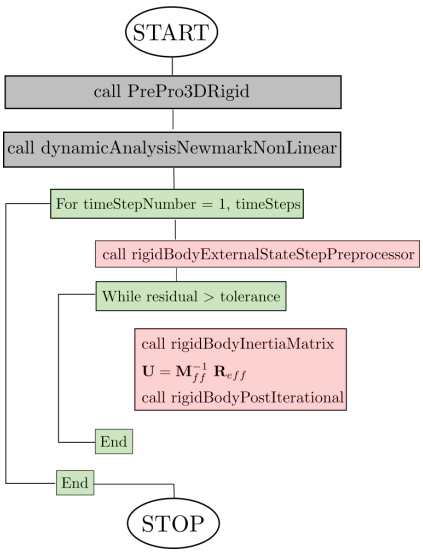

FIGURE 4.2: Algorithm for rotational rigid-body dynamics.

- *PrePro3DRigid*: It performs the initial computations for each node before the time step analysis, as follows
  - Given the initial orientation matrix $\boldsymbol{\Lambda}_1$, it computes the initial material external moment $\boldsymbol{M}_1$ from eq. (4.5).
  - Given the initial material external moment $\boldsymbol{M}_1$, the mass moment of inertia $\boldsymbol{J}$, the initial material angular velocity vector $\boldsymbol{\Omega}_1$, it computes the initial material acceleration vector by solving the equation of motion (eq. 4.1): $\boldsymbol{A}_1 = \boldsymbol{J}^{-1}\left(\boldsymbol{M}_1 - \boldsymbol{\Omega}_1 \times \boldsymbol{J}\boldsymbol{\Omega}_1\right)$.
  - If it is the case of Mäkinen's / Cardona's & Géradin's scheme,
    - By taking into account that the transpose of the tangential transformation equals to the identity matrix when the incremental rotation vector equals to zero, the first derivative of the rotation vector is set equal to $\dot{\boldsymbol{\Theta}}_1 = \boldsymbol{A}_1$ (see eq. (4.13)).
    - It computes the time derivative of the transpose of the tangential transformation using eq. (4.16).
    - It computes the second derivative of the rotation vector using eq. (4.15), thus, $\ddot{\boldsymbol{\Theta}}_1 = \boldsymbol{A}_1 - \frac{d}{dt}[\boldsymbol{T}_1]^T\dot{\boldsymbol{\Theta}}_1 = \boldsymbol{A}_1$.
  - It computes the spatial angular momentum: $\boldsymbol{\pi}_1 = \boldsymbol{\Lambda}_1\,\boldsymbol{\Pi}_1$, where $\boldsymbol{\Pi}_1$ is the material angular momentum given by $\boldsymbol{\Pi}_1 = \boldsymbol{J}\,\boldsymbol{\Omega}_1$.

  - It initializes the iterative and incremental variables of the moving frame that are going to be updated during iterations, and at the end of each time step, respectively.

- *dynamisAnalysisNewmarkNonLinear*: It performs the time domain analysis with Newton-Raphson iterations inside each time step, using the following functions

  - *rigidBodyExternalStateStepPreprocessor*: It computes the predicted conditions (at the first iteration of the time step), depending on the predictor type that is chosen in the input.

    * If it is the case of Simo's & Vu-Quoc's scheme, where it is assumed that $\boldsymbol{\Theta}_{n+1}^{(i=0)} = 0$,
      · It computes the predicted acceleration vector $\boldsymbol{A}_{n+1}^{(i=0)}$ from eq. (4.9) as $\boldsymbol{A}_{n+1}^{(i=0)} = -\frac{1}{h\beta}\boldsymbol{\Omega}_n - \frac{1}{\beta}\left(\frac{1}{2} - \beta\right)\boldsymbol{A}_n$.
      · It computes the predicted velocity vector $\boldsymbol{\Omega}_{n+1}^{(i=0)}$ as follows: the eq. (4.8) is written w.r.t. the incremental rotation vector $\boldsymbol{\Theta}_{n+1}^{(i=0)}$, and the resulting relation is substituted inside eq. (4.6):
      $\boldsymbol{\Omega}_{n+1}^{(i=0)} = \boldsymbol{\Omega}_n + h\left[(1-\gamma)\boldsymbol{A}_n + \gamma\boldsymbol{A}_{n+1}^{(i=0)}\right]$.
    * If it is the case of Mäkinen's / Cardona's & Géradin's scheme, where it is assumed that

$$\ddot{\boldsymbol{\Theta}}_{n+1}^{(i=0)} = 0 \tag{4.28}$$

      · By solving the system of eqs. (4.28), (C.6) and (C.15), the predicted values of the incremental rotation vector and the first derivative of the rotation vector are computed as follows

$$\boldsymbol{\Theta}_{n+1}^{(i=0)} = h\dot{\boldsymbol{\Theta}}_n + h^2\left(\frac{1}{2} - \beta\right)\ddot{\boldsymbol{\Theta}}_n \tag{4.29}$$

      and

$$\dot{\boldsymbol{\Theta}}_{n+1}^{(i=0)} = \dot{\boldsymbol{\Theta}}_n + h(1-\gamma)\ddot{\boldsymbol{\Theta}}_n \tag{4.30}$$

      where, as it has been explained for the initial conditions, $\dot{\boldsymbol{\Theta}}_n = \boldsymbol{\Omega}_n$ (see also eq. (4.13)), and $\ddot{\boldsymbol{\Theta}}_n = \boldsymbol{A}_n - \frac{d}{dt}[\boldsymbol{T}_n]^T\dot{\boldsymbol{\Theta}}_n = \boldsymbol{A}_n$ (see also eq. (4.15)).
      · It computes the first derivative of the rotation vector $\dot{\boldsymbol{\Theta}}_{n+1}^{(i=0)}$ from eq. (4.30). and the predicted angular velocity vector $\boldsymbol{\Omega}_{n+1}^{(i=0)}$ from eq. (4.17) using eq. (4.30).
      · It computes the predicted angular acceleration vector $\boldsymbol{A}_{n+1}^{(i=0)}$ from eq. (4.21) using eqs. (4.28) and (4.30).
    * It computes the orientation matrix based on the predicted incremental rotation vector: $\boldsymbol{\Lambda}_{n+1}^{(i=0)} = \boldsymbol{\Lambda}_n\, exp\left(\hat{\boldsymbol{\Theta}}_{n+1}^{(i=0)}\right)$.
    * It computes the external moment in a material setting from the updated orientation (see eq. (4.5)).

  - *rigidBodyInertiaMatrix*: It computes the tangent operator and the inertia vector:

  - If it is the case of Simo's & Vu-Quoc's scheme, it computes the tangent operator using eq. (4.25) and the inertia vector using the relation $\boldsymbol{P}_{n+1}^{(i)} = \boldsymbol{J}\boldsymbol{A}_{n+1}^{(i)} + \boldsymbol{\Omega}_{n+1}^{(i)} \times \boldsymbol{J}\boldsymbol{\Omega}_{n+1}^{(i)}$.
  - If it is the case of Mäkinen's / Cardona's & Géradin's scheme, it computes the tangent operator either using the eq. (4.26) for a non consistent linearization, or using the eq. (4.27) for a consistent linearization. Moreover, it computes the inertia vector using the relation $\boldsymbol{P}_{n+1}^{(i)} = \boldsymbol{J}\boldsymbol{A}_{n+1}^{(i)} + \boldsymbol{\Omega}_{n+1}^{(i)} \times \boldsymbol{J}\boldsymbol{\Omega}_{n+1}^{(i)}$.

- *rigidBodyPostIterational*: It performs the update:
  - In case of using the rotation vector parameters, it updates the material incremental rotation vector as

$$\boldsymbol{\Theta}_{n+1}^{(i+1)} = \boldsymbol{\Theta}_{n+1}^{(i)} + \Delta\boldsymbol{\Theta} \tag{4.31}$$

    and the orientation matrix as

$$\boldsymbol{\Lambda}_{n+1}^{(i+1)} = \boldsymbol{\Lambda}_n \; exp\left(\boldsymbol{\Theta}_{n+1}^{(i+1)}\right) \tag{4.32}$$

  - In case of Simo's & Vu-Quoc's scheme, it updates the angular velocities and accelerations using eqs. (4.53) and (4.58).
  - In case of Mäkinen's / Cardona's & Géradin's scheme, it updates the angular velocities and accelerations as
    1. It updates the first derivative of the material incremental rotation vector using eq. (4.20).
    2. It updates the second derivative of the material incremental rotation vector using eq. (4.24).
    3. It computes the transpose tangential transformation using eq. (4.14) with input parameter the updated material incremental rotation vector given by eq. (4.31).
    4. It computes the time derivative of transpose tangential transformation using eq. (4.16) with input parameters the updated material incremental rotation vector given by eq. (4.31) and the updated first derivative of the material incremental rotation vector given by eq. (4.20).
    5. It updates the angular velocities using eq. (4.19) for a consistent update, while using eq. (4.18) for a non consistent update.
    6. It updates the angular accelerations using eq. (4.23) for a consistent update, while using eq. (4.22) for a non consistent update.
  - It updates the material external moment.

4.5 Example: The heavy symmetrical top (Lagrange's top)

The time integration schemes that were described previously have been applied to the well-known example of the heavy symmetrical top with one point fixed; one can find the theoretical analysis of this problem in Arnold, 1989; Goldstein, Poole, and Safko, 2000. The spatial $\boldsymbol{e}$ and material $\boldsymbol{E}$ reference axes that are used in the analysis are shown in fig. 4.3. The inertia tensor in a material setting and the applied moment constant are:

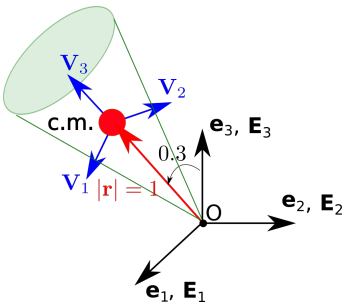

FIGURE 4.3: The heavy symmetrical top at its initial position.

$$\boldsymbol{J} = \begin{bmatrix} 5 & 0 & 0 \\ 0 & 5 & 0 \\ 0 & 0 & 1 \end{bmatrix}, \qquad mgl = 20 \tag{4.33}$$

The initial conditions (orientation and angular velocity) are:

$$\boldsymbol{\Theta}(t=0) = \begin{bmatrix} 0.3 \\ 0 \\ 0 \end{bmatrix}, \qquad \boldsymbol{\Omega}(t=0) = \begin{bmatrix} 0 \\ 0 \\ 50 \end{bmatrix} \tag{4.34}$$

In the following, the problem is solved with the Newmark parameters $\beta = 0.25$ and $\gamma = 0.5$, while the tolerance is $|\boldsymbol{R}| < 10^{-6}$ for the absolute residual norm.

4.5.1 Investigation of the Simo's & Vu-Quoc's time integration scheme

The Simo's & Vu-Quoc's time integration scheme (1988) is investigated for a long simulation time to make a conclusion regarding its stability. The problem is solved for 150 sec; this time corresponds to 60 revolutions about the origin. The following figures show the nutation angle response in the last 5 sec. The time step is gradually increased in relation with the time step that gives the exact solution, i.e. 0.001 sec. In fig. 4.4a, the *blue line* corresponds to a time step that is 10 times larger compared to the one which gives the reference solution (*red line*). As the time step increases, the periodicity of the nutation angle w.r.t. time seems to retain a good shape except from a) the peak of the oscillation that is getting smaller, and b) the shift that is observed in the period. In figs. 4.4b and 4.4c, the same are valid for a time step that is 20 times or even 40 times larger than the reference one, where the peak value of the oscillation is getting even smaller. Finally, in fig. 4.4d the time step is enlarged to 0.1 sec; still, a periodicity is retained. The code has been run for a time step until 5 sec, and the conclusion is that the scheme does not blow up; it keeps the diagram bounded between two constant values.

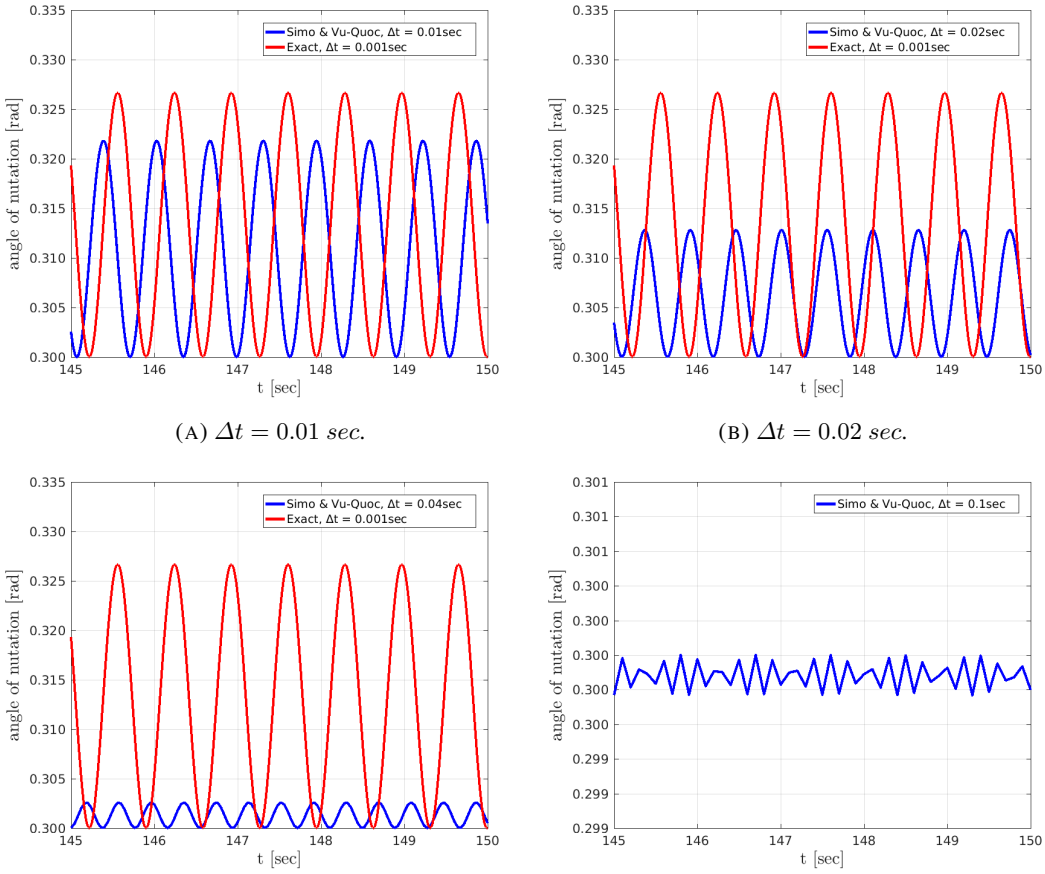

(A) $\Delta t = 0.01\ sec.$ (B) $\Delta t = 0.02\ sec.$

(C) $\Delta t = 0.04\ sec.$ (D) $\Delta t = 0.1\ sec.$

FIGURE 4.4: Simo's & Vu-Quoc's time integration scheme (1988): angle of nutation vs. time, depicted for the last 5 sec after a long simulation time t = 150 sec.

4.5.2 Investigation of the Mäkinen's / Cardona's & Géradin's time integration schemes

In this section, the approaches that are related to the research works of Mäkinen and Cardona & Géradin, are investigated. The following versions of the scheme, that correspond to the differences resulting from a consistent (or not) linearization and a consistent (or not) update are:

- non consistent linearization - non consistent update (Mäkinen's)
- non consistent linearization - consistent update (Cardona's & Géradin's)
- consistent linearization - consistent update (is added)

To make a conclusion regarding the stability of the schemes, the Lagrange's top is solved again for 150 sec. The increased time step is 0.01 sec, like previously in fig. 4.4a. Here, the picture for the whole simulation time, i.e. the 60 revolutions about the origin, is given in fig. 4.5a, where the linearization and the update are not consistent. The amplitude of the oscillation is getting larger and larger with the time. If a zoom in the last 5 sec is made, in

fig. 4.5b, a shift in the period is observed (the maximum of the exact solution happens at the time where the minimum of the solution with $\Delta t = 0.01$ sec happens, and vice versa), which is a behaviour that was also observed in the Simo's & Vu-Quoc's algorithm, in figs. 4.4a to 4.4c. In figs. 4.5c and 4.5d, where the linearization is not consistent but the update is

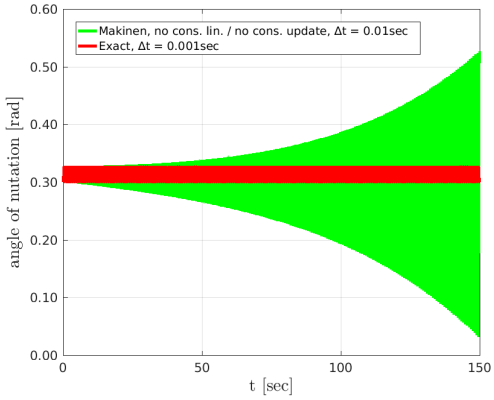

(A) $\Delta t = 0.01$ *sec.*

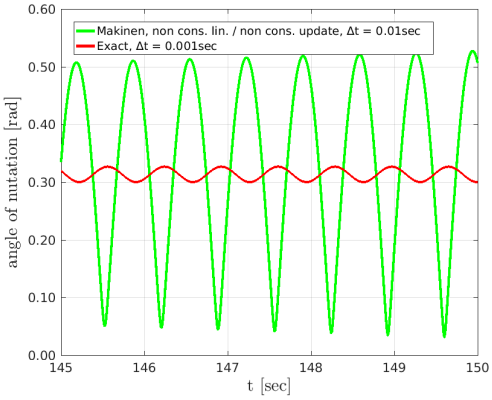

(B) Zoom in the last 5 *sec*: $\Delta t = 0.01$ *sec.*

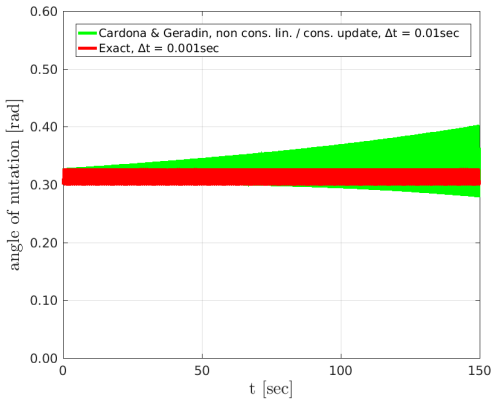

(C) $\Delta t = 0.01$ *sec.*

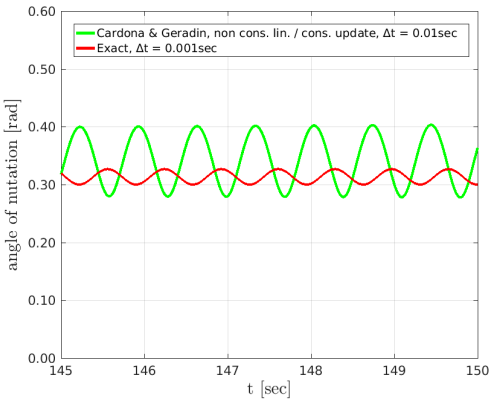

(D) Zoom in the last 5 *sec*: $\Delta t = 0.01$ *sec.*

FIGURE 4.5: Mäkinen's (2001) / Cardona's & Géradin's scheme, non consistent linearization / non consistent and consistent update: angle of nutation vs. time for a long simulation time $t = 150$ *sec.*

consistent, the same "shape" - behaviour to the previous case is observed; the crucial difference is that the "blown up" issue is smaller than previously; the final extreme values of the *green line* are about 0.4 and 0.28, whereas in the previous case the corresponding values were about 0.5 and 0.05, respectively. In figs. 4.6a and 4.6b, where the linearization and the update are consistent, exactly the same behaviour to the previous case (figs. 4.5c and 4.5d) is observed. This is expected, because, even if the tangent operator has not been derived by an exact linearization, the values of the results are not affected, once convergence is achieved.

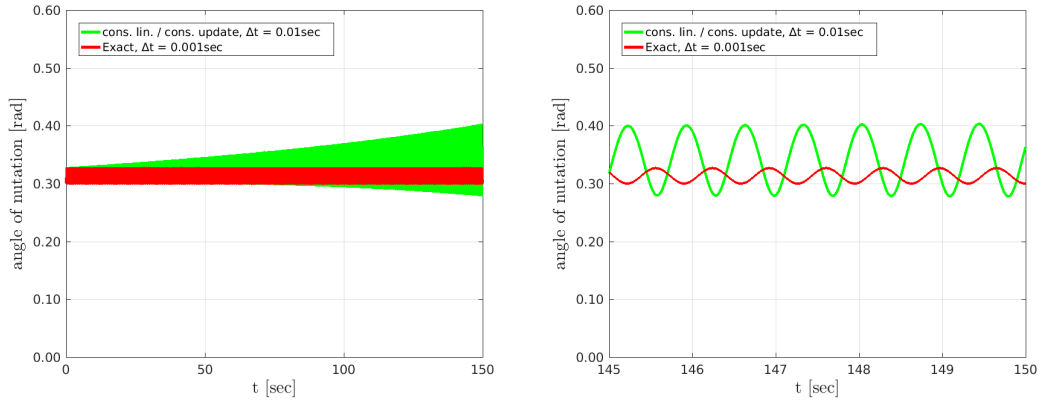

(A) $\Delta t = 0.01$ *sec.* (B) Zoom in the last 5 *sec*: $\Delta t = 0.01$ *sec.*

FIGURE 4.6: Consistent linearization / consistent update following the concept from Mäkinen's (2001) / Cardona's & Géradin's scheme: angle of nutation vs. time for a long simulation time $t = 150$ *sec.*

4.5.3 Comparison between the Simo's & Vu-Quoc's and Makinen's / Cardona's & Géradin's schemes

The algorithms from Simo & Vu-Quoc (1988) and Mäkinen (2001) / Cardona & Géradin (1988) are compared. In the following figs. 4.7a and 4.7b, the nutation and the precession angles are depicted, for the first 1.5 sec which correspond about to the $1/10^{th}$ of one revolution about the origin (0.6 rad = 34.4 degrees angle of precession). The time step is 0.005 sec, 5

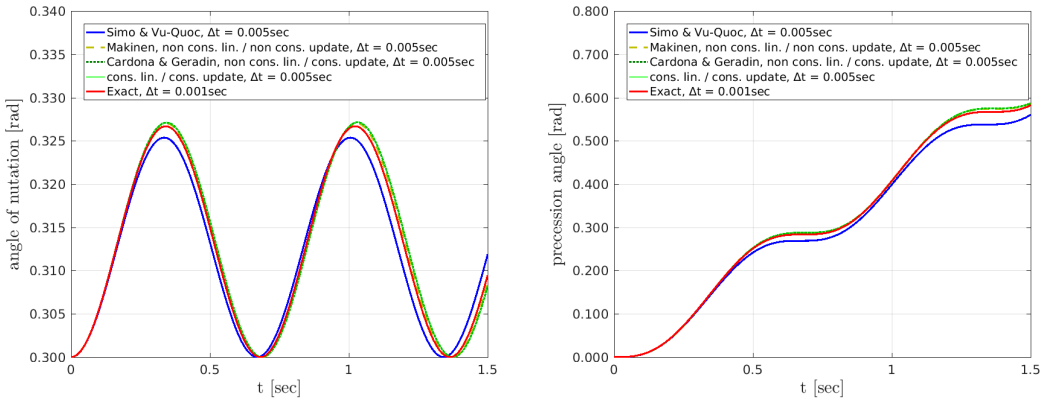

(A) Angle of nutation vs. time. (B) Precession angle vs. time.

FIGURE 4.7: Comparison between the time integration schemes for a short simulation time $t = 1.5$ *sec*, time step: $\Delta t = 0.005$ *sec.*

times larger than the reference time step (*red line*), that is 0.001 sec. In fig. 4.7a, the nutation angle is shown. The start time instant corresponds to the initial nutation of 0.3 rad = 17.2 degrees. The upper bound of the nutation angle is about 0.3275 rad = 18.76 degrees. The period of the oscillation (where the object completes one circle of nutation) is about 0.7 sec. It is observed that the Mäkinen's / Cardona's & Géradin's scheme (*all types of green line*) gives a result that is more close to the exact solution than the Simo's & Vu-Quoc's scheme (*blue line*). In fig. 4.7b, the precession angle is shown. It is shown that the same pattern of

the precession angle is repeated every 0.7 sec which is the period of the nutation oscillation. Again, the Mäkinen's / Cardona's & Géradin's scheme (*all types of green line*) gives a more accurate result than the Simo's & Vu-Quoc's scheme (*blue line*). In the following figures, a

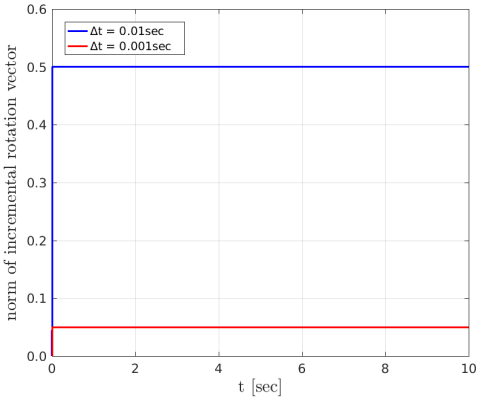

(A) Incremental rotation vector vs. time.

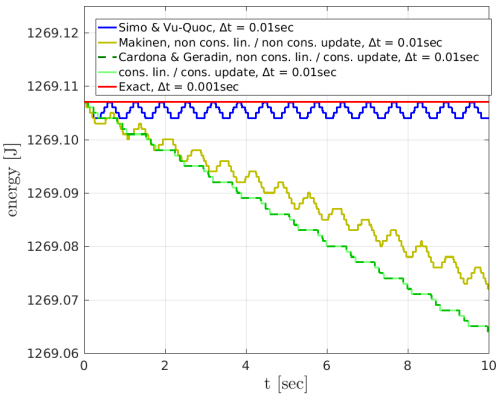

(B) Mechanical energy vs. time.

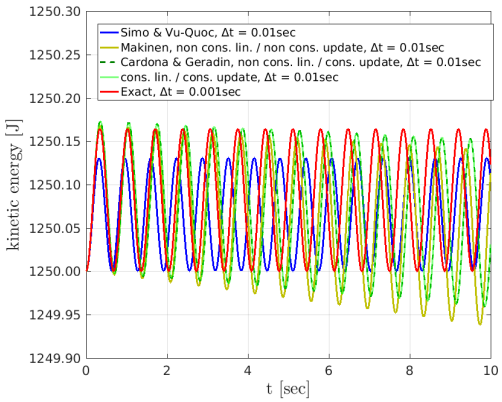

(C) Kinetic energy vs. time.

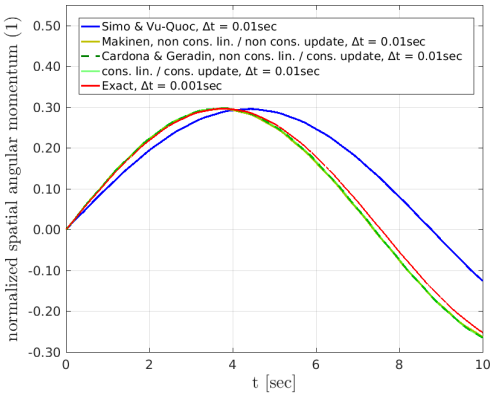

(D) Normalized spatial angular momentum term along $\boldsymbol{e}_1$ vs. time.

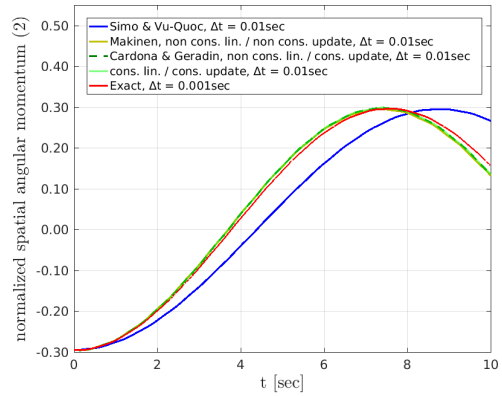

(E) Normalized spatial angular momentum term along $\boldsymbol{e}_2$ vs. time.

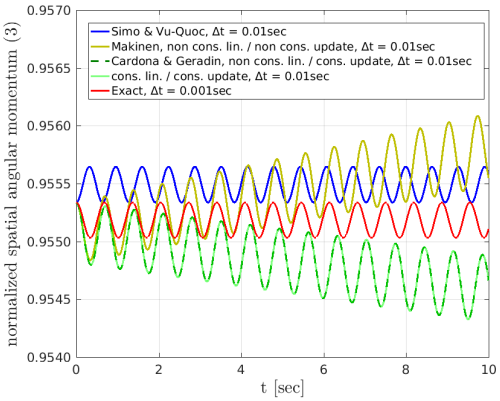

(F) Normalized spatial angular momentum term along $\boldsymbol{e}_3$ vs. time.

FIGURE 4.8: Comparison between the time integration schemes for a simulation time $t = 10\ sec$, $\Delta t = 0.01\ sec$.

comparison is given between the 2 algorithms regarding their conservation properties. The simulation time is 10 sec that corresponds to something less than one revolution about the

origin, while the time step is 0.01 sec. In this case the incremental rotation vector is about 28.6 degrees per time step, as it is depicted in fig. 4.8a. In fig. 4.8b, the mechanical energy is shown. It is observed that the upper bound of the Simo's & Vu-Quoc's scheme is identical to the exact solution, while the Mäkinen's / Cardona's & Géradin's scheme gives a result towards a downward trend of the energy. In fig. 4.8c, the kinetic energy is shown. Again, the Mäkinen's / Cardona's & Géradin's scheme gives a result towards a downward trend of the kinetic energy. Specifically, this oscillation is in front of the exact one, while in Simo's & Vu-Quoc's algorithm the oscillation remains behind of the exact one. In figs. 4.8d to 4.8f, the components of the spatial angular momentum, normalized w.r.t. its Euclidean norm, are depicted. It is observed that the Mäkinen's / Cardona's & Géradin's scheme follows the same pattern to the nutation angle; it is more accurate compared to Simo's and Vu-Quoc's scheme for a short simulation time, but it follows either an upward or a downward path during a long simulation time.

4.6 Concluding remarks

The time integration schemes for rotational rigid-body dynamics that have been studied are:

a) Simo's & Vu-Quoc's (1988), and

b) 3 versions of Mäkinen's / Cardona's & Géradin's algorithms,

- Mäkinen's (non consistent linearization and update) (2001),
- Cardona's & Géradin's (non consistent linearization yet consistent update) (1988), and
- the consistent linearization and update is added.

These algorithms are considered as Newmark-type algorithms. The difference between them, which is the motivation of their comparison in this work, is that the Newmark scheme is applied on the angular velocities and accelerations in a), while this scheme is applied on the first and second derivatives of the rotation vector in b). In the following, the conclusions that came up from the numerical results of the heavy symmetrical top are summarized.
For a short simulation time:

* The versions of the non consistent and consistent update of Mäkinen's / Cardona's & Géradin's scheme give a more accurate result in large time step than the Simo's & Vu-Quoc's algorithm.
* The Mäkinen's / Cardona's & Géradin's algorithm presents a small shift in the period that results the solution to be ahead of the exact one, whereas Simo's & Vu-Quoc's algorithm gives a periodicity in oscillation that remains behind of the exact solution.

For a long simulation time:

* The Simo's & Vu-Quoc's scheme seems to be more stable than the 3 versions of Mäkinen's / Cardona's & Géradin's algorithm.

* The Cardona's & Géradin's scheme with the consistent update (either with a consistent linearization or with a non consistent linearization) has a better behaviour regarding the 'blown-up' issue than the Mäkinen's scheme with the non consistent update.

* The 3 versions of Mäkinen's / Cardona's & Géradin's scheme have important deficiencies regarding the conservation properties.

4.7 Dynamics of beams

Following the Simo's & Vu-Quoc's time integration scheme that was presented in the previous section, the dynamics of beams is examined for the geometrically exact SR beam model. According to the kinematic assumptions (the deformation map is given in chapter 3), the cross-section of the beam follows a rigid motion. For this motion, the velocity field is given by

$$\dot{\boldsymbol{r}}(\xi, \boldsymbol{X}; t) = \dot{\boldsymbol{r}}_0(\xi; t) + \dot{\boldsymbol{\Lambda}}(\xi; t)\, \boldsymbol{X} \tag{4.35}$$

where $\dot{\boldsymbol{r}}_0(\xi; t) = \dot{\boldsymbol{u}}(\xi; t)$ is the translational velocity of the reference centre, and $\boldsymbol{X} = \begin{Bmatrix} 0 & \eta & \zeta \end{Bmatrix}^T$ are the material coordinates of an arbitrary material point. The time derivative of the rotation matrix $\dot{\boldsymbol{\Lambda}}(\xi; t)$ can be given w.r.t. either the material $\boldsymbol{\Omega}$ or the spatial $\boldsymbol{\omega}$ angular velocity vector.

$$\dot{\boldsymbol{\Lambda}}(\xi; t) = \boldsymbol{\Lambda}\hat{\boldsymbol{\Omega}} = \hat{\boldsymbol{\omega}}\boldsymbol{\Lambda} \tag{4.36}$$

The second time derivative of the rotation matrix in its material and spatial setting is also given (it will be used in the equations of motion).

$$\ddot{\boldsymbol{\Lambda}}(\xi; t) = \dot{\boldsymbol{\Lambda}}\hat{\boldsymbol{\Omega}} + \boldsymbol{\Lambda}\dot{\hat{\boldsymbol{\Omega}}} = \boldsymbol{\Lambda}\hat{\boldsymbol{\Omega}}\hat{\boldsymbol{\Omega}} + \boldsymbol{\Lambda}\hat{\boldsymbol{A}} \tag{4.37}$$

$$\ddot{\boldsymbol{\Lambda}}(\xi; t) = \hat{\boldsymbol{\omega}}\dot{\boldsymbol{\Lambda}} + \dot{\hat{\boldsymbol{\omega}}}\boldsymbol{\Lambda} = \hat{\boldsymbol{\omega}}\hat{\boldsymbol{\omega}}\boldsymbol{\Lambda} + \hat{\boldsymbol{\alpha}}\boldsymbol{\Lambda} \tag{4.38}$$

4.7.1 Linear and Angular momentum vector

The total linear momentum vector, denoted by $\boldsymbol{p}(\xi, \boldsymbol{X}; t)$, is defined as

$$\boldsymbol{p}(\xi, \boldsymbol{X}; t) := \int_{{}^0A} \rho_{ref}\, \dot{\boldsymbol{r}}\, d^0\boldsymbol{A} \overset{(4.35)}{=} \int_{{}^0A} \rho_{ref} \left(\dot{\boldsymbol{r}}_0 + \dot{\boldsymbol{\Lambda}}\, \boldsymbol{X}\right) d^0\boldsymbol{A} \Leftrightarrow$$

$$\boxed{\boldsymbol{p}(\xi; t) := \underbrace{A_m\, \dot{\boldsymbol{r}}_0}_{\boldsymbol{p}_u(t,\xi)} + \underbrace{\dot{\boldsymbol{\Lambda}}\boldsymbol{S}_m}_{\boldsymbol{p}_\psi(t,\xi)}} \tag{4.39}$$

where the independent variables $\xi; t$ are omitted from the RHS, for convenience, and $\rho_{ref} : {}^0A \rightarrow \mathcal{R}$ is the density in ${}^0A$. $\boldsymbol{p}_u(\xi; t)$ is the linear momentum vector due to the linear velocity of the reference point, $\boldsymbol{p}_\psi(\xi; t)$ is the linear momentum vector due to the angular velocity of the reference point. In eq. (4.39), the following properties have been used

- $A_m(\xi) := \int_{{}^0\boldsymbol{A}} \rho_{ref}\, d^0\boldsymbol{A}$ is a scalar defined as the mass distribution along the beam.

- $\boldsymbol{S}_m(\xi) := \int_{{}^0\boldsymbol{A}} \rho_{ref} \boldsymbol{X}\, d^0\boldsymbol{A}$ is a vector defined as the first mass moment of inertia relative to the reference axes ${}^0\boldsymbol{V}_2$ and ${}^0\boldsymbol{V}_3$ attached to the cross-section located at ξ.

The last term is not zero, $\boldsymbol{S}_m(\xi) \neq \boldsymbol{0}$, because of the choice of the reference frame so that the principal axes of inertia do not necessarily coincide to the reference axes.

Using the eqs. (3.2) and (4.35), the angular momentum vector, denoted by $\boldsymbol{l}(\xi, \boldsymbol{X}; t)$, relative to an arbitrary reference system of the cross-section, takes the following form in a spatial setting (see Simo, 1985 and Simo and Wong, 1991, where the angular momentum vector is given for rigid-bodies).

$$\boldsymbol{l}(\xi, \boldsymbol{X}; t) := \int_{{}^0\boldsymbol{A}} \rho_{ref}\ (\boldsymbol{r} - \boldsymbol{r}_0) \times \dot{\boldsymbol{r}}\, d^0\boldsymbol{A} \overset{eqs.\ (3.2) and\ (4.35)}{=} \int_{{}^0\boldsymbol{A}} \left[\rho_{ref}\ (\boldsymbol{\Lambda}\,\boldsymbol{X}) \times \left(\dot{\boldsymbol{r}}_0 + \dot{\boldsymbol{\Lambda}}\,\boldsymbol{X}\right)\right] d^0\boldsymbol{A} \tag{4.40}$$

where the independent variables $\xi; t$ are omitted from the RHS, for convenience.
The angular momentum vector in eq. (4.40) is further written as,

$$\boldsymbol{l}(\xi, \boldsymbol{X}; t) = \int_{{}^0\boldsymbol{A}} \left[\rho_{ref}\ (\boldsymbol{\Lambda}\boldsymbol{X} \times \dot{\boldsymbol{r}}_0) + \rho_{ref}\left(\boldsymbol{\Lambda}\boldsymbol{X} \times \dot{\boldsymbol{\Lambda}}\,\boldsymbol{X}\right)\right] d^0\boldsymbol{A} \tag{4.41}$$

The last term of eq. (4.41) expresses the total spatial angular momentum vector relative to the principal axes of inertia, $\boldsymbol{\pi}(\xi, \boldsymbol{X}; t)$, and is analyzed as

$$\boldsymbol{\pi}(\xi, \boldsymbol{X}; t) = \int_{{}^0\boldsymbol{A}} \left[\rho_{ref}\left(\boldsymbol{\Lambda}\boldsymbol{X} \times \dot{\boldsymbol{\Lambda}}\,\boldsymbol{X}\right)\right] d^0\boldsymbol{A} \overset{(4.36)}{=} \int_{{}^0\boldsymbol{A}} \left[\rho_{ref}\ (\boldsymbol{\Lambda}\boldsymbol{X}) \times \boldsymbol{\omega} \times \boldsymbol{\Lambda}\boldsymbol{X}\right] d^0\boldsymbol{A} \tag{4.42}$$

The vector triple product property, known as Lagrange's formula, is utilised, i.e.

Lagrange's formula

for the vectors $\boldsymbol{a}$, $\boldsymbol{b}$, $\boldsymbol{c}$:

$$\boldsymbol{a} \times (\boldsymbol{b} \times \boldsymbol{c}) = (\boldsymbol{a} \cdot \boldsymbol{c})\boldsymbol{b} - (\boldsymbol{a} \cdot \boldsymbol{b})\boldsymbol{c} \tag{4.43}$$

Thus, the eq. (4.42) is written as

$$\begin{aligned}
\boldsymbol{\pi}(\xi, \boldsymbol{X}; t) &= \int_{{}^0\boldsymbol{A}} \left\{\rho_{ref}\left[(\boldsymbol{\Lambda}\boldsymbol{X})^T \boldsymbol{\Lambda}\boldsymbol{X}\right]\boldsymbol{\omega} - \left[(\boldsymbol{\Lambda}\boldsymbol{X})^T\boldsymbol{\omega}\right]\boldsymbol{\Lambda}\boldsymbol{X}\right\} d^0\boldsymbol{A} \\
&= \int_{{}^0\boldsymbol{A}} \rho_{ref}\left\{\left[\left(\boldsymbol{X}^T\boldsymbol{X}\right)\boldsymbol{I}_3 - \boldsymbol{\Lambda}\left(\boldsymbol{X}\boldsymbol{X}^T\right)\boldsymbol{\Lambda}^T\right]\boldsymbol{\omega}\right\} d^0\boldsymbol{A} \\
&= \int_{{}^0\boldsymbol{A}} \rho_{ref}\left[\boldsymbol{\Lambda}\left(|\boldsymbol{X}|^2\boldsymbol{I}_3 - \boldsymbol{X}\boldsymbol{X}^T\right)\boldsymbol{\Lambda}^T\right]\boldsymbol{\omega}\, d^0\boldsymbol{A}
\end{aligned} \tag{4.44}$$

where the property $\boldsymbol{\Lambda}^T\boldsymbol{\Lambda} = \boldsymbol{I}_3$ is used, and, $\left(\boldsymbol{X}^T\boldsymbol{X}\right)\boldsymbol{I}_3 = \boldsymbol{\Lambda}\left(\boldsymbol{X}^T\boldsymbol{X}\right)\boldsymbol{I}_3\boldsymbol{\Lambda}^T$, because $\boldsymbol{X}^T\boldsymbol{X}$ is a scalar quantity; $\boldsymbol{I}_3$ is the 3×3 identity matrix.

Taking into account the definition of $\boldsymbol{S}_m(\xi)$ given previously, and

- $\boldsymbol{J}(\xi) := \int_{{}^0\boldsymbol{A}} \rho_{ref}\left[|\boldsymbol{X}|^2\boldsymbol{I}_3 - \boldsymbol{X}\boldsymbol{X}^T\right] d^0\boldsymbol{A}$ is the constant (material) 3×3 tensor of the second mass moments of inertia relative to the reference axes ${}^0\boldsymbol{V}_1$, ${}^0\boldsymbol{V}_2$ and ${}^0\boldsymbol{V}_3$

attached to the cross-section located at ξ. In componential form, the rotatory inertia is written as

$$\boldsymbol{J}(\xi) = \int_{{}^0\boldsymbol{A}} \rho_{ref} \left\{ \begin{bmatrix} \eta^2+\zeta^2 & 0 & 0 \\ 0 & \eta^2+\zeta^2 & 0 \\ 0 & 0 & \eta^2+\zeta^2 \end{bmatrix} - \begin{bmatrix} 0 & 0 & 0 \\ 0 & \eta^2 & \eta\zeta \\ 0 & \eta\zeta & \zeta^2 \end{bmatrix} \right\} d^0\boldsymbol{A}$$
$$= \int_{{}^0\boldsymbol{A}} \underline{\rho_{ref}} \begin{bmatrix} \eta^2+\zeta^2 & 0 & 0 \\ 0 & \zeta^2 & \underline{-\eta\zeta} \\ 0 & \underline{-\eta\zeta} & \eta^2 \end{bmatrix} d^0\boldsymbol{A} \tag{4.45}$$

[the integral in ${}^0\boldsymbol{A}$ of the underlined terms is zero if at least one of the two reference axes is an axis of symmetry],

eq. (4.41) is written w.r.t. the length parameter ξ and the time t as

$$\boldsymbol{l}(\xi;t) = \underbrace{(\boldsymbol{\Lambda}\boldsymbol{S}_m) \times \dot{\boldsymbol{r}}_0}_{\boldsymbol{l}_u(\xi;t)} + \underbrace{\left(\boldsymbol{\Lambda}\boldsymbol{J}\boldsymbol{\Lambda}^T\right)\boldsymbol{\omega}}_{\boldsymbol{\pi}(\xi;t)} \tag{4.46}$$

where the following terms are recognized:

- $\boldsymbol{l}_u(\xi;t) = (\boldsymbol{\Lambda}\,\boldsymbol{S}_m) \times \dot{\boldsymbol{r}}_0$ that is zero if the reference axes concide with the principal axes of inertia.
- $\boldsymbol{\pi}(\xi;t) = \left(\boldsymbol{\Lambda}\boldsymbol{J}\boldsymbol{\Lambda}^T\right)\boldsymbol{\omega} = \boldsymbol{I}_t\,\boldsymbol{\omega}$ is the total spatial angular momentum relative to the principal axes of inertia; $\boldsymbol{I}_t = \boldsymbol{\Lambda}\,\boldsymbol{J}\,\boldsymbol{\Lambda}^T$ is the time-dependent spatial inertia tensor.

After introducing the linear and angular momentum vectors, the governing differential equations of motion of a 3D beam in a *spatial* form can be given by (Simo and Vu-Quoc, 1988),

$$\frac{\vartheta}{\vartheta\xi}\boldsymbol{n} + \tilde{\boldsymbol{n}} = \dot{\boldsymbol{p}} \tag{4.47}$$
$$\frac{\vartheta}{\vartheta\xi}\boldsymbol{m} + \frac{\vartheta\boldsymbol{r}_0}{\vartheta\xi} \times \boldsymbol{n} + \tilde{\boldsymbol{m}} = \dot{\boldsymbol{l}} \tag{4.48}$$

where $\boldsymbol{n}$, $\boldsymbol{m}$ are the internal force and moment vectors, $\tilde{\boldsymbol{n}}$, $\tilde{\boldsymbol{m}}$ are the external load and torque vectors.

4.7.2 Weak form

In a spatial setting, the weak form of the inertia term of the residual is given by pre-multiplying the RHS of the eqs. (4.47) and (4.48) with the test functions $\boldsymbol{\chi}$ and $\boldsymbol{\phi}$ and integrating along

the length ξ of the beam, as follows

$$\begin{aligned} g_i(\boldsymbol{r}_0, \boldsymbol{\Lambda}, \boldsymbol{\chi}, \boldsymbol{\phi}) &= \int_0^L \left(\boldsymbol{\chi}^T \frac{d\boldsymbol{p}}{dt} + \boldsymbol{\phi}^T \frac{d\boldsymbol{l}}{dt} \right) d\xi \\ &\overset{eqs.\ (4.39) and\ (4.46)}{=} \int_0^L \left[\boldsymbol{\chi}^T \left(A_m \frac{d\boldsymbol{r}_0}{dt} + \frac{d\dot{\boldsymbol{\Lambda}}}{dt} \boldsymbol{S}_m \right) + \boldsymbol{\phi}^T \left(\frac{d[(\boldsymbol{\Lambda}\,\boldsymbol{S}_m) \times \dot{\boldsymbol{r}}_0]}{dt} + \frac{d\boldsymbol{\pi}}{dt} \right) \right] d\xi \\ &= \int_0^L \left\{ \boldsymbol{\chi}^T \left(A_m \ddot{\boldsymbol{r}}_0 + \ddot{\boldsymbol{\Lambda}} \boldsymbol{S}_m \right) + \boldsymbol{\phi}^T \left[(\dot{\boldsymbol{\Lambda}}\,\boldsymbol{S}_m) \times \dot{\boldsymbol{r}}_0 + (\boldsymbol{\Lambda}\,\boldsymbol{S}_m) \times \ddot{\boldsymbol{r}}_0 + \dot{\boldsymbol{\pi}} \right] \right\} d\xi \end{aligned} \tag{4.49}$$

where the independent variables t, ξ are omitted, for convenience, and

$$\dot{\boldsymbol{\pi}} = \boldsymbol{\Lambda} \left(\boldsymbol{J}\boldsymbol{A} + \hat{\boldsymbol{\Omega}} \boldsymbol{J} \boldsymbol{\Omega} \right) \tag{4.50}$$

4.8 Temporal discretization

Regarding the rotational part of the motion, the Newmark scheme is employed on the angular velocity and acceleration vectors; not on the first and second derivatives of the rotation vector. Regarding the translational part of the motion, the Newmark scheme is employed on the first and second derivatives of the translation vector, as it is well-known.

The linear velocity vector at t_{n+1} is

$$\dot{\boldsymbol{u}}_{0,n+1} = \frac{\gamma}{h\beta} (\boldsymbol{u}_{0,n+1} - \boldsymbol{u}_{0,n}) + \underbrace{\left(1 - \frac{\gamma}{\beta}\right) \dot{\boldsymbol{u}}_{0,n} + h \left(1 - \frac{\gamma}{2\beta}\right) \ddot{\boldsymbol{u}}_{0,n}}_{\dot{\boldsymbol{u}}'_{0,n}} \tag{4.51}$$

where β, γ are the Newmark constants (Newmark, 1959), h is the time-step $t_{n+1} - t_n$, and $\dot{\boldsymbol{u}}_{0,n}$, $\ddot{\boldsymbol{u}}_{0,n}$ are the linear velocity and acceleration vectors of the reference point at the initial time instant t_n. The angular velocity vector at t_{n+1} is given by eq. (4.6). The consistent update formula in the iterative N-R procedure is

$$\dot{\boldsymbol{u}}^{(i+1)}_{0,n+1} - \dot{\boldsymbol{u}}^{(i)}_{0,n+1} = \frac{\gamma}{h\beta} \left(\boldsymbol{u}^{(i+1)}_{0,n+1} - \boldsymbol{u}^{(i)}_{0,n+1} \right) \tag{4.52}$$

$$\boldsymbol{\Omega}^{(i+1)}_{n+1} - \boldsymbol{\Omega}^{(i)}_{n+1} = \frac{\gamma}{h\beta} \left(\boldsymbol{\Theta}^{(i+1)}_{n+1} - \boldsymbol{\Theta}^{(i)}_{n+1} \right) = \frac{\gamma}{h\beta} \boldsymbol{\Lambda}^T_n \left(\boldsymbol{\theta}^{(i+1)}_{n+1} - \boldsymbol{\theta}^{(i)}_{n+1} \right) = \frac{\gamma}{h\beta} \boldsymbol{\Lambda}^T_n \left(\boldsymbol{T}^{(i+1)}_{n+1} \right)^{-1} \delta\boldsymbol{\psi} \tag{4.53}$$

The tangential trasformation is given following the definitions that are presented in Ibrahimbegović, Frey, and Kožar, 1995

$$\boldsymbol{T} \left(\boldsymbol{\theta}^{(i+1)}_{n+1} \right) = \frac{sin\theta}{\theta} \boldsymbol{I} + \frac{1 - cos\theta}{\theta^2} \hat{\boldsymbol{\theta}} + \frac{\theta - sin\theta}{\theta^3} \boldsymbol{\theta} \otimes \boldsymbol{\theta} \tag{4.54}$$

$$\boldsymbol{T} \left(\boldsymbol{\theta}^{(i+1)}_{n+1} \right)^{-1} = \frac{\theta/2}{tan(\theta/2)} \boldsymbol{I} - \frac{1}{2} \hat{\boldsymbol{\theta}} + \frac{1}{\theta^2} \left[1 - \frac{\theta/2}{tan(\theta/2)} \right] \boldsymbol{\theta} \otimes \boldsymbol{\theta} \tag{4.55}$$

The linear acceleration vector at t_{n+1} is

$$\ddot{\boldsymbol{u}}_{0,n+1} = \frac{1}{h^2\beta}(\boldsymbol{u}_{0,n+1} - \boldsymbol{u}_{0,n}) \underbrace{- \frac{1}{h\beta}\dot{\boldsymbol{u}}_{0,n} - \frac{1}{\beta}\left(\frac{1}{2} - \beta\right)\ddot{\boldsymbol{u}}_{0,n}}_{\ddot{\boldsymbol{u}}'_{0,n}} \tag{4.56}$$

while the angular acceleration vector at t_{n+1} is given by eq. (4.8). The consistent update in the iterative N-R procedure

$$\ddot{\boldsymbol{u}}^{(i+1)}_{0,n+1} - \ddot{\boldsymbol{u}}^{(i)}_{0,n+1} = \frac{1}{h^2\beta}\left(\boldsymbol{u}^{(i+1)}_{0,n+1} - \boldsymbol{u}^{(i)}_{0,n+1}\right) \tag{4.57}$$

$$\boldsymbol{A}^{(i+1)}_{n+1} - \boldsymbol{A}^{(i)}_{n+1} = \frac{1}{h^2\beta}\left(\boldsymbol{\Theta}^{(i+1)}_{n+1} - \boldsymbol{\Theta}^{(i)}_{n+1}\right) = \frac{1}{h^2\beta}\boldsymbol{\Lambda}^T_n\left(\boldsymbol{\theta}^{(i+1)}_{n+1} - \boldsymbol{\theta}^{(i)}_{n+1}\right) = \frac{1}{h^2\beta}\boldsymbol{\Lambda}^T_n\left(\boldsymbol{T}^{(i+1)}_{n+1}\right)^{-1}\delta\boldsymbol{\psi} \tag{4.58}$$

4.9 Linearization of the inertia term of the residual

The weak form of the inertia term of the residual in eq. (4.49) at the time instant $t_{n+1,\epsilon}$ (that is the perturbed state) is given as a function of the perturbed position vector and orientation matrix, $\boldsymbol{r}_{0,n+1,\epsilon}$ and $\boldsymbol{\Lambda}_{n+1,\epsilon}$, given abbreviated as $\boldsymbol{r}_{0,\epsilon}$ and $\boldsymbol{\Lambda}_\epsilon$ respectively, and the test functions $\boldsymbol{\chi}$ and $\boldsymbol{\phi}$, as follows

$$g_{i,\epsilon}(\boldsymbol{r}_{0,\epsilon}, \boldsymbol{\Lambda}_\epsilon, \boldsymbol{\chi}, \boldsymbol{\phi}) = g_{i1,\epsilon}(\boldsymbol{r}_{0,\epsilon}, \boldsymbol{\chi}) + g_{i2,\epsilon}(\boldsymbol{r}_{0,\epsilon}, \boldsymbol{\Lambda}_\epsilon, \boldsymbol{\chi}) + g_{i3,\epsilon}(\boldsymbol{r}_{0,\epsilon}, \boldsymbol{\Lambda}_\epsilon, \boldsymbol{\phi}) + g_{i4,\epsilon}(\boldsymbol{\Lambda}_\epsilon, \boldsymbol{\phi}) \tag{4.59}$$

where

$$g_{i1,\epsilon}(\boldsymbol{r}_{0,\epsilon}, \boldsymbol{\chi}) = \int_0^L \left[\boldsymbol{\chi}^T\left(A_m\ddot{\boldsymbol{u}}_{0,\epsilon}\right)\right] d\xi \tag{4.60}$$

$$g_{i2,\epsilon}(\boldsymbol{r}_{0,\epsilon}, \boldsymbol{\Lambda}_\epsilon, \boldsymbol{\chi}) = \int_0^L \left[\boldsymbol{\chi}^T\left(\boldsymbol{\Lambda}_\epsilon\hat{\boldsymbol{\Omega}}_\epsilon\hat{\boldsymbol{\Omega}}_\epsilon\boldsymbol{S}_m + \boldsymbol{\Lambda}_\epsilon\hat{\boldsymbol{A}}_\epsilon\boldsymbol{S}_m\right)\right] d\xi \tag{4.61}$$

$$g_{i3,\epsilon}(\boldsymbol{r}_{0,\epsilon}, \boldsymbol{\Lambda}_\epsilon, \boldsymbol{\phi}) = \int_0^L \left[\boldsymbol{\phi}^T\left(\boldsymbol{\Lambda}_\epsilon\hat{\boldsymbol{\Omega}}_\epsilon\,\boldsymbol{S}_m \times \dot{\boldsymbol{u}}_{0,\epsilon} + \boldsymbol{\Lambda}_\epsilon\,\boldsymbol{S}_m \times \ddot{\boldsymbol{u}}_{0,\epsilon}\right)\right] d\xi \tag{4.62}$$

$$g_{i4,n+1,\epsilon}(\boldsymbol{\Lambda}_\epsilon, \boldsymbol{\phi}) = \int_0^L \left[\boldsymbol{\phi}^T\left(\boldsymbol{\Lambda}_\epsilon\,\boldsymbol{J}\,\boldsymbol{A}_\epsilon + \boldsymbol{\Lambda}_\epsilon\hat{\boldsymbol{\Omega}}_\epsilon\,\boldsymbol{J}\,\boldsymbol{\Omega}_\epsilon\right)\right] d\xi \tag{4.63}$$

where $\dot{\boldsymbol{r}}_0 = \dot{\boldsymbol{u}}_0$, $\ddot{\boldsymbol{r}}_0 = \ddot{\boldsymbol{u}}_0$ and $\dot{\boldsymbol{\Omega}} = \boldsymbol{A}$, and the eqs. (4.36) and (4.37) have been used. Taking into account eq. (3.8) which gives the perturbed orientation relative to the spin vector $\delta\boldsymbol{\psi}$, and, the perturbation of the incremental translation and the material angular velocity and acceleration vectors given by

$$\boldsymbol{u}_{0,\epsilon} = \boldsymbol{u}_0 + \epsilon\delta\boldsymbol{u}_0 \tag{4.64}$$

$$\boldsymbol{\Omega}_\epsilon = \boldsymbol{\Omega} + \epsilon\delta\boldsymbol{\Omega} \tag{4.65}$$

$$\boldsymbol{A}_\epsilon = \boldsymbol{A} + \epsilon\delta\boldsymbol{A} \tag{4.66}$$

the eqs. (4.60) to (4.63) are written as

$$g_{i1,\epsilon}(\boldsymbol{r}_{0,\epsilon}, \boldsymbol{\chi}) = \int_0^L \boldsymbol{\chi}^T \left[A_m \left(\ddot{\boldsymbol{u}}_0 + \epsilon\delta\ddot{\boldsymbol{u}}_0\right)\right] d\xi \tag{4.67}$$

$$\begin{aligned} g_{i2,\epsilon}(\boldsymbol{r}_{0,\epsilon}, \boldsymbol{\Lambda}_\epsilon, \boldsymbol{\chi}) = \int_0^L \boldsymbol{\chi}^T \Big[& exp(\epsilon\widehat{\delta\boldsymbol{\psi}})\, \boldsymbol{\Lambda} \left(\hat{\boldsymbol{\Omega}} + \epsilon\delta\hat{\boldsymbol{\Omega}}\right) \left(\hat{\boldsymbol{\Omega}} + \epsilon\delta\hat{\boldsymbol{\Omega}}\right) \boldsymbol{S}_m + \\ & exp(\epsilon\widehat{\delta\boldsymbol{\psi}})\, \boldsymbol{\Lambda} \left(\hat{\boldsymbol{A}} + \epsilon\delta\hat{\boldsymbol{A}}\right) \boldsymbol{S}_m \Big] \, d\xi \end{aligned} \tag{4.68}$$

$$\begin{aligned} g_{i3,\epsilon}(\boldsymbol{r}_{0,\epsilon}, \boldsymbol{\Lambda}_\epsilon, \boldsymbol{\phi}) = \int_0^L \boldsymbol{\phi}^T \Big[& exp(\epsilon\widehat{\delta\boldsymbol{\psi}})\, \boldsymbol{\Lambda} \left(\hat{\boldsymbol{\Omega}} + \epsilon\delta\hat{\boldsymbol{\Omega}}\right) \boldsymbol{S}_m \times \left(\dot{\boldsymbol{u}}_0 + \epsilon\delta\dot{\boldsymbol{u}}_0\right) + \\ & exp(\epsilon\widehat{\delta\boldsymbol{\psi}})\, \boldsymbol{\Lambda}\, \boldsymbol{S}_m \times \left(\ddot{\boldsymbol{u}}_0 + \epsilon\delta\ddot{\boldsymbol{u}}_0\right) \Big] \, d\xi \end{aligned} \tag{4.69}$$

$$\begin{aligned} g_{i4,n+1,\epsilon}(\boldsymbol{\Lambda}_\epsilon, \boldsymbol{\phi}) = \int_0^L \boldsymbol{\phi}^T \Big\{ & exp(\epsilon\widehat{\boldsymbol{\delta\psi}})\boldsymbol{\Lambda}\boldsymbol{J} \left(\boldsymbol{A} + \epsilon\delta\boldsymbol{A}\right) \\ & + exp(\epsilon\widehat{\boldsymbol{\delta\psi}})\boldsymbol{\Lambda} \left(\hat{\boldsymbol{\Omega}} + \epsilon\delta\hat{\boldsymbol{\Omega}}\right) \boldsymbol{J} \left(\boldsymbol{\Omega} + \epsilon\delta\boldsymbol{\Omega}\right) \Big\} \, d\xi \end{aligned} \tag{4.70}$$

For the linearization of the inertia term about the configuration at $n+1$, the directional derivative w.r.t. ϵ, for $\epsilon = 0$, is employed in eqs. eq. (4.67) - 4.70, taking into consideration eqs. (4.6), (4.8), (4.51) and (4.56). This procedure is given in appendix D.

4.9.1 Matrix form of the linearized inertia term

Proceeding into the formulation of the inertia matrix of the beam element, firstly, the eqs. D.1, D.3, D.5, and D.8 are collected and written in a matrix form, and secondly, the discretization for the trial and test functions is performed by introducing the shape functions in sections 3.7.1 and 3.7.2.

- The part of the inertia term that contains virtual accelerations is

$$Dg_{mi} = \int_0^L \begin{Bmatrix} \boldsymbol{\chi} \\ \boldsymbol{\phi} \end{Bmatrix}^T \frac{1}{h^2\beta} \begin{bmatrix} A_m \boldsymbol{I}_3 & -\boldsymbol{\Lambda}\hat{\boldsymbol{S}}_m \boldsymbol{\Lambda}_n^T \boldsymbol{T}^{-1}(\boldsymbol{\theta}_{n+1}) \\ (\boldsymbol{\Lambda}\boldsymbol{S}_m)\times & \boldsymbol{\Lambda}\boldsymbol{J}\boldsymbol{\Lambda}_n^T \boldsymbol{T}^{-1}(\boldsymbol{\theta}_{n+1}) \end{bmatrix} \begin{Bmatrix} \delta\boldsymbol{u}_0 \\ \delta\boldsymbol{\psi} \end{Bmatrix} d\xi \tag{4.71}$$

- The part of the inertia term that contains virtual velocities is

$$Dg_{di} = \int_0^L \begin{Bmatrix} \boldsymbol{\chi} \\ \boldsymbol{\phi} \end{Bmatrix}^T \frac{\gamma}{h\beta} \begin{bmatrix} \boldsymbol{0}_3 & \boldsymbol{\Lambda}\left(\boldsymbol{\Omega}\boldsymbol{S}_m^T - 2\,\boldsymbol{S}_m\boldsymbol{\Omega}^T + \boldsymbol{\Omega}^T\boldsymbol{S}_m\boldsymbol{I}_3\right)\boldsymbol{\Lambda}_n^T\boldsymbol{T}^{-1}(\boldsymbol{\theta}_{n+1}) \\ \left(\boldsymbol{\Lambda}\hat{\boldsymbol{\Omega}}\boldsymbol{S}_m\right)\times & \left[\boldsymbol{\Lambda}\left(\hat{\boldsymbol{\Omega}}\boldsymbol{J} - \widehat{\boldsymbol{J}\boldsymbol{\Omega}}\right) + \left(\dot{\boldsymbol{u}}_0 \times \boldsymbol{\Lambda}\hat{\boldsymbol{S}}_m\right)\right]\boldsymbol{\Lambda}_n^T\boldsymbol{T}^{-1}(\boldsymbol{\theta}_{n+1}) \end{bmatrix} \begin{Bmatrix} \delta\boldsymbol{u}_0 \\ \delta\boldsymbol{\psi} \end{Bmatrix} d\xi \tag{4.72}$$

- The part of the inertia term that contains virtual displacements is

$$Dg_{ki} = \int_0^L \begin{Bmatrix} \boldsymbol{\chi} \\ \boldsymbol{\phi} \end{Bmatrix}^T \begin{bmatrix} \boldsymbol{0}_3 & -\dot{\hat{\boldsymbol{p}}}_\psi \\ \boldsymbol{0}_3 & -\dot{\hat{\boldsymbol{\pi}}} - \dot{\hat{\boldsymbol{l}}}_u \end{bmatrix} \begin{Bmatrix} \delta\boldsymbol{u}_0 \\ \delta\boldsymbol{\psi} \end{Bmatrix} d\xi \tag{4.73}$$

4.9.2 Inertia vector and matrix

To obtain the inertia vector and matrix for the 3D beam with large rotations, the shape functions for the interpolation of the test and trial functions, the translation vector $\delta\boldsymbol{u}_0$ and the spin

vector $\delta\boldsymbol{\psi}$, are substituted into the matrix form of the linearized inertia terms in eqs. (4.71) to (4.73). For the spin vector, the interpolation can be employed either in an iterative or in an invariant way. Regarding the iterative variant, the same shape functions compared to the unknown translation vector are used, i.e. linear interpolation for the 2-noded straight beam elements. Regarding the invariant variant, the shape functions are configuration-dependent, which refer to the rotated state of the beam element (see section 3.7.2). The test functions are interpolated iteratively in both variants (see section 3.7.1).
Taking into account that the test functions are interpolated using eq. (3.67), the inertia vector $\boldsymbol{q}_m^i$, where i is the index that corresponds to the nodes I, J of the element, is given at time $t+\Delta t$ as follows (see also eqs. (4.61) to (4.63) and (D.1))

$$
{}^{t+\Delta t}\boldsymbol{q}_m^i = \int_0^L \begin{Bmatrix} H^i \left[(A_m \ddot{\boldsymbol{u}}_0) + \left(\boldsymbol{\Lambda}\hat{\boldsymbol{\Omega}}\hat{\boldsymbol{\Omega}}\boldsymbol{S}_m + \boldsymbol{\Lambda}\hat{\boldsymbol{A}}\boldsymbol{S}_m \right) \right] \\ H^i \left[\left(\boldsymbol{\Lambda}\hat{\boldsymbol{\Omega}}\,\boldsymbol{S}_m \times \dot{\boldsymbol{u}}_0 + \boldsymbol{\Lambda}\,\boldsymbol{S}_m \times \ddot{\boldsymbol{u}}_0 \right) + \left(\boldsymbol{\Lambda}\,\boldsymbol{J}\,\boldsymbol{A} + \boldsymbol{\Lambda}\hat{\boldsymbol{\Omega}}\,\boldsymbol{J}\,\boldsymbol{\Omega} \right) \right] \end{Bmatrix} d\xi
\tag{4.74}
$$

The inertia matrix is given as follows, taking into account that the test and trial functions are approximated according to eq. (3.67) and eqs. (3.68) and (3.69), respectively. See also eqs. (D.1), (D.3), (D.5) and (D.8).

$$
\boldsymbol{M}^{ij} = \int_0^L \begin{bmatrix} \boldsymbol{H}^i \left(A_m \frac{1}{h^2\beta}\,\boldsymbol{I} \right) \boldsymbol{H}^j & \dots \\ \boldsymbol{H}^i \left[\frac{\gamma}{h\beta} \left(\boldsymbol{\Lambda}\hat{\boldsymbol{\Omega}}\boldsymbol{S}_m \right) + \frac{1}{h^2\beta} \left(\boldsymbol{\Lambda}\boldsymbol{S}_m \right) \right] \times \boldsymbol{H}^j & \dots \end{bmatrix} d\xi
$$

$$
\boldsymbol{M}^{ij} = \int_0^L \begin{bmatrix} \dots & \boldsymbol{H}^i \left\{ -\dot{\hat{\boldsymbol{p}}}_\psi + \boldsymbol{\Lambda} \left[-\frac{1}{h^2\beta}\hat{\boldsymbol{S}}_m + \frac{\gamma}{h\beta} \left(\boldsymbol{\Omega}\boldsymbol{S}_m^T - 2\,\boldsymbol{S}_m\boldsymbol{\Omega}^T + \boldsymbol{\Omega}^T\boldsymbol{S}_m\boldsymbol{I}_3 \right) \right] \boldsymbol{\Lambda}_n^T\boldsymbol{T}^{-1}(\boldsymbol{\theta}_{n+1}) + \right\} \tilde{\boldsymbol{H}}^j \\ \dots & \boldsymbol{H}^i \left[\frac{\gamma}{h\beta} \left(\dot{\boldsymbol{u}}_0 \times \boldsymbol{\Lambda}\hat{\boldsymbol{S}}_m \right) \boldsymbol{\Lambda}_n^T\boldsymbol{T}^{-1}(\boldsymbol{\theta}_{n+1}) - \dot{\hat{\boldsymbol{l}}}_u \right] \tilde{\boldsymbol{H}}^j \\ & + \boldsymbol{H}^i \left\{ -\dot{\hat{\boldsymbol{\pi}}} + \boldsymbol{\Lambda} \left[\frac{\gamma}{h\beta} \left(\hat{\boldsymbol{\Omega}}\boldsymbol{J} - \widehat{\boldsymbol{J}\boldsymbol{\Omega}} \right) + \frac{1}{h^2\beta}\boldsymbol{J} \right] \boldsymbol{\Lambda}_n^T\boldsymbol{T}^{-1}(\boldsymbol{\theta}_{n+1}) \right\} \tilde{\boldsymbol{H}}^j \end{bmatrix} d\xi
\tag{4.75}
$$

Remark (private communication with Gordan Jelenić): It has to be stressed that no interpolation is applied to angular velocities and accelerations in the above (see e.g. Jelenić and Crisfield, 1999). In much of the research published, going back to Simo and Vu-Quoc, 1988, an interpolation is applied to these quantities, but, this is in contradiction to any interpolation of rotations and is thus bound to adversely affect Newton-Raphson convergence process. What needs to be done, is the consistent interpolation (invariant or not) of rotations only, which then uniquely defines the incremental rotation. Once this is computed at the dynamic integration points, the angular velocities and accelerations are updated using eqs. (4.53) and (4.58).

4.10 Benchmark examples

In the following examples, a verification of the implementation of the inertia terms in 2D and 3D SR beam element is employed, by comparing the results to reference ones from bibliography. For the comparison, the reference curves are digitized to give the points of the plots. This step is essential in order to check the code before simulating the dynamics of

the wind turbine system. Having as motivation the modeling of the wind turbine blades, the selected examples, all presented in Simo and Vu-Quoc, 1988, are: 1) a spin-up maneuver of a flexible beam that is imposed to an external displacement varying in time, 2) an elbow cantilever subjected to a triangular load at the elbow, and 3) the Bathe's & Bolourchi's cantilever beam subjected to a follower load at the tip. The last two examples are imposed to an external loading varying in time. The wind turbine blades, presented in the following chapter, in correlation with these examples, are subjected to the rotational motion imposed by the shaft and the vibration induced by the aerodynamic loading (i.e. a displacement and a loading varying in time, respectively). Regarding the solution procedure, the Simo's & Vu-Quoc's time integration method that was described previously is used, while the absolute norm of the residual and displacement vectors are both used for the convergence of the full Newton-Raphson scheme.

4.10.1 Spin-up maneuver of a flexible beam

This example is chosen in order to verify the inclusion of the inertia terms in 2D. The geometry and the integrated elastic and inertia properties of the cross-section are given in fig. 4.9, where a prescribed rotation at the pinned end is imposed (see fig. 4.10). The mesh consists of 8 linear SR beam elements, while 4 quadratic SR beam elements are used in the reference solution. This kind of motion of a cantilever beam is very close to the rotational motion of a blade subjected to the angular velocity of the shaft. This example was originally proposed by Kane et al. and further analyzed in Simo and Vu-Quoc, 1986b; Simo and Vu-Quoc, 1986c; Simo and Vu-Quoc, 1988.

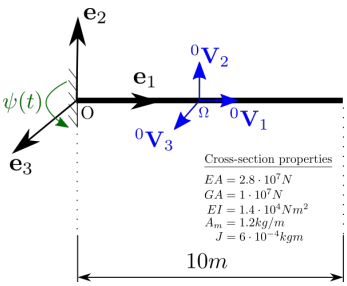

FIGURE 4.9: Spin-up maneuver of a flexible beam: Problem data.

The imposed rotation is given in eq. (4.76) for a time period $t = 30$ units of time, that is equivalent to about $\frac{135}{2\pi} = 21.5$ revolutions of the beam.

$$\psi(t) = \begin{cases} \frac{6}{15}\left[\frac{t^2}{2} + \left(\frac{15}{2\pi}\right)^2\left(cos\frac{2\pi t}{15} - 1\right)\right] rad, & 0 \le t \le 15s \\ (6t - 45) rad, & t > 15s \end{cases} \tag{4.76}$$

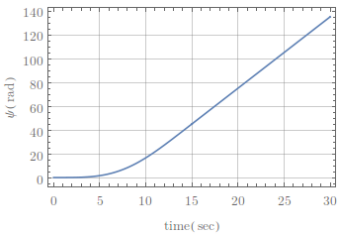

FIGURE 4.10: Spin-up maneuver of a flexible beam: Prescribed rotation $\psi(t)$ in radians.

For the solution, the time step used is $\Delta t = 0.005\, sec$, while the convergence tolerance for the norm of the absolute, residual and displacement vectors is 10^{-6}. The response is depicted in figs. 4.11 and 4.12, where the time histories of the translations and the rotation of the tip are given. To "exclude" the rigid-body rotation, these displacement components are given w.r.t. the rotating frame (or the so-called *shadow beam*). The results are very close to those reported in Simo and Vu-Quoc, 1988, depicted as *Reference* points in the plots. Initial translation and rotation components are present during the

acceleration phase ($t = 0 - 15s$), where a lag in response is shown (see the negative values of the translations in figs. 4.11a and 4.11b). After the acceleration phase, the centrifugal force straightens the beam in the constant angular velocity phase ($t > 15s$) (Simo and Vu-Quoc, 1986c). In fig. 4.11a, the extension u_{01} of the beam w.r.t. the rotating frame, in the constant angular velocity phase, is shown.

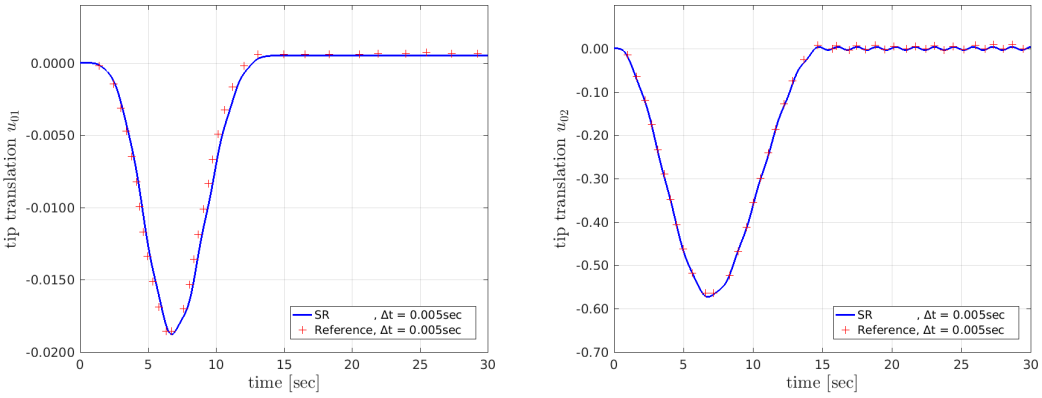

(A) (B)

FIGURE 4.11: Spin-up maneuver of a flexible beam: Tip translation components vs. time.

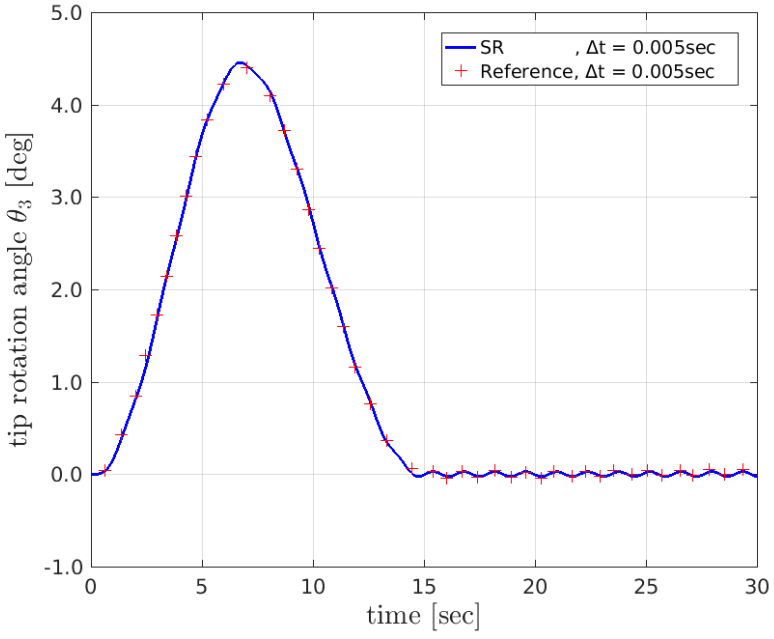

FIGURE 4.12: Spin-up maneuver of a flexible beam: Tip rotation angle vs. time.

Remark: Regarding the numerical implementation, three technical issues are given: 1) When the problem is solved as 3D, the translation along the $\boldsymbol{E}_3$ axis and the rotations about the longitudinal $\boldsymbol{E}_1$ and the $\boldsymbol{E}_2$ axes of the beam should be exactly zero. Thus, for not accounting for the gBTC (geometric Bending Torsional Coupling) effect, both the twisting stiffness and

the bending stiffness in the horizontal plane (formed by the axes $\boldsymbol{E}_1$ and $\boldsymbol{E}_3$) are given in six orders larger compared to the bending stiffness in the vertical plane (formed by the axes $\boldsymbol{E}_1$ and $\boldsymbol{E}_2$). 2) The residual force vector contains the force resulting from the difference of the imposed rotations between the two time instants at the end and the beginning of the time step, just in the first iteration of the Newton-Rapshon scheme (Jirasek, 2005). 3) The absolute convergence criterion is preferred for the small values of rotation, because it functions better than the relative one.

4.10.2 Elbow cantilever subjected to a triangular load at the elbow

This example is chosen to verify the implementation of the inertia terms in 3D. This is investigated in Simo and Vu-Quoc, 1988, and it is studied further in Jelenić and Crisfield, 1999. The geometry and material data are shown in fig. 4.13. 4 elements per leg are used. The external load has a fixed direction along the global z-axis, and it is applied at the elbow of the structure. Throughout the analysis, the time step is $\Delta t = 0.25$ and the convergence tolerance is $\delta_{f,abs} = 10^{-7}$ and $\delta_{u,abs} = 10^{-10}$, for the residual and displacement vectors, respectively. In the following graphs, the path of the tip and the elbow in $\boldsymbol{e}_3$ axis are depicted using the $SR_{inv.}$ and the $SR_{iter.}$ beam models. The points from the graph given in Jelenić and Crisfield, 1999 for the invariant formulation are also plotted for comparison. They are very close to the response given by both implementations of the SR model.

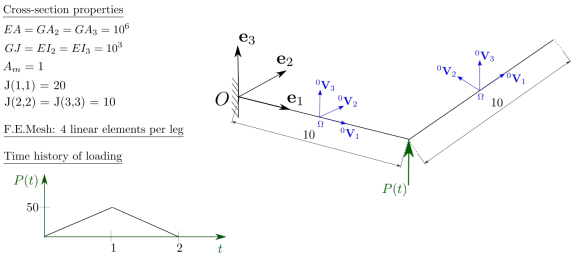

FIGURE 4.13: Elbow cantilever: problem data.

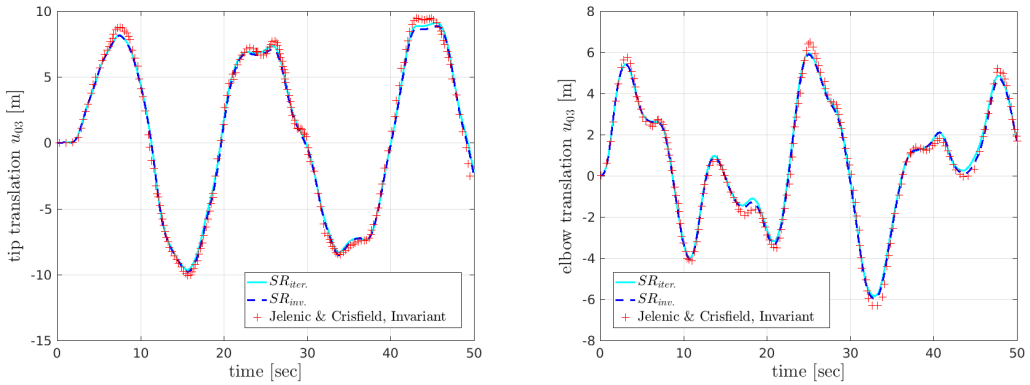

(A) (B)

FIGURE 4.14: Elbow cantilever: Tip and elbow translational components u_{03} vs. time.

Remark: As far as the numerical analysis is concerned, when the code runs for a longer simulation time (not only 50 units of time) the matrices are spoiled at the time instant 61.25 for both implementations, i.e. the inertia, the stiffness, and the effective (inertia + stiffness) matrices have some complex eigenvalues with a negative real part. Thus, the convergence

is lost. The above problem may be an indication of numerical instability of Newmark's trapezoidal rule.

4.10.3 Bathe's and Bolourchi's cantilever subjected to a follower load at the tip

This example is chosen to verify the implementation of the inertia terms in 3D. Moreover, a wind turbine blade subjected to the follower load of aerodynamics naturally comes as a next step after the study of this benchmark. Bathe's and Bolourchi's cantilever is a well-known test case in the literature as a reference example in a non-linear static analysis, to verify the geometrically exact beam modeling. Here, the same member is used for a flutter analysis as it is proposed in Simo and Vu-Quoc, 1988. The geometry and material data are shown in fig. 4.15. Note that the rotatory inertia is exaggerated on purpose, in order to take into account the inertia due to large rotations. 8 linear SR beam elements are used for the mesh. The follower load is increased at the rate of 100 units per unit of time. Throughout the analysis, the time step is $\Delta t = 0.1$ and the convergence tolerance is $\delta_{f,abs} = 10^{-7}$ and $\delta_{u,abs} = 10^{-10}$ for the residual and displacement vector, respectively. The analysis is performed following two different technical options: a) a nodal update for the angular velocities and accelerations is computed using the Newmark's formulas, and then, the interpolation of these nodal quantities is employed (Simo and Vu-Quoc, 1988), b) an interpolation of the incremental material rotation vector is employed, and then, the update for the angular velocities and accelerations is computed at the Gauss point using the Newmark's formulas (Jelenić and Crisfield, 1999). In fig. 4.16, the two different treatments of the update of the angular velocities and accelerations are used to evaluate the three translational components of the tip and the number of Newton's iterations. The results are given for the iterative interpolation. In fig. 4.16a, it is shown that both techniques give the same translations, while in fig. 4.16b, it is depicted that the accumulative number of Newton's iterations are larger in case a) compared to the case b). Thus, it is shown that the convergence process is improved when a consistency w.r.t. the configuration is followed.

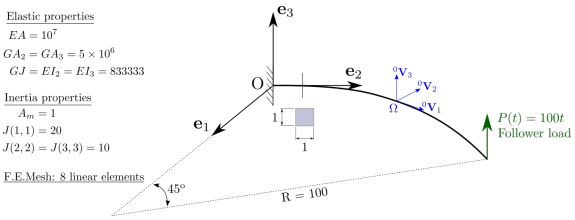

FIGURE 4.15: Bathe's and Bolourchi's cantilever under a follower load: Problem data.

Remark: For this specific case where $\Delta t = 0.1$, the stiffness matrix is not positive definite for several iterations of some time steps beyond the time instant $t = 10.6$, for both the iterative and invariant interpolations. This results to the overall spoil of the matrices, i.e. the mass matrix, and consequently, the effective matrix, at the time instant $t = 18.1$, for both interpolations (fig. 4.17). The reason for this behaviour may

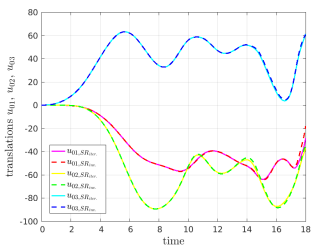

FIGURE 4.17: Bathe's and Bolourchi's cantilever under a follower load: Translations vs. time for the SR iterative and invariant formulations.

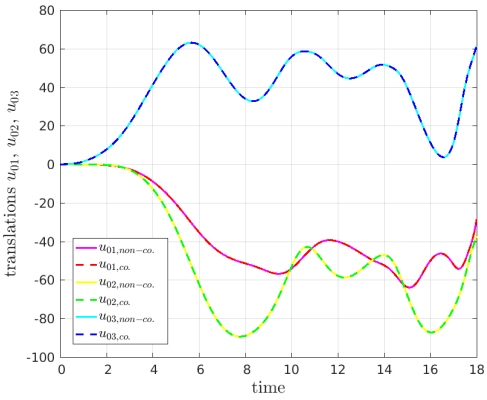

(A) Translations vs. time.

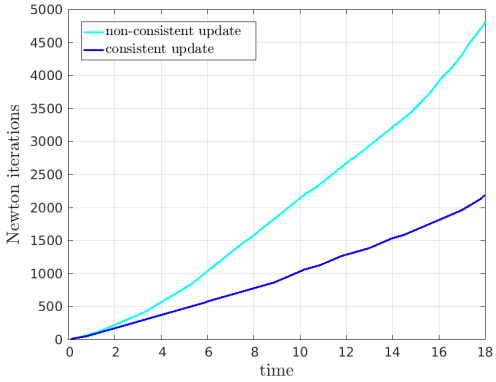

(B) Accumulative number of Newton iterations vs. time.

FIGURE 4.16: Bathe's and Bolourchi's cantilever under a follower load: (a) Translations vs. time, (b) Accumulative number of Newton iterations vs. time, for non-consistent and consistent update of the angular velocities and accelerations.

be that the Newmark trapezoidal rule is numerically unstable in the non-linear dynamics regime, like in the previous example.

Chapter 5

Dynamics of the coupled wind turbine system

5.1 Introduction

In this chapter, the objective of the work is the incorporation of the geometrically exact SR beam model into the multi-body, hydro-servo-aero-elastic code hGAST. This is a general simulation platform for analyzing the fully-coupled dynamic behaviour of the wind turbine system, which has been developed at the Fluid Section of the Mechanical Engineering School of NTUA. The analysis performed belongs to the branch of dynamic aero-elasticity, as it is clearly shown in fig. 5.1, that *studies the interactions between the inertial, elastic, and aerodynamic forces occurring while an elastic body is exposed to a fluid flow* (*Aeroelasticity*). In Riziotis and Voutsinas, 1997, the code is presented in its first version, while in Manolas, Riziotis, and Voutsinas, 2015, the improved version of the code is used to show the importance of geometric non-linearity to predict the blades' deflections and loads (especially, the twist angle should be as accurate as possible, because it affects significantly the angle of incidence in aerodynamics). Regarding the modeling capabilities, the Horizontal Axis WT and the Vertical Axis WT can be analyzed, with all the onshore and offshore support structures, and mooring lines. Regarding the analysis types, the static, the modal, and the time domain analysis can be performed. The main modules of hGAST are:

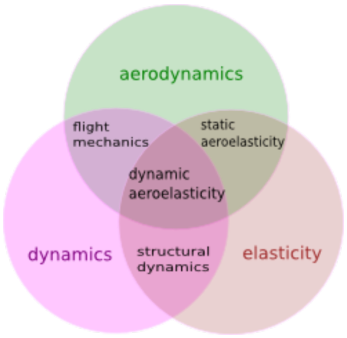

FIGURE 5.1: The branch of dynamic aero-elasticity.

- *dynamics*. A multi-body formulation is followed. This formulation is adopted from robotics, and can concern large rigid-body motions. Each body follows the deformation from the other, previous bodies. Thus, the analysis is performed at the deformed geometry, and the non-linear dynamic effects can be captured.

- *elasticity*. By incorporating the elasticity module, the whole system can be viewed as a complex, flexible mechanism. Shear deformable geometrically non-linear beam models are used. The current version of hGAST provides the capability to perform the analysis using a linear Timoshenko beam model, combined with the SB modeling

for capturing the non-linear effects. In SB modeling, the multi-body concept can be further utilized at the one body level to account for large displacements (translations and rotations). The improved version of hGAST resulting from the present work has the ability to perform the analysis using the geometrically exact, SR beam model.

- *aerodynamics*. The wind loading is evaluated using the Blade Element Momentum Theory (BEMT), or the vortex flow model, which is more sophisticated than BEMT, and mostly targeted to the analysis of complex flow conditions that lie outside the range of validity of the BEMT model (e.g., extreme shear, high yaw misalignment or partial wake (Manolas et al., 2020; Manolas, Riziotis, and Voutsinas, 2014)). The BEMT based method is exclusively used in the present work. It considers dynamic inflow effects based on cylindrical wake approximation and skewed wake induced effects due to yaw misalignment (Voutsinas, Riziotis, and Chaviaropoulos, 1997). It is also combined with the ONERA (Petot, 1989) or the Beddoes Leishman (Hansen, Gaunaa, and Madsen, 2004) dynamic stall model in order to account for local sectional unsteady aerodynamic effects and dynamic stall conditions.

The hydrodynamics part of the code (not employed in the present work since the configurations addressed concern onshore turbines) uses the methods based on linear potential theory and Morison's empirical equation. The controls refer primarily to the speed and pitch regulation, but also to load mitigation control features (Manolas et al., 2018a; Manolas et al., 2018b). A built-in generic control library or an externally provided controller is called in every time step. Such a subroutine independently solves the control equations and provides the pitch and the generator demand values. For a detailed description of the available aerodynamics, hydrodynamics and controls modeling within the hGAST solver the reader is cited to Manolas et al., 2020; Manolas, 2015.
In the following, the structural dynamics is of interest, together with its implementation into the multi-body framework.

5.2 General issues for the wind turbine blades

The wind turbine blades have a complex geometry. Information about the blades' geometry and their optimal design one could get from Burton et al., 2001. The blades constitute the main parts of a wind turbine system, that are responsible to transform the wind energy to electricity. The components of a wind turbine system are shown in fig. 5.2a; the first three are the blades that are fixed at the so-called hub (the centre of the rotor), the fourth is the shaft, while the fifth is the tower. The blade is modeled as a cantilever beam which is fixed at the hub, and free at the other end. It has a hollow cross-section at its root, while airfoils follow into the length beyond the region about the root. A typical airfoil is shown in fig. 5.2b.

To state the structural problem of the blades, the data used is summarized into the following:

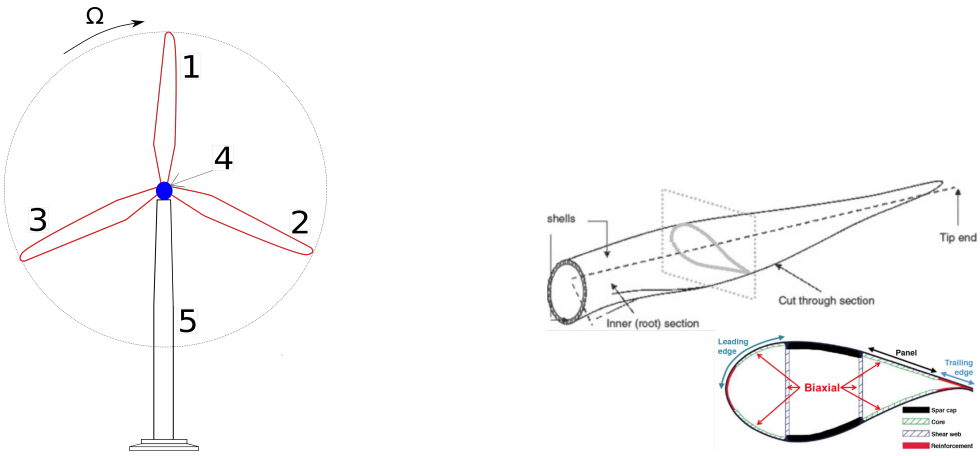

(A) Components of a wind turbine system. (B) Blade geometry and airfoil.

FIGURE 5.2: (a) The components of a wind turbine system, and (b) the geometry and cross-section of a typical blade.

- Regarding the geometry, a pre-twisted and pre-curved beam with an airfoil cross-sectional shape is given. The work presented herein refers to blades that are just pre-twisted, that is an essential property for having an optimized power output.

- Regarding the material, fibre-reinforced composite materials have gained popularity (despite their generally high cost) in high-performance products such as the blades, that need to be lightweight (*Composite material*). A pre-processor, the BECAS (**BE**am **C**ross section **A**nalysis **S**oftware) package from DTU, that computes the generalized properties of the cross-section (including geometry and material) is used, while the procedure of computing them is not the focus of this work.

- Regarding the boundary conditions, a rotational fixed end is considered, that is modeled through the multi-body formulation described in the following.

- Regarding the loading, the self weight, the wind loading, and the inertia forces are taken into consideration; the offshore hydrodynamic and the earthquake forces are out of scope of the present work. The loads are shown in a conceptual sense in fig. 5.3a for a cantilever beam, that can be the blade model. The functions g_1 and g_2 refer to the inertia terms that come from the oscillation and the rotational motion of the rotor blades, respectively. The function f refers to the gravitational loading, while the last two terms (the lift and the drag) result from the aerodynamics and act at the so-called aerodynamic centre of the cross-section. A reference that explains how to compute the wind loads according to the BEMT (that is the theory used in the present work) is Hansen, 2008. In fig. 5.3b, the velocity triangle showing the induced velocities and the lift and drag coefficients (C_L and C_D, respectively), used from the BEMT, for a cross-section of the blade are depicted. $U_\infty(1-a)$ is the axial velocity, while $\Omega r(1+a')$ is the circumferential velocity on the rotor. The axial induction factor a expresses the reduction of the wind speed as it passes through the disk, while the circumferential induction factor a' the rotational trajectory which is added to the flow

by the rotor (Manolas, 2015). α is the angle of attack between the direction of the effective velocity U_{eff} and the blade's chord. $\theta_t + \theta_p$ is the sum of the local twist angle and the blade's pitch angle.

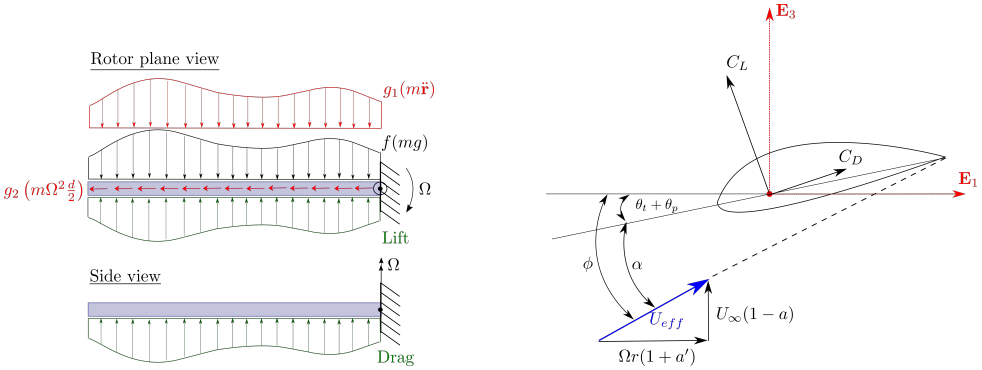

(A) Loads on the wind turbine blade.

(B) The triangle of velocities.

FIGURE 5.3: (a) Loads on the wind turbine blade, and (b) the triangle of velocities.

Regarding the response of the blades, non-linear, large translations and rotations, and small strains appear. In this case, to predict the phenomena that arise, the equilibrium is established at the deformed shape of the blades that is simply depicted in fig. 5.4a, and expressed by the position vector $\boldsymbol{r}_0$ given in relation with the parameters $\boldsymbol{u}$ and $\boldsymbol{\theta}$. Details about the geometrically exact SR beam element used to analyze the blades are given in chapter 3. The phenomena need to be predicted are tension, bending and shear in two directions, torsion, and their interactions. In fig. 5.4b, the corresponding deformation states are graphically shown for a blade (Houbolt and Brooks, 1956). The interaction of these deformation modes are

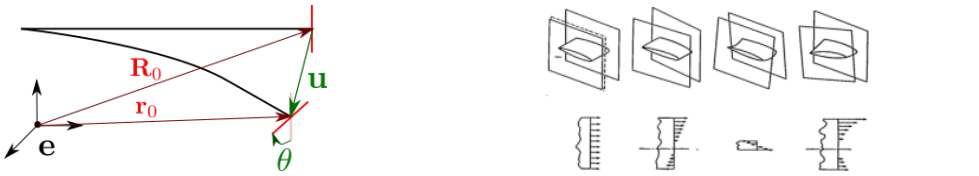

(A) Undeformed and deformed shape of the cantilever beam (that is the blade model).

(B) Deformation states need to be predicted from the analysis of the blades.

FIGURE 5.4: (a) Undeformed and deformed shape of the cantilever beam, and (b) deformation states predicted from the analysis of the blades.

explained by illustrating the blade at its deformed configuration. The bending-torsion coupling is the most important interaction in blades' dynamics because it affects significantly the angle of attack through the change in the local twist angle of the blade; this is geometrically explained in fig. 5.5. The torsion M_2 results from the analysis of the *blue*, local bending moment M_3 w.r.t. the system of the blade $\boldsymbol{E}$. Note that the SR beam element takes into account the shear deformation, an assumption that is crucial in modeling the blades that oscillate in higher modes, because of the short wavelength of deformation (Hodges, 2006). A picture of what is the meaning of the *short wavelength* is given in fig. 5.6, compared to the *long wavelength* predicted by an Euler-Bernoulli beam element.

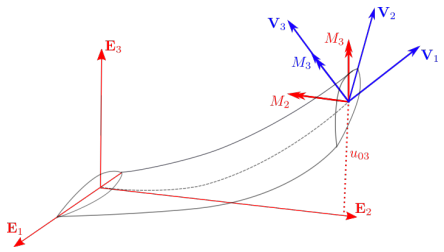

FIGURE 5.5: The bending-torsion coupling effect.

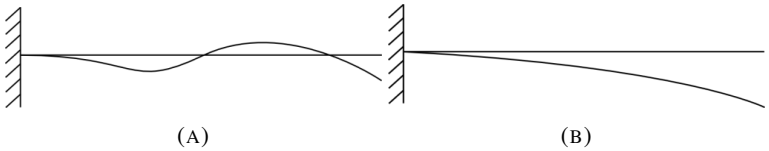

FIGURE 5.6: (a) Short wavelength of deformation predicted by a Timoshenko beam theory, and (b) long wavelength of deformation predicted by an Euler-Bernoulli beam theory.

5.3 The Reference Wind Turbine (RWT)

In this section, the Reference Wind Turbine (RWT) for which the analyses presented in the following are performed, is described. This is the DTU 10-MW RWT; its geometry and material data is taken from Bak et al., 2013, where the generalized cross-sectional, structural and inertia properties per unit length are given after computing them with BECAS. The main distances in the overall geometry of the wind turbine are shown in fig. 5.7. These are the length of the tower (115.63 m) and its cross-sectional dimensions for the top and the bottom of it, the blade length (86.366 m), the hub and the nacelle properties, including the hub elevation above the ground (119.00 m), the position of the centre of mass of the nacelle, and the length of the shaft (7.10 m). The mass of the corresponding components are 628 kg for the tower, 228 kg for the rotor (blades and hub), and 446 kg for the nacelle. The performance

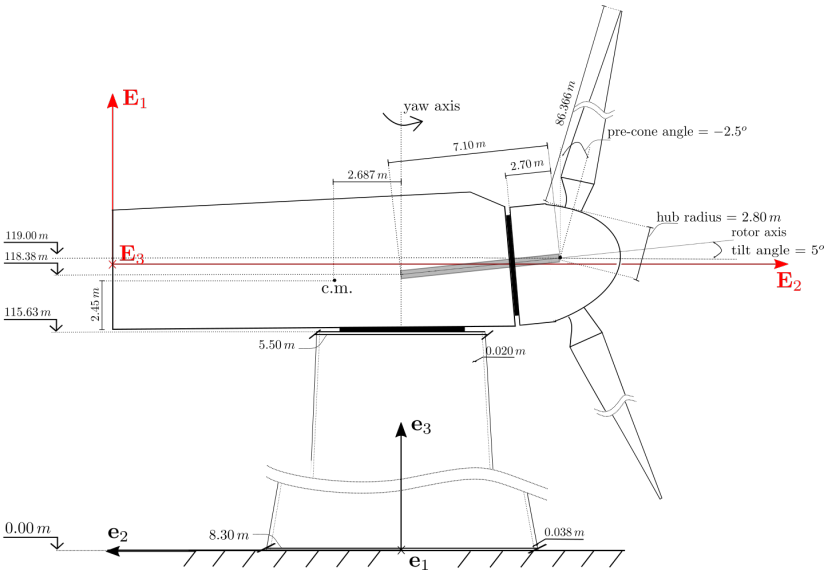

FIGURE 5.7: The main distances in the overall geometry of the DTU 10-MW RWT.

curves of mechanical power and thrust are depicted in fig. 5.8. At 11.4 m/s, the machine attains the rated power of 10 MW and the maximum thrust on the rotor. The characterization

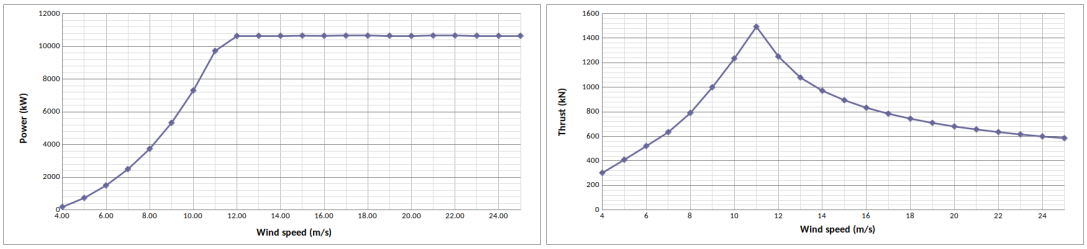

(A) The mechanical power of the rotor in relation with the wind speed.

(B) The thrust on the rotor in relation with the wind speed.

FIGURE 5.8: (a) The mechanical power, and (b) the thrust on the rotor, in relation with the wind speed.

of the modes and the corresponding frequencies of the wind turbine at standstill are given in table 5.1. The cases *free-fixed* and *free-free* mean the different boundary conditions at the

TABLE 5.1: WT standstill frequencies at 0^o pitch [Hz].

	mode	free-fixed	free-free
1	1^{st} tower bending side-side	0.249	0.257
2	1^{st} tower bending fore-aft	0.252	0.252
3	1^{st} symmetric rotor in-plane	**0.506**	**1.774**
4	1^{st} asymmetric rotor out-of-plane (yaw)	0.581	0.580
5	1^{st} asymmetric rotor out-of-plane (tilt)	0.635	0.635
6	1^{st} symmetric rotor out-of-plane	0.729	0.713
7	1^{st} asymmetric rotor in-plane (vertical)	0.925	0.925
8	1^{st} asymmetric rotor in-plane (horizontal)	0.962	0.962
9	2^{nd} asymmetric rotor out-of-plane (yaw)	1.504	1.504
10	2^{nd} asymmetric rotor out-of-plane (tilt)	1.660	1.660
11	2^{nd} symmetric rotor in-plane	**1.877**	**3.726**
12	2^{nd} symmetric rotor out-of-plane	2.143	2.073
13	2^{nd} tower bending side-side	2.394	2.301
14	2^{nd} tower bending fore-aft	2.326	2.327
15	2^{nd} asymmetric rotor in-plane (vertical)	2.612	2.608
16	2^{nd} asymmetric rotor in-plane (horizontal)	2.935	2.935
17	3^{rd} asymmetric rotor out-of-plane (yaw)	3.123	3.123
18	3^{rd} asymmetric rotor out-of-plane (tilt)	3.617	3.616

ends of the drive train. In the first case, the two ends (at both the generator and hub sides) are free to rotate, while in the second case, the generator side is fixed (the brake is enabled). It is shown that the frequencies associated to the torsion of the shaft, i.e. the 1^{st} and 2^{nd} symmetric rotor in-plane modes, are different between the two models. The shapes of the first eight modes are depicted in figs. 5.9 to 5.12.

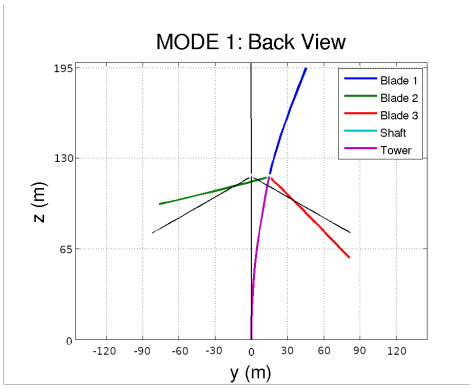

(A) 1^{st} bending mode of the tower (lateral). (B) 1^{st} bending mode of the tower (fore-aft).

FIGURE 5.9: DTU 10-MW RWT: The shapes of the first two modes.

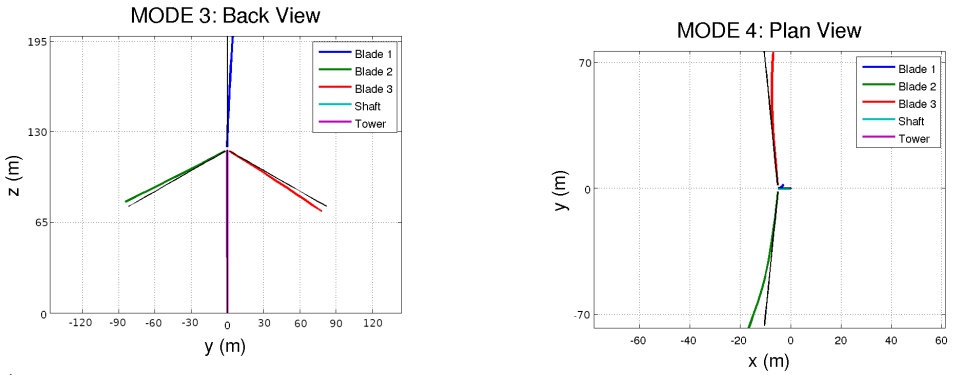

(A) 1^{st} symmetric (collective) edge-wise mode / shaft torsion. (B) 1^{st} asymmetric flap-wise mode (yaw).

FIGURE 5.10: DTU 10-MW RWT: The shapes of the third and fourth modes.

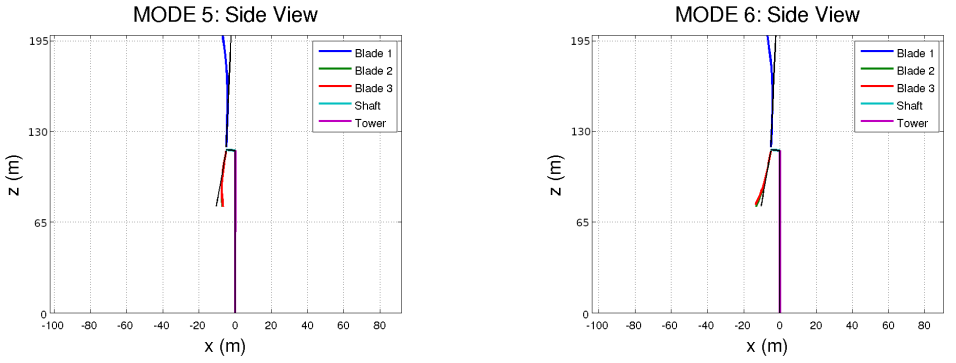

(A) 1^{st} asymmetric flap-wise mode (tilt). (B) 1^{st} symmetric (collective) flap-wise mode.

FIGURE 5.11: DTU 10-MW RWT: The shapes of the fifth and sixth modes.

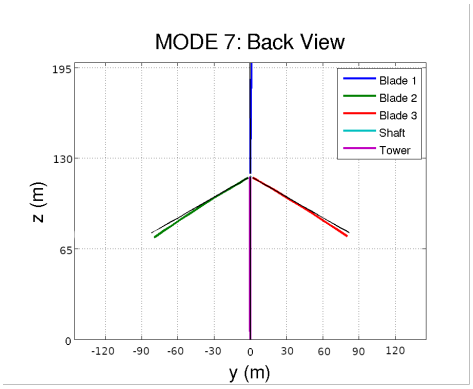

(A) 1^{st} asymmetric edge-wise mode (vertical).

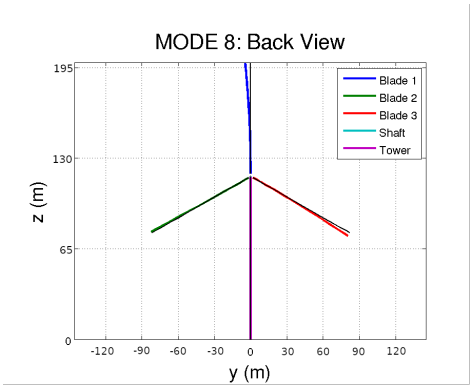

(B) 1^{st} asymmetric edge-wise mode (horizontal).

FIGURE 5.12: DTU 10-MW RWT: The shapes of the seventh and eighth modes.

5.4 Multi-body formulation

The multi-body dynamics framework applied in hGAST is based on the following concept. The fully coupled wind turbine is considered as a multi-component dynamic system having as components the blades, the drive train and the tower, all approximated as Timoshenko beam structures (fig. 5.13). Assembly of the above components into the full system is carried out in the framework of the so-call multi-body approach. It consists of considering each component separately from the others, subjected to specific free-body kinematic and loading conditions, imposed at the connection points of the components. Regarding kinematics, each body is subjected to the elastic motion of the preceding bodies as well as to prescribed or controlled rigid-body motions. For example, at the connection point between the blade and the shaft at the blade root, the elastic deformation corresponding to the motion of the shaft and the tower is imposed to the blade, which is also subjected to the pitch, azimuthal and yaw, rigid-body rotations. Regarding dynamics, each body receives the internal forces and moments of the body that is ahead of it, e.g., the tower receives the internal forces and moments from the drive-train. In the multi-body dynamics context, a material (body) frame **E** is attached to each body that follows the rigid-body rotations and translations of it (floating frame, Simo and Vu-Quoc, 1986b; Simo and Vu-Quoc, 1986c). The kinematics of each body is firstly written with respect to the spatial (inertial) frame **e**, and then, it is transformed to the material (body) frame **E**, for incorporating it into the balance equations of the body. The dynamic equations are integrated in time using the Newmark's method following a Newton-Raphson iterative procedure to get the solution of the non-linear problem.

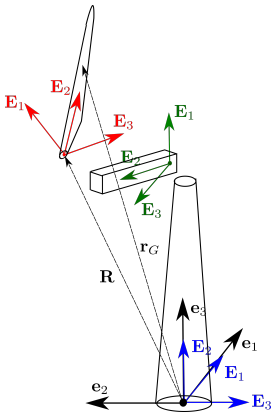

FIGURE 5.13: Wind turbine configuration.

The multi-body formulation is also extended to the component level. Highly flexible components, such as the blades are divided into a number of interconnected "sub-bodies", considered as an assembly of linear beam elements. Large translations and rotations gradually build up, whereas non-linear dynamics are introduced by imposing to each sub-body the translations and rotations of preceding sub-bodies as rigid-body, non-linear motions. This approach allows capturing the geometrically non-linear effects due to large deflections using linear beam theory at the element level, but considering non-linear effects at the sub-body level (Manolas, Riziotis, and Voutsinas, 2015). In fig. 5.14, the position vector with respect to the inertial frame **e** of an arbitrary material particle on a cross-section of the elements along the ν^{th} sub-body of the k^{th} body is given by

$$\boldsymbol{r}^{\nu}_{G,k} = \boldsymbol{R}_k(\boldsymbol{q}_k;t) + \boldsymbol{A}_k(\boldsymbol{q}_k;t)\ [\boldsymbol{R}^{\nu}_k(\boldsymbol{q}^{\nu}_k;t) + \boldsymbol{A}^{\nu}_k(\boldsymbol{q}^{\nu}_k;t)\,\boldsymbol{r}^{\nu}_k] \tag{5.1}$$

where $\boldsymbol{R}_k(\boldsymbol{q}_k;t)$ and $\boldsymbol{A}_k(\boldsymbol{q}_k;t)$ are the position vector and the orientation matrix of the k^{th} body, given in **e** frame with respect to time t. The vector $\boldsymbol{q}_k$ denotes the set of the multi-body kinematic degrees of freedom containing elementary translations and rotations that define the kinematics of the body frame due to the elastic and rigid-body motions of the preceding

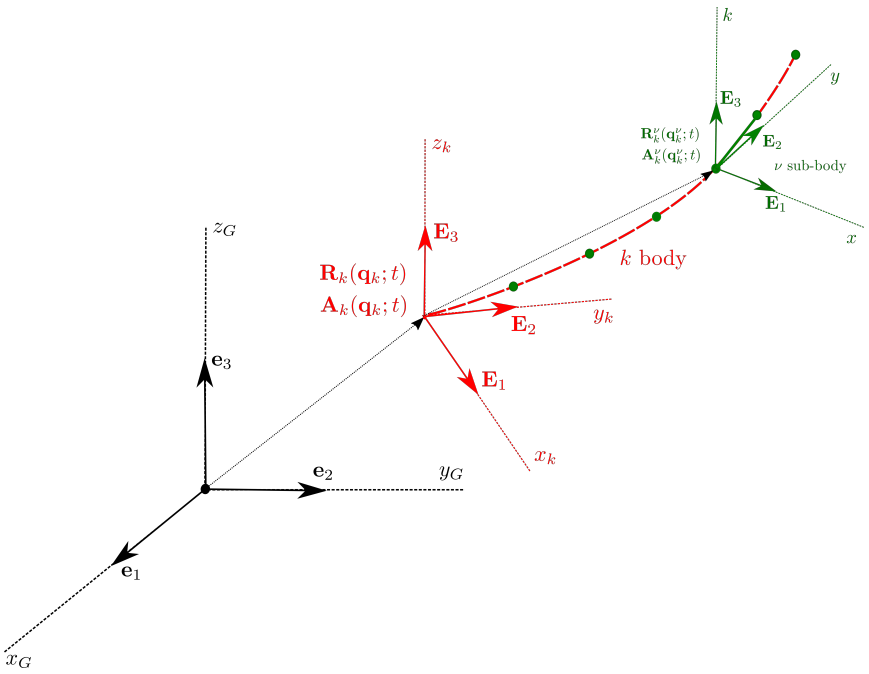

FIGURE 5.14: The kinematics for the SB modeling.

bodies. Similarly, $\boldsymbol{R}_k^\nu(\boldsymbol{q}_k^\nu;t)$ and $\boldsymbol{A}_k^\nu(\boldsymbol{q}_k^\nu;t)$ are the position vector and the orientation matrix of the ν^{th} sub-body, given in $\mathbf{E}$ frame of the k^{th} body (red frame in fig. 5.14) with respect to time t and $\boldsymbol{q}_k^\nu$ is the corresponding vector with the kinematic degrees of freedom that expresses the motion of the preceding sub-bodies of the k^{th} body. $\boldsymbol{r}_k^\nu$ is the position vector of the beam reference point that is defined according to the linear Timoshenko beam theory with respect to the frame $\mathbf{E}$ assigned to the ν^{th} sub-body (green frame in fig. 5.14). For a detailed description of the linear Timoshenko beam and the SB modeling with fully populated stiffness matrix the reader is cited to Manolas et al., 2020.

5.5 Geometrically exact non-linear beam formulation

5.5.1 Extension of the SR beam model to anisotropic beams

In this section, the SR beam model is enriched with the terms resulting from a fully-populated constitutive matrix of the cross-section. The element presented in the following is suitable to model general cross-sections where the reference point is not necessarily identical to the centroid, and also, the reference axes are not necessarily identical to the principal axes of area. This extension is necessary for simulating highly flexible wind turbine blades with anisotropic composite material couplings undergoing large deformation.

Constitutive equations

The material is assumed inhomogeneous, anisotropic and linear elastic, while the cross-section can have a general shape. Under these assumptions, the material axial/shear internal force and twist/bending internal moment vectors, $\boldsymbol{F}(\xi)$ and $\boldsymbol{M}(\xi)$, are given by a linear

relation between the stress and stress-couple resultants and the strain measures as

$$\begin{aligned} \boldsymbol{F}(\xi) &= \boldsymbol{C}^{F\Gamma}\,\boldsymbol{\Gamma} + \underline{\boldsymbol{C}^{FK}\,\boldsymbol{K}} \\ \boldsymbol{M}(\xi) &= \underline{\boldsymbol{C}^{M\Gamma}\,\boldsymbol{\Gamma}} + \boldsymbol{C}^{MK}\,\boldsymbol{K} \end{aligned} \tag{5.2}$$

where the matrices $\boldsymbol{C}^{F\Gamma}$, $\boldsymbol{C}^{FK}$, $\boldsymbol{C}^{M\Gamma}$ and $\boldsymbol{C}^{MK}$ constitute the sub-matrices of the following fully-populated constitutive matrix

$$\boldsymbol{C} = \begin{bmatrix} \boldsymbol{C}^{F\Gamma} & \boldsymbol{C}^{FK} \\ \boldsymbol{C}^{M\Gamma} & \boldsymbol{C}^{MK} \end{bmatrix} \tag{5.3}$$

The underlined terms are added to the original formulation, together with the non-diagonal terms from the sub-matrices $\boldsymbol{C}^{F\Gamma}$ and $\boldsymbol{C}^{MK}$.
The constitutive matrix $\boldsymbol{C}$ is constant, thus, the infinitesimal change of eq. (5.2) is

$$\begin{aligned} d\boldsymbol{F}(\xi) &= \boldsymbol{C}^{F\Gamma}\,d\boldsymbol{\Gamma} + \underline{\boldsymbol{C}^{FK}\,d\boldsymbol{K}} \\ d\boldsymbol{M}(\xi) &= \underline{\boldsymbol{C}^{M\Gamma}\,d\boldsymbol{\Gamma}} + \boldsymbol{C}^{MK}\,d\boldsymbol{K} \end{aligned} \tag{5.4}$$

Weak form of the elastic term

The elastic part of the weak form of the equations of motion is

$$G_k = \int_{0_L} \left(\boldsymbol{\chi}'^T\,\boldsymbol{\Lambda}\boldsymbol{F} - \boldsymbol{\phi}^T\,\hat{\boldsymbol{r}}_0'\boldsymbol{\Lambda}\boldsymbol{F} + \boldsymbol{\phi}'^T\,\boldsymbol{\Lambda}\boldsymbol{M}\right)\,d\xi \tag{5.5}$$

where the test functions, $\boldsymbol{\chi}$, $\boldsymbol{\phi}$ are given in section 3.7.1, while $\boldsymbol{\Lambda}\boldsymbol{F}$, $\boldsymbol{\Lambda}\boldsymbol{M}$ is the spatial setting of the internal force and moment vectors given in eq. (5.2). By taking the infinitesimal change of each unknown of eq. (5.5), results in the following relation

$$\begin{aligned} dG_k = \int_{0_L} (&\boldsymbol{\chi}'^T\,d\boldsymbol{\Lambda}\,\boldsymbol{F} + \boldsymbol{\chi}'^T\,\boldsymbol{\Lambda}\,d\boldsymbol{F} \\ &-\boldsymbol{\phi}^T\,d\hat{\boldsymbol{r}}_0'\,\boldsymbol{\Lambda}\,\boldsymbol{F} - \boldsymbol{\phi}^T\,\hat{\boldsymbol{r}}_0'\,d\boldsymbol{\Lambda}\,\boldsymbol{F} - \boldsymbol{\phi}^T\,\hat{\boldsymbol{r}}_0'\,\boldsymbol{\Lambda}\,d\boldsymbol{F} \\ &+\boldsymbol{\phi}'^T\,d\boldsymbol{\Lambda}\,\boldsymbol{M} + \boldsymbol{\phi}'^T\,\boldsymbol{\Lambda}\,d\boldsymbol{M})\,d\xi \end{aligned} \tag{5.6}$$

where $d\boldsymbol{r}_0$ and $d\boldsymbol{\Lambda}$ are derived after employing the directional derivative w.r.t. ϵ, for $\epsilon = 0$, in eqs. (3.6) and (3.8) (interchanging δ with d), respectively

$$d\boldsymbol{r}_0(\xi) = d\boldsymbol{u}_0 \tag{5.7}$$

$$d\boldsymbol{\Lambda}(\xi) = d\boldsymbol{\psi} \times \boldsymbol{\Lambda} \tag{5.8}$$

$d\boldsymbol{\psi}$ is the axial vector of the matrix $d\boldsymbol{\Psi}$. Inserting into eq. (5.6) the eqs. (5.7) and (5.8), and after some algebraic manipulations, the infinitesimal change of the elastic part of the weak

form is written in a matrix form as follows

$$dG_k = \int_{0_L} \begin{Bmatrix} \boldsymbol{\chi}' \\ \boldsymbol{\phi} \\ \boldsymbol{\phi}' \end{Bmatrix} \begin{bmatrix} \boldsymbol{c}^{f\gamma} & \boldsymbol{c}^{f\gamma}\hat{\boldsymbol{r}}_0' - \widehat{\boldsymbol{\Lambda F}} & \boldsymbol{c}^{f\kappa} \\ \widehat{\boldsymbol{\Lambda F}} - \hat{\boldsymbol{r}}_0'\boldsymbol{c}^{f\gamma} & -\hat{\boldsymbol{r}}_0'\boldsymbol{c}^{f\gamma}\hat{\boldsymbol{r}}_0' + \hat{\boldsymbol{r}}_0'\widehat{\boldsymbol{\Lambda F}} & -\hat{\boldsymbol{r}}_0'\boldsymbol{c}^{f\kappa} \\ \boldsymbol{c}^{m\gamma} & -\widehat{\boldsymbol{\Lambda M}} + \boldsymbol{c}^{m\gamma}\hat{\boldsymbol{r}}_0' & \boldsymbol{c}^{m\kappa} \end{bmatrix} \begin{Bmatrix} d\boldsymbol{u}_0' \\ d\boldsymbol{\psi} \\ d\boldsymbol{\psi}' \end{Bmatrix} d\xi \tag{5.9}$$

where

$$\boldsymbol{c}^{f\gamma} = \boldsymbol{\Lambda}\boldsymbol{C}^{F\Gamma}\boldsymbol{\Lambda}^T; \qquad \boldsymbol{c}^{f\kappa} = \boldsymbol{\Lambda}\boldsymbol{C}^{FK}\boldsymbol{\Lambda}^T \tag{5.10}$$

$$\boldsymbol{c}^{m\gamma} = \boldsymbol{\Lambda}\boldsymbol{C}^{M\Gamma}\boldsymbol{\Lambda}^T; \qquad \boldsymbol{c}^{m\kappa} = \boldsymbol{\Lambda}\boldsymbol{C}^{MK}\boldsymbol{\Lambda}^T \tag{5.11}$$

The same relation to eq. (5.9) is derived following the virtual work method in a material setting.

Stiffness matrix

By inserting into the linearized elastic term (eq. 5.9) of the virtual work equation the approximations of the test and trial functions (eqs. 3.67 - 3.69), the infinitesimal change of the approximated elastic term of the weak form dG_k^h is

$$dG_k^h = \int_0^L \Big\langle \underbrace{\begin{bmatrix} H^{i'}(\xi)\boldsymbol{I} & \boldsymbol{0} \\ \boldsymbol{0} & H^{i}(\xi)\boldsymbol{I} \\ \boldsymbol{0} & H^{i'}(\xi)\boldsymbol{I} \end{bmatrix} \begin{Bmatrix} \boldsymbol{\chi}_i \\ \boldsymbol{\phi}_i \end{Bmatrix}}_{(9\times6)\,(6\times1)} \Big\rangle^T \underbrace{\begin{bmatrix} \boldsymbol{c}^{f\gamma} & \boldsymbol{c}^{f\gamma}\hat{\boldsymbol{r}}_0' - \widehat{\boldsymbol{\Lambda F}} & \boldsymbol{c}^{f\kappa} \\ \widehat{\boldsymbol{\Lambda F}} - \hat{\boldsymbol{r}}_0'\boldsymbol{c}^{f\gamma} & -\hat{\boldsymbol{r}}_0'\boldsymbol{c}^{f\gamma}\hat{\boldsymbol{r}}_0' + \hat{\boldsymbol{r}}_0'\widehat{\boldsymbol{\Lambda F}} & -\hat{\boldsymbol{r}}_0'\boldsymbol{c}^{f\kappa} \\ \boldsymbol{c}^{m\gamma} & -\widehat{\boldsymbol{\Lambda M}} + \boldsymbol{c}^{m\gamma}\hat{\boldsymbol{r}}_0' & \boldsymbol{c}^{m\kappa} \end{bmatrix}}_{(9\times9)}$$

$$\underbrace{\begin{bmatrix} H^{i'}(\xi)\boldsymbol{I} & \boldsymbol{0} \\ \boldsymbol{0} & \tilde{\boldsymbol{H}}^{i}(\xi) \\ \boldsymbol{0} & \tilde{\boldsymbol{H}}^{i'}(\xi) \end{bmatrix} \begin{Bmatrix} d\boldsymbol{u}_i \\ d\boldsymbol{\psi}_i \end{Bmatrix}}_{(9\times6)\,(6\times1)} d\xi \tag{5.12}$$

from which the stiffness matrix $\boldsymbol{K}_k^{ij}$ is derived after some algebraic manipulation as

$$\boldsymbol{K}_k^{ij} = \int_0^L \begin{bmatrix} \boldsymbol{H}^{i'}\boldsymbol{c}^{f\gamma}\boldsymbol{H}^{j'} & \underline{\boldsymbol{H}^{i'}}\{(\boldsymbol{c}^{f\gamma}\hat{\boldsymbol{r}}_0' - \widehat{\boldsymbol{\Lambda F}})\tilde{\boldsymbol{H}}^{j} + \underline{\boldsymbol{c}^{f\kappa}\tilde{\boldsymbol{H}}^{j'}}\} \\ \boldsymbol{H}^{i}\{(\widehat{\boldsymbol{\Lambda F}} - \hat{\boldsymbol{r}}_0\boldsymbol{c}^{f\gamma})\boldsymbol{H}^{j'}\} + \underline{\boldsymbol{H}^{i'}\boldsymbol{c}^{m\gamma}\boldsymbol{H}^{j'}} & \underline{\boldsymbol{H}^{i}}\{(-\hat{\boldsymbol{r}}_0'\boldsymbol{c}^{f\gamma}\hat{\boldsymbol{r}}_0' + \hat{\boldsymbol{r}}_0'\widehat{\boldsymbol{\Lambda F}})\tilde{\boldsymbol{H}}^{j} \underline{-\hat{\boldsymbol{r}}_0'\boldsymbol{c}^{f\kappa}\tilde{\boldsymbol{H}}^{j'}}\} \\ & +\underline{\boldsymbol{H}^{i'}}\{(-\widehat{\boldsymbol{\Lambda M}} + \underline{\boldsymbol{c}^{m\gamma}\hat{\boldsymbol{r}}_0'})\tilde{\boldsymbol{H}}^{j} + \boldsymbol{c}^{m\kappa}\tilde{\boldsymbol{H}}^{j'}\} \end{bmatrix} d\xi \tag{5.13}$$

5.5.2 Inertial terms: incorporation into the multi-body dynamics code hGAST

Let **E** denote the material (rotating) frame attached to the body and **V** the cross-sectional frame that is moving together with the beam following its deformation. $\mathbf{V}_1$ is the vector that is normal to the cross-sectional area. $\boldsymbol{\xi} = \{\xi\ \eta\ \zeta\}^T$ defines the position of an arbitrary material particle, where ξ is the arc-length variable along the length of the beam and η, ζ are the cross-sectional coordinates. The configuration of the beam at the undeformed and the deformed state is shown in fig. 5.15.

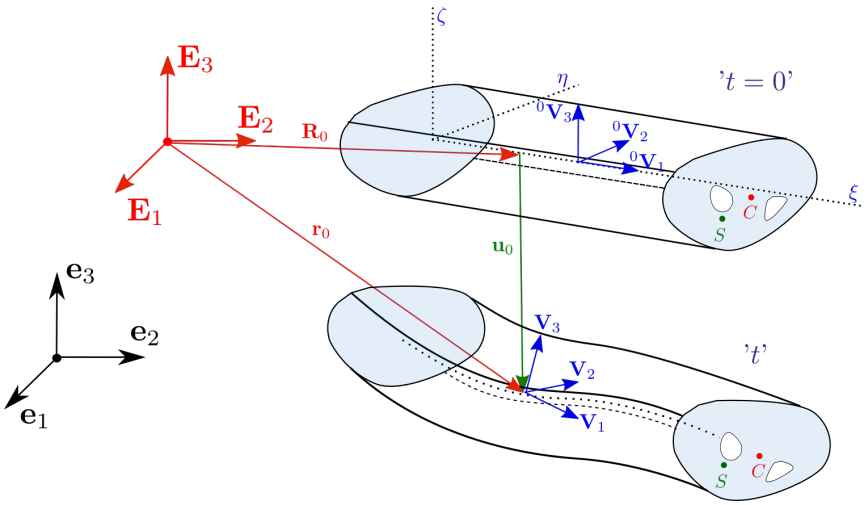

FIGURE 5.15: Initial and deformed configurations of the beam.

Let $\boldsymbol{R}(\boldsymbol{q};t)$ and $\boldsymbol{A}(\boldsymbol{q};t)$ denote the position and orientation of the body with respect to the inertial frame $\mathbf{e}$. The position vector $\boldsymbol{r}_G(\boldsymbol{q},\boldsymbol{\xi};t)$ of any arbitrary material particle $\boldsymbol{\xi}=\{\xi\ \eta\ \zeta\}$ of the beam with respect to the inertial frame at time t is given through eq. (5.1) by

$$\boldsymbol{r}_G(\boldsymbol{q},\boldsymbol{\xi};t)=\boldsymbol{R}+\boldsymbol{A}\boldsymbol{r} \tag{5.14}$$

where the indices k, ν that appear in eq. (5.1) have been omitted from the expressions for convenience. Note that eq. (5.1) reduces to eq. (5.14) when only one sub-body is considered (i.e. $\nu=1$). $\boldsymbol{r}(\boldsymbol{\xi};t)$ is the position vector of the material particle with respect to the body frame $\mathbf{E}$ given in eq. (3.2) for the SR beam model. The rotation matrix $\boldsymbol{A}(\boldsymbol{q};t)$ is parameterized using the three Euler angles about follower axes (intrinsic Euler angles). The velocity and acceleration vectors expressed in the body frame $\mathbf{E}$ are given by (Manolas, 2015)

$$\left(\boldsymbol{A}^T\dot{\boldsymbol{r}}_G\right)(\boldsymbol{q},\dot{\boldsymbol{q}},\boldsymbol{\xi};t)=\underline{\boldsymbol{A}^T\dot{\boldsymbol{R}}+\boldsymbol{A}^T\dot{\boldsymbol{A}}\boldsymbol{r}}+\dot{\boldsymbol{r}} \tag{5.15}$$

$$\left(\boldsymbol{A}^T\ddot{\boldsymbol{r}}_G\right)(\boldsymbol{q},\dot{\boldsymbol{q}},\boldsymbol{\xi};t)=\underline{\boldsymbol{A}^T\ddot{\boldsymbol{R}}+\boldsymbol{A}^T\ddot{\boldsymbol{A}}\boldsymbol{r}+2\boldsymbol{A}^T\dot{\boldsymbol{A}}\dot{\boldsymbol{r}}}+\ddot{\boldsymbol{r}} \tag{5.16}$$

where $\dot{\boldsymbol{R}}(\boldsymbol{q},\dot{\boldsymbol{q}},\boldsymbol{\xi};t)$, $\ddot{\boldsymbol{R}}(\boldsymbol{q},\dot{\boldsymbol{q}},\boldsymbol{\xi};t)$ and $\dot{\boldsymbol{A}}(\boldsymbol{q},\dot{\boldsymbol{q}},\boldsymbol{\xi};t)$, $\ddot{\boldsymbol{A}}(\boldsymbol{q},\dot{\boldsymbol{q}},\boldsymbol{\xi};t)$ are the first and the second time derivatives of the position vector and the orientation of the body with respect to the inertial frame $\mathbf{e}$ at time t. The first and second time derivatives of the position vector, $\dot{\boldsymbol{r}}$ and $\ddot{\boldsymbol{r}}$ respectively, of the material particle with respect to the body frame $\mathbf{E}$ at time t, are given in section 4.7.

The time derivative of the linear momentum $\dot{\boldsymbol{p}}\left(\boldsymbol{q},\dot{\boldsymbol{q}},\ddot{\boldsymbol{q}},\boldsymbol{\xi};t\right)$ expressed on the body frame $\mathbf{E}$ is defined as

$$\dot{\boldsymbol{p}}_{tot}\left(\boldsymbol{q},\dot{\boldsymbol{q}},\ddot{\boldsymbol{q}},\boldsymbol{\xi};t\right)=\int_{0_A}\rho_{ref}\left(\boldsymbol{A}^T\ddot{\boldsymbol{R}}+\boldsymbol{A}^T\ddot{\boldsymbol{A}}\boldsymbol{r}+2\,\boldsymbol{A}^T\dot{\boldsymbol{A}}\dot{\boldsymbol{r}}+\ddot{\boldsymbol{r}}\right)d^0\boldsymbol{A} \tag{5.17}$$

where

$$\dot{\boldsymbol{p}}\left(\boldsymbol{\xi};t\right)=\int_{{}^{0}A}\rho_{ref}\ddot{\boldsymbol{r}}\,d^{0}\boldsymbol{A}=\underbrace{A_{m}\ddot{\boldsymbol{r}}_{0}}_{\dot{\boldsymbol{p}}_{u}}+\underbrace{\ddot{\boldsymbol{\Lambda}}\boldsymbol{S}_{m}}_{\dot{\boldsymbol{p}}_{\psi}} \tag{5.18}$$

eq. (5.18) expresses the time derivative of the linear momentum of any material particle $(\boldsymbol{\xi})$ with respect to the body frame **E** in case the multi-body terms (i.e. underlined terms in eqs. (5.15) and (5.16) are omitted in eq. (5.17)), see section 4.7. $\rho_{ref}:{}^{0}A\rightarrow\mathcal{R}$ is the density in ${}^{0}A$. $\dot{\boldsymbol{p}}_{u}(\xi;t)$ and $\dot{\boldsymbol{p}}_{\psi}(\xi;t)$ are the time derivatives of the linear momentum vector due to the linear and the angular acceleration of the reference point, respectively.
The weak form of the inertia terms with respect to the body frame **E** is given by

$$\delta W_{\dot{\boldsymbol{p}}_{tot}}\left(\boldsymbol{q},\dot{\boldsymbol{q}},\ddot{\boldsymbol{q}},\boldsymbol{\xi};t\right)=\int_{{}^{0}L}\left(\delta\boldsymbol{r}_{0}^{T}\dot{\boldsymbol{p}}_{tot}\right)d\xi \tag{5.19}$$

where $\delta\boldsymbol{r}_{0}$ is the variation of the position vector of the reference center.
The time derivative of the angular momentum vector $\dot{\boldsymbol{l}}_{tot}\left(\boldsymbol{q},\dot{\boldsymbol{q}},\ddot{\boldsymbol{q}},\boldsymbol{\xi};t\right)$ with respect to the body frame **E** is given by

$$\begin{aligned}\dot{\boldsymbol{l}}_{tot}\left(\boldsymbol{q},\dot{\boldsymbol{q}},\ddot{\boldsymbol{q}},\boldsymbol{\xi};t\right)=\int_{{}^{0}A}\rho_{ref}\Big[&\left(\dot{\boldsymbol{\Lambda}}\boldsymbol{X}\right)\times\left(\boldsymbol{A}^{T}\dot{\boldsymbol{R}}+\boldsymbol{A}^{T}\dot{\boldsymbol{A}}\boldsymbol{r}+\dot{\boldsymbol{r}}\right)\\&+\left(\boldsymbol{\Lambda}\boldsymbol{X}\right)\times\left(\boldsymbol{A}^{T}\ddot{\boldsymbol{R}}+\boldsymbol{A}^{T}\ddot{\boldsymbol{A}}\boldsymbol{r}+2\,\boldsymbol{A}^{T}\dot{\boldsymbol{A}}\dot{\boldsymbol{r}}+\ddot{\boldsymbol{r}}\right)\Big]\,d^{0}\boldsymbol{A}\end{aligned} \tag{5.20}$$

where in a similar manner

$$\begin{aligned}\dot{\boldsymbol{l}}\left(\boldsymbol{\xi};t\right)&=\int_{{}^{0}A}\rho_{ref}\left[\dot{\overline{\left(\boldsymbol{r}-\boldsymbol{r}_{0}\right)\times\dot{\boldsymbol{r}}}}\right]d^{0}\boldsymbol{A}=\int_{{}^{0}A}\rho_{ref}\left(\dot{\boldsymbol{\Lambda}}\boldsymbol{X}\times\dot{\boldsymbol{r}}+\boldsymbol{\Lambda}\boldsymbol{X}\times\ddot{\boldsymbol{r}}\right)d^{0}\boldsymbol{A}\\&=\underbrace{\left(\dot{\boldsymbol{\Lambda}}\boldsymbol{S}_{m}\right)\times\dot{\boldsymbol{r}}_{0}+\left(\boldsymbol{\Lambda}\boldsymbol{S}_{m}\right)\times\ddot{\boldsymbol{r}}_{0}}_{\dot{\boldsymbol{l}}_{u}}+\underbrace{\int_{{}^{0}A}\rho_{ref}\left(\boldsymbol{\Lambda}\boldsymbol{X}\times\ddot{\boldsymbol{\Lambda}}\boldsymbol{X}\right)d^{0}\boldsymbol{A}}_{\dot{\boldsymbol{l}}_{\psi}}\end{aligned} \tag{5.21}$$

eq. (5.21) expresses the time derivative of the angular momentum of any material particle ξ with respect to the body frame **E** without considering the multi-body terms. $\dot{\boldsymbol{l}}_{u}(\xi;t)$ and $\dot{\boldsymbol{l}}_{\psi}(\xi;t)$ are the time derivatives of the angular momentum vector due to the linear and the angular acceleration of the reference point, respectively.

$$\boldsymbol{l}_{\psi}(\xi;t)=\boldsymbol{I}_{t}\,\boldsymbol{\omega} \tag{5.22}$$

is the total spatial angular momentum relative to the principal axes of inertia, see section 4.7. The standard cross-sectional inertial properties considered in eqs. (5.20) to (5.22) are the linear mass density $A_{m}(\xi)$, the first moment of inertia $\boldsymbol{S}_{m}(\xi)$ and the second moment of inertia tensor $\boldsymbol{J}$, while $\boldsymbol{I}_{t}(\xi;t)=\boldsymbol{\Lambda}\boldsymbol{J}\boldsymbol{\Lambda}^{T}$ is the time-dependent second moment of inertia (see also section 4.7).
The weak form of the inertial terms with respect to the body frame is given by

$$\delta W_{\dot{\boldsymbol{l}}_{tot}}(\boldsymbol{q},\dot{\boldsymbol{q}},\ddot{\boldsymbol{q}},\boldsymbol{\xi};t)=\int_{{}^{0}L}\delta\boldsymbol{\psi}^{T}\,\dot{\boldsymbol{l}}_{tot}\,d\xi \tag{5.23}$$

where $\delta\psi$ is the spin vector that expresses the variation of the cross-sectional orientation (see chapter 3).
For the linearization of the inertial terms the reader is referred to the appendix E.

5.6 Implementation details

- For the spatial discretization, the displacement-based finite elements are used. A Newton-Raphson iterative procedure is employed to get the solution of the non-linear problem. Convergence of the finite element solution is established when the absolute maximum displacement norm is reduced to the tolerance $\delta_{u,max}$.

- For both the SR and SB models, 2-noded elements are used with linear Lagrange interpolating polynomials. Thus, a reduced Gauss integration (i.e. 1 Gauss point) is performed to compute the stiffness matrix preventing the shear locking effect. It should be noted that modified C^1 Hermitian shape functions are considered by default in SB beam model for the two bending displacements (Manolas et al., 2020). However, this choice is made to eliminate the effect of the shape functions and to exclusively assess the effect of the beam modeling on the beam response under large deformations.

- In the SR modeling, the angle-axis representation is used for the rotation of the cross-sections, while, in the SB technique, the Euler angles in an intrinsic sense are used for the rigid-body rotation of the sub-bodies. In the SB technique, the balance equations of motion are written with respect to the frame of each SB and so the degrees of freedom of the beam are computed with respect to this frame. Thus, the total translational and rotational deformations with respect to the blade frame are derived through post-processing.

- In the SR model, the spin vector $\delta\psi$ is used in the iterative process instead of the rotation vector. Using this option, the linearization of the elastic term is simpler than using a rotation vector parameterization, because of the absence of the tangential transformation in the computation of the stiffness matrix. In addition, this choice is in line with the original formulation (Simo and Vu-Quoc, 1986a) and also convenient for the strain-invariant implementation (Jelenić and Crisfield, 1999).

- The strain-invariance is an issue that is taken under consideration for retaining the consistency with the rotation manifold $SO(3)$ in the linearization and in the discretization level (Jelenić and Crisfield, 1999; Panteli and Spiliopoulos, 2020). The SB model automatically guarantees the strain-invariance of the solution. For the SR model, to ensure having a consistent approximation of large rotations, the orientation of the cross-section is decomposed into the rotation of the element and into the local rotation with respect to the element, while the discretization is employed just for the local rotations (Jelenić and Crisfield, 1999; Dukić, Jelenić, and Gaćeša, 2014). The SR beam that has been incorporated in hGAST follows exactly the formulation by Jelenić and Crisfield,

1999, which preserves the objectivity of the adopted strain measures and the geometric exactness of the theory.

5.7 Numerical results

Firstly, the implementation of the SR and SB models is verified on two static benchmark cases with cantilever beams. The first is the well-known 45^o curved beam (Bathe and Bolourchi, 1979), whereas the second is a prismatic beam with a hollow box-shaped cross-section of inhomogeneous and anisotropic material. The second example is reported in Bagherpour et al., 2018, where verification and validation of the SB model was performed regarding the implementation of the non-diagonal terms of the cross-section constitutive matrix (arising from the anisotropic character of the material) using public available numerical and experimental data. Secondly, a wind turbine system is examined. The geometry and material data, as well as the aerodynamic and control properties are taken from Bak et al., 2013 for the DTU 10-MW Reference Wind Turbine (RWT). Three loading scenarios are considered. At first, static load cases are performed to assess the non-linearity in the response of a real blade structure. Then, time domain aeroelastic computations are presented for the isolated rotor under uniform inflow and finally for the entire wind turbine system under stochastic inflow. The BEMT based method in combination with the ONERA dynamic stall model is used in all the simulations. These simulation examples are specifically selected with the aim i) to verify the implementation of the newly developed SR model and ii) to compare the SR and SB modeling options regarding their efficiency to capture the non-linear behaviour of slender beams in statics and dynamics. For this comparison, the solution obtained by a dense discretization of the SR model is considered as the exact one, with respect to which the relative percentage error is calculated. The reason is that the SB model converges to the SR model as the discretization increases. This is justified theoretically as follows. The SB model could be considered as an early version of a geometrically exact beam modeling, in which the same kinematics to the SR model is applied from sub-body to sub-body (not from point to point) along the body. In addition, in order to provide a quantitative measure of the non-linearity of the addressed cases, the results of the linear Timoshenko beam model are added in selected graphs in comparison to the SR and SB models. The centrifugal stiffening, bending-tension coupling term is the only non-linear term considered in the above-mentioned linear model as it considerably affects the overall stiffness and response frequency and therefore it cannot be neglected. It is noted that all the above three modeling options are implemented into hGAST, meaning that the same software framework is used for all of them. In the two benchmark static cases, discretization-independent results are provided for the SB and the SR model in order to i) numerically prove that the SB model converges to the SR model as the discretization increases and ii) highlight the much denser discretization required in the SB model to achieve the same accuracy (in highly non-linear cases with large deformations). In both cases, the considered structural members are prismatic and thus no approximation is performed for the cross-sectional properties, meaning that the numerical results are not affected by the interpolation of the beam properties of the various FEM grids (i.e., number of

elements) considered, as opposed to the case where the real wind turbine blade is analyzed. In the latter case, the comparison between the two non-linear beam models aims at assessing the effect of the beam fidelity with a reasonable number of elements (up to 69 elements are considered per blade), rather than to compare grid independent solutions by the two models.

5.7.1 Verification of the geometrically non-linear beam models in benchmark cases of two cantilevers

A 45^o curved cantilever beam undergoing large deformations

The curved (45^o circle arc) cantilever beam defined in Bathe and Bolourchi, 1979 is a well-known benchmark test case that is herein used in verifying the implementation of the SR and SB models within hGAST framework. It represents a highly non-linear problem with large translations and rotations. The geometry and material data is shown in fig. 5.16. The slenderness ratio of the beam is defined as $\zeta = \frac{l}{r} = \frac{76.54}{1} \approx 77$, where l is the arc-length of the beam, and r is the characteristic dimension of the cross-section. The higher the ratio, the higher the effect of the non-linearity is expected on the response. The beam is subjected to a transverse load of 600 N at its tip with fixed direction along the e_3 axis. The baseline dis-

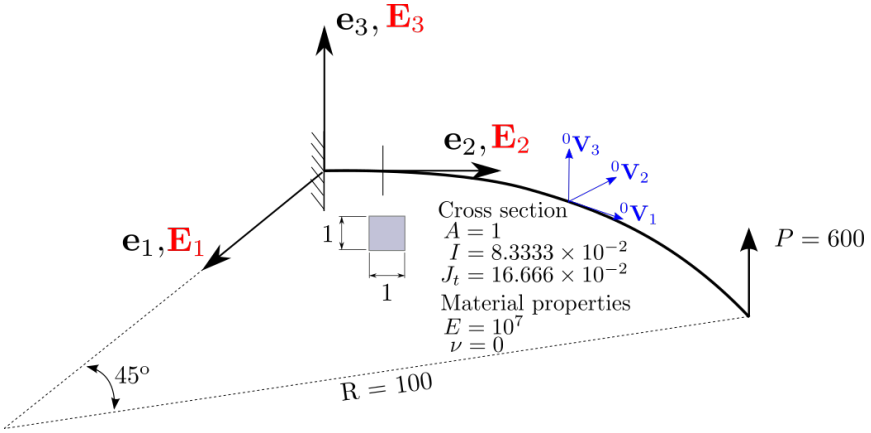

FIGURE 5.16: 45-degree curved cantilever: problem data.

cretization of the beam considered in the present analysis consists of 8 equally spaced beam elements for the SR model, and 8 equally spaced sub-bodies, with one element each, for the SB model. It corresponds to the discretization adopted in Bathe and Bolourchi, 1979 and in a number of subsequent papers that simulated the same test case e.g. Simo and Vu-Quoc, 1986a; Jelenić and Crisfield, 1999; Romero, 2008. Furthermore, higher number of elements or sub-bodies is considered, i.e. 16, 32, 64 elements for the SR model and 16, 32, 64, 128, 256 sub-bodies (with one element per sub-body) for the SB model, with the aim to attain grid independent solution for both modeling options. The tolerance used in the convergence of the nonlinear beam equations is $\delta_{u,max} = 10^{-11}$ in all models.

In tables 5.2 and 5.3, the absolute values of the three translations (u_{01}, u_{02}, and u_{03}) and rotations (θ_1, θ_2, and θ_3) at the tip of the beam are shown for the SR and SB models for different number N of elements and sub-bodies, respectively. The translational components

TABLE 5.2: 45-degree curved cantilever: translations at the tip for the SR, SB and linear beam models for different discretization. Relative percentage errors are defined with respect to the SR-64 solution.

	N	$u_{01}(m)$	err. (%)	$u_{02}(m)$	err. (%)	$u_{03}(m)$	err. (%)
Ref. Jelenić and Crisfield, 1999	8	−13.483	−0.88%	−23.479	−0.34%	53.371	−0.19%
SR	8	−13.482	−0.88%	−23.479	−0.34%	53.371	−0.19%
	16	−13.574	−0.21%	−23.540	−0.08%	53.449	−0.05%
	32	−13.597	−0.04%	−23.555	−0.02%	53.468	−0.01%
	64	−13.603		−23.559		53.473	
SB	8	−12.426	−8.65%	−23.746	0.80%	53.468	−0.01%
	16	−13.042	−4.12%	−23.723	0.70%	53.471	0.00%
	32	−13.329	−2.01%	−23.659	0.42%	53.471	0.00%
	64	−13.468	−0.99%	−23.613	0.23%	53.472	0.00%
	128	−13.537	−0.49%	−23.588	0.12%	53.473	0.00%
	256	−13.570	−0.24%	−23.574	0.06%	53.474	0.00%

reported in Jelenić and Crisfield, 1999, for the baseline discretization (i.e. 8 elements), are added in the first line for verification. As mentioned, the finite element formulation of the SR beam theory used in the current work follows the strain-invariant formulation in Jelenić and Crisfield, 1999 that preserves the geometric exactness of the theory. The solution using the SR model with 64 elements is considered as the reference for computing the relative percentage errors.

As far as the solution with the 8 elements is concerned (table 5.2), the SR model gives very satisfactory results in all directions compared to those reported in Jelenić and Crisfield, 1999. It is noted that predictions of the SB model in $\boldsymbol{e}_1$ direction are not the same good, when using the 8 elements discretization. More precisely, the error in the prediction of the u_{01} translation by the SB model is -8.65% (-7.84% compared to [36]), while for the other two translations, u_{02} and u_{03}, an error less than 1% is obtained (+1.14% and +0.18% respectively compared to Jelenić and Crisfield, 1999). It is shown that the translation in $\boldsymbol{e}_1$ direction, which is exclusively triggered by geometrically non-linear effects, is better predicted by the SR model when a coarse discretization is considered.The same conclusion is drawn when predictions obtained using more than 8 elements (or sub-bodies), are compared to the reference solution by the SR model using 64 elements. While the error for the SR model begins at -0.88% for 8 elements and becomes almost negligible (-0.04%) for a number of 32 elements, the corresponding error of the SB model is -8.65% for 8 sub-bodies while an overwhelming number of sub-bodies is required in order to make the error vanish (256 sub-bodies for an error of -0.24%). On the other hand, the error for the translations u_{02} and u_{03} remain below 1% for both models.

Regarding rotations, higher errors are noted in the prediction of θ_3 angle when low numbers of elements are considered, for the same reason mentioned above for the transverse translation u_{01}. It is also noted that convergence of the SR results to the reference predictions is much faster compared to the SB model. The latter requires an overwhelming number of sub-bodies (i.e., 256) in order to obtain a moderate error at the level of 1.53%. Faster convergence and much lower errors are obtained though for θ_1 and θ_2 angles, where non-linear

TABLE 5.3: 45-degree curved cantilever: rotations at the tip for the SR, SB and linear beam models for different discretization. Relative percentage errors are defined with respect to the SR-64 solution.

	N	$\theta_1(deg)$	err. (%)	$\theta_2(deg)$	err. (%)	$\theta_3(deg)$	err. (%)
	8	58.308	0.33%	−32.227	0.14%	3.333	−2.95%
SR	16	58.162	0.08%	−32.192	0.03%	3.410	−0.70%
	32	58.125	0.02%	−32.183	0.01%	3.430	−0.14%
	64	58.116		−32.181		3.434	
	8	57.699	−0.72%	−33.372	3.70%	1.507	−56.13%
SB	16	57.865	−0.43%	−32.739	1.74%	2.523	−26.53%
	32	57.979	−0.24%	−32.449	0.84%	2.993	−12.86%
	64	58.043	−0.13%	−32.312	0.41%	3.218	−6.31%
	128	58.077	−0.07%	−32.245	0.20%	3.328	−3.11%
	256	58.095	−0.04%	−32.212	0.10%	3.382	−1.53%

effects are less important.

In fig. 5.17, the distributions of the translations and rotations along the length of the beam are shown. The graphs are given for the SR-64 elements and for the SB-256 sub-bodies, as

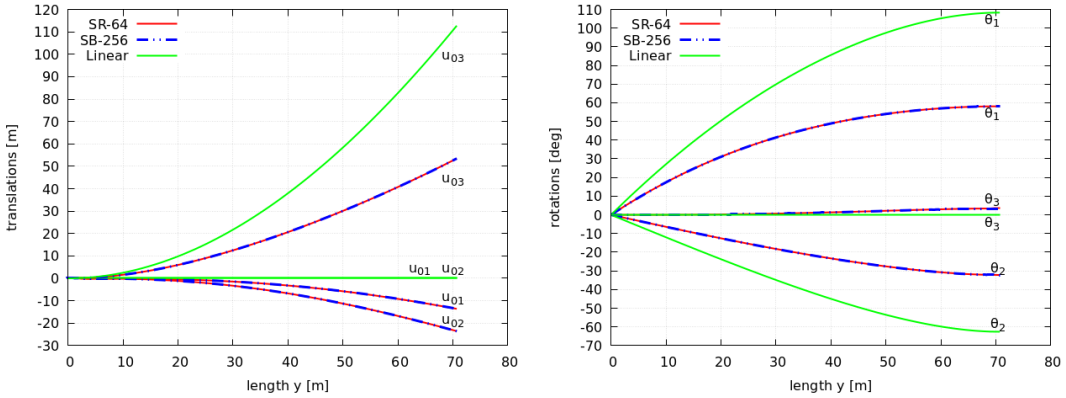

(A) Translations along the length.

(B) Rotations along the length.

FIGURE 5.17: 45-degree curved cantilever: distribution of the translations and rotations along the length, for the SR, the SB and the linear model.

well as for the linear beam model. Both the shape and the values are very similar for the two non-linear beam models. For the considered symmetric cross-section, without anisotropic composite material couplings, translations u_{01} and u_{02} are exclusively triggered by geometrically non-linear effects due to bending-tension and bending-torsion couplings and consequently they cannot be predicted by the linear beam model (zero spanwise distributions are predicted). The translation u_{03} at the tip (in the direction of the load) is about 120% decreased as compared to the linear model prediction, due to the bending-torsion coupling effect. As far as rotations are concerned, the torsional deformation θ_2 is triggered by the applied load and it is due to the initial curvature of the reference line that gives rise to a twisting arm with respect to the body frame **E**. This is a linear effect, which is apparently predicted by the linear beam model. What is not considered though, is the reduction of the twisting moment

due to bending-torsion coupling, which is proportional to the out-of-plane bending deformation u_{03}. The linear model prediction for the tip torsional deformation is about 70% higher as compared to that provided by the non-linear models. The bending angles θ_1 and θ_3 are proportional to the associated deformations u_{03} and u_{01}. The former is over predicted by the linear model by 83%, while the latter attains zero value along the beam span similar to u_{01}.

An anisotropic cantilever beam

This test case was originally investigated in Wang et al., 2014 to examine the ability of BeamDyn to analyze a composite beam. BeamDyn is the beam module used in the FAST code for modeling initially curved and twisted composite wind turbine blades undergoing large deformations (Wang et al., 2017). It is based on the geometrically exact beam theory by Hodges (Hodges, 2006) following the strain-invariant formulation in Jelenić and Crisfield, 1999. Regarding the FEM discretization, Legendre Spectral Finite Elements are used in case prismatic beams with constant cross sectional properties are analyzed. In Bagherpour et al., 2018, the anisotropic beam example was simulated in order to validate the fully populated stiffness matrix implementation for the SB model. It is replicated herein in order to check and verify the ability of the extended version of the SR beam model to capture the bending-twist coupling effect. It is noted that this is an important structural coupling that is often leveraged in modern wind turbine blades for passive load control purposes (Bagherpour et al., 2018). A 10m thin-walled cantilever beam with an anisotropic box-shaped cross-section is considered (fig. 5.18), constructed by laminates that are placed in $[\pm 15^o]_6$ and $[\pm 15^o]_3$ angles along the caps and the walls, respectively. The slenderness ratio of the beam is $\zeta = \frac{l}{r} = \frac{10}{0.953} \approx 10$.

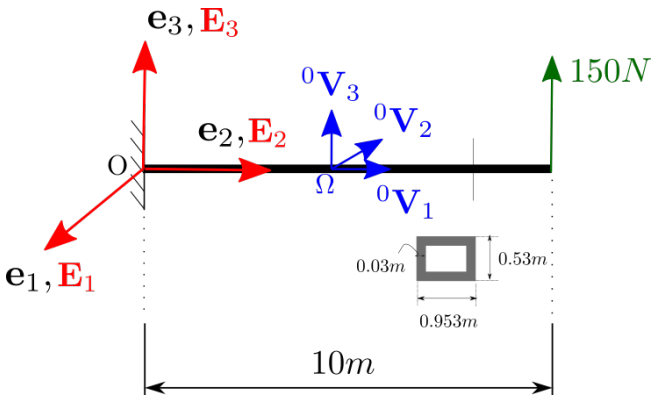

FIGURE 5.18: Anisotropic beam: problem data.

The derivation of the cross-sectional properties is given in Yu et al., 2002b, whereas the fully

populated constitutive matrix with respect to the local basis ${}^0\boldsymbol{V}$ is

$$\boldsymbol{C} = \begin{bmatrix} 1368.17 & 0 & 0 & & & \\ 0 & 88.56 & 0 & & \mathbf{0} & \\ 0 & 0 & 38.78 & & & \\ & & & 16.96 & 17.61 & 0.351 \\ & sym. & & & 59.12 & 0.37 \\ & & & & & 141.47 \end{bmatrix} 10^3 \tag{5.24}$$

where the sub-matrix $\boldsymbol{C}(1,1)_{3\times3}$ is measured in N, while the sub-matrix $\boldsymbol{C}(2,2)_{3\times3}$ is measured in Nm^2. The bend-twist coupling (BTC) effect is accounted for through the non-diagonal terms in the 4^th line of the constitutive matrix that relates the torsion moment (M_1) to the bending curvatures (K_2 and K_3), with respect to the ${}^0\boldsymbol{V}$ frame. The beam is subjected to a conservative transverse load of 150 N along the $\boldsymbol{e}_3$ axis at the tip (fig. 5.18). The tolerance used in the convergence of the nonlinear beam equations is $\delta_{u,max}$ in all models. The translations and rotations at the tip with respect to the **e** basis predicted by the SR and SB models are shown in tables 5.4 and 5.5 for different spatial discretizations (number of elements or sub-bodies). The numerical results obtained by the software BeamDyn using two 5^{th} order Legendre Spectral Finite Elements (LSFE) are added in the first line for comparison (Wang et al., 2014). Along with the absolute values of the elastic deflections, the relative differences of the various solutions with respect to the SR solution using 64 elements (considered as the reference) are also provided. For the SB model a maximum number of 256 sub-bodies are considered (up to 64 sub-bodies were considered in Bagherpour et al., 2018). In tables 5.4 and 5.5, the translation u_{03} and the associated rotation θ_1 are the main deformations driven directly by the load applied along the $\boldsymbol{e}_3$ axis.

TABLE 5.4: Anisotropic beam: translations at the tip for the SR, SB and linear beam models for different discretization. Relative percentage errors are defined with respect to the SR-64 solution.

	N	$u_{01}(m)$	err. (%)	$u_{02}(m)$	err. (%)	$u_{03}(m)$	err. (%)
BeamDyn	2	0.0648	0.15%	−0.0906	0.42%	1.2300	0.03%
SR	8	0.0639	−1.27%	−0.0895	−0.90%	1.2253	−0.35%
	16	0.0645	−0.31%	−0.0901	−0.21%	1.2286	−0.08%
	32	0.0647	−0.07%	−0.0902	−0.04%	1.2295	−0.02%
	64	0.0647		−0.0903		1.2297	
SB	8	0.0503	−22.36%	−0.0884	−2.07%	1.2274	−0.18%
	16	0.0575	−11.25%	−0.0897	−0.58%	1.2296	0.00%
	32	0.0611	−5.63%	−0.0901	−0.17%	1.2299	0.02%
	64	0.0629	−2.81%	−0.0902	−0.05%	1.2299	0.02%
	128	0.0638	−1.40%	−0.0902	−0.01%	1.2298	0.01%
	256	0.0643	−0.70%	−0.0903	0.00%	1.2298	0.01%

These two are well captured, even when considering 8 elements (in SR model) or 8 sub-bodies (in SB model). By increasing the number of elements for the SR model and sub-bodies for the SB model, the error in the translation u_{03} is reduced to -0.02% and 0.01%,

TABLE 5.5: Anisotropic beam: rotations at the tip for the SR, SB and linear beam models for different discretization. Relative percentage errors are defined with respect to the SR-64 solution.

	N	$\theta_1(deg)$	err. (%)	$\theta_2(deg)$	err. (%)	$\theta_3(deg)$	err. (%)
$BeamDyn$	2	10.3046	0.16%	10.5682	0.22%	0.2796	0.21%
SR	8	10.2903	0.02%	10.5488	0.03%	0.2793	0.09%
	16	10.2889	0.00%	10.5463	0.01%	0.2792	0.07%
	32	10.2885	0.00%	10.5457	0.00%	0.2792	0.06%
	64	10.2886		10.5453		0.2790	
SB	8	10.2960	0.07%	10.5597	0.14%	0.3907	40.01%
	16	10.2913	0.03%	10.5497	0.04%	0.3349	20.02%
	32	10.2895	0.01%	10.5468	0.01%	0.3070	10.03%
	64	10.2888	0.00%	10.5459	0.01%	0.2931	5.04%
	128	10.2885	0.00%	10.5456	0.00%	0.2861	2.55%
	256	10.2884	0.00%	10.5454	0.00%	0.2827	1.30%

respectively. The corresponding error of the θ_1 rotation vanishes in both models as the number of elements or sub-bodies increases. The shortening effect u_{02}, that is a geometrically non-linear effect, is well captured for 8 elements or sub-bodies and more; the corresponding deviations start from about 1.00% for the SR model and 2.00% for the SB model, while the SR model presents a higher convergence rate. The error in the prediction of the twist angle (with respect to the SR-64 elements' reference solution) is negligible, independent of the model used or the number of elements/sub-bodies considered. This indicates that the corresponding deformation is driven by the BTC effect (linear coupling term in the fully populated constitutive matrix) rather than by geometrical non-linearity. The BTC effect is predicted well by both models, confirming the consistent implementation of the fully populated constitutive matrix of the cross-section in the extended version of the SR model.

Regarding the secondary bending direction along the $\boldsymbol{e}_1$ axis, the non-zero values of the translation u_{01} and rotation θ_3 for the SR and SB models indicate geometrically non-linear coupling effects. Deviations of the SR model predictions from the reference solution for the different number of elements considered in the analysis are much smaller compared to those of the SB model (for different number of sub-bodies). The distribution of the translation u_{01} along the beam length is depicted in fig. 5.19 for the different numbers of the sub-bodies in comparison to the reference solution. To obtain the coupling in the $\boldsymbol{e}_1$ direction (both u_{01} and θ_3 values) at a reasonable level of accuracy 3% more than 64 sub-bodies are needed. It should be mentioned though that u_{01} deflection is rather small both in absolute value (0.064m) but also in comparison to deflection u_{03} ($\frac{u_{03}}{u_{01}} \approx 19$).

5.7.2 Analysis of the coupled DTU 10-MW RWT system

The DTU 10-MW RWT blade under static loading

In order to assess the non-linearity in the response of a real wind turbine blade structure, static analyses of the DTU-10MW RWT blade are first performed under the action of a fixed

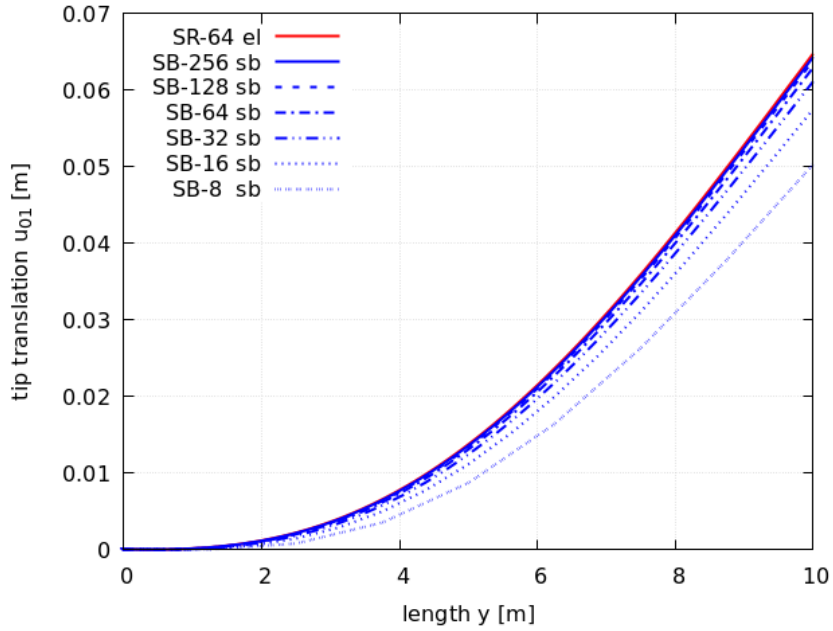

FIGURE 5.19: Anisotropic beam: distribution of the translation u_{01} along the length.

point force at the tip of the blade along the flap-wise direction $\boldsymbol{E}_3$ (see fig. 5.13 for the definition of the reference axes considered). The imposed load gradually increases from 25 kN to 250 kN with a step of 25 kN. In figs. 5.20 to 5.22, the $P - \delta$ diagrams are depicted for the SR, the SB, and the linear models. In SR simulations 69 elements are considered. SB simulations are performed using 69 sub-bodies consisting of one element each. Linear beam analyses are performed with the SB model considering that the whole blade consists of one sub-body which is discretized by 69 finite elements.

As far as the translations are concerned, the results of the two non-linear models, the SR and the SB, agree well. This implies that geometric non-linearities are well reproduced by both models. Specifically, the response to the externally applied flap-wise load, mainly consisting of a significant flap-wise translation component u_{03} (see fig. 5.21a), a smaller extension component u_{02}, obtained as a result of the blade shortening due to extreme bending (fig. 5.20b) and an even smaller edgewise translation u_{01} (fig. 5.20a) mainly due to material flap/edge coupling, is similarly predicted by both models. As deduced by the linear model predictions in the same figures, the non-linear models are indispensable for the accurate prediction of the blade deformation. As seen in fig. 5.21a, where the blade tip flap-wise translation is depicted, beyond the 75 kN of load where the response is still linear up to 250 kN the deviation between the non-linear and the linear models increases by a continuously growing rate, towards the maximum of 16%. On the other hand, the shortening effect cannot be captured by the linear model. In fig. 5.20a, the translation u_{01} in the edge-wise direction is a combined result of the material (linear cross bending stiffness coupling term) and the geometrically non-linear coupling; the second not being as important as the first though. Although the predicted by the different models edge-wise deflections do not significantly deviate, the shape of their

variation with the load is somewhat different. The linear model predicts a linear increase of the edge-wise deflection with the load while the SR and SB models, both predict a nonlinear variation.

As far as the rotations are concerned, in fig. 5.21b, the deviations between the linear and the non-linear models in the prediction of the rotation θ_1 follow a similar pattern as in the translation u_{03}. The corresponding maximum deviation between the non-linear and the linear models, when the load reaches its maximum value of 250 kN, is 18%. On the other hand, in fig. 5.22, a slight difference between the two non-linear approaches is noted in the rotations θ_2 and θ_3. This difference vanishes as the number of sub-bodies is further increased (higher than 69 sub-bodies used in the present study).

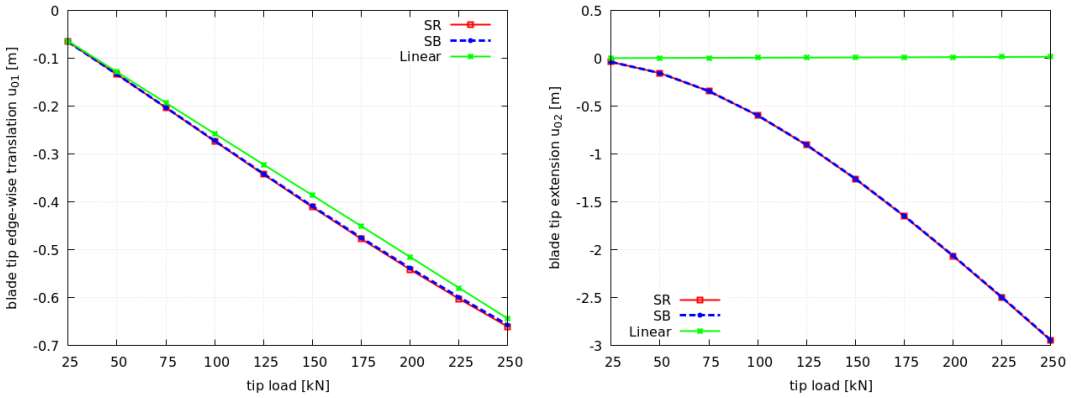

(A) Tip load vs. translation along the edge-wise direction. (B) Tip load vs. translation along the longitudinal direction.

FIGURE 5.20: DTU 10-MW RWT blade under static loading: tip load vs. translation along (a) $\boldsymbol{E}_1$ and (b) $\boldsymbol{E}_2$ axes.

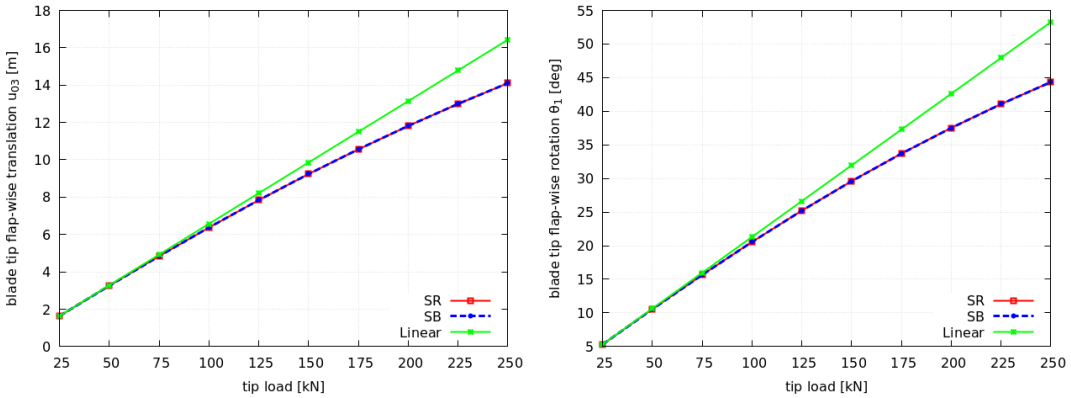

(A) Tip load vs. translation along the flap-wise direction. (B) Tip load vs. rotation about the edge-wise direction.

FIGURE 5.21: DTU 10-MW RWT blade under static loading: tip load vs. (a) translation along the $\boldsymbol{E}_3$ axis and (b) rotation about the $\boldsymbol{E}_2$ axis.

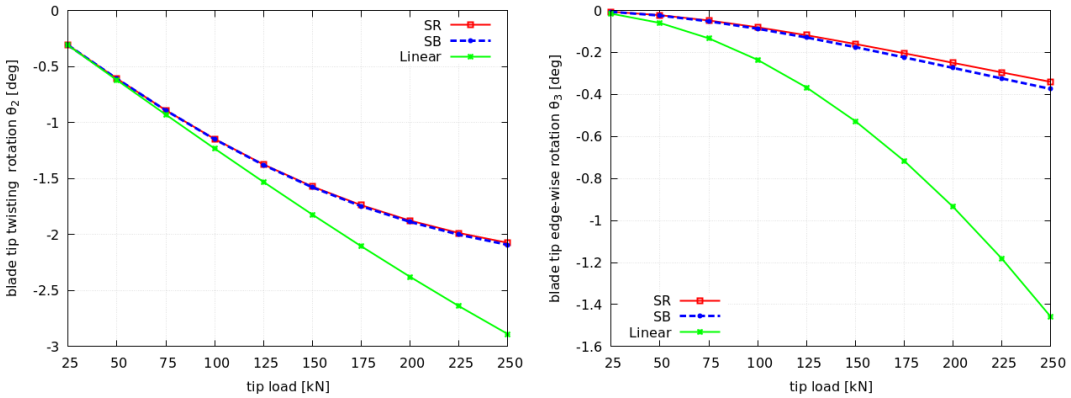

(A) Tip load vs. rotation about the longitudinal direction. (B) Tip load vs. rotation about the flap-wise direction.

FIGURE 5.22: DTU 10-MW RWT blade under static loading: tip load vs. translation along the (a) $\boldsymbol{E}_2$ and (b) $\boldsymbol{E}_3$ axes.

The DTU 10-MW RWT rotor under uniform inflow

The isolated rotor, consisting only of the three rotating blades, is examined under a uniform inflow and the effect of gravity. In this case, the aerodynamic tower shadow effect is included. The FEM mesh consists of 69 elements per blade for all beam models. In order to better highlight what has already been observed in the previous sections, i.e., that SB predictions come closer to the SR predictions as the number of sub-bodies is increased, the SB grids employing 9, 17 and 35 sub-bodies are all considered in addition to the fine grid of 69 sub-bodies. The aim of the comparison between the two non-linear beam models is to assess the effect of the beam fidelity with a reasonable number of elements (up to 69 elements are considered per blade), rather than to compare grid independent solutions by the two models. Uniform inflow conditions are considered at the rated wind speed of 11.4 m/s, where the deflections are expected to attain their maximum value (due to maximum thrust) and consequently, non-linear effects will be more pronounced. The rotor is operated at the fixed rotational speed of 9.6 rpm and at zero pitch angle (open loop operation, i.e., the controller is not active), corresponding to average operating conditions at the rated wind speed. The results are presented in terms of time histories, after the initial transients are damped.

In fig. 5.23, the torsion moment M_2 at the root and the torsion angle θ_2 at the tip of the blade are shown. Both SR and SB models agree well in the predicted phase and mean values of the two signals, while the SR model predicts higher variation amplitude of both signals. However, as the number of sub-bodies of the SB model increases, the predicted by the model amplitude converges towards the SR predictions. The linear model considerably under-predicts the amplitudes of the variation of both the moment and the angle, while it predicts an almost zero mean value of the torsion moment and 0.3^o higher mean torsion angle (in absolute value). Regarding the flap-wise direction triggered by the thrust force due to the wind inflow, in fig. 5.24, the flap-wise moment M_1 at the root of the blade and the corresponding deflection u_{03} at its tip are shown. In fig. 5.24a, the two non-linear models provide very similar results. The small difference observed in the graph is measured less than 1%. In fig. 5.24b, the mean value of the translation u_{03} is about the 10% of the rotor radius (for

the DTU 10-MW RWT the rotor radius is 89.2 m) and it is well predicted by both non-linear models (difference 0.6%). The reduced mean value compared to the linear model results from the bending-twist coupling effect, and the same holds for the amplitude of the variation. The increase in the amplitude of the twist angle in fig. 5.23b, gives rise to a decrease in the amplitude of the flap-wise deflection in fig. 5.24b, which comes as a result of the change of the effective angle of attack of the blade sections. As in the case of torsion, the more the sub-bodies used the closer is the agreement of the two non-linear models (fig. 5.24).

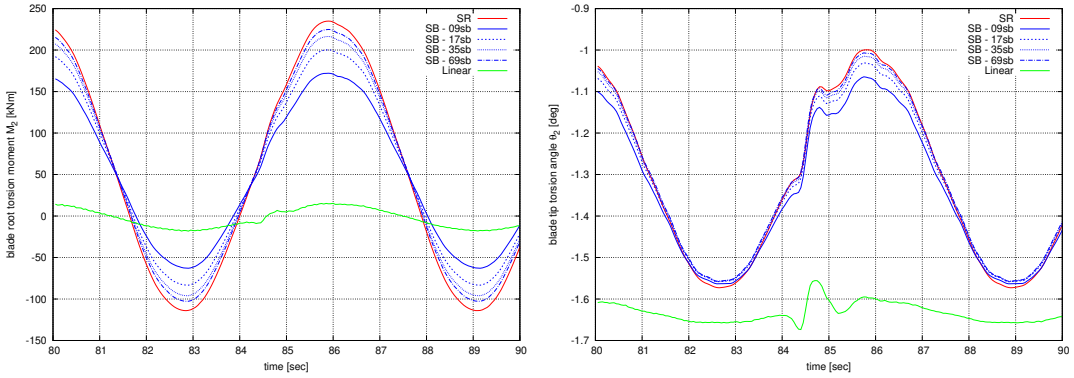

(A) (B)

FIGURE 5.23: DTU 10-MW RWT RWT rotor under uniform inflow: time series of blade torsion (a) root moment M_2 and (b) tip angle θ_2.

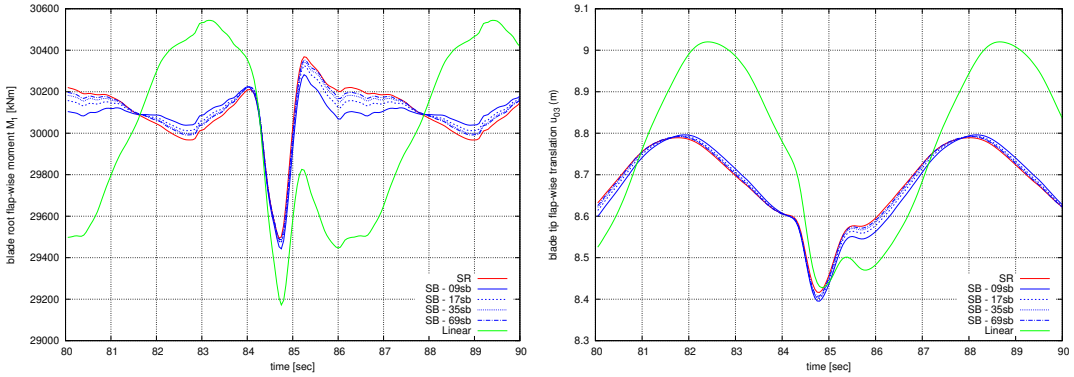

(A) Blade root flap-wise moment M_1 about the $\boldsymbol{E}_1$ axis.

(B) Blade tip flap-wise translation u_{03} along the $\boldsymbol{E}_3$ axis.

FIGURE 5.24: DTU 10-MW RWT RWT rotor under uniform inflow: time series of blade flap-wise (a) root moment M_1 and (b) tip translation u_{03}.

The DTU 10-MW RWT under turbulent (stochastic) inflow

The onshore version of the DTU 10-MW RWT is analyzed under a stochastic inflow. The aim of the analysis is to assess the loads of the turbine in accordance with the specification of the IEC 61400-1 standard (IEC, 2003-2004) and to identify differences in the predictions of the various modeling options (linear, SB and SR models). Three realizations of 10 minutes each are simulated per wind speed bin. For assessing the fatigue limit state (FLS), the design

load case (DLC) 1.2 is considered, where a normal turbulence model (NTM) in normal operation is used. For assessing the ultimate limit state (ULS), the DLC 1.3 is considered where an extreme turbulence model (ETM) in normal operation is used. Two additional cases are examined for the ultimate load analysis, the DLC 6.1 and 6.2 considering the wind turbine in idling mode under extreme wind conditions (EWM). The definition of the performed DLCs is given in table 5.6. The wind turbine class is 1A that designates the category for higher

TABLE 5.6: The data associated with each DLC according to the IEC.

DLC	Wind	Wind Speed (m/s)	Yaw Error	Analysis	SF	Runs
1.2	NTM	$05-25,\ step=2$	0^o	FLS	-	11×3
1.3	ETM	$11-25,\ step=2$	0^o	ULS	1.35	8×3
6.1	EWM	50	$0^o, \pm 8^o$	ULS	1.35	3×3
6.2	EWM	50	$\pm 15^o, \pm 30^o,$ $\pm 45^o, \pm 60^o$	ULS	1.10	8×3

turbulence characteristics. The effects of wind shear (shear exponent = 0.20), tower shadow and wind inclination (= 8^o) are considered according to IEC 61400-1 standard. The stochastic wind inflow is based on the Kaimal spectrum and is generated in a polar grid consisting of 64 x 32 points along the periphery and the radius, respectively. Wind velocities at given positions are derived through linear interpolation. Furthermore, the wind turbine is operated in closed loop (i.e. the controller is activated). The FEM mesh consists of 35 elements for each blade (as previously) and of 20 elements for the tower. The sub-bodies discretization (in the SB model) amounts 35 sub-bodies with one element each for the blades and 5 sub-bodies with 4 elements each for the tower.

In table 5.7, the damage equivalent loads (DELs) of the wind turbine components are shown for the SR, the SB and the linear model. The SR solution is chosen as the reference one, compared to which the relative percentage differences are given for the SB and the linear model. The DELs are computed assuming a lifetime of 20 years and 107 reference cycles. The considered Wöhler coefficients are m = 10 for the blades, m = 8 for the shaft, and m = 4 for the steel tower, whereas the Weibull parameters are C = 11.3 m/s and k = 2. Similar

TABLE 5.7: Fatigue loads (DEL's) analysis results from DLC 1.2. Comparison between the SR, SB-35 and linear beam models.

Signal	SR DEL (kNm)	SB diff (%)	Lin. diff (%)
Blades root edge-wise moment	28291	0.4	1.4
Blades root flap-wise moment	34378	0.2	−0.5
Blades root pitching moment	437	−1.6	−36.9
Shaft torque	4814	0.3	0.5
Shaft yawing moment at main bearing	30567	0.1	−1.7
Shaft tilt moment at main bearing	32447	0.2	−0.6
Tower base side-to-side bending moment	57516	4.7	4.6
Tower base fore-aft bending moment	118409	0.5	−0.5
Tower base yawing moment	29573	0.6	0.1

blade fatigue loads are predicted by all modeling options, except for the blades root pitching moment where the deviation in relation to the SR approach is -37% for the linear model. The SB model with 35 sub-bodies predicts slightly lower DEL (1.6%) being in-line with the results of fig. 5.23. Slightly higher DELs are predicted by the linear and the SB model for the tower base side-to-side bending moment (4.6-4.7%), while the DEL of the tower base fore-aft bending moment, which is directly excited by the wind, is in good agreement for all models (absolute value of relative percentage differences of 0.5% are obtained). The other loads are very similar for both the SB and the linear model (absolute value of relative percentage differences are below 1.7%).

In table 5.8, the results of the ultimate load analysis are shown. The maximum absolute value

TABLE 5.8: Ultimate load analysis results from DLC 1.3, 6.1 and 6.2. Comparison between the SR, SB-35 and linear beam models.

	SR	SB	Lin.	
Signal (moments)	Max Loa (kNm)	diff (%)	diff (%)	DLC
Blades root edge-wise	31244	5.1	42.4	$6.2-30^o$
Blades root flap-wise	61240	0.3	2.4	$1.3-13m/s$
Blades root pitching	934	4.0	-8.0	$6.2-330^o, 315^o, 8^o$
Blades root combined	64354	0.3	1.8	$1.3-13m/s$
Shaft torque	16907	0.1	0.1	$1.3-25m/s$
Shaft yawing at main bearing	52389	1.2	1.2	$1.3-25m/s$
Shaft tilt at main bearing	59322	0.1	21.9	$1.3-25m/s\,(nl), 6.2-30^o\,(l)$
Shaft combined at main bearing	64306	0.5	13.0	$1.3-25m/s\,(nl), 6.2-30^o\,(l)$
Tower base side-to-side bending	460076	2.9	-2.2	$6.2-45^o$
Tower base fore-aft bending	327059	0.9	7.7	$1.3-13m/s\,(nl), 6.2-30^o\,(l)$
Tower base yawing	54538	0.1	-0.6	$1.3-25m/s$
Tower base combined	509105	4.2	11.3	$6.2-45^o, 45^o, 30^o$

of the moments is provided for the SR model, while for the SB and the linear model the relative percentage differences are given, as previously. Moreover, the DLC per load signal at which the ultimate load occurs is presented in the last column (the DLC id and either the wind speed for DLC 1.3 or the yaw misalignment for the idling DLCs 6.X). A single DLC is provided in case it is the same for all beam models, while two DLCs are given in case there are differences between the non-linear (nl) and the linear (l) modeling. For the two non-linear models the driving DLCs are the same for all signals.

Differences between the two non-linear models do not exceed 5%. Higher absolute values of relative percentage differences are obtained for the blade root edgewise and pitching moment and for the tower side-to-side and combined moment. What is common in all the above signals is the driving DLC, which is the idling case DLC 6.2. Ultimate loads in idling mode mostly appear when instabilities due to negative aerodynamic damping take place. Parked or idling rotors, experiencing extreme wind speeds, are likely to encounter high angles of attack within the post-stall region (Wang, Riziotis, and Voutsinas, 2017). Whether these high angles of attack will appear depends on the inclination of the topography, the tilt angle of the nacelle, as well as the yaw misalignment of the inflow, static or dynamic (due to the wind turbulence). Such high angles of attack may give rise to stall-induced, edge-wise vibrations

on the blades, which, on many occasions, drive the design loads. In this case, slightly different loads between the two non-linear models may be predicted. Differences due to the model fidelity may appear (i.e. the ability of the SB model to capture non-linear effects depends on the number of sub-bodies considered), but also due to the stochastic nature of the idling DLCs that cannot be completely eliminated by considering the same turbulent wind inflow. This is because small accumulated differences in the rotor azimuth might give rise to different loads due to the different wind velocity seen by the blades. Differences in the remaining signals that are driven by the operational DLC 1.3 remain small, in the order of 1%.

On the contrary, significantly high differences between the predictions of the two non-linear models versus the linear model are encountered. The highest deviation concerns the blade root edgewise moment (42.4%), obtained in DLC 6.2 at 30^o yaw misalignment. As mentioned, in this DLC, significant edgewise vibrations on the rotor appear that are over-predicted by the linear beam model. The same holds for all the other loading signals that are affected by the excessive blade (edge-wise) loading (i.e. the shaft tilt and combined moment and the tower fore-aft and combined moment). For these signals, the ultimate value is obtained in DLC 6.2 at 30^o, which is different to the ones predicted by the non-linear models. It should be mentioned that the three beam models share the same aero-dynamic module, i.e., the BEMT based method combined with the ONERA dynamics stall model that is considered in all the simulations of table 5.6. Consequently, the differences in the edgewise moments in the present analyses are driven by the structural model considered. They are due to the geometrically non-linear bending-tension coupling effect that cannot be accounted for by the linear model. In the nonlinear models, tension force gradually increases as the blade bends (i.e., when stall vibrations appear). As a result, virtual bending stiffening of the blade takes place which has a relieving effect on edgewise vibrations. This implies that in the occurrence of stall induced vibrations on parked or idling rotors, the loads predicted by a linear structural model are always more conservative than those obtained by a geometrically nonlinear one. The second notable difference between the predictions of the two non-linear models versus the linear model concerns the blade pitching moment (-8%) that has been sufficiently discussed in the previous sections. It is due to the geometrically non-linear bending-torsion coupling effect that cannot again be predicted by the linear model.

To further elaborate on the above findings, time series and power spectral density (PSD) plots for selected load signals are presented in the sequel. Safety factors have not been considered in the plots, as opposed to the loads in table 5.8. The analysis is exclusively focused on the loads assessment, while expected differences in the deformations due to non-linear effects have been discussed in the previous sections. In fig. 5.25, the time series and the PSD plot of the blade root edgewise bending moment resulting from DLC 6.2 at 30^o yaw misalignment are shown. The time series demonstrate that the linear model significantly over-predicts the moment amplitudes due to stall vibrations, while the two non-linear models predict very similar load response. In the PSD plot, the frequency peak of the three rotor edgewise modes (note the pitch setting of 90^o in idling DLCs 6.X) and especially of the 1st edgewise asymmetric mode at 0.8Hz are higher than the non-linear ones. In fig. 5.26, the pitching moment of the blade at the root is shown from DLC 1.3 at 11m/s. This wind speed is close to the

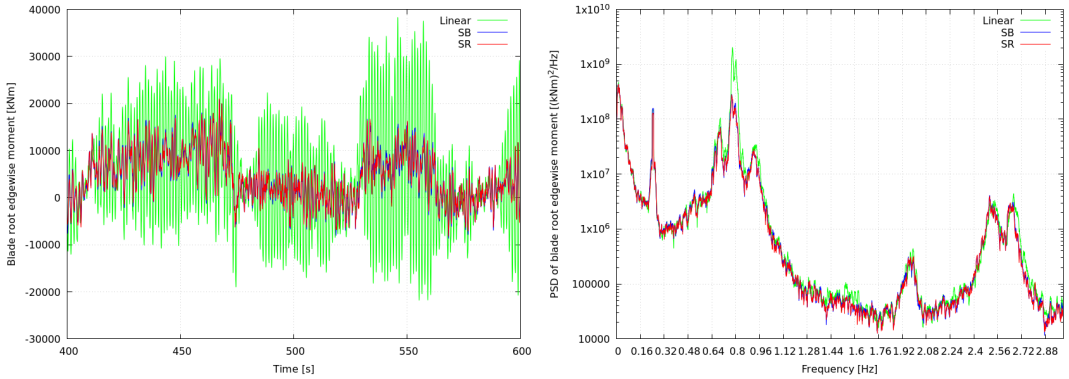

(A) (B)

FIGURE 5.25: DTU 10-MW RWT under stochastic inflow (DLC 6.2-30°): (a) time series and (b) PSD of the blade root edgewise bending moment M_3.

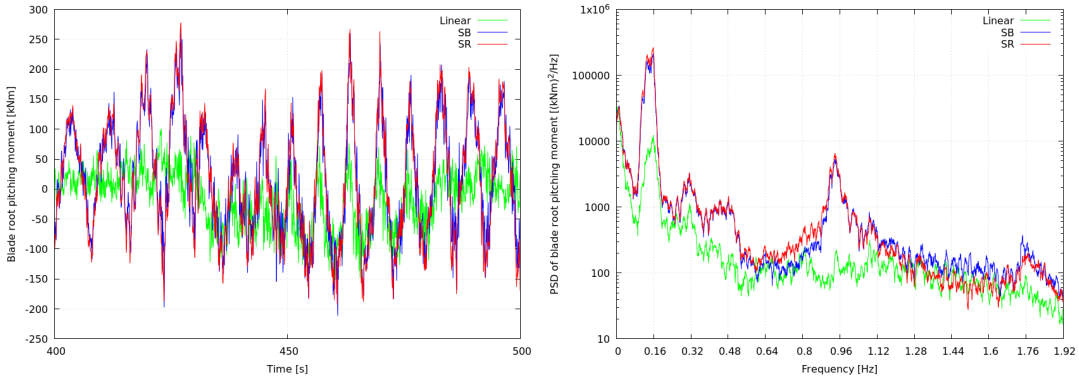

(A) (B)

FIGURE 5.26: DTU 10-MW RWT under stochastic inflow (DLC 1.3-11m/s): (a) time series and (b) PSD of the blade root pitching moment M_2.

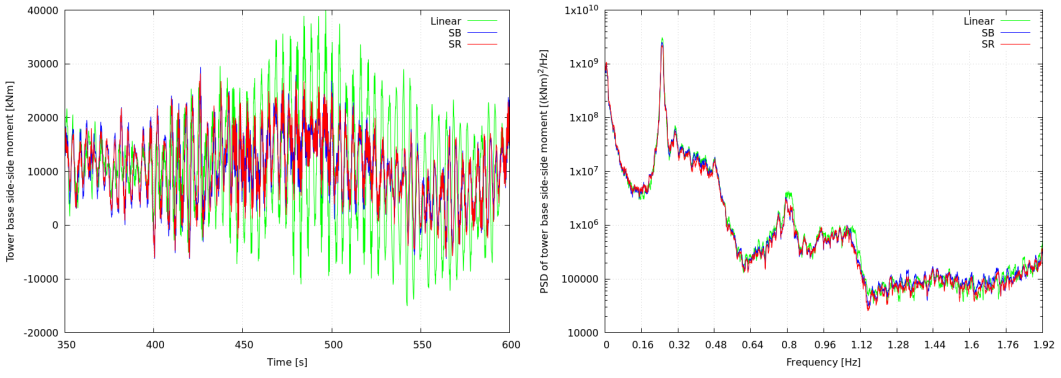

(A) (B)

FIGURE 5.27: DTU 10-MW RWT under stochastic inflow (DLC 1.3-11m/s): (a) time series and (b) PSD of the tower base side-side bending moment M_1.

rated speed of the DTU-10MW RWT (11.4m/s) and the highest flapwise deflections are anticipated that give rise to the geometrically non-linear bending-torsion coupling effect. As seen in previous sections the linear model predicts significantly lower moment amplitudes,

while the non-linear models are in good agreement. The SB-35 model predicts slightly lower moment amplitudes as compared to the SR model that can be increased by further increasing the SB discretization. The PSD plot shows that the linear model under predicts all frequency peaks, i.e. at the 1P, 2P and 3P excitation frequencies at 0.16Hz and its multiples, at the 1st rotor in-plane asymmetric horizontal frequency at 0.96Hz and also at the 1st rotor edgewise symmetric free-free frequency at 1.77Hz. In fig. 5.27, the tower base side-to-side bending moment is presented for the same case (DLC 1.3 at 11m/s). Although the maximum value of this load is depicted in DLC 6.2 at 45^o yaw misalignment (see table 5.8), the selected plots are included to demonstrate the obtained differences between the linear and the non-linear modeling. During normal operation the side-side tower (and the rotor edgewise direction) is low damped. Aerodynamic damping mainly affects the rotor flapwise and the tower fore-aft direction. In the time series plot, the linear model predicts significantly higher load amplitudes within the range 450-600s that mainly correspond to the frequency of the 1st tower side-side bending mode at 0.25 Hz, as shown in the PSD plot.

5.8 Conclusions

In the present work, the geometrically exact SR beam model was integrated into the multi-body dynamics aeroelastic code hGAST, following a strain-invariant implementation. Along this line, the original beam model was enriched by the multi-body inertia terms. Moreover, the SR beam model was extended to general-shaped cross-sections with anisotropic composite material couplings such as the material bend-twist coupling effect that is used in wind turbine blades as a passive load control mechanism for loads mitigation. Numerical comparisons between the two most popular modeling options amongst Wind Energy community, the SR model and the existing SB model, which predicts the geometric non-linearity through a multi-body approach at the body level, were performed. The two models have been developed within the same tool, as opposed to other similar works. The obvious advantage of the above approach is that possible deviations or uncertainties related to the numerical details of the models and the modeling assumptions considered are eliminated. In addition, the results of the linear Timoshenko beam model were added in selected cases to provide a quantitative measure of the non-linearity.

Comparisons of the two non-linear beam models indicate that both modeling options can accurately predict geometrically non-linear effects due to large deflections. Their main difference is that as non-linearities become more pronounced, the number of sub-bodies used in the multi-body analysis need to increase in order to accurately capture these effects. On the other hand, the SR beam model provides the same level of accuracy at all conditions (in terms of the deflections) without increasing the spatial discretization. In SR model, the geometric exactness is preserved at the beam level, as opposed to the SB model where the geometrically non-linear effects are only accounted for at the connecting nodes of the multi-body formulation. The almost perfect agreement of the grid independent solutions by the two models with benchmark cases suggests that the SR beam model has been consistently incorporated within hGAST and that both models are adequate for simulating highly flexible wind turbine blades

with anisotropic composite material couplings undergoing large deformations. As far as the IEC-based load analysis is concerned, the agreement of the two non-linear models is satisfactory when a reasonable number of elements and sub-bodies is considered (35) that does not however absolutely pursue grid independency. Specifically, in normal operation cases, the SB model slightly over-predicts the ultimate loads (1%), whereas in idling cases (when instabilities exist) the maximum difference is 5%. This is because the SR model achieves discretization-independency faster (i.e., with lower number of elements).

Comparisons against the linear beam model indicate that the non-linear models predict higher blade torsional moments during normal operation due to the bending-torsion coupling effect that is mostly triggered near the rated wind speed where the flapwise deflections attain their maximum value. The bending moments of the main turbine components are still well captured by the linear model during normal operation. On the contrary, the non-linear models may predict lower design loads when stall-driven instabilities occur. For example, for the DTU-10MW RWT considered in the present analysis, the ultimate design load of the blade edgewise moment was over-predicted by the linear model (+42.4%) when the idling operation mode of the turbine was simulated under the 50-year storm conditions. The above suggest that the linear models can be still used in the design/certification process of the main turbine components, as non-linear effects marginally affect the loads. However when instabilities do exist, the linear model is conservative as it omits the non-linear couplings that tend to suppress instabilities. The linear model may only provide smaller loads in case the non-linear coupling effect is pronounced and is significantly affecting the obtained load amplitude, as for example the blade pitching moment of the blade (near rated conditions) due to the bending-torsion coupling effect.

Chapter 6

Overview and outlook

6.1 Overview

The present thesis had three main objectives:

1. The study of two beam models that are available in the literature for solving spatial beam-like structures, which are slender and undergo large translations and rotations, but small strains.

2. The study of two time integration algorithms that are available in the literature for solving problems with large rotations in time domain.

3. The extension of the multi-body dynamics, aeroelastic code hGAST regarding its structural dynamics part. This improvement refers to the incorporation of a geometrically exact beam model for the simulation of the wind turbine blades, and the modification of the solution procedure such as to be consistent with the rotation manifold SO(3).

With respect to the first objective, two models for geometrically non-linear shear deformable 3D beams with small strains that are derived from different working pairs are compared. The first one is the Simo-Reissner model (Simo, 1985), whereas the second one is the 1D formulation of a degenerate-continuum beam model which uses the Green-Lagrange strains (Dvorkin, Onate, and Olivier, 1988). The derivation was made in a way so that one may have a clear comparison with the SR model. Two different (regarding rotations) formulations, the iterative and the invariant, are tested within the framework of these two models. The geometric illustration given on the rotation manifold SO(3) clarifies the way of creating an invariant 3D beam element with large rotations: one should refer to the same tangent space on SO(3) when interpolation is performed. Four versions of a geometrically non-linear finite element formulation are derived (SR invariant, GL invariant, SR iterative, GL iterative) and used in 2D and 3D examples. The numerical results compare the proposed invariant formulation of the GL model to the other three finite element formulations and the strain measures between the four of them. The main conclusions are the following: 1) It is verified numerically that the model based on the Green-Lagrange strains gives a different approximation inside the element compared to the model that uses the Simo-Reissner strains, because in this case the neutral axis changes during deformation. 2) The incorporation to the GL model of the update procedure that splits the rotation into a rigid-body part and a local cross-sectional part,

offers the invariance properties to this beam formulation. This implementation may be combined with all the beam models with small strains that use spin parameters as the rotational unknowns. 3) The invariant formulation, either in the SR or in the GL model, is more suitable for problems with 3D large rotations. 4) The SR and GL beam models require similar computational cost to converge to the correct solution.
With respect to the second objective, the following time integration schemes for rotational rigid-body dynamics have been studied: a) Simo's & Vu-Quoc's (Simo and Vu-Quoc, 1988), b) 3 versions of Mäkinen's / Cardona's & Géradin's scheme (Mäkinen, 2001; Cardona and Géradin, 1988)

- Mäkinen's (non consistent linearization and update),
- Cardona's & Géradin's (non consistent linearization yet consistent update), and
- consistent linearization and consistent update.

The difference between these two algorithms, which is the motivation of their comparison in this work, is that the Newmark scheme is applied on the angular velocities and accelerations in the first algorithm, while this scheme is applied on the first and second derivatives of the rotation vector in the second algorithm. The conclusions that came up from the numerical results of the heavy symmetrical top are summarized.
For a short simulation time: The versions of a non consistent and consistent update of the second scheme give a more accurate result in large time step than Simo's & Vu-Quoc's algorithm. They also present a small shift in the period that results the solution to be ahead of the exact one, whereas Simo's & Vu-Quoc's algorithm gives a periodicity in oscillation that remains behind of the exact solution.
For a long simulation time: Simo's & Vu-Quoc's algorithm seems to be more stable than the 3 versions of Mäkinen's / Cardona's & Géradin's algorithm. The scheme with the consistent update (either with a consistent linearization or with a non consistent linearization) has a better behaviour regarding the 'blown-up' issue than the algorithm with the non consistent update.

With respect to the third objective, the geometrically exact SR beam model has been incorporated into the multi-body dynamics, aeroelastic code hGAST, following a strain-invariant implementation. The SR model has been extended to general-shaped cross-sections with an inhomogeneous and anisotropic material. Comparisons between the SR and the SB model, that predicts the geometric non-linearity through a multi-body approach at the body level, are performed. Either the benchmark examples in statics, or the aeroelastic computations show that the geometrically exact beam predicts the torsional deformation state more sufficiently compared to the sub-body modeling. The last one needs many sub-bodies to converge to the solution given by the SR model.

6.1.1 Novelties

Statics of beam structural members is investigated. Through this thorough study, a new beam model is proposed combining the theory that uses the Green-Lagrange strain measures and the strain invariant formulation for the linearization of the weak form and the finite element discretization. This model, the so-called *GL* model, results from a degenerate continuum formulation after integrating analytically the cross-sectional integrals and defining appropriately the elastic properties of the cross-section that appear in the resulting 1D equilibrium equations. Having the equations in 1D integration form derived, a linearization and discretization procedure follow. A strain-invariant formulation is chosen to be applied in order to improve the numerical performance of the beam model. Along this line, the error in strains induced by a rigid-body rotation of the element disappears. This is depicted in the numerical results given for the so-called *GL invariant* model in contrast to the original *GL iterative* model. Furthermore, the numerical comparison between the GL and the SR models is for the first time reported in the literature. This is depicted in the strain difference between the GL and SR models that is computed at the Gauss point inside the finite element. On the other hand, the theoretical comparison is presented in a consistent way, meaning that the derived generalized strains of the GL model are given in a vector form that is directly compared to the corresponding vector form of the generalized strains used by the SR model.
Regarding dynamics, the investigation of a rigid-body dynamics example (the heavy symmetrical top) shows interesting properties of the two time integration algorithms that have been studied. The distinct difference between these two Newmark-type schemes is that they use different kinematic parameters inside the Newmark relations, i.e. the one uses the angular velocities and accelerations, while the other uses the first and second derivatives of the rotation vector. The accuracy and stability of the algorithms are depicted on the time series graphs that show the response (nutation and precession angles, energy, momentum) along time. This study constitutes a first step of a thorough comparison between these time integration schemes that does not appear in the literature.
When the one of the two time integration schemes is applied on beam dynamics, the resulting solution procedure can be used to solve the equation of motion of the wind turbine blades. In this case, the original SR model is extended to include the couplings because of the generality of the cross-sectional shape, as well as the heterogeneity and the anisotropy of the material. The original SR model is also enriched by the inertia terms that are necessary for a multi-body dynamics formulation. Its integration in the hydro-servo-aeroelastic tool hGAST constitutes an improvement of the software, since, until now the sub-body technique has been used for the modeling of the wind turbine blades. The sub-body technique is not a geometrically exact one, in contrast to the SR modeling. Both techniques (the sub-body and the geometrically exact one) are now included in the same multi-body dynamics framework for having a direct comparison between them. This is presented for the first time in the literature; the obvious advantage is that possible deviations or uncertainties related to the numerical details of the models (e.g. time integration scheme), to modeling assumptions (e.g. modeling of lumped properties such as the generator inertia or nacelle mass) or to the imposed external excitation (e.g. calculation of aerodynamic loads) are eliminated.

6.2 Outlook

There are several aspects of beam analysis worth exploring.

1. Further research can be performed in the direction of the generalization of the geometrically exact beam theory models presented in this thesis. This means that additional degrees of freedom should be added in order to capture the deformation of the cross-section. The warping and distorsional phenomena predicted by such an advanced beam model have already been presented in Argyridi, 2019 and similar references, thus, a study that would combine this work with the geometrically exact GL or SR beam models in their invariant (or even their iterative) form could be a very promising future task.

2. As a result from the previous higher order beam theory implementation, the effect of the end restraints can be investigated either in statics or in dynamics, since the stress evaluation nearby the constraints could be achieved. Along this line, the local buckling effects of a wind turbine blade could be studied.

3. Open questions in the field of the material non-linearity could also be answered. As it is described above, the main advantage of using a general displacement field is that a full stress and strain field can be obtained on each material point of the cross section and, therefore, a large set of constitutive equations can be employed. As it is noted in Hodges, 2006: Applications in civil engineering with steel-reinforced concrete demand at least an elastic-plastic model. Most composites today tolerate larger shear strain and is better treated with non-linear elastic models. Finally, the progress in the area of visco-elasto-plasticity allows treatment of beams made of elastomers and contributes to the modeling of damping in structures.

4. Another possible contribution in further works can be given by the extension of the present formulation to coupled thermal-mechanics problems. Again, the constitutive part should be altered for including the full thermodynamical laws in the theory and the corresponding treatment in numerical simulations.

5. An extension of the present work to geometrically exact shell elements could also be a very interesting future task. Shell elements is another type of structural elements widely applied in several areas of engineering, e.g., in civil, aerospace, and mechanical engineering.

6. Regarding the numerical part of the work, further research can be done on the structural anisotropy with respect to the interpolation functions used when the constitutive matrix of the cross-section is fully populated. The so-called linked interpolation could be investigated, whereby the interpolations of the displacement field depends not only on the nodal displacements, but also on the nodal rotations. Although a previous work has been presented in the literature (Jelenić and Papa, 2011; Dukić and Jelenić, 2014; Dukić, Jelenić, and Gaćeša, 2014), there are still open questions for higher-order beam elements in non-linear analysis.

7. To improve further the dynamics of beams, and also, the hydro-servo-aeroelastic tool hGAST, the time integration algorithm could be upgraded in order to consider about the total energy and momentum preservation. In this case, numerical instabilities can be avoided, and therefore, the numerical results in large rotations regime can be improved. In companion to the conservation properties of the time integration algorithm, the strain invariance is an issue that is good to be considered, when the algorithm is applied on beams.

Appendix A

Linearization of the internal virtual work about the configuration at $t + \Delta t$

A.1 Linearization of the internal virtual work for the SR beam model

For the linearization of the internal virtual work about $t + \Delta t$, the directional derivative w.r.t. ϵ, for $\epsilon = 0$, is employed in eq. (3.15); at the same time, a conservative external loading is assumed. Thus, the linearized equilibrium equation is derived as follows

$$\int_{0_L} \left(C^F_{jk}\, d\Gamma_k\, \delta\Gamma_j + C^M_{jk}\, dK_k\, \delta K_j \right) d\xi + \int_{0_L} \left({}^{t+\Delta t}F_j\, d\delta\Gamma_j + {}^{t+\Delta t}M_j\, d\delta K_j \right) d\xi$$
$$= {}^{t+\Delta t}\mathcal{R} - \int_{0_L} \left({}^{t+\Delta t}F_j\, \delta\Gamma_j + {}^{t+\Delta t}M_j\, \delta K_j \right) d\xi; \qquad j,k = \xi,\eta,\zeta \tag{A.1}$$

where $\delta\Gamma_j$ and δK_j are the components of eqs. (3.16) and (3.17). By interchanging δ with d one may have the corresponding expressions for the infinitesimal strains $d\Gamma_k$, dK_k. C^F_{jk} and C^M_{jk} are given by the components of eq. (3.14), while F_j and M_j are given by the components of eqs. (3.12) and (3.13). Finally, $d\delta\Gamma_j$ and $d\delta K_j$ are derived by the infinitesimal change of eqs. (3.16) and (3.17) w.r.t. the position $\boldsymbol{r}_0$ and the orientation $\boldsymbol{\Lambda}$, see e.g. Krenk, 2009

$$d\delta\Gamma_j = \delta\boldsymbol{\psi}^T \left(\boldsymbol{V}_i\times\right) d\boldsymbol{r}_{0,\xi} - \delta\boldsymbol{r}^T_{0,\xi} \left(\boldsymbol{V}_i\times\right) d\boldsymbol{\psi} + \delta\boldsymbol{\psi}^T \left(\boldsymbol{V}_i \boldsymbol{r}^T_{0,\xi} - \boldsymbol{V}_i^T \boldsymbol{r}_{0,\xi} \boldsymbol{I} \right) d\boldsymbol{\psi} \tag{A.2}$$

$$d\delta K_j = -\delta\boldsymbol{\psi}^T_{,\xi} (\boldsymbol{V}_i\times)\, d\boldsymbol{\psi} \tag{A.3}$$

For $d\delta\Gamma_j$ and $d\delta K_j$ with $j = \xi,\eta,\zeta$, the vectors $\boldsymbol{V}_i$ with $i = 1-3$ are used, correspondingly.

A.2 Linearization of the internal virtual work for the GL beam model

For the linearization of the internal virtual work the directional derivative w.r.t. ϵ, for $\epsilon = 0$, is employed in eq. (3.21); at the same time, the external loading is assumed conservative.

$$\int_{{}^0V} C_{ijrs}\, d\epsilon_{rs}\, \delta\epsilon_{ij}\, d^0V + \int_{{}^0V} {}^{t+\Delta t}S_{ij}\, d\delta\epsilon_{ij}\, d^0V = {}^{t+\Delta t}\mathcal{R} - \int_{{}^0V} {}^{t+\Delta t}S_{ij}\, \delta\epsilon_{ij} d^0V; \quad i,j,r,s = \xi,\eta,\zeta \tag{A.4}$$

where $d\epsilon_{rs}$ are the infinitesimal strain components that are given by the same relations as the virtual ones (eq. (3.22)) by interchanging δ with d, ${}^{t+\Delta t}S_{ij}$ is given by eq. (3.19), and $d\delta\epsilon_{ij}$ is derived by taking the infinitesimal change of eq. (3.22) w.r.t. the translation $\boldsymbol{u}_0$ and the cross-sectional directors $\boldsymbol{V}_2,\ \boldsymbol{V}_3$.

Substituting into the eq. (A.4) the strain and stress definitions (eqs. (3.18) and (3.19)), the virtual and infinitesimal strains (eq. (3.22)), and taking into account the 1D strain measures (eqs. (3.33) to (3.35), (3.41) and (3.43)) and stress resultants (eqs. (3.28) to (3.30), (3.36) to (3.38) and (3.42)), the following terms of the linearized, w.r.t. ϵ for $\epsilon = 0$, 1D internal virtual work equation are derived. The same result is derived after the linearization of the 1D expressions (see eqs. (3.26) and (3.27)).

- Material ('mat') stiffness terms in relation to normal ('n') and shear ('s') stresses that result to the material stiffness matrix

$$\begin{aligned} d\delta W_{\text{int,mat,n}}(\xi) &= \int_{{}^0V} (C_{\xi\xi\xi\xi} d\epsilon_{\xi\xi}\, \delta\epsilon_{\xi\xi})\, d^0V \\ &= \int_{{}^0L} \{EA\ (\delta\Gamma_\xi\, d\Gamma_\xi) + EI_\zeta\ (\delta K_\zeta\, dK_\zeta + \delta\Gamma_\xi\, dK_{\zeta,nl,2} + \delta K_{\zeta,nl,2}\, d\Gamma_\xi) \\ &\quad + EI_\eta\ (\delta K_\eta\, dK_\eta + \delta\Gamma_\xi\, dK_{\eta,nl,2} + \delta K_{\eta,nl,2}\, d\Gamma_\xi) \\ &\quad + EI_{\eta 2}\ (\delta K_{\eta,nl,2}\, dK_{\eta,nl,2}) + EI_{\zeta 2}\ (\delta K_{\zeta,nl,2}\, dK_{\zeta,nl,2}) \\ &\quad + EI_{\zeta\eta}\ (\delta K_{\zeta,nl,2}\, dK_{\eta,nl,2} + \delta K_{\eta,nl,2}\, dK_{\zeta,nl,2} + \delta K_{\zeta\eta,nl,2}\, dK_{\zeta\eta,nl,2})\}\ d\xi \end{aligned} \tag{A.5}$$

$$\begin{aligned} d\delta W_{\text{int,mat,s}}(\xi) &= \int_{{}^0V} (2C_{\xi\eta\xi\eta} d\epsilon_{\xi\eta}\, 2\delta\epsilon_{\xi\eta} + 2C_{\xi\zeta\xi\zeta} d\epsilon_{\xi\zeta}\, 2\delta\epsilon_{\xi\zeta})\, d^0V \\ &= \int_{{}^0L} \{k_\eta GA\, (\delta\Gamma_\eta\, d\Gamma_\eta) + k_\zeta GA\, (\delta\Gamma_\zeta\, d\Gamma_\zeta) + k_\xi GI_p\, (\delta K_\xi\, dK_\xi)\}\ d\xi \end{aligned} \tag{A.6}$$

The infinitesimal strain measures $d\Gamma_\xi$; $d\Gamma_\eta$; $d\Gamma_\zeta$, dK_ξ; dK_η; dK_ζ and $dK_{\eta,nl,2}$; $dK_{\zeta,nl,2}$; $dK_{\zeta\eta,nl,2}$ are given using the same relations with the virtual ones (eqs. (3.47) to (3.51)), by interchanging δ with d.

- Geometric ('$geom$') stiffness terms in relation to normal ('n') and shear ('s') stresses that result to the geometric stiffness matrix

$$
\begin{aligned}
d\delta W_{\text{int,geom},n}(\xi) &= \int_{0_V} ({}^{t+\Delta t}S_{\xi\xi}\, d\delta\epsilon_{\xi\xi})\, d^0V \\
&= \int_{0_L} \big({}^{t+\Delta t}F_\xi\, d\delta\Gamma_\xi + {}^{t+\Delta t}M_\eta\, d\delta K_\eta + {}^{t+\Delta t}M_\zeta\, d\delta K_\zeta + \\
&\quad {}^{t+\Delta t}M_{R1}\, d\delta K_{\eta,nl,2} + {}^{t+\Delta t}M_{R2}\, d\delta K_{\zeta,nl,2} + {}^{t+\Delta t}M_{R3}\, d\delta K_{\zeta\eta,nl,2}\big)\, d\xi
\end{aligned} \tag{A.7}
$$

$$
\begin{aligned}
d\delta W_{\text{int,geom,s}}(\xi) &= \int_{0_V} \big({}^{t+\Delta t}S_{\xi\eta}\, 2d\delta\epsilon_{\xi\eta} + {}^{t+\Delta t}S_{\xi\zeta}\, 2d\delta\epsilon_{\xi\zeta}\big)\, d^0V \\
&= \int_{0_L} \big({}^{t+\Delta t}F_\eta\, d\delta\Gamma_\eta + {}^{t+\Delta t}F_\zeta\, d\delta\Gamma_\zeta + {}^{t+\Delta t}M_\xi\, d\delta K_\xi\big)\, d\xi
\end{aligned} \tag{A.8}
$$

where the components $d\delta\Gamma_\xi$; $d\delta\Gamma_\eta$; $d\delta\Gamma_\zeta$, $d\delta K_\xi$; $d\delta K_\eta$; $d\delta K_\zeta$ and $d\delta K_{\eta,nl,2}$; $d\delta K_{\zeta,nl,2}$; $d\delta K_{\zeta\eta,nl,2}$ are derived by taking the infinitesimal change of eqs. (3.47) to (3.51) with respect to the position $\boldsymbol{r}_0$ and the orientation $\boldsymbol{V}_i$; $i = 1 - 3$.

$$d\delta\Gamma_\xi = \delta\boldsymbol{r}_{0,\xi}^T\, d\boldsymbol{r}_{0,\xi} \tag{A.9}$$

$$d\delta\Gamma_\eta = \delta\boldsymbol{r}_{0,\xi}^T\,(-\boldsymbol{V}_2\times)\, d\boldsymbol{\psi} + \delta\boldsymbol{\psi}^T\,(\boldsymbol{V}_2\times)\, d\boldsymbol{r}_{0,\xi} + \delta\boldsymbol{\psi}^T\,(\boldsymbol{V}_2\boldsymbol{r}_{0,\xi}^T - \boldsymbol{V}_2^T\boldsymbol{r}_{0,\xi}\boldsymbol{I})\, d\boldsymbol{\psi} \tag{A.10}$$

$$d\delta\Gamma_\zeta = \delta\boldsymbol{r}_{0,\xi}^T\,(-\boldsymbol{V}_3\times)\, d\boldsymbol{\psi} + \delta\boldsymbol{\psi}^T\,(\boldsymbol{V}_3\times)\, d\boldsymbol{r}_{0,\xi} + \delta\boldsymbol{\psi}^T\,(\boldsymbol{V}_3\boldsymbol{r}_{0,\xi}^T - \boldsymbol{V}_3^T\boldsymbol{r}_{0,\xi}\boldsymbol{I})\, d\boldsymbol{\psi} \tag{A.11}$$

$$d\delta K_\xi = \delta\boldsymbol{\psi}_{,\xi}^T\,(-\boldsymbol{V}_1\times) d\boldsymbol{\psi} \tag{A.12}$$

$$
\begin{aligned}
d\delta K_\eta = {} & (\delta\boldsymbol{\psi}_{,\xi}^T\,[\boldsymbol{V}_3\times] + \delta\boldsymbol{\psi}^T\,[\boldsymbol{V}_{3,\xi}\times])\, d\boldsymbol{r}_{0,\xi} + \delta\boldsymbol{r}_{0,\xi}^T\,([-\boldsymbol{V}_3\times]\, d\boldsymbol{\psi}_{,\xi} + [-\boldsymbol{V}_{3,\xi}\times]\, d\boldsymbol{\psi}) \\
& + \delta\boldsymbol{\psi}^T\,(\boldsymbol{V}_3\boldsymbol{r}_{0,\xi}^T - \boldsymbol{V}_3^T\boldsymbol{r}_{0,\xi}\boldsymbol{I})\, d\boldsymbol{\psi}_{,\xi} + \delta\boldsymbol{\psi}_{,\xi}^T\,(\boldsymbol{V}_3\boldsymbol{r}_{0,\xi}^T - \boldsymbol{V}_3^T\boldsymbol{r}_{0,\xi}\boldsymbol{I})\, d\boldsymbol{\psi} \\
& + \delta\boldsymbol{\psi}^T\,(\boldsymbol{V}_{3,\xi}\boldsymbol{r}_{0,\xi}^T - \boldsymbol{V}_{3,\xi}^T\boldsymbol{r}_{0,\xi}\boldsymbol{I})\, d\boldsymbol{\psi}
\end{aligned} \tag{A.13}
$$

$$
\begin{aligned}
d\delta K_\zeta = {} & (\delta\boldsymbol{\psi}_{,\xi}^T\,[-\boldsymbol{V}_2\times] + \delta\boldsymbol{\psi}^T\,[-\boldsymbol{V}_{2,\xi}\times])\, d\boldsymbol{r}_{0,\xi} + \delta\boldsymbol{r}_{0,\xi}^T([\boldsymbol{V}_2\times]\, d\boldsymbol{\psi}_{,\xi} + [\boldsymbol{V}_{2,\xi}\times]\, d\boldsymbol{\psi}) \\
& - \delta\boldsymbol{\psi}^T\,(\boldsymbol{V}_2\boldsymbol{r}_{0,\xi}^T - \boldsymbol{V}_2^T\boldsymbol{r}_{0,\xi}\boldsymbol{I})\, d\boldsymbol{\psi}_{,\xi} - \delta\boldsymbol{\psi}_{,\xi}^T\,(\boldsymbol{V}_2\boldsymbol{r}_{0,\xi}^T - \boldsymbol{V}_2^T\boldsymbol{r}_{0,\xi}\boldsymbol{I})\, d\boldsymbol{\psi} \\
& - \delta\boldsymbol{\psi}^T\,(\boldsymbol{V}_{2,\xi}\boldsymbol{r}_{0,\xi}^T - \boldsymbol{V}_{2,\xi}^T\boldsymbol{r}_{0,\xi}\boldsymbol{I})\, d\boldsymbol{\psi}
\end{aligned} \tag{A.14}
$$

$$d\delta K_{\eta,nl,2} = \delta\boldsymbol{\psi}_{,\xi}^T\,(\boldsymbol{I} - \boldsymbol{V}_3\boldsymbol{V}_3^T)\, d\boldsymbol{\psi}_{,\xi} \tag{A.15}$$

$$d\delta K_{\zeta,nl,2} = \delta\boldsymbol{\psi}_{,\xi}^T\,(\boldsymbol{I} - \boldsymbol{V}_2\boldsymbol{V}_2^T)\, d\boldsymbol{\psi}_{,\xi} \tag{A.16}$$

$$d\delta K_{\zeta\eta,nl,2} = \delta\boldsymbol{\psi}_{,\xi}^T\,\left(-\boldsymbol{V}_2\boldsymbol{V}_3^T - \boldsymbol{V}_3\boldsymbol{V}_2^T\right)\, d\boldsymbol{\psi}_{,\xi} \tag{A.17}$$

Note that the infinitesimal change of the virtual spins, $d\delta\boldsymbol{\psi}$, has been ignored.

Appendix B

Trigonometric functions

B.1 $\alpha' s$

$$\alpha_0(\Theta) = cos(\Theta), \quad \alpha_1(\Theta) = \frac{sin(\Theta)}{\Theta}, \quad \alpha_2(\Theta) = \frac{1 - cos(\Theta)}{\Theta^2}, \quad \alpha_3(\Theta) = \frac{\Theta - sin(\Theta)}{\Theta^3} \tag{B.1}$$

B.1.1 $\alpha' s \ when \ \Theta = 0$

After evaluating the power series expansions for cos and sin, and substituting $\Theta = 0$ into $\alpha' s$

$$\alpha_0(\Theta) = 1, \quad \alpha_1(\Theta) = 1, \quad \alpha_2(\Theta) = \frac{1}{2}, \quad \alpha_3(\Theta) = \frac{1}{6} \tag{B.2}$$

B.2 $b' s$

$$b_0(\Theta) = -\frac{sin(\Theta)}{\Theta}, \quad b_1(\Theta) = \frac{\Theta cos(\Theta) - sin(\Theta)}{\Theta^3}, \quad b_2(\Theta) = \frac{\Theta sin(\Theta) - 2 + 2cos(\Theta)}{\Theta^4}, \quad b_3(\Theta) = \frac{3sin(\Theta) - 2\Theta - \Theta cos(\Theta)}{\Theta^5} \tag{B.3}$$

B.2.1 $b' s \ when \ \Theta = 0$

After evaluating the power series expansions for cos and sin, and substituting $\Theta = 0$ into $b' s$

$$b_0(\Theta) = -1, \quad b_1(\Theta) = -\frac{1}{3}, \quad b_2(\Theta) = -\frac{1}{12}, \quad b_3(\Theta) = -\frac{1}{60} \tag{B.4}$$

B.3 $c's$

$$
\begin{aligned}
c_0(\Theta) &= \frac{sin(\Theta) - \Theta cos(\Theta)}{\Theta^3} \\
c_1(\Theta) &= \frac{3sin(\Theta) - \Theta^2 sin(\Theta) - 3\Theta cos(\Theta)}{\Theta^5} \\
c_2(\Theta) &= \frac{8 - 8cos(\Theta) - 5\Theta sin(\Theta) + \Theta^2 cos(\Theta)}{\Theta^6} \\
c_3(\Theta) &= \frac{8\Theta + 7\Theta cos(\Theta) + \Theta^2 sin(\Theta) - 15sin(\Theta)}{\Theta^7}
\end{aligned} \tag{B.5}
$$

B.3.1 $c's\ when\ \Theta = 0$

After evaluating the power series expansions for cos and sin, and substituting $\Theta = 0$ into $c's$

$$
c_0(\Theta) = \frac{1}{3}, \quad c_1(\Theta) = \frac{1}{15}, \quad c_2(\Theta) = \frac{1}{90}, \quad c_3(\Theta) = \frac{1}{630} \tag{B.6}
$$

Appendix C

Linearization of the residual in the rotational motion of a rigid-body

In the following, the material incremental rotation vector $\boldsymbol{\Theta}_{n+1}$ is written without the right subscript $_{n+1}$ for convenience.

C.1 Linearization of the residual for the Simo's & Vu-Quoc's and Mäkinen's / Cardona's & Géradin's schemes

The residual at a perturbed state is written as

$$\begin{aligned}\boldsymbol{g}_{n+1}(\boldsymbol{\Theta}+\epsilon\boldsymbol{\Delta\Theta}) = \boldsymbol{J}\boldsymbol{A}_{n+1}(\boldsymbol{\Theta}+\epsilon\boldsymbol{\Delta\Theta}) + \boldsymbol{\Omega}_{n+1}(\boldsymbol{\Theta}+\epsilon\boldsymbol{\Delta\Theta})\times\boldsymbol{J}\boldsymbol{\Omega}_{n+1}(\boldsymbol{\Theta}+\epsilon\boldsymbol{\Delta\Theta}) \\ - \boldsymbol{M}_{n+1}(\boldsymbol{\Theta}+\epsilon\boldsymbol{\Delta\Theta})\end{aligned} \tag{C.1}$$

where $\boldsymbol{\Delta\Theta}$ is a material vector field, interpreted for $\epsilon > 0$, as superposed infinitesimal rotation onto the moving frame at $t = 0$ (Simo's and Vu-Quoc's interpretation) or at t_n (Makinen's, and Cardona's and Géradin's interpretation).
The directional derivative of the residual at a perturbed state is

$$\begin{aligned}D\boldsymbol{g}_{n+1}(\boldsymbol{\Theta},\boldsymbol{\Delta\Theta}) &= \left.\frac{d}{d\epsilon}\right|_{\epsilon=0}[\boldsymbol{g}_{n+1}(\boldsymbol{\Theta}+\epsilon\boldsymbol{\Delta\Theta})] \\ &= \underbrace{\boldsymbol{J}\left.\frac{d}{d\epsilon}\right|_{\epsilon=0}[\boldsymbol{A}_{n+1}(\boldsymbol{\Theta}+\epsilon\boldsymbol{\Delta\Theta})]}_{D\boldsymbol{g}_{\boldsymbol{A}_{n+1}}(\boldsymbol{\Theta},\boldsymbol{\Delta\Theta})} + \underbrace{\left.\frac{d}{d\epsilon}\right|_{\epsilon=0}[\boldsymbol{\Omega}_{n+1}(\boldsymbol{\Theta}+\epsilon\boldsymbol{\Delta\Theta})\times\boldsymbol{J}\boldsymbol{\Omega}_{n+1}(\boldsymbol{\Theta}+\epsilon\boldsymbol{\Delta\Theta})]}_{D\boldsymbol{g}_{\boldsymbol{\Omega}_{n+1}}(\boldsymbol{\Theta},\boldsymbol{\Delta\Theta})} \\ &\quad - \underbrace{\left.\frac{d}{d\epsilon}\right|_{\epsilon=0}[\boldsymbol{M}_{n+1}(\boldsymbol{\Theta}+\epsilon\boldsymbol{\Delta\Theta})]}_{D\boldsymbol{g}_{\boldsymbol{M}_{n+1}}(\boldsymbol{\Theta},\boldsymbol{\Delta\Theta})}\end{aligned} \tag{C.2}$$

C.1.1 Simo's & Vu-Quoc's scheme: consistent linearization of the term that includes the angular velocity

The consistent linearized form of the residual term related to the angular velocity is

$$
\begin{aligned}
D\boldsymbol{g}_{\boldsymbol{\Omega}_{n+1}}(\boldsymbol{\Theta},\Delta\boldsymbol{\Theta}) = & \left.\frac{d}{d\epsilon}\right|_{\epsilon=0}[\boldsymbol{\Omega}_{n+1}(\boldsymbol{\Theta}+\epsilon\Delta\boldsymbol{\Theta})]\times\boldsymbol{J}\boldsymbol{\Omega}_{n+1}(\boldsymbol{\Theta}) \\
& + \boldsymbol{\Omega}_{n+1}(\boldsymbol{\Theta})\times\boldsymbol{J}\left.\frac{d}{d\epsilon}\right|_{\epsilon=0}[\boldsymbol{\Omega}_{n+1}(\boldsymbol{\Theta}+\epsilon\Delta\boldsymbol{\Theta})] \\
& \overset{eq.\ (4.6)}{=} \left(\frac{\gamma}{h\beta}\left.\frac{d}{d\epsilon}\right|_{\epsilon=0}\left[(\boldsymbol{\Theta}+\epsilon\Delta\boldsymbol{\Theta})+\boldsymbol{\Omega}'_n\right]\right)\times\boldsymbol{J}\,\boldsymbol{\Omega}_{n+1}(\boldsymbol{\Theta}) \\
& + \boldsymbol{\Omega}_{n+1}(\boldsymbol{\Theta})\times\boldsymbol{J}\left(\frac{\gamma}{h\beta}\left.\frac{d}{d\epsilon}\right|_{\epsilon=0}\left[(\boldsymbol{\Theta}+\epsilon\Delta\boldsymbol{\Theta})+\boldsymbol{\Omega}'_n\right]\right) \Leftrightarrow
\end{aligned}
$$

$$
\boxed{D\boldsymbol{g}_{\boldsymbol{\Omega}_{n+1}}(\boldsymbol{\Theta},\Delta\boldsymbol{\Theta}) = \frac{\gamma}{h\beta}\Delta\boldsymbol{\Theta}\times\boldsymbol{J}\,\boldsymbol{\Omega}_{n+1}(\boldsymbol{\Theta}) + \boldsymbol{\Omega}_{n+1}(\boldsymbol{\Theta})\times\boldsymbol{J}\,\frac{\gamma}{h\beta}\Delta\boldsymbol{\Theta}} \tag{C.3}
$$

C.1.2 Mäkinen's / Cardona's & Géradin's schemes: non consistent linearization of the term that includes the angular velocity

Neither Mäkinen, 2001 nor Cardona and Géradin, 1988 presents the linearization process of the part of the residual related to the angular velocity term. The modified / non consistent linearized form of this term that is used in the current work, is given by

$$
\boxed{D\boldsymbol{g}_{\boldsymbol{\Omega}_{n+1}}(\boldsymbol{\Theta},\Delta\boldsymbol{\Theta}) = \frac{\gamma}{h\beta}\boldsymbol{T}^T_{n+1}(\boldsymbol{\Theta})\Delta\boldsymbol{\Theta}\times\boldsymbol{J}\boldsymbol{\Omega}_{n+1}(\boldsymbol{\Theta}) + \boldsymbol{\Omega}_{n+1}(\boldsymbol{\Theta})\times\boldsymbol{J}\frac{\gamma}{h\beta}\boldsymbol{T}^T_{n+1}(\boldsymbol{\Theta})\Delta\boldsymbol{\Theta}} \tag{C.4}
$$

C.1.3 Mäkinen's / Cardona's & Géradin's schemes: consistent linearization of the term that includes the angular velocity

By employing the directional derivative on the perturbed form $\boldsymbol{\Omega}_{n+1}(\boldsymbol{\Theta}+\epsilon\Delta\boldsymbol{\Theta})$ of eq. (4.17)

$$
D\boldsymbol{\Omega}_{n+1}(\boldsymbol{\Theta},\dot{\boldsymbol{\Theta}},\Delta\boldsymbol{\Theta}) = \left.\frac{d}{d\epsilon}\right|_{\epsilon=0}\left[\boldsymbol{T}^T_{n+1}(\boldsymbol{\Theta}+\epsilon\Delta\boldsymbol{\Theta})\right]\dot{\boldsymbol{\Theta}} + \boldsymbol{T}^T_{n+1}(\boldsymbol{\Theta})\Delta\dot{\boldsymbol{\Theta}} \tag{C.5}
$$

where

$$
\dot{\boldsymbol{\Theta}}_{n+1} = \frac{\gamma}{h\beta}\boldsymbol{\Theta}_{n+1} + \left(1-\frac{\gamma}{\beta}\right)\dot{\boldsymbol{\Theta}}_n + h\left(1-\frac{\gamma}{2\beta}\right)\ddot{\boldsymbol{\Theta}}_n \tag{C.6}
$$

and

$$
\Delta\dot{\boldsymbol{\Theta}} = \frac{\gamma}{h\beta}\Delta\boldsymbol{\Theta} \tag{C.7}
$$

By taking into account the relation (19) from Ritto-Corrêa and Camotim, 2002, the directional derivative of the transpose of the tangential transformation matrix is given by

$$\begin{aligned} D\boldsymbol{T}_{n+1}^{T}(\boldsymbol{\Theta},\Delta\boldsymbol{\Theta}) = &-\alpha_2(\Theta)\Delta\hat{\boldsymbol{\Theta}} + \alpha_3(\Theta)(\Delta\boldsymbol{\Theta}\boldsymbol{\Theta}^T + \boldsymbol{\Theta}\Delta\boldsymbol{\Theta}^T) \\ &+ b_1(\Theta)(\boldsymbol{\Theta}^T\Delta\boldsymbol{\Theta})\boldsymbol{I} - b_2(\Theta)(\boldsymbol{\Theta}^T\Delta\boldsymbol{\Theta})\hat{\boldsymbol{\Theta}} \\ &+ b_3(\Theta)(\boldsymbol{\Theta}^T\Delta\boldsymbol{\Theta})\boldsymbol{\Theta}\boldsymbol{\Theta}^T \end{aligned} \tag{C.8}$$

The above relation is multiplied by $\dot{\boldsymbol{\Theta}}$ in eq. (C.5). By taking into account the operator $\boldsymbol{\Xi}_{D\boldsymbol{T}^T}(\boldsymbol{a})$ from Cardona and Géradin, 1988, the term $\frac{d}{d\epsilon}\big|_{\epsilon=0}\left[\boldsymbol{T}_{n+1}^{T}(\boldsymbol{\Theta}+\epsilon\Delta\boldsymbol{\Theta})\right]\dot{\boldsymbol{\Theta}}$ from eq. (C.5) is written as

$$\begin{aligned} \boldsymbol{\Xi}_{D\boldsymbol{T}_{n+1}^{T}}(\boldsymbol{\Theta},\dot{\boldsymbol{\Theta}})\cdot\Delta\boldsymbol{\Theta} = \Big(&\alpha_2(\Theta)\dot{\hat{\boldsymbol{\Theta}}} + \alpha_3(\Theta)(\boldsymbol{\Theta}^T\dot{\boldsymbol{\Theta}})\boldsymbol{I} + \alpha_3(\Theta)(\boldsymbol{\Theta}\dot{\boldsymbol{\Theta}}^T) \\ &+b_1(\Theta)(\dot{\boldsymbol{\Theta}}\boldsymbol{\Theta}^T) - b_2(\Theta)(\hat{\boldsymbol{\Theta}}\dot{\boldsymbol{\Theta}}\boldsymbol{\Theta}^T) \\ &+b_3(\Theta)(\boldsymbol{\Theta}^T\dot{\boldsymbol{\Theta}})(\boldsymbol{\Theta}\boldsymbol{\Theta}^T)\Big)\,\Delta\boldsymbol{\Theta} \end{aligned} \tag{C.9}$$

Thus, the eq. (C.5) is written as

$$D\boldsymbol{\Omega}_{n+1}(\boldsymbol{\Theta},\dot{\boldsymbol{\Theta}},\Delta\boldsymbol{\Theta}) = \left[\boldsymbol{\Xi}_{D\boldsymbol{T}_{n+1}^{T}}(\dot{\boldsymbol{\Theta}}) + \frac{\gamma}{h\beta}\boldsymbol{T}^T(\boldsymbol{\Theta})\right]\Delta\boldsymbol{\Theta} \tag{C.10}$$

From the above, the consistent linearized form of the residual term related to the angular velocity is

$$\begin{aligned} D\boldsymbol{g}_{\boldsymbol{\Omega}_{n+1}}(\boldsymbol{\Theta},\dot{\boldsymbol{\Theta}},\Delta\boldsymbol{\Theta}) &\overset{eq.\ (C.2)}{=} \frac{d}{d\epsilon}\bigg|_{\epsilon=0}[\boldsymbol{\Omega}_{n+1}(\boldsymbol{\Theta}+\epsilon\Delta\Theta)]\times\boldsymbol{J}\boldsymbol{\Omega}_{n+1}(\boldsymbol{\Theta}) \\ &+ \boldsymbol{\Omega}_{n+1}(\boldsymbol{\Theta})\times\boldsymbol{J}\,\frac{d}{d\epsilon}\bigg|_{\epsilon=0}[\boldsymbol{\Omega}_{n+1}(\boldsymbol{\Theta}+\epsilon\Delta\Theta)] \\ &\overset{eq.\ (C.10)}{=} \left[\boldsymbol{\Xi}_{D\boldsymbol{T}_{n+1}^{T}}(\boldsymbol{\Theta},\dot{\boldsymbol{\Theta}}) + \frac{\gamma}{h\beta}\boldsymbol{T}_{n+1}^{T}(\boldsymbol{\Theta})\right]\Delta\boldsymbol{\Theta}\times\boldsymbol{J}\boldsymbol{\Omega}_{n+1}(\boldsymbol{\Theta}) \\ &+ \boldsymbol{\Omega}_{n+1}(\boldsymbol{\Theta})\times\boldsymbol{J}\left[\boldsymbol{\Xi}_{D\boldsymbol{T}_{n+1}^{T}}(\boldsymbol{\Theta},\dot{\boldsymbol{\Theta}}) + \frac{\gamma}{h\beta}\boldsymbol{T}_{n+1}^{T}(\boldsymbol{\Theta})\right]\Delta\boldsymbol{\Theta} \Leftrightarrow \end{aligned}$$

$$\boxed{D\boldsymbol{g}_{\boldsymbol{\Omega}_{n+1}}(\boldsymbol{\Theta},\dot{\boldsymbol{\Theta}},\Delta\boldsymbol{\Theta}) = \left[(-\boldsymbol{J}\boldsymbol{\Omega}_{n+1}(\boldsymbol{\Theta}))\times\left(\boldsymbol{\Xi}_{D\boldsymbol{T}_{n+1}^{T}}(\boldsymbol{\Theta},\dot{\boldsymbol{\Theta}}) + \frac{\gamma}{h\beta}\boldsymbol{T}_{n+1}^{T}(\boldsymbol{\Theta})\right)\right.}$$

$$\boxed{\left.+\boldsymbol{\Omega}_{n+1}(\boldsymbol{\Theta})\times\boldsymbol{J}\left(\boldsymbol{\Xi}_{D\boldsymbol{T}_{n+1}^{T}}(\boldsymbol{\Theta},\dot{\boldsymbol{\Theta}}) + \frac{\gamma}{h\beta}\boldsymbol{T}_{n+1}^{T}(\boldsymbol{\Theta})\right)\right]\Delta\boldsymbol{\Theta}} \tag{C.11}$$

C.1.4 Simo's & Vu-Quoc's scheme: consistent linearization of the term that includes the angular acceleration

The consistent linearized form of the residual term related to the acceleration is

$$D\boldsymbol{g}_{\boldsymbol{A}_{n+1}}(\Delta\boldsymbol{\Theta}) \overset{eq.\ (4.8)}{=} \frac{1}{h^2\beta}\boldsymbol{J}\left.\frac{d}{d\epsilon}\right|_{\epsilon=0}\left[(\boldsymbol{\Theta}+\epsilon\Delta\boldsymbol{\Theta})+\boldsymbol{A}'_n\right] = \frac{1}{h^2\beta}\boldsymbol{J}\Delta\boldsymbol{\Theta} \tag{C.12}$$

C.1.5 Mäkinen's / Cardona's & Géradin's schemes: non consistent linearization of the term that includes the angular acceleration

The tangent operator that Mäkinen, 2001 has used is not presented in his work. On the contrary, Cardona and Géradin, 1988 present the tangent operator, where they do not use the second term (see below, eq. C.13) that includes the time derivative of the tangential transformation, but only the first term.

The modified / non consistent linearized form of the residual term related to the angular acceleration that is used in the current work, is

$$\boxed{D\boldsymbol{g}_{\boldsymbol{A}_{n+1}}(\boldsymbol{\Theta},\dot{\boldsymbol{\Theta}},\Delta\boldsymbol{\Theta}) = \frac{1}{h^2\beta}\boldsymbol{J}\boldsymbol{T}^T_{n+1}(\boldsymbol{\Theta})\Delta\boldsymbol{\Theta} + \frac{\gamma}{h\beta}\boldsymbol{J}\dot{\boldsymbol{T}}^T_{n+1}(\boldsymbol{\Theta})\Delta\boldsymbol{\Theta}} \tag{C.13}$$

C.1.6 Mäkinen's / Cardona's & Géradin's schemes: consistent linearization of the term that includes the angular acceleration

By employing the directional derivative on the perturbed form $\boldsymbol{A}_{n+1}(\boldsymbol{\Theta}+\epsilon\Delta\boldsymbol{\Theta})$ of eq. (4.21)

$$\begin{aligned} D\boldsymbol{A}_{n+1}(\boldsymbol{\Theta},\dot{\boldsymbol{\Theta}},\ddot{\boldsymbol{\Theta}},\Delta\boldsymbol{\Theta}) = {} & \left.\frac{d}{d\epsilon}\right|_{\epsilon=0}\left[\frac{d}{dt}\left(\boldsymbol{T}^T_{n+1}(\boldsymbol{\Theta}+\epsilon\Delta\boldsymbol{\Theta})\right)\right]\dot{\boldsymbol{\Theta}} + \frac{d}{dt}\left(\boldsymbol{T}^T_{n+1}(\boldsymbol{\Theta})\right)\Delta\dot{\boldsymbol{\Theta}} + \\ & \left.\frac{d}{d\epsilon}\right|_{\epsilon=0}\left[\boldsymbol{T}^T_{n+1}(\boldsymbol{\Theta}+\epsilon\Delta\boldsymbol{\Theta}\right]\ddot{\boldsymbol{\Theta}} + \boldsymbol{T}^T_{n+1}(\boldsymbol{\Theta})\Delta\ddot{\boldsymbol{\Theta}} \end{aligned} \tag{C.14}$$

where $\frac{d}{dt}\left(\boldsymbol{T}^T_{n+1}(\boldsymbol{\Theta})\right)$ is given by eq. (4.16), $\left.\frac{d}{d\epsilon}\right|_{\epsilon=0}\left[\boldsymbol{T}^T_{n+1}(\boldsymbol{\Theta}+\epsilon\Delta\boldsymbol{\Theta})\right]\ddot{\boldsymbol{\Theta}}$ is given by eq. (C.9) where the first derivative of the rotation vector $\dot{\boldsymbol{\Theta}}$ is substituted by the second derivative of the rotation vector $\ddot{\boldsymbol{\Theta}}$, $\dot{\boldsymbol{\Theta}}$ is given by eq. (C.6), $\Delta\dot{\boldsymbol{\Theta}}$ is given by eq. (C.7), while

$$\ddot{\boldsymbol{\Theta}}_{n+1} = \frac{1}{h^2\beta}\boldsymbol{\Theta}_{n+1} - \frac{1}{h\beta}\dot{\boldsymbol{\Theta}}_n - \frac{1}{\beta}\left(\frac{1}{2}-\beta\right)\ddot{\boldsymbol{\Theta}}_n \tag{C.15}$$

$$\Delta\ddot{\boldsymbol{\Theta}}_{n+1} = \frac{1}{h^2\beta}\Delta\boldsymbol{\Theta} \tag{C.16}$$

and, by taking into account eq. (21) from Ritto-Corrêa and Camotim, 2002, the directional derivative of the time derivative of the transpose tangential transformation is written as

$$
\begin{aligned}
D^2\boldsymbol{T}_{n+1}^T[\boldsymbol{\Theta},\dot{\boldsymbol{\Theta}},\Delta\boldsymbol{\Theta}] = \left.\frac{d}{d\epsilon}\right|_{\epsilon=0}\left[\frac{d}{dt}\left(\boldsymbol{T}_{n+1}^T(\boldsymbol{\Theta}+\epsilon\Delta\boldsymbol{\Theta})\right)\right] = \\
&\alpha_3(\Theta)(\dot{\boldsymbol{\Theta}}\Delta\boldsymbol{\Theta}^T + \Delta\boldsymbol{\Theta}\dot{\boldsymbol{\Theta}}^T) + b_1(\Theta)(\dot{\boldsymbol{\Theta}}^T\Delta\boldsymbol{\Theta})\boldsymbol{I} - \\
&b_2(\Theta)\left[(\boldsymbol{\Theta}^T\dot{\boldsymbol{\Theta}})\hat{\Delta\boldsymbol{\Theta}} + (\boldsymbol{\Theta}^T\Delta\boldsymbol{\Theta})\hat{\dot{\boldsymbol{\Theta}}} + (\dot{\boldsymbol{\Theta}}^T\Delta\boldsymbol{\Theta})\hat{\boldsymbol{\Theta}}\right] + \\
&b_3(\Theta)\left[(\boldsymbol{\Theta}^T\dot{\boldsymbol{\Theta}})(\Delta\boldsymbol{\Theta}\boldsymbol{\Theta}^T + \boldsymbol{\Theta}\Delta\boldsymbol{\Theta}^T) + \right. \\
&\left.(\boldsymbol{\Theta}^T\Delta\boldsymbol{\Theta})(\dot{\boldsymbol{\Theta}}\boldsymbol{\Theta}^T + \boldsymbol{\Theta}\dot{\boldsymbol{\Theta}}^T) + (\dot{\boldsymbol{\Theta}}^T\Delta\boldsymbol{\Theta})\boldsymbol{\Theta}\boldsymbol{\Theta}^T\right] + \\
&c_1(\Theta)(\boldsymbol{\Theta}^T\Delta\boldsymbol{\Theta})(\boldsymbol{\Theta}^T\dot{\boldsymbol{\Theta}})\boldsymbol{I} - \\
&c_2(\Theta)(\boldsymbol{\Theta}^T\Delta\boldsymbol{\Theta})(\boldsymbol{\Theta}^T\dot{\boldsymbol{\Theta}})\hat{\boldsymbol{\Theta}} + \\
&c_3(\Theta)(\boldsymbol{\Theta}^T\Delta\boldsymbol{\Theta})(\boldsymbol{\Theta}^T\dot{\boldsymbol{\Theta}})\boldsymbol{\Theta}\boldsymbol{\Theta}^T
\end{aligned}
\tag{C.17}
$$

By post-multiplying the above expression with $\dot{\boldsymbol{\Theta}}$ as it appears in eq. (C.14) and re-arrange the terms, the following expression is derived

$$
\begin{aligned}
\boldsymbol{\Xi}_{D^2\boldsymbol{T}_{n+1}^T}(\boldsymbol{\Theta},\dot{\boldsymbol{\Theta}})\cdot\Delta\boldsymbol{\Theta} = \left.\frac{d}{d\epsilon}\right|_{\epsilon=0}\left[\frac{d}{dt}\left(\boldsymbol{T}_{n+1}^T(\boldsymbol{\Theta}+\epsilon\Delta\boldsymbol{\Theta})\right)\right]\dot{\boldsymbol{\Theta}} = \\
&\left(\alpha_3(\Theta)(\dot{\boldsymbol{\Theta}}\dot{\boldsymbol{\Theta}}^T + \dot{\boldsymbol{\Theta}}^T\dot{\boldsymbol{\Theta}}\boldsymbol{I}) + b_1(\Theta)(\dot{\boldsymbol{\Theta}}\dot{\boldsymbol{\Theta}}^T) + \right. \\
&b_2(\Theta)\left[(\boldsymbol{\Theta}^T\dot{\boldsymbol{\Theta}})\hat{\dot{\boldsymbol{\Theta}}} - (\hat{\dot{\boldsymbol{\Theta}}}\dot{\boldsymbol{\Theta}}\boldsymbol{\Theta}^T) - (\hat{\boldsymbol{\Theta}}\dot{\boldsymbol{\Theta}}\dot{\boldsymbol{\Theta}}^T)\right] + \\
&b_3(\Theta)\left[(\dot{\boldsymbol{\Theta}}\dot{\boldsymbol{\Theta}}^T)(\boldsymbol{\Theta}\boldsymbol{\Theta}^T) + (\boldsymbol{\Theta}^T\dot{\boldsymbol{\Theta}})((\boldsymbol{\Theta}\dot{\boldsymbol{\Theta}}^T) + (\boldsymbol{\Theta}^T\dot{\boldsymbol{\Theta}})\boldsymbol{I}) + \right. \\
&\left.(\dot{\boldsymbol{\Theta}}\boldsymbol{\Theta}^T + \boldsymbol{\Theta}\dot{\boldsymbol{\Theta}}^T)(\dot{\boldsymbol{\Theta}}\boldsymbol{\Theta}^T)\right] + \\
&(c_1(\Theta)(\dot{\boldsymbol{\Theta}}\dot{\boldsymbol{\Theta}}^T) - \\
&c_2(\Theta)(\hat{\dot{\boldsymbol{\Theta}}}\dot{\boldsymbol{\Theta}}\dot{\boldsymbol{\Theta}}^T) + \\
&\left.c_3(\Theta)(\boldsymbol{\Theta}^T\dot{\boldsymbol{\Theta}})(\boldsymbol{\Theta}^T\dot{\boldsymbol{\Theta}}))\boldsymbol{\Theta}\boldsymbol{\Theta}^T\right)\Delta\boldsymbol{\Theta}
\end{aligned}
\tag{C.18}
$$

Thus, eq. (C.14) is written as

$$
\begin{aligned}
D\boldsymbol{A}_{n+1}(\boldsymbol{\Theta},\dot{\boldsymbol{\Theta}},\ddot{\boldsymbol{\Theta}},\Delta\boldsymbol{\Theta}) = \left[\boldsymbol{\Xi}_{D^2\boldsymbol{T}_{n+1}^T}(\boldsymbol{\Theta},\dot{\boldsymbol{\Theta}}) + \frac{\gamma}{h\beta}\frac{d[\boldsymbol{T}^T(\boldsymbol{\Theta})]}{dt}\right. \\
\left. + \boldsymbol{\Xi}_{D\boldsymbol{T}_{n+1}^T}(\boldsymbol{\Theta},\ddot{\boldsymbol{\Theta}}) + \frac{1}{h^2\beta}\boldsymbol{T}_{n+1}^T(\boldsymbol{\Theta})\right]\Delta\boldsymbol{\Theta}
\end{aligned}
\tag{C.19}
$$

From the above, the consistent linearized form of the residual term related to the angular acceleration is

$$
D\boldsymbol{g}_{\boldsymbol{A}_{n+1}}(\boldsymbol{\Theta},\dot{\boldsymbol{\Theta}},\ddot{\boldsymbol{\Theta}},\Delta\boldsymbol{\Theta}) \overset{eqs.\ (C.2) and\ (C.19)}{=}
$$

$$\boxed{\boldsymbol{J}\left[\boldsymbol{\Xi}_{D^2\boldsymbol{T}^T_{n+1}}(\boldsymbol{\Theta},\dot{\boldsymbol{\Theta}})+\frac{\gamma}{h\beta}\frac{d[\boldsymbol{T}^T_{n+1}(\boldsymbol{\Theta})]}{dt}+\boldsymbol{\Xi}_{D\boldsymbol{T}^T_{n+1}}(\boldsymbol{\Theta},\ddot{\boldsymbol{\Theta}})+\frac{1}{h^2\beta}\boldsymbol{T}^T_{n+1}(\boldsymbol{\Theta})\right]\Delta\boldsymbol{\Theta}} \tag{C.20}$$

C.1.7 Linearization of the term that includes the applied torque in a material setting

The linearized form of the term related to the external moment in a material setting is

$$\begin{aligned} D\boldsymbol{g}_{\boldsymbol{M}_{n+1}}(\boldsymbol{\Theta},\Delta\boldsymbol{\Theta}) &\overset{eq.\,(4.5)}{=} mgl\,\frac{d}{d\epsilon}\Big|_{\epsilon=0}\left[\boldsymbol{\Lambda}(\boldsymbol{\Theta}+\epsilon\Delta\boldsymbol{\Theta})\right]^T\boldsymbol{e}_3\times\boldsymbol{E}_3 \\ &= mgl\,\frac{d}{d\epsilon}\Big|_{\epsilon=0}\left[\boldsymbol{\Lambda}^T(\boldsymbol{\Theta}+\epsilon\Delta\boldsymbol{\Theta})\right]\boldsymbol{e}_3\times\boldsymbol{E}_3 \end{aligned} \tag{C.21}$$

By taking into account the relation (18) from Ritto-Corrêa and Camotim, 2002, the directional derivative of the transpose of the orientation matrix is written as

$$\begin{aligned} D\boldsymbol{\Lambda}^T_{n+1}(\Delta\boldsymbol{\Theta}) = &-\alpha_1(\Theta)\Delta\hat{\boldsymbol{\Theta}}+\alpha_2(\Theta)(\Delta\boldsymbol{\Theta}\boldsymbol{\Theta}^T+\boldsymbol{\Theta}\Delta\boldsymbol{\Theta}^T)+b_0(\Theta)(\boldsymbol{\Theta}^T\Delta\boldsymbol{\Theta})\boldsymbol{I} \\ &-b_1(\Theta)(\boldsymbol{\Theta}^T\Delta\boldsymbol{\Theta})\hat{\boldsymbol{\Theta}}+b_2(\Theta)(\boldsymbol{\Theta}^T\Delta\boldsymbol{\Theta})\boldsymbol{\Theta}\boldsymbol{\Theta}^T \end{aligned} \tag{C.22}$$

where $b_0(\Theta)$ is the trigonometric function given at the appendix B (see also Ritto-Corrêa and Camotim, 2002).

In eq. (C.21), the above relation (eq. (C.22)) is multiplied by $\boldsymbol{e}_3$. By taking into account the operator $\boldsymbol{\Xi}_{D\boldsymbol{\Lambda}^T}(\boldsymbol{a})$ from Ritto-Corrêa and Camotim, 2002, the term $\frac{d}{d\epsilon}\big|_{\epsilon=0}\left[\boldsymbol{\Lambda}^T(\boldsymbol{\Theta}+\epsilon\Delta\boldsymbol{\Theta})\right]\boldsymbol{e}_3$ from eq. (C.21) is written as

$$\begin{aligned} \boldsymbol{\Xi}_{D\boldsymbol{\Lambda}^T_{n+1}}(\boldsymbol{e}_3)\Delta\boldsymbol{\Theta} = \big[&\alpha_1(\Theta)\hat{\boldsymbol{e}}_3+\alpha_2(\Theta)(\boldsymbol{\Theta}^T\boldsymbol{e}_3)\boldsymbol{I}+\alpha_2(\Theta)(\boldsymbol{\Theta}\boldsymbol{e}_3^T)+b_0(\Theta)(\boldsymbol{e}_3\boldsymbol{\Theta}^T) \\ &-b_1(\Theta)(\hat{\boldsymbol{\Theta}}\boldsymbol{e}_3\boldsymbol{\Theta}^T)+b_2(\Theta)(\boldsymbol{\Theta}^T\boldsymbol{e}_3)(\boldsymbol{\Theta}\boldsymbol{\Theta}^T)\big]\,\Delta\boldsymbol{\Theta} \end{aligned} \tag{C.23}$$

Therefore, the tangent operator related to the external moment is computed using the following matrix that multiplies the unknown parameter $\Delta\boldsymbol{\Theta}$

$$\boxed{D\boldsymbol{g}_{\boldsymbol{M}_{n+1}}(\boldsymbol{\Theta},\Delta\boldsymbol{\Theta})=mgl\,\left[-\boldsymbol{E}_3\times\boldsymbol{\Xi}_{D\boldsymbol{\Lambda}^T_{n+1}}(\boldsymbol{e}_3)\right]\Delta\boldsymbol{\Theta}} \tag{C.24}$$

Appendix D

Linearization of the residual in the dynamics of beams

The following terms are written in such a way that the unknown quantities $\delta\boldsymbol{u}$ and $\delta\boldsymbol{\psi}$ are kept in the right. The Lagrange's formula (or the triple cross product expansion eq. 4.43) is used. The subscript $_{n+1}$ is ommitted from the RHS for convenience.

$$\boxed{Dg_{i1,n+1}(\delta\boldsymbol{u}_0,\boldsymbol{\chi}) = \int_0^L \left[\boldsymbol{\chi}^T\left(A_m\frac{1}{h^2\beta}\boldsymbol{I}\right)\delta\boldsymbol{u}_0\right]d\xi} \tag{D.1}$$

$$Dg_{i2,n+1}(\delta\boldsymbol{u}_0,\delta\boldsymbol{\Theta},\delta\boldsymbol{\psi},\boldsymbol{\chi}) = \int_0^L \left[\boldsymbol{\chi}^T\left(\delta\boldsymbol{\psi}\times\boldsymbol{\Lambda}\hat{\boldsymbol{\Omega}}\hat{\boldsymbol{\Omega}}\boldsymbol{S}_m + \frac{\gamma}{h\beta}\boldsymbol{\Lambda}\delta\hat{\boldsymbol{\Theta}}\hat{\boldsymbol{\Omega}}\boldsymbol{S}_m + \frac{\gamma}{h\beta}\boldsymbol{\Lambda}\hat{\boldsymbol{\Omega}}\delta\hat{\boldsymbol{\Theta}}\boldsymbol{S}_m\right.\right.$$
$$\left.\left. + \delta\boldsymbol{\psi}\times\boldsymbol{\Lambda}\hat{\boldsymbol{A}}\boldsymbol{S}_m + \frac{1}{h^2\beta}\boldsymbol{\Lambda}\delta\hat{\boldsymbol{\Theta}}\boldsymbol{S}_m\right)\right]d\xi \tag{D.2}$$

Using eqs. 4.53 and 4.58, the linearized term D.2 is written as follows

$$\boxed{Dg_{i2,n+1}(\delta\boldsymbol{u},\delta\boldsymbol{\psi},\boldsymbol{\chi}) = \int_0^L \boldsymbol{\chi}^T\left\{-\dot{\hat{\boldsymbol{p}}}_\psi +\right.}$$
$$\boxed{\left.\boldsymbol{\Lambda}\left[-\frac{1}{h^2\beta}\hat{\boldsymbol{S}}_m + \frac{\gamma}{h\beta}\left(\boldsymbol{\Omega}\boldsymbol{S}_m^T - 2\,\boldsymbol{S}_m\boldsymbol{\Omega}^T + \boldsymbol{\Omega}^T\boldsymbol{S}_m\boldsymbol{I}_3\right)\right]\boldsymbol{\Lambda}_n^T\boldsymbol{T}^{-1}(\boldsymbol{\theta}_{n+1})\right\}\delta\boldsymbol{\psi}\,d\xi} \tag{D.3}$$

where the time derivative of the linear momentum because of the rotation, $\dot{\boldsymbol{p}}_\psi(t,\xi) = \left(\boldsymbol{\Lambda}\hat{\boldsymbol{\Omega}}\hat{\boldsymbol{\Omega}}\boldsymbol{S}_m\right) + \left(\boldsymbol{\Lambda}\hat{\boldsymbol{A}}\boldsymbol{S}_m\right)$, is recognized.

$$Dg_{i3,n+1}(\delta\boldsymbol{u}_0,\delta\boldsymbol{\Theta},\delta\boldsymbol{\psi},\boldsymbol{\phi}) = \int_0^L \left[\boldsymbol{\phi}^T\left(\delta\boldsymbol{\psi}\times\boldsymbol{\Lambda}\hat{\boldsymbol{\Omega}}\boldsymbol{S}_m\times\dot{\boldsymbol{u}}_0 + \frac{\gamma}{h\beta}\boldsymbol{\Lambda}\delta\hat{\boldsymbol{\Theta}}\boldsymbol{S}_m\times\dot{\boldsymbol{u}}_0\right.\right.$$
$$\left.\left. + \frac{\gamma}{h\beta}\boldsymbol{\Lambda}\hat{\boldsymbol{\Omega}}\boldsymbol{S}_m\times\delta\boldsymbol{u}_0 + \delta\boldsymbol{\psi}\times\boldsymbol{\Lambda}\boldsymbol{S}_m\times\ddot{\boldsymbol{u}}_0 + \frac{1}{h^2\beta}\boldsymbol{\Lambda}\boldsymbol{S}_m\times\delta\boldsymbol{u}_0\right)\right]d\xi \tag{D.4}$$

Using eqs. 4.53 and 4.58, the linearized term D.4 is written as follows

$$Dg_{i3,n+1}(\delta\boldsymbol{u},\delta\boldsymbol{\psi},\boldsymbol{\phi}) = \int_0^L \boldsymbol{\phi}^T \left[\frac{\gamma}{h\beta}\left(\boldsymbol{\Lambda}\hat{\boldsymbol{\Omega}}\boldsymbol{S}_m\right) + \frac{1}{h^2\beta}\left(\boldsymbol{\Lambda}\boldsymbol{S}_m\right)\right]\times\delta\boldsymbol{u}_0$$

$$+\boldsymbol{\phi}^T\left[\frac{\gamma}{h\beta}\left(\dot{\boldsymbol{u}}_0\times\boldsymbol{\Lambda}\hat{\boldsymbol{S}}_m\right)\boldsymbol{\Lambda}_n^T\boldsymbol{T}^{-1}(\boldsymbol{\theta}_{n+1}) - \dot{\hat{\boldsymbol{l}}}_u\right]\delta\boldsymbol{\psi}\,d\xi \tag{D.5}$$

where the time derivative of the angular momentum because of the translation, $\dot{\boldsymbol{l}}_u(t,\xi) = \left(\boldsymbol{\Lambda}\hat{\boldsymbol{\Omega}}\boldsymbol{S}_m\right)\times\dot{\boldsymbol{u}}_0 + \left(\boldsymbol{\Lambda}\boldsymbol{S}_m\right)\times\ddot{\boldsymbol{u}}_0$, is recognized. This term that includes the $\dot{\boldsymbol{l}}_u(t,\xi)$ can be analyzed further using the Lagrange's formula, as follows

$$\left[\left(\boldsymbol{\Lambda}\hat{\boldsymbol{\Omega}}\boldsymbol{S}_m\right)\dot{\boldsymbol{u}}_0^T - \dot{\boldsymbol{u}}_0\left(\boldsymbol{\Lambda}\hat{\boldsymbol{\Omega}}\boldsymbol{S}_m\right)^T + \left(\boldsymbol{\Lambda}\boldsymbol{S}_m\right)\ddot{\boldsymbol{u}}_0^T - \ddot{\boldsymbol{u}}_0\left(\boldsymbol{\Lambda}\boldsymbol{S}_m\right)^T\right]\delta\boldsymbol{\psi} \tag{D.6}$$

Analysis of the term $\frac{\gamma}{h\beta}\left(\boldsymbol{\Lambda}\delta\hat{\boldsymbol{\Theta}}\boldsymbol{S}\times\dot{\boldsymbol{u}}_0\right)$

It is worth noting that the algebra followed for the manipulation of the term $\left(\boldsymbol{\Lambda}\,\delta\hat{\boldsymbol{\Theta}}\,\boldsymbol{S}_m\times\dot{\boldsymbol{u}}_0\right)$ to bring $\delta\boldsymbol{\Theta}$ to the right, is given as

$$\begin{aligned}\left[\boldsymbol{\Lambda}\left(\delta\boldsymbol{\Theta}\times\boldsymbol{S}_m\right)\right]\times\dot{\boldsymbol{u}}_0 &= -\dot{\boldsymbol{u}}_0\times\left[\boldsymbol{\Lambda}\left(\delta\boldsymbol{\Theta}\times\boldsymbol{S}_m\right)\right] = \dot{\boldsymbol{u}}_0\times\left[\boldsymbol{\Lambda}\left(\boldsymbol{S}_m\times\delta\boldsymbol{\Theta}\right)\right]\\ &= \dot{\boldsymbol{u}}_0\times\left[\left(\boldsymbol{\Lambda}\boldsymbol{S}_m\right)\times\left(\boldsymbol{\Lambda}\delta\boldsymbol{\Theta}\right)\right] = \dot{\boldsymbol{u}}_0\times\left(\boldsymbol{\Lambda}\hat{\boldsymbol{S}}_m\boldsymbol{\Lambda}^T\boldsymbol{\Lambda}\delta\boldsymbol{\Theta}\right)\\ &= \dot{\boldsymbol{u}}_0\times\left(\boldsymbol{\Lambda}\hat{\boldsymbol{S}}_m\delta\boldsymbol{\Theta}\right)\end{aligned}$$

where the relations $\widehat{\boldsymbol{\Lambda}\boldsymbol{S}_m} = \boldsymbol{\Lambda}\,\hat{\boldsymbol{S}}_m\,\boldsymbol{\Lambda}^T$ and $\boldsymbol{\Lambda}^T\,\boldsymbol{\Lambda} = \boldsymbol{I}_3$; $\boldsymbol{I}_3$ is the 3×3 identity matrix, have been used.

$$\begin{aligned}Dg_{i4,n+1}(\delta\boldsymbol{\psi},\boldsymbol{\phi}) = \int_0^L \boldsymbol{\phi}^T\Big(&\delta\boldsymbol{\psi}\times\boldsymbol{\Lambda}\,\boldsymbol{J}\,\boldsymbol{A} + \boldsymbol{\Lambda}\,\boldsymbol{J}\,\frac{1}{h^2\beta}\delta\boldsymbol{\Theta} + \delta\boldsymbol{\psi}\times\boldsymbol{\Lambda}\,\hat{\boldsymbol{\Omega}}\boldsymbol{J}\,\boldsymbol{\Omega}\\ &+\boldsymbol{\Lambda}\,\frac{\gamma}{h\beta}\delta\hat{\boldsymbol{\Theta}}\boldsymbol{J}\boldsymbol{\Omega} + \boldsymbol{\Lambda}\hat{\boldsymbol{\Omega}}\boldsymbol{J}\,\frac{\gamma}{h\beta}\delta\boldsymbol{\Theta}\Big)\,d\xi\end{aligned} \tag{D.7}$$

Using eqs. 4.53 and 4.58, the linearized term D.7 is written as follows

$$Dg_{i4,n+1}(\delta\boldsymbol{\psi},\boldsymbol{\phi}) = \int_0^L \boldsymbol{\phi}^T\left\{-\dot{\hat{\boldsymbol{\pi}}} + \boldsymbol{\Lambda}\left[\frac{\gamma}{h\beta}\left(\hat{\boldsymbol{\Omega}}\boldsymbol{J} - \widehat{\boldsymbol{J}\boldsymbol{\Omega}}\right) + \frac{1}{h^2\beta}\boldsymbol{J}\right]\boldsymbol{\Lambda}_n^T\boldsymbol{T}^{-1}(\boldsymbol{\theta}_{n+1})\right\}\delta\boldsymbol{\psi}\;d\xi \tag{D.8}$$

where the time derivative of the spatial angular momentum vector relative to the principal axes of inertia, $\boldsymbol{\pi}(t,\xi) = \boldsymbol{\Lambda}\left(\boldsymbol{J}\boldsymbol{A} + \hat{\boldsymbol{\Omega}}\boldsymbol{J}\boldsymbol{\Omega}\right)$, is recognized.

Appendix E

Linearization of the inertial terms in multi-body formulation

For the linear momentum, in a perturbed state $t + \epsilon\Delta t$, the eq. (5.19) is written as follows

$$\delta W_{\dot{\boldsymbol{p}}_{tot,\epsilon}}\left(\boldsymbol{q}_{,\epsilon}, \dot{\boldsymbol{q}}_{,\epsilon}, \ddot{\boldsymbol{q}}_{,\epsilon}, \xi; t\right) = \int_{0_L} \left(\delta \boldsymbol{r}_0^T \dot{\boldsymbol{p}}_{tot,\epsilon}\right) d\xi = \int_{0_L} \left[\delta \boldsymbol{r}_0^T \left(\dot{\boldsymbol{p}}^1_{tot,\epsilon} + \dot{\boldsymbol{p}}^2_{tot,\epsilon}\right)\right] d\xi \tag{E.1}$$

where the individual terms of the time derivative of the linear momentum $\dot{\boldsymbol{p}}_{m,\epsilon}$ in the perturbed state are

$$\begin{aligned}
\dot{\boldsymbol{p}}^1_{tot,\epsilon} &= M\left[\left(\boldsymbol{A}_\epsilon^T \ddot{\boldsymbol{R}}_\epsilon\right) + \left(\boldsymbol{A}_\epsilon^T \ddot{\boldsymbol{A}}_\epsilon\right) \boldsymbol{r}_{0,\epsilon} + 2\left(\boldsymbol{A}_\epsilon^T \dot{\boldsymbol{A}}_\epsilon\right) \dot{\boldsymbol{r}}_{0,\epsilon} + \ddot{\boldsymbol{r}}_{0,\epsilon}\right] \\
\dot{\boldsymbol{p}}^2_{tot,\epsilon} &= \left(\boldsymbol{A}_\epsilon^T \ddot{\boldsymbol{A}}_\epsilon\right) \boldsymbol{\Lambda}\boldsymbol{S}_m + 2\left(\boldsymbol{A}_\epsilon^T \dot{\boldsymbol{A}}_\epsilon\right) \dot{\boldsymbol{\Lambda}}\boldsymbol{S}_m + \ddot{\boldsymbol{\Lambda}}\boldsymbol{S}_m
\end{aligned} \tag{E.2}$$

and manipulated separately in the following. In eq. (E.2), the perturbed position $\boldsymbol{R}_\epsilon$ and orientation $\boldsymbol{A}_\epsilon$, appear. They are given as

$$\boldsymbol{R}_\epsilon = \boldsymbol{R}(\boldsymbol{q}^0) + \epsilon\delta\boldsymbol{R} \tag{E.3}$$

$$\boldsymbol{A}_\epsilon = \boldsymbol{A}(\boldsymbol{q}^0) + \epsilon\delta\boldsymbol{A} \tag{E.4}$$

where $\boldsymbol{R}(\boldsymbol{q}^0)$ and $\boldsymbol{A}(\boldsymbol{q}^0)$ are the corresponding converged quantities in relation with the converged vector $\boldsymbol{q}^0$ at the beginning of the time step, and $\delta\boldsymbol{R} = \frac{\vartheta \boldsymbol{R}(\boldsymbol{q}^0)}{\vartheta \boldsymbol{q}}\delta\boldsymbol{q}$, $\delta\boldsymbol{A} = \frac{\vartheta \boldsymbol{A}(\boldsymbol{q}^0)}{\vartheta \boldsymbol{q}}\delta\boldsymbol{q}$. For the linearization of the above terms, the directional derivative w.r.t. ϵ for $\epsilon = 0$ is employed. The Lagrange's formula is used for the triple vector cross product. The linearization of the terms $\boldsymbol{A}_\epsilon^T \ddot{\boldsymbol{R}}_\epsilon$, $\boldsymbol{A}_\epsilon^T \ddot{\boldsymbol{A}}_\epsilon$, and $\boldsymbol{A}_\epsilon^T \dot{\boldsymbol{A}}_\epsilon$ have already employed in a previous work (Manolas, 2015). The linearization of the first and second derivatives of $\boldsymbol{A}$ (or $\boldsymbol{R}$) are repeated here,

following the classical chain rule.

$$\dot{\boldsymbol{A}}(\boldsymbol{q}) = \frac{\vartheta \boldsymbol{A}(\boldsymbol{q})}{\vartheta \boldsymbol{q}} \frac{\vartheta \boldsymbol{q}}{\vartheta t} \simeq \left[\frac{\vartheta \boldsymbol{A}(\boldsymbol{q}^0)}{\vartheta q_j} + \frac{\vartheta^2 \boldsymbol{A}(\boldsymbol{q}^0)}{\vartheta q_j \vartheta q_k} \delta q_k \right] \left(\dot{q}_j^0 + \delta \dot{q}_j \right)$$
$$\simeq \frac{\vartheta \boldsymbol{A}(\boldsymbol{q}^0)}{\vartheta q_j} \dot{q}_j^0 + \frac{\vartheta^2 \boldsymbol{A}(\boldsymbol{q}^0)}{\vartheta q_j \vartheta q_k} \dot{q}_j^0 \delta q_k + \frac{\vartheta \boldsymbol{A}(\boldsymbol{q}^0)}{\vartheta q_j} \delta \dot{q}_j \tag{E.5}$$

$$\ddot{\boldsymbol{A}}(\boldsymbol{q}) = \frac{\vartheta^2 \boldsymbol{A}(\boldsymbol{q})}{\vartheta^2 \boldsymbol{q}} \frac{\vartheta \boldsymbol{q}}{\vartheta t} \frac{\vartheta \boldsymbol{q}}{\vartheta t} + \frac{\vartheta \boldsymbol{A}(\boldsymbol{q})}{\vartheta \boldsymbol{q}} \frac{\vartheta^2 \boldsymbol{q}}{\vartheta t^2} \simeq \left[\frac{\vartheta^2 \boldsymbol{A}(\boldsymbol{q}^0)}{\vartheta q_j \vartheta q_k} + \frac{\vartheta^3 \boldsymbol{A}(\boldsymbol{q}^0)}{\vartheta q_j \vartheta q_k \vartheta q_m} \delta q_m \right] \left(\dot{q}_k^0 + \delta \dot{q}_k \right) \left(\dot{q}_j^0 + \delta \dot{q}_j \right)$$
$$+ \left[\frac{\vartheta \boldsymbol{A}(\boldsymbol{q}^0)}{\vartheta q_j} + \frac{\vartheta^2 \boldsymbol{A}(\boldsymbol{q}^0)}{\vartheta q_j \vartheta q_k} \delta q_k \right] \left(\ddot{q}_j^0 + \delta \ddot{q}_j \right)$$
$$\simeq \left(\frac{\vartheta^2 \boldsymbol{A}(\boldsymbol{q}^0)}{\vartheta q_j \vartheta q_k} \dot{q}_k^0 \dot{q}_j^0 + \frac{\vartheta \boldsymbol{A}(\boldsymbol{q}^0)}{\vartheta q_j} \ddot{q}_j^0 \right)$$
$$+ \left(\frac{\vartheta^3 \boldsymbol{A}(\boldsymbol{q}^0)}{\vartheta q_j \vartheta q_k \vartheta q_m} \dot{q}_k^0 \dot{q}_j^0 \delta q_m + \frac{\vartheta^2 \boldsymbol{A}(\boldsymbol{q}^0)}{\vartheta q_j \vartheta q_k} \ddot{q}_j^0 \delta q_k \right)$$
$$+ \left(\frac{\vartheta^2 \boldsymbol{A}(\boldsymbol{q}^0)}{\vartheta q_j \vartheta q_k} \dot{q}_k^0 \delta \dot{q}_j + \frac{\vartheta^2 \boldsymbol{A}(\boldsymbol{q}^0)}{\vartheta q_j \vartheta q_k} \dot{q}_j^0 \delta \dot{q}_k \right)$$
$$+ \frac{\vartheta \boldsymbol{A}(\boldsymbol{q}^0)}{\vartheta q_j} \delta \ddot{q}_j \tag{E.6}$$

In hGAST, these terms are written in a systematic way as follows

$$\dot{\boldsymbol{A}}(\boldsymbol{q}) = \boldsymbol{DA} + \boldsymbol{DA0} \delta \boldsymbol{q} + \boldsymbol{A0} \delta \dot{\boldsymbol{q}} \tag{E.7}$$
$$\ddot{\boldsymbol{A}}(\boldsymbol{q}) = \boldsymbol{DDA} + \boldsymbol{DDA0} \delta \boldsymbol{q} + \boldsymbol{DA0} \delta \dot{\boldsymbol{q}} + \boldsymbol{A0} \delta \ddot{\boldsymbol{q}} \tag{E.8}$$

A similar concept is followed for the first and second derivatives of the position vector $\boldsymbol{R}$ of the body's origin. In the following, the linearization of the above terms are written shortly for completeness, while the terms which contain the linearization of $\boldsymbol{r}_{0,\epsilon}$ and $\boldsymbol{\Lambda}_\epsilon$ are further analyzed.

$$\left. \frac{d}{d\epsilon} \right|_{\epsilon=0} \left(\dot{\boldsymbol{p}}_{tot,\epsilon}^1 \right) = M \left[d \left(\boldsymbol{A}^T \ddot{\boldsymbol{R}} \right) + d \left(\boldsymbol{A}^T \ddot{\boldsymbol{A}} \right) \boldsymbol{r}_0 + 2\, d \left(\boldsymbol{A}^T \dot{\boldsymbol{A}} \right) \dot{\boldsymbol{r}}_0 + \left(\boldsymbol{A}^T \ddot{\boldsymbol{A}} \right) \delta \boldsymbol{r}_0 + 2 \left(\boldsymbol{A}^T \dot{\boldsymbol{A}} \right) \delta \dot{\boldsymbol{r}}_0 + \delta \ddot{\boldsymbol{r}}_0 \right]$$
$$\left. \frac{d}{d\epsilon} \right|_{\epsilon=0} \left(\dot{\boldsymbol{p}}_{tot,\epsilon}^2 \right) = d \left(\boldsymbol{A}^T \ddot{\boldsymbol{A}} \right) \boldsymbol{\Lambda} \boldsymbol{S}_m + 2\, d \left(\boldsymbol{A}^T \dot{\boldsymbol{A}} \right) \dot{\boldsymbol{\Lambda}} \boldsymbol{S}_m + \left(\boldsymbol{A}^T \ddot{\boldsymbol{A}} \right) \widehat{\delta \psi} \boldsymbol{\Lambda} \boldsymbol{S}_m$$
$$+ 2 \left(\boldsymbol{A}^T \dot{\boldsymbol{A}} \right) \left(\widehat{\delta \psi} \boldsymbol{\Lambda} \hat{\boldsymbol{\Omega}} \boldsymbol{S}_m + \boldsymbol{\Lambda} \delta \hat{\boldsymbol{\Omega}} \boldsymbol{S}_m \right) + \delta \left(\ddot{\boldsymbol{\Lambda}} \right) \boldsymbol{S}_m \tag{E.9}$$

For the angular momentum, in a perturbed state $t + \epsilon \Delta t$, the eq. (5.23) is written as follows

$$\delta W_{\boldsymbol{l}_{tot,\epsilon}} (\boldsymbol{q}_{,\epsilon}, \dot{\boldsymbol{q}}_{,\epsilon}, \ddot{\boldsymbol{q}}_{,\epsilon}, \xi; t) = \int_{0_L} \delta \boldsymbol{\psi}^T \dot{\boldsymbol{l}}_{tot,\epsilon}\, d\xi = \int_{0_L} \delta \boldsymbol{\psi}^T \left(\dot{\boldsymbol{l}}_{tot,\epsilon}^1 + \dot{\boldsymbol{l}}_{tot,\epsilon}^2 + \dot{\boldsymbol{l}}_{tot,\epsilon}^3 + \dot{\boldsymbol{l}}_{tot,\epsilon}^4 \right) d\xi \tag{E.10}$$

where the individual terms of the time derivative of the angular momentum $\dot{\boldsymbol{l}}_{tot,\epsilon}$ in the perturbed state are

$$\begin{aligned}
\dot{\boldsymbol{l}}^1_{tot,\epsilon} &= \left(\dot{\boldsymbol{\Lambda}}_\epsilon \boldsymbol{S}_m\right) \times \left(\boldsymbol{A}^T_\epsilon \dot{\boldsymbol{R}}_\epsilon + \boldsymbol{A}^T_\epsilon \dot{\boldsymbol{A}}_\epsilon \boldsymbol{r}_{0,\epsilon} + \dot{\boldsymbol{r}}_{0,\epsilon}\right) \\
\dot{\boldsymbol{l}}^2_{tot,\epsilon} &= \int_{0_A} \rho_{ref} \left(\dot{\boldsymbol{\Lambda}}_\epsilon \boldsymbol{X}\right) \times \left(\boldsymbol{A}^T_\epsilon \dot{\boldsymbol{A}}_\epsilon \boldsymbol{\Lambda}_\epsilon \boldsymbol{X}\right) d^0\boldsymbol{A} \\
\dot{\boldsymbol{l}}^3_{tot,\epsilon} &= \left(\boldsymbol{\Lambda}_\epsilon \boldsymbol{S}_m\right) \times \left(\boldsymbol{A}^T_\epsilon \ddot{\boldsymbol{R}}_\epsilon + \boldsymbol{A}^T_\epsilon \ddot{\boldsymbol{A}}_\epsilon \boldsymbol{r}_{0,\epsilon} + 2\,\boldsymbol{A}^T_\epsilon \dot{\boldsymbol{A}}_\epsilon \dot{\boldsymbol{r}}_{0,\epsilon} + \ddot{\boldsymbol{r}}_{0,\epsilon}\right) \\
\dot{\boldsymbol{l}}^4_{tot,\epsilon} &= \int_{0_A} \rho_{ref} \left(\boldsymbol{\Lambda}_\epsilon \boldsymbol{X}\right) \times \left(\boldsymbol{A}^T_\epsilon \ddot{\boldsymbol{A}}_\epsilon \boldsymbol{\Lambda}_\epsilon \boldsymbol{X} + 2\,\boldsymbol{A}^T_\epsilon \dot{\boldsymbol{A}}_\epsilon \dot{\boldsymbol{\Lambda}}_\epsilon \boldsymbol{X} + \ddot{\boldsymbol{\Lambda}}_\epsilon \boldsymbol{X}\right) d^0\boldsymbol{A}
\end{aligned} \tag{E.11}$$

and manipulated separately in the following.

The terms $\dot{\boldsymbol{l}}^2_{tot}$ and $\dot{\boldsymbol{l}}^4_{tot}$ that contain the material particle coordinates $\boldsymbol{X}$ twice in their components, need further manipulation, so that the second moment of inertia appears (ϵ is omitted for convenience). For the term $\dot{\boldsymbol{l}}^4_{tot}$

$$\begin{aligned}
\dot{\boldsymbol{l}}^4_{tot} &= \int_{0_A} \rho_{ref} \left(\boldsymbol{\Lambda}\boldsymbol{X}\right) \times \left[\underbrace{\left(\boldsymbol{A}^T \ddot{\boldsymbol{A}}\right)}_{\boldsymbol{C}} \boldsymbol{\Lambda}\boldsymbol{X} + 2\,\boldsymbol{A}^T \dot{\boldsymbol{A}} \dot{\boldsymbol{\Lambda}} \boldsymbol{X}\right] d^0\boldsymbol{A} \\
&= \int_{0_A} \rho_{ref} \left(\boldsymbol{\Lambda}\boldsymbol{X}\right) \times \boldsymbol{C}\boldsymbol{\Lambda}\boldsymbol{X}\, d^0\boldsymbol{A} + 2 \int_{0_A} \rho_{ref} \left[\left(\boldsymbol{\Lambda}\boldsymbol{X}\right) \times \left(\boldsymbol{A}^T \dot{\boldsymbol{A}} \boldsymbol{\Lambda}\boldsymbol{\Omega} \times \boldsymbol{A}^T \dot{\boldsymbol{A}} \boldsymbol{\Lambda}\boldsymbol{X}\right)\right] d^0\boldsymbol{A} \\
&\overset{eq.(4.43)}{=} \int_{0_A} \rho_{ref} \left(\boldsymbol{\Lambda}\boldsymbol{X}\right) \times \boldsymbol{C}\boldsymbol{\Lambda}\boldsymbol{X}\, d^0\boldsymbol{A} \\
&+ 2 \int_{0_A} \rho_{ref} \left[\left(\boldsymbol{X}^T \underbrace{\boldsymbol{\Lambda}^T \boldsymbol{A}^T \dot{\boldsymbol{A}} \boldsymbol{\Lambda}}_{\boldsymbol{K}\boldsymbol{0}_{coriol.}} \boldsymbol{X}\right) - \left(\boldsymbol{A}^T \dot{\boldsymbol{A}} \boldsymbol{\Lambda} \boldsymbol{X} \boldsymbol{X}^T \boldsymbol{\Lambda}^T\right)\right] \boldsymbol{A}^T \dot{\boldsymbol{A}} \boldsymbol{\Lambda}\boldsymbol{\Omega}\, d^0\boldsymbol{A}
\end{aligned} \tag{E.12}$$

In eq. (E.12), the first component is manipulated as,

$$\begin{aligned}
\int_{0_A} \rho_{ref} \left(\boldsymbol{\Lambda}\boldsymbol{X}\right) \times \boldsymbol{C}\boldsymbol{\Lambda}\boldsymbol{X}\, d^0\boldsymbol{A} &= \int_A \rho_{ref} \boldsymbol{\Lambda} \hat{\boldsymbol{X}} \underbrace{\boldsymbol{\Lambda}^T \boldsymbol{C} \boldsymbol{\Lambda}}_{\boldsymbol{K}\boldsymbol{0}_{centri.}} \boldsymbol{X}\, dA \\
&= \boldsymbol{\Lambda} \begin{Bmatrix} \boldsymbol{K}(3,2)\boldsymbol{J}(3,3) - (\boldsymbol{K}(3,3) - \boldsymbol{K}(2,2))\boldsymbol{J}(2,3) - \boldsymbol{K}(2,3)\boldsymbol{J}(2,2) \\ -\boldsymbol{K}(1,2)\boldsymbol{J}(2,3) + \boldsymbol{K}(1,3)\boldsymbol{J}(2,2) \\ -\boldsymbol{K}(1,2)\boldsymbol{J}(3,3) + \boldsymbol{K}(1,3)\boldsymbol{J}(2,3) \end{Bmatrix}
\end{aligned} \tag{E.13}$$

where $\hat{\boldsymbol{X}}\boldsymbol{K}\boldsymbol{0}_{centri.}\boldsymbol{X}$ is written in componential form as

$$\hat{\boldsymbol{X}}\boldsymbol{K}\boldsymbol{0}_{centri.}\boldsymbol{X} = \begin{Bmatrix} \boldsymbol{K}(3,2)\eta^2 + (\boldsymbol{K}(3,3) - \boldsymbol{K}(2,2))\eta\zeta - \boldsymbol{K}(2,3)\zeta^2 \\ \boldsymbol{K}(1,2)\eta\zeta + \boldsymbol{K}(1,3)\zeta^2 \\ -\boldsymbol{K}(1,2)\eta^2 - \boldsymbol{K}(1,3)\eta\zeta \end{Bmatrix} \tag{E.14}$$

In eq. (E.12), the second component is manipulated as,

$$\dot{\boldsymbol{l}}^4_{tot} = \int_{0_A} \rho_{ref}\,(\boldsymbol{\Lambda X}) \times \left(\boldsymbol{A}^T \dot{\boldsymbol{A}} \boldsymbol{\Lambda \Omega}\right) \times \left(\boldsymbol{A}^T \dot{\boldsymbol{A}} \boldsymbol{\Lambda X}\right) d^0\boldsymbol{A}$$
$$\overset{(eq.4.43)}{=} 2 \int_{0_A} \rho_{ref} \left\{ \left[\boldsymbol{X}^T \underbrace{\boldsymbol{\Lambda}^T \left(\boldsymbol{A}^T \dot{\boldsymbol{A}}\right) \boldsymbol{\Lambda}}_{\boldsymbol{K0}_{coriol.}} \boldsymbol{X} \right] - \left[\boldsymbol{A}^T \dot{\boldsymbol{A}} \boldsymbol{\Lambda X X}^T \boldsymbol{\Lambda}^T\right] \right\} \boldsymbol{A}^T \dot{\boldsymbol{A}} \boldsymbol{\Lambda \Omega}\, d^0\boldsymbol{A} \tag{E.15}$$

where $\boldsymbol{X}$ is

$$\boldsymbol{X} = \begin{Bmatrix} 0 & \eta & \zeta \end{Bmatrix}^T \tag{E.16}$$

Thus, for the matrix $\boldsymbol{K0}_{coriol.}$

$$\boldsymbol{X}^T\, \boldsymbol{K0}_{coriol.}\, \boldsymbol{X} = \boldsymbol{K0}_{coriol.}(2,2)\,\eta^2 + \boldsymbol{K0}_{coriol.}(2,3)\eta\zeta + \boldsymbol{K0}_{coriol.}(3,2)\eta\zeta + \boldsymbol{K0}_{coriol.}(3,3)\zeta^2 \tag{E.17}$$

while

$$\boldsymbol{X X}^T = \begin{bmatrix} 0 & 0 & 0 \\ 0 & \eta^2 & \eta\zeta \\ 0 & \eta\zeta & \zeta^2 \end{bmatrix} \tag{E.18}$$

From the above, eq. (E.15) is written as

$$\dot{\boldsymbol{l}}^4_{tot} = \underbrace{\left(\boldsymbol{K0}_{coriol.}(2,2)\boldsymbol{J}(3,3) - \boldsymbol{K0}_{coriol.}(2,3)\boldsymbol{J}(2,3) - \boldsymbol{K0}_{coriol.}(3,2)\boldsymbol{J}(3,2) + \boldsymbol{K0}_{coriol.}(3,3)\boldsymbol{J}(2,2)\right)\boldsymbol{I}_3}_{\boldsymbol{J0}_{coriol.}}$$
$$- \left(\boldsymbol{A}^T \dot{\boldsymbol{A}}\right) \boldsymbol{\Lambda} \begin{bmatrix} 0 & 0 & 0 \\ 0 & \boldsymbol{J}(3,3) & -\boldsymbol{J}(2,3) \\ 0 & -\boldsymbol{J}(3,2) & \boldsymbol{J}(2,2) \end{bmatrix} \boldsymbol{\Lambda}^T \left(\boldsymbol{A}^T \dot{\boldsymbol{A}}\right) \boldsymbol{\Lambda \Omega} \tag{E.19}$$

For the third component of $\dot{\boldsymbol{l}}^4_{tot}$ see section 4.7. In $\dot{\boldsymbol{l}}^2_{tot}$, the term is manipulated as the second term in eq. (E.12).

For the linearization of the terms in eq. (E.11), the directional derivative w.r.t. ϵ for $\epsilon = 0$ is employed. The Lagrange's formula is used for the triple vector cross product. The linearization of the terms $\boldsymbol{A}^T_\epsilon \dot{\boldsymbol{R}}_\epsilon$, $\boldsymbol{A}^T_\epsilon \dot{\boldsymbol{A}}_\epsilon$, $\boldsymbol{A}^T_\epsilon \ddot{\boldsymbol{R}}_\epsilon$ and $\boldsymbol{A}^T_\epsilon \ddot{\boldsymbol{A}}_\epsilon$ have already employed in a previous work. In the following, the linearization of the above terms are written shortly for completeness, while the terms which contain the linearization of $\boldsymbol{r}_{0,\epsilon}$ and $\boldsymbol{\Lambda}_\epsilon$ are further

analyzed

$$
\begin{aligned}
\frac{d}{d\epsilon}\Big|_{\epsilon=0}\left(\dot{\boldsymbol{l}}^1_{tot,\epsilon}\right) &= \left[\widehat{\delta\boldsymbol{\psi}}\boldsymbol{\Lambda}\hat{\boldsymbol{\Omega}}\boldsymbol{S}_m + \boldsymbol{\Lambda}\delta\hat{\boldsymbol{\Omega}}\boldsymbol{S}_m\right]\times\left(\boldsymbol{A}^T\dot{\boldsymbol{R}} + \boldsymbol{A}^T\dot{\boldsymbol{A}}\boldsymbol{r}_0 + \dot{\boldsymbol{r}}_0\right)\\
&\quad + \left(\boldsymbol{\Lambda}\hat{\boldsymbol{\Omega}}\boldsymbol{S}_m\right)\times\left[d\left(\boldsymbol{A}^T\dot{\boldsymbol{R}}\right) + d\left(\boldsymbol{A}^T\dot{\boldsymbol{A}}\right)\boldsymbol{r}_0 + \boldsymbol{A}^T\dot{\boldsymbol{A}}\delta\boldsymbol{r}_0 + \delta\dot{\boldsymbol{r}}_0\right]\\
\frac{d}{d\epsilon}\Big|_{\epsilon=0}\left(\dot{\boldsymbol{l}}^2_{tot,\epsilon}\right) &= \int_{0_A}\rho_{ref}\left\{\left(\widehat{\delta\boldsymbol{\psi}}\boldsymbol{\Lambda}\hat{\boldsymbol{\Omega}}\boldsymbol{X}\right)\times\left(\boldsymbol{A}^T\dot{\boldsymbol{A}}\boldsymbol{\Lambda}\boldsymbol{X}\right) + \left(\boldsymbol{\Lambda}\delta\hat{\boldsymbol{\Omega}}\boldsymbol{X}\right)\times\left(\boldsymbol{A}^T\dot{\boldsymbol{A}}\boldsymbol{\Lambda}\boldsymbol{X}\right)\right.\\
&\quad \left. + \left(\boldsymbol{\Lambda}\hat{\boldsymbol{\Omega}}\boldsymbol{X}\right)\times\left[d\left(\boldsymbol{A}^T\dot{\boldsymbol{A}}\right)\boldsymbol{\Lambda}\boldsymbol{X} + \boldsymbol{A}^T\dot{\boldsymbol{A}}\widehat{\delta\boldsymbol{\psi}}\boldsymbol{\Lambda}\boldsymbol{X}\right]\right\}d^0\boldsymbol{A}\\
\frac{d}{d\epsilon}\Big|_{\epsilon=0}\left(\dot{\boldsymbol{l}}^3_{tot,\epsilon}\right) &= \left(\widehat{\delta\boldsymbol{\psi}}\boldsymbol{\Lambda}\boldsymbol{S}_m\right)\times\left[\left(\boldsymbol{A}^T\ddot{\boldsymbol{R}}\right) + \left(\boldsymbol{A}^T\ddot{\boldsymbol{A}}\right)\boldsymbol{r}_0 + 2\,\boldsymbol{A}^T\dot{\boldsymbol{A}}\dot{\boldsymbol{r}}_0 + \ddot{\boldsymbol{r}}_0\right]\\
&\quad + \left(\boldsymbol{\Lambda}\boldsymbol{S}_m\right)\times\left[d\left(\boldsymbol{A}^T\ddot{\boldsymbol{R}}\right) + d\left(\boldsymbol{A}^T\ddot{\boldsymbol{A}}\right)\boldsymbol{r}_0 + 2\,d\left(\boldsymbol{A}^T\dot{\boldsymbol{A}}\right)\dot{\boldsymbol{r}}_0\right.\\
&\quad \left. + \left(\boldsymbol{A}^T\ddot{\boldsymbol{A}}\right)\delta\boldsymbol{r}_0 + 2\,\boldsymbol{A}^T\dot{\boldsymbol{A}}\delta\dot{\boldsymbol{r}}_0 + \delta\ddot{\boldsymbol{r}}_0\right]\\
\frac{d}{d\epsilon}\Big|_{\epsilon=0}\left(\dot{\boldsymbol{l}}^4_{tot,\epsilon}\right) &= \int_{0_A}\rho\left\{\left(\widehat{\delta\boldsymbol{\psi}}\boldsymbol{\Lambda}\boldsymbol{X}\right)\times\left[\left(\boldsymbol{A}^T\ddot{\boldsymbol{A}}\right)\boldsymbol{\Lambda}\boldsymbol{X} + 2\,\boldsymbol{A}^T\dot{\boldsymbol{A}}\dot{\boldsymbol{\Lambda}}\boldsymbol{X} + \ddot{\boldsymbol{\Lambda}}\boldsymbol{X}\right]\right.\\
&\quad + \left(\boldsymbol{\Lambda}\boldsymbol{X}\right)\times\left[d\left(\boldsymbol{A}^T\ddot{\boldsymbol{A}}\right)\boldsymbol{\Lambda}\boldsymbol{X} + 2\,d\left(\boldsymbol{A}^T\dot{\boldsymbol{A}}\right)\dot{\boldsymbol{\Lambda}}\boldsymbol{X}\right.\\
&\quad \left.\left. + \left(\boldsymbol{A}^T\ddot{\boldsymbol{A}}\right)\widehat{\delta\boldsymbol{\psi}}\boldsymbol{\Lambda}\boldsymbol{X} + 2\,\boldsymbol{A}^T\dot{\boldsymbol{A}}\left(\widehat{\delta\boldsymbol{\psi}}\boldsymbol{\Lambda}\hat{\boldsymbol{\Omega}}\boldsymbol{X} + \boldsymbol{\Lambda}\delta\hat{\boldsymbol{\Omega}}\boldsymbol{X}\right) + \delta\left(\ddot{\boldsymbol{\Lambda}}\right)\boldsymbol{X}\right]\right\}d^0\boldsymbol{A}
\end{aligned}
\tag{E.20}
$$

The Lagrange's formula in eq. (4.43) is used to further manipulate the above linearized terms which are connected to the elastic DOFs of the beam (the second and the fourth terms are connected to a beam with a solid cross-section, while the first and the third terms are added

to the previous when the beam has a general cross-section).

$$
\begin{aligned}
\left.\frac{d}{d\epsilon}\right|_{\epsilon=0}\left(\boldsymbol{i}^1_{tot,\epsilon}\right) &= \left[\dot{\boldsymbol{\Lambda}}\boldsymbol{S}_m\left(\boldsymbol{A}^T\dot{\boldsymbol{R}}+\boldsymbol{A}^T\dot{\boldsymbol{A}}\boldsymbol{r}_0+\dot{\boldsymbol{r}}_0\right)^T-\left(\boldsymbol{A}^T\dot{\boldsymbol{R}}+\boldsymbol{A}^T\dot{\boldsymbol{A}}\boldsymbol{r}_0+\dot{\boldsymbol{r}}_0\right)^T\dot{\boldsymbol{\Lambda}}\boldsymbol{S}_m\boldsymbol{I}\right]\delta\boldsymbol{\psi}\\
&+\left[\boldsymbol{\Lambda}\boldsymbol{S}_m\left(\boldsymbol{A}^T\dot{\boldsymbol{R}}+\boldsymbol{A}^T\dot{\boldsymbol{A}}\boldsymbol{r}_0+\dot{\boldsymbol{r}}_0\right)^T-\left(\boldsymbol{A}^T\dot{\boldsymbol{R}}+\boldsymbol{A}^T\dot{\boldsymbol{A}}\boldsymbol{r}_0+\dot{\boldsymbol{r}}_0\right)^T\boldsymbol{\Lambda}\boldsymbol{S}_m\right]\boldsymbol{\Lambda}\delta\boldsymbol{\Omega}\\
&+d\left(\boldsymbol{A}^T\dot{\boldsymbol{A}}\right)\boldsymbol{\Lambda}\boldsymbol{S}_m\times\left(\boldsymbol{A}^T\dot{\boldsymbol{R}}+\boldsymbol{A}^T\dot{\boldsymbol{A}}\boldsymbol{r}_0+\dot{\boldsymbol{r}}_0\right)\\
&+\left[\left(\boldsymbol{A}^T\dot{\boldsymbol{A}}\boldsymbol{\Lambda}\boldsymbol{S}_m\right)\left(\boldsymbol{A}^T\dot{\boldsymbol{R}}+\boldsymbol{A}^T\dot{\boldsymbol{A}}\boldsymbol{r}_0+\dot{\boldsymbol{r}}_0\right)^T-\left(\boldsymbol{A}^T\dot{\boldsymbol{R}}+\boldsymbol{A}^T\dot{\boldsymbol{A}}\boldsymbol{r}_0+\dot{\boldsymbol{r}}_0\right)\left(\boldsymbol{A}^T\dot{\boldsymbol{A}}\boldsymbol{\Lambda}\boldsymbol{S}_m\right)^T\right]\boldsymbol{A}^T\dot{\boldsymbol{A}}\delta\boldsymbol{\psi}\\
&+\left(\boldsymbol{A}^T\dot{\boldsymbol{A}}\boldsymbol{\Lambda}\boldsymbol{S}_m+\boldsymbol{\Lambda}\hat{\boldsymbol{\Omega}}\boldsymbol{S}_m\right)\times\left[d\left(\boldsymbol{A}^T\dot{\boldsymbol{R}}\right)+d\left(\boldsymbol{A}^T\dot{\boldsymbol{A}}\right)\boldsymbol{r}_0+\left(\boldsymbol{A}^T\dot{\boldsymbol{A}}\right)\delta\boldsymbol{r}_0+\delta\dot{\boldsymbol{r}}_0\right]\\
\left.\frac{d}{d\epsilon}\right|_{\epsilon=0}\left(\boldsymbol{i}^2_{tot,\epsilon}\right) &= \int_{0_A}\rho_{ref}\left\{\left[\dot{\boldsymbol{\Lambda}}\boldsymbol{X}\boldsymbol{X}^T\boldsymbol{\Lambda}^T\left(\boldsymbol{A}^T\dot{\boldsymbol{A}}\right)^T-\left(\boldsymbol{X}^T\boldsymbol{\Lambda}^T\left(\boldsymbol{A}^T\dot{\boldsymbol{A}}\right)^T\dot{\boldsymbol{\Lambda}}\boldsymbol{X}\right)\boldsymbol{I}\right]\delta\boldsymbol{\psi}\right.\\
&+\left[\boldsymbol{\Lambda}\boldsymbol{X}\boldsymbol{X}^T\boldsymbol{\Lambda}^T\left(\boldsymbol{A}^T\dot{\boldsymbol{A}}\right)^T-\boldsymbol{X}^T\boldsymbol{\Lambda}^T\left(\boldsymbol{A}^T\dot{\boldsymbol{A}}\right)^T\boldsymbol{\Lambda}\boldsymbol{X}\boldsymbol{I}\right]\boldsymbol{\Lambda}\delta\boldsymbol{\Omega}\\
&\left.+\left(\dot{\boldsymbol{\Lambda}}\boldsymbol{X}\right)\times\left[d\left(\boldsymbol{A}^T\dot{\boldsymbol{A}}\right)\boldsymbol{\Lambda}\boldsymbol{X}\right]+\left[\boldsymbol{X}^T\dot{\boldsymbol{\Lambda}}^T\boldsymbol{A}^T\dot{\boldsymbol{A}}\boldsymbol{\Lambda}\boldsymbol{X}-\left(\boldsymbol{A}^T\dot{\boldsymbol{A}}\boldsymbol{\Lambda}\boldsymbol{X}\boldsymbol{X}^T\dot{\boldsymbol{\Lambda}}^T\right)\boldsymbol{I}\right]\boldsymbol{A}^T\dot{\boldsymbol{A}}\delta\boldsymbol{\psi}\right\}d^0\boldsymbol{A}\\
\left.\frac{d}{d\epsilon}\right|_{\epsilon=0}\left(\boldsymbol{i}^3_{tot,\epsilon}\right) &= \left[\boldsymbol{\Lambda}\boldsymbol{S}_m\boldsymbol{a}^T_{MB}-\boldsymbol{a}^T_{MB}\boldsymbol{\Lambda}\boldsymbol{S}_m\right]\delta\boldsymbol{\psi}\\
&+\left(\boldsymbol{\Lambda}\boldsymbol{S}_m\right)\times\left[d\left(\boldsymbol{A}^T\ddot{\boldsymbol{R}}\right)+d\left(\boldsymbol{A}^T\ddot{\boldsymbol{A}}\right)\boldsymbol{r}_0+2\,d\left(\boldsymbol{A}^T\dot{\boldsymbol{A}}\right)\dot{\boldsymbol{r}}_0\right.\\
&\left.+\left(\boldsymbol{A}^T\ddot{\boldsymbol{A}}\right)\delta\boldsymbol{r}_0+2\,\boldsymbol{A}^T\dot{\boldsymbol{A}}\delta\dot{\boldsymbol{r}}_0+\delta\ddot{\boldsymbol{r}}_0\right];\ \boldsymbol{a}_{MB}=\boldsymbol{A}^T\ddot{\boldsymbol{R}}\\
\left.\frac{d}{d\epsilon}\right|_{\epsilon=0}\left(\boldsymbol{i}^4_{tot,\epsilon}\right) &= \int_{0_A}\rho_{ref}\left\{\left[\boldsymbol{\Lambda}\boldsymbol{X}\boldsymbol{X}^T\boldsymbol{\Lambda}^T\left(\boldsymbol{A}^T\ddot{\boldsymbol{A}}\right)^T-\boldsymbol{X}^T\boldsymbol{\Lambda}^T\left(\boldsymbol{A}^T\ddot{\boldsymbol{A}}\right)^T\boldsymbol{\Lambda}\boldsymbol{X}\boldsymbol{I}\right]\delta\boldsymbol{\psi}\right.\\
&+2\left[\boldsymbol{\Lambda}\boldsymbol{X}\boldsymbol{X}^T\dot{\boldsymbol{\Lambda}}^T\left(\boldsymbol{A}^T\dot{\boldsymbol{A}}\right)^T-\boldsymbol{X}^T\dot{\boldsymbol{\Lambda}}^T\left(\boldsymbol{A}^T\dot{\boldsymbol{A}}\right)^T\boldsymbol{\Lambda}\boldsymbol{X}\boldsymbol{I}\right]\delta\boldsymbol{\psi}\\
&+\left(\boldsymbol{\Lambda}\boldsymbol{X}\right)\times\left[d\left(\boldsymbol{A}^T\ddot{\boldsymbol{A}}\right)\boldsymbol{\Lambda}\boldsymbol{X}+2\,d\left(\boldsymbol{A}^T\dot{\boldsymbol{A}}\right)\dot{\boldsymbol{\Lambda}}\boldsymbol{X}+\delta\left(\ddot{\boldsymbol{A}}\right)\boldsymbol{X}\right]\\
&+\left[\boldsymbol{X}^T\boldsymbol{\Lambda}^T\left(\boldsymbol{A}^T\ddot{\boldsymbol{A}}\right)\boldsymbol{\Lambda}\boldsymbol{X}\boldsymbol{I}-\left(\boldsymbol{A}^T\ddot{\boldsymbol{A}}\right)\boldsymbol{\Lambda}\boldsymbol{X}\boldsymbol{X}^T\boldsymbol{\Lambda}^T\right]\left(\boldsymbol{A}^T\ddot{\boldsymbol{A}}\right)\delta\boldsymbol{\psi}\\
&+2\left[\boldsymbol{X}^T\boldsymbol{\Lambda}^T\left(\boldsymbol{A}^T\dot{\boldsymbol{A}}\right)\dot{\boldsymbol{\Lambda}}\boldsymbol{X}\boldsymbol{I}-\left(\boldsymbol{A}^T\dot{\boldsymbol{A}}\right)\dot{\boldsymbol{\Lambda}}\boldsymbol{X}\boldsymbol{X}^T\boldsymbol{\Lambda}^T\right]\left(\boldsymbol{A}^T\dot{\boldsymbol{A}}\right)\delta\boldsymbol{\psi}\\
&\left.+2\left[\boldsymbol{X}^T\boldsymbol{\Lambda}^T\left(\boldsymbol{A}^T\dot{\boldsymbol{A}}\right)\boldsymbol{\Lambda}\boldsymbol{X}\boldsymbol{I}-\left(\boldsymbol{A}^T\dot{\boldsymbol{A}}\right)\boldsymbol{\Lambda}\boldsymbol{X}\boldsymbol{X}^T\boldsymbol{\Lambda}^T\right]\left(\boldsymbol{A}^T\dot{\boldsymbol{A}}\right)\boldsymbol{\Lambda}\delta\boldsymbol{\Omega}\right\}d^0\boldsymbol{A}
\end{aligned}
\tag{E.21}
$$

Bibliography

Abambres, M., D. Camotim, and N. Silvestre (2014). "GBT-Based Elastic-Plastic Post-Buckling Analysis of Stainless Steel Thin-Walled Members". In: *Thin-Walled Structures* 83, pp. 85–102. URL: https://doi.org/10.1016/j.tws.2014.01.004.

Ageze, Mesfin Belayneh, Yefa Hu, and Huachun Wu (2017). "Wind Turbine Aeroelastic Modeling: Basics and Cutting Edge Trends". In: *International Journal of Aerospace Engineering* 1, pp. 1–15. URL: https://doi.org/10.1155/2017/5263897.

Antman, Stuart S. (2005). *Nonlinear Problems of Elasticity, Second Edition*. Springer.

Argyridi, K.A. (2019). "Linear and Non-linear Elastic Stability of Beams by Higher Order Beam Theories". PhD thesis. School of Civil Engineering, NTUA, Athens.

Argyris, J. (1982). "An excursion into large rotations". In: *Computer Methods in Applied Mechanics and Engineering* 32, pp. 85–155. URL: https://doi.org/10.1016/0045-7825(82)90069-X.

Arnold, V. I. (1989). *Mathematical Methods of Classical Mechanics*. Springer-Verlag, New York.

Auricchio, F., P. Carotenuto, and A. Reali (2008). "On the geometrically exact beam model: A consistent, effective and simple derivation from three-dimensional finite-elasticity". In: *International Journal of Solids and Structures* 45, pp. 4766–4781. URL: https://doi.org/10.1016/j.ijsolstr.2008.04.015.

Bagherpour, Tohid. et al. (2018). "Modeling of material bend-twist coupling on wind turbine blades". In: *Composite Structures* 193, pp. 237–246. URL: https://doi.org/10.1016/j.compstruct.2018.03.071.

Bak, Christian et al. (2013). "Description of the DTU 10 MW Reference Wind Turbine". In: *DTU Wind Energy Report-I-0092*.

Baranski, Przemyslaw. *Quaternions*. Available at https://www.mathworks.com/matlabcentral/fileexchange/35475-quaternions.

Bathe, K-J. (1996). *Finite Element Procedures*. Prentice-Hall, Inc.

Bathe, K-J. and S. Bolourchi (1979). "Large displacement analysis of three-dimensional beam structures". In: *International Journal for Numerical Methods in Engineering* 14, pp. 961–986. URL: https://doi.org/10.1002/nme.1620140703.

Bauchau, O. A. (2011). *Flexible Multibody Dynamics*. Springer.

Bauchau, O. A., G. Damilano, and N. J. Theron (1995). "Numerical integration of non-linear elastic multi-body systems". In: *International Journal for Numerical Methods in Engineering* 38, pp. 2727–2751. URL: DOI:10.1002/NME.1620381605.

Bazoune, A., Y. A. Khulief, and N. G. Stephen (2003). "Shape functions of three-dimensional Timoshenko beam element". In: *Journal of Sound and Vibration* 259(2), pp. 473–480. URL: http://dx.doi.org/10.1006/jsvi.2002.5122.

Berdichevsky, V. L. (2009). *Variational Principles of Continuum Mechanics I. Fundamentals*. Springer, Berlin.

Betsch, P. and P. Steinmann (2002). "Frame-indifferent beam finite elements based upon the geometrically exact beam theory". In: *International Journal for Numerical Methods in Engineering* 54, pp. 1775–1788. URL: https://doi.org/10.1002/nme.487.

Blasques, J. (2012). "User's Manual for BECAS: A Cross Section Analysis Tool for Anisotropic and Inhomogeneous Beam Sections of Arbitrary Geometry". In: *National Laboratory of Sustainable Energy, Denmark. Forskningscenter Risoe, Risoe-R No. 1785 (EN)*.

Bonet, Javier and Richard D. Wood (1997). *Nonlinear continuum mechanics for finite element analysis*. Cambridge university press.

Borst, R. de et al. (2012a). *Non-linear Finite Element Analysis of Solids and Structures*. Vol. Second edition. A John Wiley & Sons Ltd. Publication.

Borst, René De et al. (2012b). *Non-linear finite element analysis of solids and structures*. Wiley series in computational mechanics. John Wiley & Sons Ltd.

Bottasso, C. L. and M. Borri (1998). "Integrating finite rotations". In: *Computer Methods in Applied Mechanics and Engineering* 164, pp. 307–331. URL: https://doi.org/10.1016/S0045-7825(98)00031-0.

Bottasso, C. L., M. Borri, and L. Trainelli (2002). "Geometric invariance". In: *Computational Mechanics* 29, pp. 163–169. URL: DOI:10.1007/s00466-002-0329-8.

Bottasso, C.L. and A. Croce (2006-2015). In: *Cp Lambda, User's Manual*. Politecnico di Milano.

Burton, Tony et al. (2001). *Wind Energy Handbook*. John Wiley & Sons, Ltd.

Cardona, A. and M. Géradin (1988). "A beam finite element non-linear theory with finite rotations". In: *International Journal for Numerical Methods in Engineering* 26, pp. 2403–2438. URL: https://doi.org/10.1002/nme.1620261105.

Chen, Z.Q. and T.J. Agar (1993). "Geometric nonlinear analysis of flexible spatial beam structures". In: *Computers and Structures* 49(6), pp. 1083–1094. URL: https://doi.org/10.1016/0045-7949(93)90019-A.

Chiras, Dan (2010). *Wind Power*. Basics. New Society Publishers.

Crisfield, M. A. (1981). "A fast incremental/iterative solution procedure that handles "snap-through"". In: *Computers & Structures* 13(1-3), pp. 55–62. URL: https://doi.org/10.1016/0045-7949(81)90108-5.

— (1997). *Non-linear finite element analysis of solids and structures*. Vol. 2. Advanced topics. John Wiley & Sons Ltd.

Crisfield, M. A. and G. Jelenić (1999). "Objectivity of strain measures in the geometrically exact three-dimensional beam theory and its finite-element implementation". In: *Proc. R. Soc. Lond. Ser. A Math. Phys. Eng. Sci.* 455, pp. 1125–1147. URL: https://doi.org/10.1098/rspa.1999.0352.

Dikaros, Ioannis Ch. (2016). "Advanced Beam Theories for the Analysis of Beam Structures". PhD thesis. NTUA, Athens.

Dukić, E. P., G. Jelenić, and M. Gaćeša (2014). "Configuration-dependent interpolation in higher-order 2D beam finite elements". In: *Finite Elements in Analysis and Design* 78, pp. 47–61. URL: https://doi.org/10.1016/j.finel.2013.10.001.

Dukić, Edita Papa and Gordan Jelenić (2014). "Exact solution of 3D Timoshenko beam problem: problem-dependent formulation". In: *Arch Appl Mech* 84, pp. 375–384. URL: DOI10.1007/s00419-013-0805-y.

Dvorkin, E.N., E. Onate, and J. Olivier (1988). "On a non-linear formulation for curved Timoshenko beam elements considering large displacement/rotation increments". In: *International Journal for Numerical Methods in Engineering* 26, pp. 1597–1613. URL: https://doi.org/10.1002/nme.1620260710.

Eade, Ethan (2017). In: *Lie Groups for 2D and 3D Transformations*.

Fafard, M. and B. Massicotte (1993). "Geometrical interpretation of the arc-length method". In: *Computer & Structures* 46(4), pp. 603–615. URL: https://doi.org/10.1016/0045-7949(93)90389-U.

Gaćeša, M. and G. Jelenić (2015). "Modified fixed-pole approach in geometrically exact spatial beam finite elements". In: *Finite Elements in Analysis and Design* 99, pp. 39–48. URL: https://doi.org/10.1016/j.finel.2015.02.001.

Gaćeša, Maja (2015). "Fixed-Pole Concept in 3D Beam Finite Elements - Relationship to Standard Approaches and Analysis of Different Interpolations". PhD thesis. Rijeka.

Gambier, Adrian and Claudio Balzani (2019). "The challenge of teaching control of wind turbines in a civil engineering school". In: *IFAC PapersOnLine* 52-9, pp. 212–217. URL: DOI:10.1016/j.ifacol.2019.08.199.

Géradin, Michel and Alberto Cardona (2001). *Flexible Multibody Dynamics*. A John Wiley & Sons Ltd. Publication.

Ghiringhelli, G. L. (1997). "On the linear three-dimensional behaviour of composite beams". In: *Composites Part B: Engineering* 28(5-6), pp. 613–626. URL: https://doi.org/10.1016/S1359-8368(96)00075-3.

Gilmore, Robert (1974). *Lie Groups, Lie Algebras, and Some of Their Applications*. John Wiley & Sons.

Goldstein, H., C. Poole, and J. Safko (2000). *Classical Mechanics 3rd edition*. Addison-Wesley.

Goss, V.G.A. (2003). "Snap buckling, writhing and loop formation in twisted rods". PhD thesis. Center for Nonlinear Dynamics, University College London.

Goto, Yoshiaki et al. (1992). "Elastic buckling phenomenon applicable to deployable rings". In: *International Journal of Solids and Structures* 29, pp. 893–909. URL: https://doi.org/10.1016/0020-7683(92)90024-N.

Hall, Brian C. (2000). *Lie Groups, Lie Algebras, and Representations*. An Elementary Introduction. Springer.

Hansen, Martin O.L. (2008). *Aerodynamics of Wind Turbines*. Vol. Second Edition. Earthscan.

Hansen, M.H., M. Gaunaa, and H.A. Madsen (2004). "A Beddoes-Leishman Type Dynamic Stall Model in State-Space and Indicial Formulation". In: *Risoe Report, Risoe-R-1354(EN)*. URL: Availableonline:https://backend.orbit.dtu.dk/ws/portalfiles/portal/7711084/ris_r_1354.pdf.

Hassan, GL Garrad (2011). In: *V4.3 Bladed Multibody dynamics, User manual*.

Hinkelmann, Th., G. Lumpe, and H. Rothert (1985). "On a general theory of large rotations and small strain with application to three-dimensional beam structures". In: *Proceedings of the Euromech Colloquium (Jabłonna, Poland)*. Vol. 197. Finite Rotations in Structural Mechanics, pp. 136–147. URL: https://doi.org/10.1007/978-3-642-82838-6.

Hodges, D. H. (2006). *Nonlinear Composite Beam Theory*. Vol. 213. Progress in Astronautics and Aeronautics. American Institute of Aeronautics and Astronautics Inc.

Hodges, D. H. and E. H. Dowell (1974). "Nonlinear equations of motion for the elastic bending and torsion of twisted nonuniform rotor blades". In: *Ames Research Center, NASA and U.S. Army Air Mobility R&D Laboratory, Moffett Field, Calif., 94035, NASA TN D-7818*.

Houbolt, John C. and George W. Brooks (1956). "Differential equations of motion for combined flapwise bending, chordwise bending, and torsion of twisted nonuniform rotor blades". In: *Report 1346 - National advisory committee for aeronautics*.

Ibrahimbegović, A., F. Frey, and I. Kožar (1995). "Computational aspects of vector-like parametrization of three-dimensional finite rotations". In: *International Journal for Numerical Methods in Engineering* 38, pp. 3653–3673. URL: https://doi.org/10.1002/nme.1620382107.

Ibrahimbegović, A. and Mazen Al. Mikdad (1998). "Finite rotations in dynamics of beams and implicit time-stepping schemes". In: *International Journal for Numerical Methods in Engineering* 41, 781–814. URL: https://doi.org/10.1002/(SICI)1097-0207(19980315)41:5<781::AID-NME308>3.0.CO;2-9.

Ibrahimbegović, Adnan and Said Mamouri (2002). "Energy conserving/decaying implicit time-stepping scheme for nonlinear dynamics of three-dimensional beams undergoing finite rotations". In: *Computer methods in applied mechanics and engineering* 191, 4241–4258. URL: https://doi.org/10.1016/S0045-7825(02)00377-8.

IEC (2003-2004). *IEC 61400-1, IEC 2003, 188184CDV, 2004, edited by TC88-MT1*. Vol. 3rd ed.

Jelenić, G. and M. A. Crisfield (1999). "Geometrically exact 3D beam theory: implementation of a strain-invariant finite element for statics and dynamics". In: *Computer Methods in Applied Mechanics and Engineering* 171, pp. 141–171. URL: https://doi.org/10.1016/S0045-7825(98)00249-7.

Jelenić, Gordan and Edita Papa (2011). "Exact solution of 3D Timoshenko beam problem using linked interpolation of arbitrary order". In: *Arch Appl Mech* 81, pp. 171–183. URL: DOI10.1007/s00419-009-0403-1.

Jirasek, M. (2005). "Lecture notes - Short course given by M. Jirasek at the Czech Technical University in Prague". In: *Modeling of Localized Inelastic Deformation*.

Jonkman, J.M. and Jr. M.L. Buhl (2005). In: *FAST User's Guide, Technical Report NREL/TP-500-38230*. National Renewable Energy Laboratory.

Júnior, Celso Jaso Faccio et al. (2019). "Modeling wind turbine blades by geometrically-exact beam and shell elements: A comparative approach". In: *Engineering Structures* 180, pp. 357–378. URL: https://doi.org/10.1016/j.engstruct.2018.09.032.

Kim, Taeseong, Anders M. Hansen, and Kim Branner (2013). "Development of an anisotropic beam finite element for composite wind turbine blades in multibody system". In: *Renewable Energy* 59, pp. 172–183. URL: https://doi.org/10.1016/j.renene.2013.03.033.

Klumpp, A. R. (1976). "Singularity-free extraction of a quaternion from a direction-cosine matrix". In: *Journal of spacecraft and rockets* 13, pp. 754–755. URL: https://doi.org/10.2514/3.27947.

Krenk, Steen (2009). *Non-linear Modeling and Analysis of Solids and Structures*. Cambridge University Press.

Larsen, Torben J. and Anders M. Hansen (2021). In: *How 2 HAWC2, the user's manual, Riso-R-1597 (ver. 12.9)*. Riso National Laboratory, Technical University of Denmark.

Linn, J., H. Lang, and A. Tuganov (2013). "Geometrically exact Cosserat rods with Kelvin-Voigt type viscous damping". In: *Mechanical Sciences* 4(1), pp. 79–96. URL: DOI:10.5194/ms-4-79-2013.

Luo, Yunhua (2008). "An efficient 3D Timoshenko beam element with consistent shape functions". In: *Advances in Theoretical and Applied Mechanics* 1(3), pp. 95–106.

Mäkinen, J. (2001). "Critical study of Newmark-scheme in manifold of finite rotations". In: *Computer Methods in Applied Mechanics and Engineering* 191, pp. 817–828. URL: https://doi.org/10.1016/S0045-7825(01)00291-2.

Mäkinen, Jari (2008). "Rotation manifold SO(3) and its tangential vectors". In: *Computational Mechanics* 42(6), pp. 907–919. URL: DOI:10.1007/s00466-008-0293-z.

Manolas, D., V. Riziotis, and S. Voutsinas (2014). "Assessment of 3D aerodynamic effects on the behaviour of floating wind turbines". In: *J. Phys. Conf. Ser.* 555(1), p. 012067. URL: https://doi.org/10.1088/1742-6596/555/1/012067.

Manolas, D.I. (2015). "Hydro-Aero-Elastic Analysis of Offshore Wind Turbines". PhD thesis. School of Mechanical Engineering, Laboratory of Aerodynamics, National Technical University of Athens.

Manolas, D.I., V.A. Riziotis, and S.G. Voutsinas (2015). "Assessing the importance of geometric nonlinear effects in the prediction of wind turbine blade loads". In: *Journal of computational and nonlinear dynamics* 10(4). URL: https://doi.org/10.1115/1.4027684.

Manolas, D.I. et al. (2015). "Cross comparison of aeroelastic state-of-the-art design tools on a 10 MW scale wind turbine". In: *In Proceedings of the European Wind Energy Association (EWEA2015) Annual event*. Vol. Paris, France, 17-20 November.

Manolas, D.I. et al. (2018a). "Assessment of load reduction capabilities using passive and active control methods on a 10MW-scale wind turbine". In: *J. Phys. Conf. Ser.* 1037(3), p. 032042. URL: https://doi.org/10.1088/1742-6596/1037/3/032042.

Manolas, D.I. et al. (2018b). "Inflow-based flap control on a 10MW-scale wind turbine using a spinner anemometer". In: *J. Phys. Conf. Ser.* 1037(3), p. 032045. URL: https://doi.org/10.1088/1742-6596/1037/3/032045.

Manolas, D.I. et al. (2020). "Hydro-servo-aero-elastic analysis of floating offshore wind turbines". In: *Fluids* 5(4), 200. URL: https://doi.org/10.3390/fluids5040200.

Manwell, J.F., J.G. Mcgowan, and A.L. Rogers (2009). *Wind Energy Explained*. Vol. Second Edition. Theory, Design and Application. John Wiley & Sons, Ltd.

McGinty, B. *Continuum Mechanics*. Available at https://www.continuummechanics.org.

Meier, Christoph, Alexander Popp, and Wolfgang A. Wall (2014). "An objective 3D large deformation finite element formulation for geometrically exact curved Kirchhoff rods". In: *Computer Methods in Applied Mechanics and Engineering* 278, pp. 445–478. URL: https://doi.org/10.1016/j.cma.2014.05.017.

— (2015). "A locking-free finite element formulation and reduced models for geometrically exact Kirchhoff rods". In: *Computer Methods in Applied Mechanics and Engineering* 290, pp. 314–341. URL: https://doi.org/10.1016/j.cma.2015.02.029.

Meier, Christoph, Wolfgang A. Wall, and Alexander Popp (2019). "Geometrically exact finite element formulations for curved slender beams: Kirchhoff-Love theory vs. Simo-Reissner theory". In: *Archives of Computational Methods in Engineering* 26, pp. 163–243. URL: https://doi.org/10.1007/s11831-017-9232-5.

Miranda, S. De et al. (2017). "A corotational based geometrically nonlinear Generalized Beam Theory: buckling FE analysis". In: *International Journal of Solids and Structures* 121, pp. 212–227. URL: https://doi.org/10.1016/j.ijsolstr.2017.05.030.

Mueller, Andreas (2013). "Part I, I.a - Mathematical Background". In: *CISM Lectures: Differential-Geometric Methods in Computational Multibody System Dynamics*.

Newmark, N. M. (1959). "A method of computation for structural dynamics". In: *Journal of the Engineering Mechanics Division* 85(3), pp. 67–94.

OpenFAST. *BeamDyn Theory*. https://openfast.readthedocs.io/en/dev/source/user/beamdyn/theory.html.

Pai, Perngjin F., Anthony N. Palazotto, and Jr James M. Greer (1998). "Polar decomposition and appropriate strains and stresses for nonlinear structural analyses". In: *Computers and Structures* 66(6), pp. 823–840. URL: https://doi.org/10.1016/S0045-7949(98)00004-2.

Pai, P.F. and A.H. Nayfeh (1994). "A new method for the modeling of geometric nonlinearities in structures". In: *Computers and Structures* 53(4), pp. 877–895. URL: https://doi.org/10.1016/0045-7949(94)90376-X.

Panteli, Anthoula N., Dimitris I. Manolas, and Konstantinos V. Spiliopoulos (2016). "A degenerate-continuum based Timoshenko beam approach for the aeroelastic analysis of

the wind turbine blades". In: *Proceedings of the ECCOMAS Congress (Crete Island, Greece)*.

Panteli, Anthoula N. and Konstantinos V. Spiliopoulos (2020). "Comparative study of two geometrically non-linear beam models with different strain measures". In: *International Journal of Non-Linear Mechanics* 123(4). URL: DOI:10.1016/j.ijnonlinmec.2020.103480.

Papadrakakis, Manolis (1998). *Non-Linear Finite Elements (in Greek)*. National Technical University of Athens.

Papazafeiropoulos, G. *Arc Length Matlab*. Available at https://www.researchgate.net/profile/George_Papazafeiropoulos2/contributions.

Pavese, Christian et al. (2015). "HAWC2 and BeamDyn: Comparison Between Beam Structural Models for Aero-Servo-Elastic Frameworks". In: *EWEA 2015, Paris, France, November 17-10*.

Petot, D. (1989). "Differential equation modeling of dynamic stall". In: *Recherche Aerospatiale* 5, pp. 59–72.

Petrov, E. and M. Géradin (1998). "Finite element theory for curved and twisted beams based on exact solutions for three-dimensional solids, Part 1: Beam concept and geometrically exact nonlinear formulation". In: *Computer methods in applied mechanics and engineering* 165, pp. 43–92. URL: https://doi.org/10.1016/S0045-7825(98)00061-9.

Reissner, E. (1972). "On one-dimensional finite-strain beam theory: the plane problem". In: *Journal of applied mathematics and physics (ZAMP)* 23, pp. 795–804.

— (1981). "On finite deformations of space-curved beams". In: *Journal of applied mathematics and physics (ZAMP)* 32, pp. 734–744.

Riks, E. (1979). "An incremental approach to the solution of snapping and buckling problems". In: *International Journal of Solids and Structures* 15, pp. 529–551. URL: https://doi.org/10.1016/0020-7683(79)90081-7.

Ritto-Corrêa, M. and D. Camotim (2002). "On the differentiation of the Rodrigues formula and its significance for the vector-like parameterization of Reissner-Simo beam theory". In: *International Journal for Numerical Methods in Engineering* 55, pp. 1005–1032. URL: https://doi.org/10.1002/nme.532.

Ritto-Corrêa, M. and D. Camotim (2008). "On the arc-length and other quadratic control methods: Established, less known and new implementation procedures". In: *Computers & Structures* 86, pp. 1353–1368. URL: https://doi.org/10.1016/j.compstruc.2007.08.003.

Riziotis, V. (2003). "Aerodynamic and aeroelastic analysis of dynamic stall on wind turbine rotors". PhD thesis. NTUA, Athens.

Riziotis, V., P. Chaviaropoulos, and S. Voutsinas (1996). "Development of a state-of-the art aeroelastic simulator for horizontal axis wind turbines. Part 2: Aerodynamic aspects and application". In: *Wind Engineering* 20(6), pp. 423–440. URL: https://www.jstor.org/stable/43749810.

Riziotis, V. and S. Voutsinas (1997). "GAST: A general aerodynamic and structural prediction tool for wind turbines". In: *Proceedings of the EWEC conference (Dublin Castle, Ireland)*.

Romero, I. and F. Armero (2002). "An objective finite element approximation of the kinematics of geometrically exact rods and its use in the formulation of an energy-momentum conserving scheme in dynamics". In: *International Journal for Numerical Methods in Engineering* 54, pp. 1683–1716. URL: https://doi.org/10.1002/nme.486.

Romero, Ignacio (2004). "The interpolation of rotations and its application to finite element models of geometrically exact rods". In: *Computational Mechanics* 34, 121–133. URL: DOI10.1007/s00466-004-0559-z.

— (2008). "A comparison of finite elements for nonlinear beams: the absolute nodal coordinate and geometrically exact formulations". In: *Multibody System Dynamics* 20, pp. 51–68. URL: http://dx.doi.org/10.1007/s11044-013-9374-7.

Sapountzakis, E.J. and I.C. Dikaros (2011). "Non-linear flexural-torsional dynamic analysis of beams of arbitrary cross section by BEM". In: *International Journal of Non-Linear Mechanics* 46, pp. 782–794. URL: 10.1016/j.ijnonlinmec.2011.02.012.

Saravanos, D. et al. (2006). "A shear beam finite element for the damping analysis of tubular laminated composite beams". In: *J. Sound Vib.* 291 (3-5), pp. 802–823. URL: https://doi.org/10.1016/j.jsv.2005.06.045.

Serafeim, Giannis P. et al. (2022). "Optimized blade mass reduction of a 10MW-scale wind turbine via combined application of passive control techniques based on flap-edge and bend-twist coupling effects". In: *J. Wind Eng. Ind. Aerod.* 222, 105002. URL: https://doi.org/10.1016/j.jweia.2022.105002.

Silvestre, N., D. Camotim, and N.F. Silva (2011). "Generalised Beam Theory Revisited: from the Kinematical Assumptions to the Deformation Mode Determination". In: *International Journal of Structural Stability and Dynamics* 11.5, pp. 969–997. URL: https://doi.org/10.1142/S0219455411004427.

Simo, J. C. (1985). "A finite strain beam formulation. The three-dimensional dynamic problem. Part I". In: *Computer Methods in Applied Mechanics and Engineering* 49, pp. 55–70. URL: https://doi.org/10.1016/0045-7825(85)90050-7.

Simo, J. C., N. Tarnow, and M. Doblare (1995). "Non-linear dynamics of three-dimensional rods: exact energy and momentum conserving algorithms". In: *International Journal for Numerical Methods in Engineering* 38, 1431–1473. URL: https://doi.org/10.1016/0045-7825(92)90115-Z.

Simo, J. C. and L. Vu-Quoc (1986a). "A three-dimensional finite-strain rod model. Part II: Computational aspects". In: *Computer Methods in Applied Mechanics and Engineering* 58, pp. 79–116. URL: https://doi.org/10.1016/0045-7825(86)90079-4.

— (1988). "On the dynamics in space of rods undergoing large motions - A geometrically exact approach". In: *Computer Methods in Applied Mechanics and Engineering* 66, pp. 125–161. URL: https://doi.org/10.1016/0045-7825(88)90073-4.

Simo, J. C. and L. Vu-Quoc (1991). “A geometrically-exact rod model incorporating shear and torsion-warping deformation”. In: *International Journal of Solids and Structures* 27, pp. 371–393. URL: https://doi.org/10.1016/0020-7683(91)90089-X.

Simo, J. C. and K. K. Wong (1991). “Unconditionally stable algorithms for rigid body dynamics that exactly preserve energy and momentum”. In: *International Journal for Numerical Methods in Engineering* 31, pp. 19–52. URL: https://doi.org/10.1002/nme.1620310103.

Simo, J.C. and L. Vu-Quoc (1986b). “On the Dynamics of Flexible Beams Under Large Overall Motions - The Plane Case: Part I”. In: *Journal of applied mechanics* 53(4), pp. 849–854. URL: https://doi.org/10.1115/1.3171870.

— (1986c). “On the Dynamics of Flexible Beams Under Large Overall Motions - The Plane Case: Part II”. In: *Journal of computational and nonlinear dynamics* 53(4), pp. 855–863. URL: https://doi.org/10.1115/1.3171871.

Sonneville, V., A. Cardona, and O. Brüls (2014). “Geometrically exact beam finite element formulated on the special Euclidean group $SE(3)$”. In: *Computer Methods in Applied Mechanics and Engineering* 268, pp. 451–474. URL: https://doi.org/10.1016/j.cma.2013.10.008.

Souza Neto, E.A. de and Y.T. Feng (1999). “On the determination of the path direction for arc-length methods in the presence of bifurcations and ’snap-backs’”. In: *Computer Methods in Applied Mechanics and Engineering* 179, pp. 81–89. URL: https://doi.org/10.1016/S0045-7825(99)00042-0.

Spurrier, R. A. (1978). “Comment on "Singularity-Free Extraction of a Quaternion from a Direction-Cosine Matrix"”. In: *Journal of spacecraft and rockets* 15, pp. 255–255. URL: https://doi.org/10.2514/3.57311.

Stäblein, Alexander R. and Morten H. Hansen (2016). “Timoshenko beam element with anisotropic cross-sectional properties”. In: *Proceedings of the ECCOMAS Congress (Crete, Greece)*.

Tursa, James. *Angle from rotation matrix*. Available at https://www.math-forums.com/threads/angle-from-rotation-matrix.171323/page-2..

Voutsinas, S.G., V.A. Riziotis, and P. Chaviaropoulos (1997). “Non-Linear Aerodynamics and Fatigue Loading on Wind Turbines Operating at Extreme Sites”. In: *35th AIAA Annual Meeting, Reno, Nevada, U.S.A.* AIAA paper 97-0935.

Wang, Kai, Vasilis A. Riziotis, and S.G. Voutsinas (2017). “Aeroelastic stability of idling wind turbines”. In: *Wind Energy Science* 2, pp. 415–437. URL: https://doi.org/10.5194/wes-2-415-2017.

Wang, Lin, Xiongwei Liu, and Athanasios Kolios (2016). “State of the art in the aeroelasticity of wind turbine blades: Aeroelastic modelling”. In: *Renewable and Sustainable Energy Reviews* 64, pp. 195–210. URL: https://doi.org/10.1016/j.rser.2016.06.007.

Wang, Q. et al. (2014). "Nonlinear Legendre Spectral Finite Elements for Wind Turbine Blade Dynamics". In: *To be presented at the 32nd ASME Wind Energy Symposium National Harbor*. Vol. Maryland, January 13-17. National Renewable Energy Laboratory, Colorado School of Mines.

Wang, Qi et al. (2017). "BeamDyn: a high-fidelity wind turbine blade solver in the FAST modular framework". In: *Wind Energy* 20, pp. 1439–1462. URL: https://doi.org/10.1002/we.2101.

Wikipedia. *Aeroelasticity*. Available at https://en.wikipedia.org/wiki/Aeroelasticity.

— *Axis-angle representation*. Available at https://en.wikipedia.org/wiki/Axis-angle_representation.

— *Composite material*. Available at https://en.wikipedia.org/wiki/Composite_material.

— *Differentiable manifold*. Available at https://en.wikipedia.org/wiki/Differentiable_manifold.

— *Exponential map (Lie theory)*. Available at https://en.wikipedia.org/wiki/Exponential_map_(Lie_theory).

— *Lie group*. Available at https://en.wikipedia.org/wiki/Lie_group.

— *Manifold*. Available at https://en.wikipedia.org/wiki/Manifold.

— *Tangent space*. Available at https://en.wikipedia.org/wiki/Tangent_space.

Yu, W. et al. (2002a). "Validation of the variational asymptotic beam sectional analysis (VABS)". In: *AIAA J.* 40 (10), pp. 2105–2113. URL: https://doi.org/10.2514/2.1545.

Yu, Wenbin et al. (2002b). "On Timoshenko-like modeling of initially curved and twisted composite beams". In: *International Journal of Solids and Structures* 39, pp. 5101–5121. URL: http://dx.doi.org/10.2514/6.2000-1405.